COLLOIDAL GEOCHEMISTRY OF SPELEOTHEM-FORMING GROUNDWATERS

by

ADAM HARTLAND

A thesis submitted to the
University of Birmingham for the degree of
DOCTOR OF PHILOSOPHY

School of Geography, Earth and Environmental Sciences
College of Life and Environmental Sciences
University of Birmingham
United Kingdom
March 2011

ABSTRACT

Natural aquatic colloids (solids with dimensions between 1 nm and 1 μm) were studied in cave waters that feed secondary carbonates [speleothems]. Results show that during hydrologically quiescent periods, trace metal (Tr) binding (e.g. Cu, Ni, Co) is dominated by humic-like, natural organic matter (NOM), with the smallest NOM-Tr complexes (≤1 to ca. 4 nm diameter) being the least labile at high pH (>pH 10). Partitioning of NOM:Tr between solution and crystal occurs minimally for the strongest complexes, providing a measure of NOM adsorption. Rapid fluxes of coarse (>100 nm) soil organic matter (SOM) and Tr in dripwaters often follow peak infiltration events, the coarse fraction of NOM quenching fluorescence in finer fractions (<100 nm). Termed 'high-flux' (HF), this mode of NOM-metal transport contrasts with the humic-like or 'low-flux' (LF) mode both hydrologically and chemically, resulting in shifts in trace metal ratios (e.g. Cu:Ni) which are characteristic of changes in the competitive binding of metals for suitable sites in NOM, and diagnostic of qualitative shifts in NOM composition (i.e. relatively more aromatic/hydrophobic). This process becomes manifest in speleothems, resulting in high- and low-flux trace metal end-members and providing information on NOM aromaticity. Changes in HF:LF metal ratios in speleothems are linked to processes in soils which are ultimately mediated by climate (i.e. ambient temperature and infiltrating precipitation); they may provide information on infiltrating precipitation, on the occurrence of surface disturbances (e.g. deforestation) and NOM composition. HF:LF indices complement the existing array of speleothem climate proxies, but each specific system and setting must be understood to ensure their proper interpretation.

For Abbie

ACKNOWLEDGMENTS

I am indebted to so many, both professionally and personally for making this last four years both successful and greatly rewarding. Firstly, to my wonderful wife Abbie, thank you for supporting me and for believing in me. To my son Zachery, thank you for allowing me to work most of the time, and for preventing me from working the rest of the time. Thanks to my parents and wider family for their enduring love and support; and to my brother for convincing me that I am a scientist and for his endless patience in tutoring me in the early years. Thanks also to Carol Jones for providing a perfect working environment and a plentiful supply of baking.

I must also acknowledge my superb supervisors- Ian Fairchild and Jamie Lead, the best supervisory team I could have asked for. In particular, thank you Ian, for always doing your honest best by me, for all the opportunities you put my way and for including me in your 'academic family'. I must also thank Graham Fenwick for getting me started in research, Sandy Milner for making it all possible and two (nameless) drunken geologists for convincing me to take on the PhD at all.

Much of the research conducted over the last four years would have not been possible without the generous contributions of Mohammed Baalousha (TEM and Fl-FFF training), Yon Ju Nam (AFM analyses), Stephen Baker (ICP-MS analyses and training), Andy Baker (fluorescence and TOC training), Ian Boomer (stable isotope analyses and training),

Jonathon Dredge (scanning stalagmite fluorescence analyses), Hao Zhang (DGT training and interpretation), and Wolfgang Müller (LA-ICP-MS analyses and training). Thanks also to Gretchel Coldicott, Jamie Peart, Richard Thompson, Paul Hands, Aruna Mistry, Andy Moss, Steve Swoffer, Gillian Kingston and Jane Harris for lab, field, technical and administrative support, without which, most likely nothing would have got off the ground.

Thanks to Anna De Momi and Renza Miorandi for saving me from being lost in translation more than once during my Italian fieldwork and thanks to Andrea Borsato for facilitating access to Grotta di Ernesto. Special thanks also to Alan Walker and the staff of Poole's Cavern and to Arthur Price of Frocester Court for invaluable assistance with UK fieldwork. Thanks also to John Gunn for getting me started, for helping with site selection and for your bottomless enthusiasm for caves. Finally, thanks to all those (once) of Room 425 and 325, for making this a tolerable experience and for many a good time in 'Staffy'- getting to know you all has made this a worthwhile experience in itself.

This research was undertaken with financial support from the Natural Environment Research Council (NERC) (PhD studentship NER/S/A/2007/14396) and partially via funding through grant NE/G009317/1 (IJF, JRL, HZ investigators) and through an award to AH by the British Cave Research Association (BCRA).The support of the NERC Facility for Environmental Nanoscience Analysis and Characterization, University of Birmingham and its technical staff is also gratefully acknowledged.

CONTENTS

LIST OF TABLES

LIST OF FIGURES

ABBREVIATIONS

A	Area
AAS	Atomic Absorption Spectroscopy
AEM	Alkaline Earth Metals
AFM	Atomic Force Microscopy
Al	Aluminium
Ba	Barium
Ca	Calcium
$CaCl_2$	Calcium Chloride
$CaCO_3$	Calcium Carbonate (calcite)
Cd	Cadmium
C_{DGT}	Concentration DGT
C_e	Concentration of the eluted resin (DGT)
CEC	Cation Exchange Capacity
C_i	Initial concentration in solution (DGT)
C_f	Final concentration in solution (DGT)
Cl	Chloride
Co	Cobolt
CO_2	Carbon Dioxide
CO_3	Carbonate
Cr	Chromium
Cu	Copper
D	Diffusion Coefficient
d_H	Hydrodynamic diameter (Fl-FFF)
DGT	Diffusive Gradients in Thin Films
DIC	Dissolved Inorganic Carbon
DOC	Dissolved Organic Carbon
DOM	Dissolved Organic Matter
Em	Emission (fluorescence)
ERN	Grotta di Ernesto
EPS	Extracellular Polymeric Substances
Ex	Excitation (fluorescence)
EXAFS	Extended X-ray Absorption Fine Structure
FA	Fulvic Acid
FAAS	Flame Atomic Absorption Spectroscopy
Fe	Iron
FI	Fluorescence Intensity
FFF	Field-Flow Fractionation
Fl-FFF	Flow Field-Flow Fractionation
g	Gram
GCMS	Gas Chromatography Mass Spectrometry
h	Hour

HA	Humic Acid
HCl	Hydrochloric Acid
HCO_3	Bicarbonate
HMW	High Molecular Weight
HNO_3	Nitric Acid
HS	Humic Substances
I	Ionic Strength
IHSS	International Humic Substances Society
IC	Ion Chromatography
ISC	Inner Sphere Complex
ICP-MS	Inductively Coupled Plasma Mass Spectrometry
IR-MS	Isotope Ratio Mass Spectrometry
IRL	Inclusion Rich Layers
K	Potassium
L	Litre
LA-ICP-MS	Laser Ablation Inductively Coupled Plasma Mass Spectrometry
LBGM	Lower Balls Green Mine
LMW	Low Molecular Weight
LD	Limit of Detection
Ln	Lanthanide
M	Molar
m	Metre
meq	Milli equivalent
Mg	Magnesium
mM	Milli-molar
mm	Milli-metre
mS	Milli-Siemens
Mn	Manganese
N_2	Nitrogen Gas
Na	Sodium
NaCl	Sodium Chloride
$NaNO_3$	Sodium Nitrate
NaOH	Sodium Hydroxide
ng	Nano Gram
Ni	Nickel
NICA	Non Ideal Competitive Adsorption
NOM	Natural Organic Matter
NPOC	Non-Purgable Organic Carbon
O_2	Oxygen Gas
OC	Organic Carbon
OM	Organic Matter
OP	Open Pore (DGT)
OSC	Outer Sphere Complex
P	Phosphorus
Pb	Lead

PC	Poole's Cavern
PCP	Prior Calcite Precipitation
R^2	Coefficient of determination for a fitted regression curve
REE^{3+}	Rare Earth Elements
RG	Restrictive Gel (DGT)
RSD	Relative Standard Deviation (%)
S	Siemens
SEM	Scanning Electron Microscopy
SEM-EBD	Scanning Electron Microscopy Electron Backscatter Diffraction
Si	Silicon
SO_4	Sulphate
Sr	Strontium
SRFA	Suwannee River Fulvic Acid
SSA	Specific Surface Area
t	Time
T	Temperature
TEM	Transmission Electron Microscopy
Ti	Titanium
TOC	Total Organic Carbon
TM	Transition Metals
µg	Microgram
µm	Micrometer
µmol	Micro-molar
µS	Micro-Siemens
µXRF	Micro X-ray Fluorescence
UV	Ultra Violet
V	Vanadium
V_A	Attractive van der Waals force
Ve	Volume of acid added to elute resin (DGT)
Vg	V_g Volume of the resin layer (DGT)
V_R	Retention volume (Fl-FFF)
V_R	Repulsive electrostatic potential
WHAM	Windermere Humic Aqueous Model
XANES	X-ray Absorption Near Edge Structure
X-EDS	X-ray Energy Dispersive Spectroscopy
Y	Yttrium
Zn	Zinc
z/r	Ionic potential (charge/radius)
Δg	Diffusion layer thickness (DGT)
δ	Delta (stable isotope notation)
‰	per mil (Parts per thousand- stable isotope notation)

1. INTRODUCTION

1.1 RESEARCH CONTEXT

This study focuses on the role of natural aquatic colloids in speleothem-forming groundwaters. Specifically, it seeks to answer questions relating to their role in influencing the solution chemistry of karstic groundwaters throughout the hydrologic year, and ultimately the chemical composition of speleothems.

The chemical composition of precipitates forming in cave environs [speleothems] reflect both the composition of their parent waters and the physical conditions (e.g. ambient temperature, fluid exchange processes) prevailing at the time of formation (Fairchild *et al.*, 2006a). In annually laminated speleothems (e.g. stalagmites and stalactites), studies of the variation in their chemical and physical properties have yielded high-resolution palaeo-records of regional and global climatic conditions, as well as information relating to possible climatic forcing mechanisms (e.g. solar variance (Wang *et al.*, 2005)). Uniquely amongst palaeo-archives, speleothems have the potential to yield intra-annual to seasonal resolution data where, for example, the cave system displays a particular hydrological sensitivity, or where the climate regime shows a distinct seasonality (e.g. in sub-tropical climates where two wet seasons predominate) (Fairchild *et al.*, 2001).

The occurrence of UV-fluorescent inclusion-rich layers (IRLs) in speleothem laminae from certain shallow cave systems has been known for some time (Baker *et al*., 1993). Most notably, Tartair, NW Scotland (Baker *et al*., 1993; Roberts *et al.*, 1998), Ballynamintra, SE Ireland (Fairchild *et al.*, 2001), and Grotta di Ernesto, NE Italy (McDermott *et al.*, 1999; Huang *et al.*, 2001; Borsato *et al.*, 2007). Detailed work on Ernesto speleothems (Huang *et al.*, 2001; Borsato *et al.*, 2007) has revealed the occurrence of annual to sub-annual trace element variations centred on these fluorescent layers, inferred to be adsorbed, co-precipitated, colloidal organic matter (organic solids with dimensions between 1 nm and 1 μm) originating from overlying soils. IRLs most probably form during the autumn in temperate forested regions when periods of high-intensity rainfall, unimpeded by canopy interception, exceed the infiltration capacity of the overlying soils and flush soil-derived organic material and associated trace metals through into the underlying cave.

IRLs provide both a visual marker of the advent of the hydrologic year, and through the coincident elemental variations may encode important information of palaeoclimatic significance (e.g. Jo *et al.*, 2010). In the studies conducted to date numerous inferences have been drawn relating to the role of colloids, yet without detailed information on colloid-metal interactions in dripwaters, the elemental variations coincident with IRLs cannot be properly interpreted.

There is currently very little information relating to the properties of natural organic matter (NOM) present within karst waters and speleothems. Little is yet known about colloids

within dripwaters, about the influence of hydrochemistry on their composition and mobility, their trace element binding behaviour, or indeed how colloid-bound metals become incorporated in speleothems

1.2 AIM AND OBJECTIVES

Aim

To understand the relationship between colloids and trace metals in dripwaters and their partitioning into speleothems in order to determine their potential as a palaeoenvironmental proxy.

Objectives

1) Characterise colloidal properties in dripwaters through appropriate bulk analyses.
2) Examine the size, speciation and metal binding properties of colloids in cave dripwaters.
3) Investigate the link between colloid-facilitated trace metal transport and hydrology.
4) Understand the processes affecting colloid-metal partitioning into calcite.
5) Determine the palaeoclimatic relevance of colloid-metal signals in speleothems.

2. LITERATURE REVIEW

2.1 SCOPE AND RELEVANCE OF REVIEW

Speleothems often exhibit annual laminae and may be precisely dated enabling information to be extracted at a range of resolutions. Indeed much recent work has focused on decoding the past magnitude and variability of climatic and biogeochemical processes based on their physical, optical and chemical properties, including: 1) fluorescence (Baker *et al.,* 1999a; 2002), 2) sulphate (concentration, $\delta^{32}S$, $\delta^{18}O$) (Wynn *et al.,* 2007; 2008), 3) carbon isotopes $\delta^{13}C$ (Genty *et al.,* 2001), 4) oxygen isotopes $\delta^{18}O$ (Baldini *et al.,* 2005), 5) trace metals (Pb, Zn, Cu, Y (Borsato *et al.,* 2007; Jo *et al.,* 2010)) and 6) organic molecules in general (Blyth *et al.,* 2008).

To date, there have been no specific studies of trace element binding by colloids in cave dripwaters and thus this review draws mainly on data from other systems. In the following sections, the themes examined in detail are (1) the colloidal properties of soils and waters (Section 2.2), (2) colloid mobilisation from soils and their chemical and physical behaviour in groundwater (Section 2.3), and (3) the controls on speleothem formation and the incorporation of organic and other impurities (Section 2.4). Within this review aspects of theory that of particular relevance are separated from the main text in boxes. Figure 2.1

summarises the four main strands of this review and indicates how these form the theoretical basis for the later chapters.

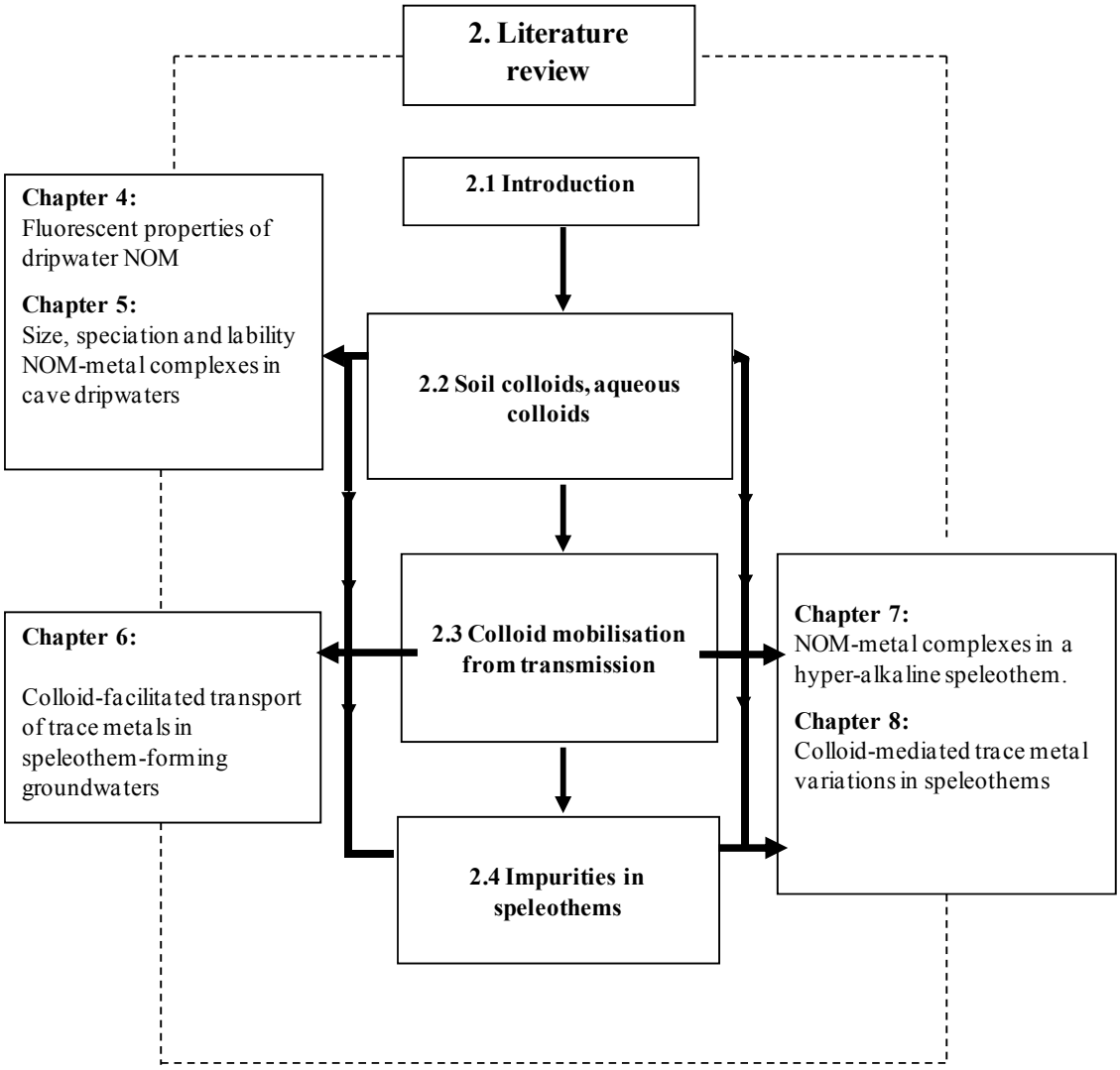

Figure 2.1 Summary of literature review structure and its relevance to the later chapters.

2.2 SOIL COLLOIDS, AQUEOUS COLLOIDS

Soil colloids either exist in solution, or in the pore spaces between particles. Once dispersed within soil water as aqueous colloids, they may be displaced and translocated by percolating solutions. This process is central to the development of impoverished and accumulative soil horizons and ultimately, to the migration of colloids and associated trace elements into groundwater.

Box 2.1 Aqueous colloids

In water, the term 'colloid' encompasses all solids which are larger than individual molecules (> ca. 1 nm), but which are small enough to be microscopic (< ca. 1 μm). Colloids are characterised by high surface to volume ratios or specific surface areas (SSA), they typically (at the pH of natural waters) have a negative electrostatic charge at their surfaces, and tend to remain dispersed in water, forming a suspension. Because of these properties, up to 100% of trace elements in natural waters may be bound by colloidal materials (depending on the element measured). Materials below 1 nm are considered 'truly dissolved' and include small organic molecules which may also be of importance in trace metal binding (Lead & Wilkinson, 2006).

Aqueous colloids are recognised to be of central importance to trace element binding in natural waters (Lead & Wilkinson, 2006) and increasingly, to trace element transport through porous and fractured media (Doucet *et al.,* 2007). This importance largely relates to the sheer size of the colloidal pool: small colloids are typically present in numbers which are orders of magnitude greater than particulates (e.g. 10^6 times more 10 nm colloids than the equivalent number of 1 μm particles) (Doucet *et al.,* 2007). Natural colloidal

suspensions are complex, heterogeneous mixtures of a range of materials in intimate associations.

2.2.1 Colloidal composition of soil

Like other natural waters the chemistry of soil solution is governed to a large extent by its colloidal content (Ashman & Puri, 2002). Soils contain a range of materials in the colloidal size range which possess a surface electrostatic charge (Fig. 2.2 and Fig. 2.3), these include: clay minerals, hydrous oxides (iron, aluminium and manganese), bacteria and microbial extra polymeric substances (EPS), and other organic biopolymers, often collectively termed 'humic substances' (HS). Geographical influences play a major role in determining the colloidal composition of a given soil, being as it is, the product of the materials and processes involved in its formation and development:

> Soil formation = climate, parent material, topography, organisms (plants and animals) and time.
>
> (Jenny, 1941).

Of these factors, climate exerts the dominant influence on soil colloidal composition. In the tropics, high rates of mineralization of organic matter drive the weathering of clays leading to the formation of secondary mineral horizons. In soils receiving high levels of rainfall, the products of this weathering process (e.g. Fe^{2+}, Al^{3+} and Mn^{2+}) may be translocated down the soil profile (Ashman & Puri, 2002) (see Table 2.1; Master soil horizons; and Table 2.2;

which describes the major features of diagnostic horizons used to differentiate between mineral soils).

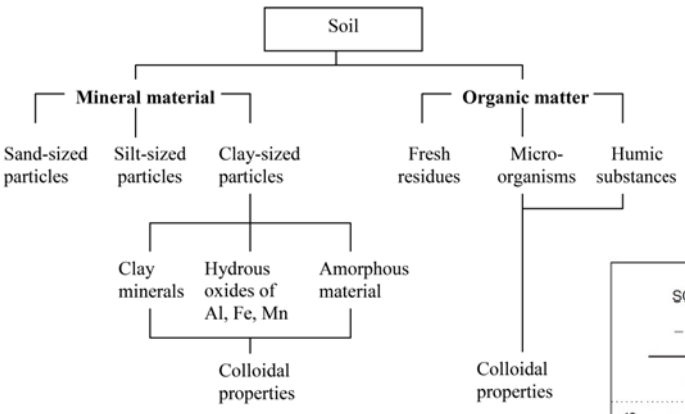

Figure 2.2 Types of colloidal materials found in soils (redrawn from Ashman & Puri, 2002).

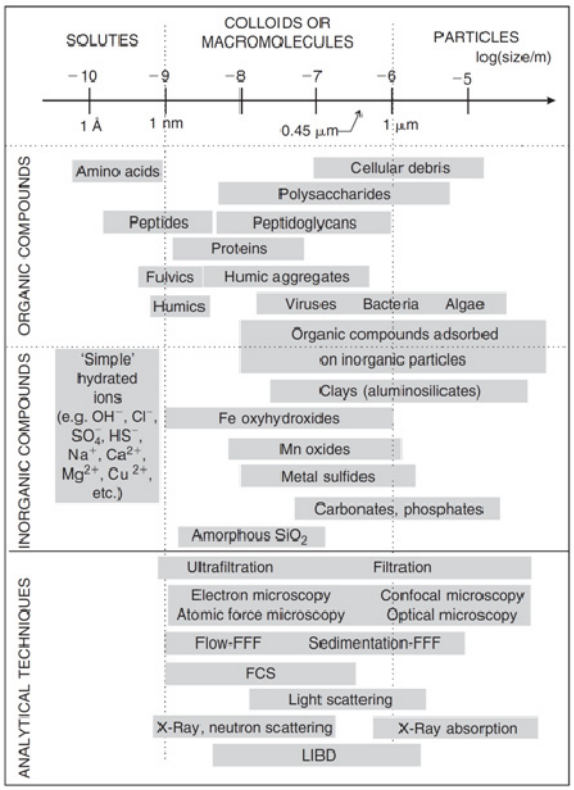

Figure 2.3 Size distributions of various types of environmental colloids and particles and several of the analytical techniques used to characterise them. Abbreviations employed: FFF=field-flow fractionation; FCS=fluorescence correlation spectroscopy; LIBD=laser induced breakdown detection (Source: Lead & Wilkinson, 2006).

O	Loose leaves and organic debris, largely undecomposed
O	Organic debris, partially decomposed
A	A dark-coloured horizon of mixed mineral and organic matter with much biological activity
E	A light-coloured horizon of maximum eluvation
EB	Transitional to B but more like E than B: may be present
BE	Transitional to B but more like B than E: may be present
B	Maximum accumulation of silicate clay minerals or of sesquioxides and organic matter
BC	Transitional to C but more like B than C: may be absent
C	Weathered parent material, occasionally absent,: formation of horizons may follow weathering so closely that the A, E or B horizon rests on consolidated rocks
R	Layer of consolidated rock beneath the soil

Table 2.1 Master soil horizons (Redrawn from: Gerrard, 2000)

Diagnostic horizon (and designation)	Major features
Surface horizons = epipedons	
Mollic (A)	Thick, dark coloured, high base saturation, strong structure
Umbric (A)	Same as mollic except low base saturation
Ochric (A)	Light coloured, low organic content, may be hard and massive when dry
Melanic (A)	Thick, black, high in organic matter (>6% organic C) common in volcanic ash soils
Histic (O)	Very high in organic content, wet during some part of the year
Anthropic (A)	Human-modified mollic-like horizon, high in available P
Plaggen (A)	Human-made sod-like horizon created by years of manuring
Subsurface horizons	
Argillic (Bt)	Silicate clay accumulation
Natric (Btn)	Argillic, high in sodium, columnar or prismatic structure
Spodic (Bhs)	Organic matter, Fe and Al oxides accumulation
Cambic (Bw, Bg)	Changed or altered by physical movement or by chemical reactions
Agric (A or B)	Organic and clay accumulation just below plow layer resulting from cultivation
Oxic (Bo)	Highly weathered, primarily mixture of Fe, Al oxides and non-sticky-type silicate clays
Duripan (qm)	Hardpan, strongly cemented by silica
Fragipan (x)	Brittle pan, usually loamy textured, weakly cemented
Albic (E)	Light coloured, clay and Fe and Al oxides mostly removed
Calcic (k)	Accumulation of $CaCO_3$ or $CaCO_3 \cdot MgCO_3$
Gypsic (y)	Accumulation of gypsum
Salic (z)	Accumulation of salts
Kandic	Accumulation of low-activity clays
Petrocalcic (km)	Cemented calcic horizon
Petrogypsic (ym)	Cemented gypsic horizon
Placic (sm)	Thin pan cemented by iron alone or with manganese and organic matter
Sombric (Bh)	Organic matter accumulation
Sulphuric	Highly acid with Jarosite mottles

Table 2.2 Major features of diagnostic horizons in mineral soils used to differentiate at the higher levels of soil taxonomy (Source: Brady & Weil, 1996)

2.2.2 Fundamentals of colloidal suspensions

Colloidal materials are considered as distinct from particulates because of their propensity to remain in solution. Under quiescent conditions particulates above 1 μm in size will eventually settle out of suspension under the influence of gravity, whilst colloidal materials are generally stable (Peavy *et al.,* 1985) and will not agglomerate efficiently: in freshwaters only around 1 in 10^3 – 10^6 collisions may lead to successful agglomeration (Stumm and Morgan, 1996).

Box 2.2 Charge system in a colloidal suspension

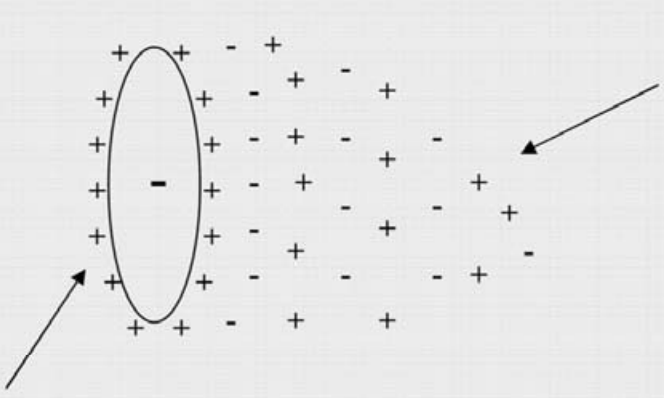

High concentrations of counter ions having a charge which is opposite to the colloidal primary charge lead to compression of the electric double layer. The effectiveness with which counter ions are able to destabilise negatively charged colloids increases markedly with the charge of the counter ion. Compared with Na^+, Ca^{2+} is 100 times more effective, and Al^{3+} 1000 times more effective.

(Diagram adapted from Peavy *et al*, 1985, p. 132).

The surface charge of colloids is equalised by counter ions, which form a double layer around the particle (Box 2.2). Two opposing forces act on colloids which come into close proximity: the repulsive electrostatic potential V_R, created by the 'halo' of counter ions surrounding each colloid, and the attractive van der Waals force, V_A (Peavy *et al.,* 1985; Howard, 1998). Fig. 2.4*a* shows the combined effect of forces V_A and V_R. The net force is repulsive at greater distances and becomes attractive only after overcoming a net repulsive force. A means of overcoming this energy barrier is needed before agglomeration can take place e.g. under highly ionic conditions the double layer becomes compressed and the net interaction is one of attraction (Fig. 2.4*b*).

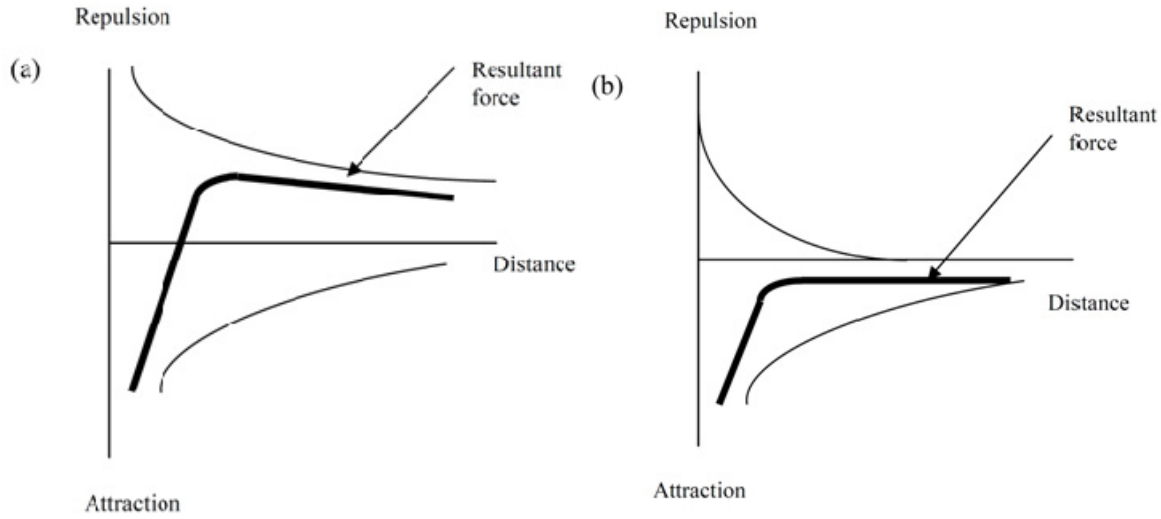

Figure 2.4 (a) Combined forces acting on two interacting particles in a low ionic strength medium. (b) Combined forces acting on two interacting particles under high ionic strength conditions (Redrawn from: Howard, 1998).

2.2.3 The major soil colloids and their chemical properties

To a large extent, colloids control the storage and release of trace elements in soils through reversible ion exchange (adsorption) reactions between their surfaces and the soil solution. The principles that govern these adsorption reactions are thought to be similar, regardless of the size and chemistry of the colloids (Gaillard, 2007) and typically occur via either outer-sphere or inner-sphere surface complexation with surface functional groups (Box 2.3). This is the case for phylosilicate clay surfaces, hydrous oxide surfaces and the various oxygen-containing functional groups of organic and inorganic compounds (Tipping, 2001; Avena *et al.,* 2003; Gaillard, 2007). Adsorption may also occur through formation of surface precipitates (e.g. multinuclear surface overgrowths), ionic substitution, and by filling of atomic vacancies, but these mechanisms are considered less common (Gaillard, 2007).

Outer-sphere complexes reflect the coordinative environment of ions in solution: the oxygen donor atom is either from a water molecule or from the colloid surface (Gaillard, 2007). **Outer-sphere complexes therefore correspond to a situation where the metal is likely to be labile (exchangeable between surface complexes and solution) in response to changes in the ionic composition or pH of soil solution (Gaillard, 2007).** This is typical of clays and is reflected in the largely pH dependent binding of metals by soils, commonly referred to as the CEC (cation exchange capacity) (McBride, 1994; Ashman & Puri, 2002).

Box 2.3 Inner-sphere and Outer-sphere complexation

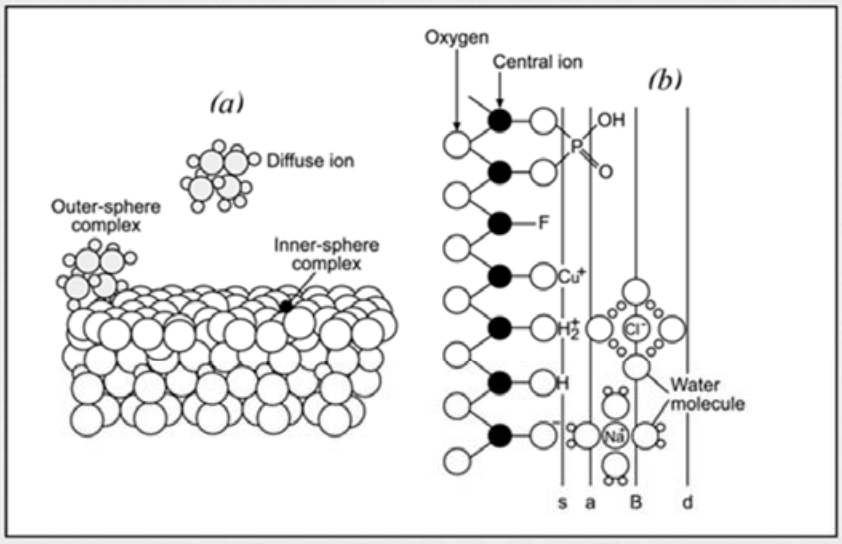

(a) Surface complex formation of an ion (e.g. cation) at the water-mineral interface. The ion may form an inner-sphere complex (chemical bond), an outer-sphere complex (ion pair), or be in the diffuse swarm of the electric double layer.

(b) Schematic portrayal of a hydrous mineral surface, showing planes associated with surface hydroxyl groups (s), inner-sphere complexes (a), outer-sphere complexes (β), and the diffuse ion swarm (d). (Source: Stumm & Morgan, 1996).

2.2.3.1 Phylosilicate Clays (layer silicates)

Layer silicates occur as weathering products (secondary minerals) in the clay fraction of soils (Sparks, 1995). Although many primary minerals occur in soils, including island, chain, and framework silicates, layer (sheet) silicates are the most stable and persistent fraction (Sparks, 1995). Layer silicates can be subdivided into 1:1 clays having one layer of silica to one layer of aluminium hydroxide, and 2:1 clays which have two layers of silica to one layer of aluminium hydroxide (Ashman & Puri, 2002). These structural differences

result in different charge characteristics depending on the extent of isomorphous substitution, i.e. incorporation of ions of lower charge but of similar size within the sheet. The charge of 2:1 clays can be both permanent and variable, whereas 1:1 clays possess only variable charge (Ashman & Puri, 2002) (Table 2.2).

Charge defects are also responsible for important structural differences between types of 2:1 clays. If substitution occurs mainly in the silicate sheet (as in muscovite and illite), charge is relatively localised and is neutralised by potassium ions which link adjacent minerals together (Ashman & Puri, 2002). Alternatively, if substitution mainly occurs in the aluminium hydroxide sheet (as in smectites like montmorillonite and hectorite) a more delocalised charge arises that allows water to penetrate between individual minerals, thereby, enabling delamination, and offering a larger surface area for interactions with dissolved ions (Ashman & Puri, 2002; Kaufhold & Dohrmann, 2008). Hence, smectites exhibit the propensity towards colloidal dispersivity.

Adsorption of cations onto layer silicates takes place via both outer-sphere complexation at permanently charged basal surfaces (2:1 clays only), and inner-sphere complexation at oxide-type hydroxyl groups at edge surfaces (1:1 and 2:1 clays) (Strawn & Sparks, 1999; Bourg *et al.,* 2007). Outer-sphere complexes are insensitive to pH changes and are considered exchangeable because adsorption is via electrostatic attraction (Zhang *et al.,* 2001). Edge groups (inner-sphere) are formed from broken and hydrolysed Al-O and Si-O bonds which act as Lewis acids (electron acceptors) and undergo protonation-deprotonation in a normal pH range (Strawn & Sparks, 1999). For example, montmorillonite edge

hydroxyl groups deprotonate above pH ≈ 8.5 (Avena & De Pauli, 1998; Bourg *et al.,* 2007), via reactions of the form:

(2.1) $\equiv S\text{-}OH \leftrightarrow \equiv S\text{-}O + H^+$

≡S represents the structural cation(s) to which a surface O atom is attached. Edge site valence and additional surface protons are omitted for convenience (Bourg *et al.,* 2007).

Montmorillonites retain their overall negative charge even at low pHs, because proton adsorption takes place mainly via equilibrium H^+-Na^+ exchange (Avena & De Pauli, 1998; Avena *et al.,* 2003; Bourg *et al.,* 2007):

(2.2) $\equiv XNa + H^+ \leftrightarrow \equiv XH + Na^+$

The edge surface chemistry of layer silicates becomes increasingly important at high pH. Avena & De Pauli (1998) demonstrated that proton adsorption-desorption kinetics in montmorillonite increase above pH 8.5, and slow down below this value. The experimental results of Baeyens and Bradbury (1997) and Duc *et al.* (2005) (Fig. 2.5) are instructive in this respect: both acid-base titration curves decline sharply after ~pH 9 indicating deprotonation from edge sites.

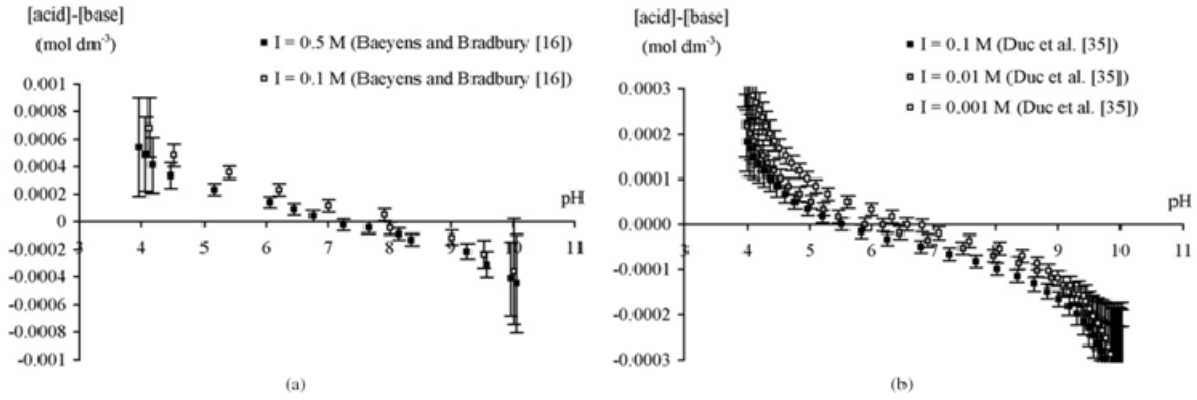

Figure 2.5 Acid-base titration data of Baeyens and Bradbury (1997) (SWy-1 Na-montmorillonite, a) and Duc *et al.* (2005) (MX-80 Na-montmorillonite, b) (Source: Bourg *et al.,* 2007).

Adsorption of divalent alkaline earth metal (AEM) ions such as Ca^{2+}, Mg^{2+}, Sr^{2+} and Ba^{2+} is generally non-specific, i.e. involving outer-sphere surface complexation (Chen & Hayes, 1999; Zhang *et al.,* 2001), but a small amount of adsorption does occur via inner-sphere complexation at edge sites (Kim *et al.,* 1996; Parkman *et al.,* 1998; Zhang *et al.,* 2001). The transition metal (TM) ions Co^{2+}, Ni^{2+}, and Zn^{2+} form inner-sphere surface complexes with layer silicates, and display an increasing affinity at higher pH values (O'Day *et al.,* 1994; Scheidegger *et al.,* 1997; Schlegel *et al.,* 1999; Schlegel *et al.,* 2001). Unlike other TM ions, Pb^{2+} sorption to layer silicates occurs typically via outer-sphere complexation under low ionic strength and variable pH conditions (Strawn & Sparks, 1999; Zhang *et al.,* 2001). Inner-sphere complexation by Pb^{2+} on montmorillonite is enhanced under high ionic strength (I = 0.1 M) and pH conditions (pH 7.8) and, therefore, Pb^{2+} adsorption behaviour resembles that of the alkaline earth metals (Strawn & Sparks, 1999; Zhang *et al.,* 2001).

Interactions of metal ions with layer silicates at trace concentrations have been studied less frequently, but a review of the available data indicates that at low surface densities TM adsorption to clays may occur via multi-dentate complexation reactions with edge hydroxyl groups (O'Day *et al.,* 1994a; Scheidegger *et al.,* 1997). Thus, at lower surface loadings the amount of exchangeable (labile) metal is likely to decrease depending on the specific conditions of ionic strength, pH and residence time. Layer silicates in soils, therefore, probably act to buffer the availability of TM ions for binding with other (more mobile) mineral and organic colloids. However, 2:1 clays prone to de-lamination (e.g. montmorillonite) may potentially act as agents of trace element transport.

2.2.3.2 Oxides

The most important non-silicate minerals in soils are the Fe, Al, and Mn oxides and hydroxides. Unlike layer silicates, oxides do not develop structural charge through isomorphous substitution and do not, therefore, contribute significantly to CEC (McBride, 1994; Ashman & Puri, 2002). However, oxide surfaces do exhibit variable charge in response to changes in solution pH, and are capable of binding strongly with metal ions, as well as inorganic and organic anions (McBride, 1994; Seaman *et al*., 1999).

Inner-sphere complexation between TM ions and common metal oxides has been shown to be the predominant mechanism of adsorption (Bargar *et al.,* 1997; Alcachio *et al.,* 2001) and can be conceptualised as of the type in Equation 2.3, where complexation of M^{z+} follows deprotonation of a hydroxyl group at the hydrous oxide surface:

(2.3) $\equiv S\text{-}OH + M^{z+} \leftrightarrow \equiv S\text{-}OM + H^{+}$

As in Equations 2.1 and 2.2, edge site valence and additional surface protons are omitted for convenience.

Above pH 6, Pb^{2+} binding to hydrous iron and aluminium oxides corresponds to a bi-dentate mechanism (Bargar *et al.,* 1997; Strawn *et al.,* 1998). Similarly, Cd^{2+} adsorption to goethite studied via EXAFS (Extended X-ray Absorption Fine Structure) corresponds to inner-sphere complexation by bi-dentate double corner sharing (i.e. bridging of O atoms by adjacent Fe(III) atoms) at the goethite surface (Collins *et al.,* 1999b). Sorption of Cd^{2+} to oxide surfaces is known to be strongly pH dependent rising from 0 to 100% between pH 6 and 10 (Collins *et al.,* 1999a). However, this range of pH dependency is non-uniform amongst the oxide minerals. Adsorption experiments conducted with a Mn oxide mineral (cryptomelane, Mn_8O_{16}) demonstrated that at pH values as low as 2, up to two thirds of available cadmium had adsorbed at inner-sphere (tunnel) sites (Randall *et al.,* 1998).

The oxide minerals display a more complex array of metal binding mechanisms than clays. Adsorption of Ni^{2+} to kaolinite, for example, results in formation of a Ni-Al layered double hydroxide (LDH) which is resistant to proton dissolution (Nachtegaal & Sparks, 2003). As with the clay colloids, adsorption of metals to oxide surfaces displays a rate dependency whereby adsorption initially progresses quickly, probably reflecting electrostatic interaction

and inner-sphere complexation, followed by a slow reaction (Strawn & Sparks, 2000). The slow reaction is possibly due to one of the following factors (Strawn & Sparks, 2000):

- Slow intra-particle diffusion in porous minerals;
- formation of precipitates on surfaces;
- adsorption on sites with relatively large activation energies.

Most significantly, rates of TM desorption are typically much slower than the equivalent forward reaction (Strawn & Sparks, 2000; Peacock, 2009). This probably reflects the transformation of the TM ion into a less reactive state (e.g. surface precipitate) which requires a higher activation energy than adsorption, and hence proceeds more slowly (Strawn & Sparks, 2000), or the time-dependant intercalation of metal ions into vacancies in the mineral lattice (Peacock, 2009). One exception is Pb^{2+} desorption from mineral surfaces, which has shown to occur at a similar rate to adsorption (Strawn *et al.,* 1998). Ergo, experimental data suggest that Pb^{2+} binding affinity to mineral colloids is closer to that of the alkaline earth metals.

Experiments performed with manganese oxyhydroxide isolated from Bribin cave, Gunung Sewu, Java, Indonesia, found that adsorption capacities for Ni^{2+} (178 μmol g^{-1}), Zn^{2+} (217 μmol g^{-1}) and Cd^{2+} (285 μmol g^{-1}) exceeded reported values for synthetic and natural manganese oxides (Tiede *et al.,* 2007). Indeed, Moberly *et al.* (2009) found that Fe and Mn oxyhydroxides in contaminated river sediments dominated the sorption of Pb^{2+} and Zn^{2+}. In

freshwaters, metal oxides are generally coated with organic compounds which affect both their mobility and reactivity (Section 2.2.3.5).

2.2.3.4 Natural Organic Matter

The organic materials commonly associated with the colloidal fraction of soils are generally referred to as humic substances (HS), an operationally defined fraction representing the bulk of the recalcitrant OM in soils (Stevenson, 1994) and around 70% of natural organic matter (NOM) in freshwaters (Tipping, 2001). Humics have traditionally been conceptualised as novel categories of cross-linked, polyelectric, macromolecular structures produced by the biodegradation of plant and microbial organic materials (Stevenson, 1994). Recent studies have challenged this view, suggesting that the composition of HS can be explained as complex mixtures of identifiable plant and microbial biopolymers or closely related breakdown products (Kelleher & Simpson, 2006; Lehmann *et al.,* 2008).

Although various structures have been proposed for HS, the view that an average structure and functionality is sufficient to understand their chemical behaviour is increasingly accepted (McDonald *et al.,* 2004). HS are chemically heterogeneous, containing several major functional groups: carboxylic (COOH), alcoholic (OH), and carbonyl (C=O), as well as less abundant moieties including phenolic (-OH) and quinone (R=O) groups (Table 2.3) (Stevenson, 1994; Xia *et al.,* 1997a). **Importantly, HS composition varies depending upon the source** (e.g. soil HS vs. riverine HS) (Stern *et al.,* 2007) and the separation

technique adopted (McDonald *et al.,* 2004); thus the metal binding capacity of HS varies between systems (Baker *et al*., 2008).

The various ionisable functional sites in HS impart solubility and the ability to complex metals. Metal binding by HS has been widely studied through spectroscopic techniques such as XANES and EXAFS. The binding environments of the transition metals with soil HS have been shown to correspond to inner-sphere complexation: Cu^{2+} and Pb^{2+} (Xia *et al.,* 1997a), Co^{2+}, Ni^{2+}, Cu^{2+} and Zn^{2+} (Xia *et al.,* 1997b), and Fe^{2+} forms monodentate and bi-dentate complexes with riverine NOM (Rose *et al.,* 1998).

Acid	**Formula**	**pKa Range**
Carboxylic acids	R-COOH	1-5
Saturated alcohols	R-OH	> 14
Phenols	ar-OH	1-11
Saturated thiols	R-SH	8.5-12.5
Aromatic thiols	ar-SH	3-8
Saturated amines	$R\text{-}NH_3^+$	8.5-12.5
Aniline	$C_6H_6NH_3^+$	4.6
m-Nitroaniline	$NO_2C_6H_4NH_3^+$	2.6
Pyridine	C_5H_5NH	5.1

Table 2.3 Acidity of Organic Acids (reproduced from Stumm & Morgan, 1996).

Modelling of ion-humic binding has predicted humic-metal complexes to be the dominant species in world average river water (5 mg L^{-1} DOC, 80% fulvic acid (FA) and 20% humic acid (HA)) for the pH range 5 to 8 (Tipping & Hurley, 1992; Tang & Johannesson, 2003), including rare earth elements (REE) (Sonke and Salters, 2006).

Experimental studies have shown that carboxylic groups account for 78-90% of the total acidity of FA and 69-82% of HA (Ritchie & Perdue, 2003). Plaschke *et al.* (2004) implicated carboxylic functional groups in the binding of REE to HA. At pH values typical of natural waters (> pH 7) COOH groups are 80-100% ionised, unlike phenolic groups, which deprotonate less readily (Stamberg *et al.,* 2003). These facts have been used to justify the use of single (carboxylic) site binding models (e.g. Stern *et al.,* 2007).

The findings of experimental binding studies are, however, only relevant under the specific experimental conditions (e.g. pH, T, *I*). For example, metal loading can have a strong effect on metal-HS complexation. At high metal loading complexation is controlled by abundant weak sites, whereas, at trace metal concentrations, binding is dominated by stronger sites such as phenolic and amino-carboxylic acids, and may involve a greater degree of denticity (Buffle *et al*., 1998; Hummel *et al.,* 2000; Sonke & Salters, 2006).

Stern *et al.* (2007) studied the lanthanide (Ln) binding by a range of HS and NOM at low HS/Ln ratios. Their data show an overall increase in binding strength (log $K_{c\ LnHS}$; Equation 2.4) with decreasing ionic radius (higher z/r) from La to Lu, and increasing pH (Fig. 2.6a), in broad agreement with findings from previous studies (Glaus *et al.* 2000; Sonke & Salters, 2004; 2006). $K_{c\ LnHS}$ describes the conditional binding constant for the reaction between a lanthanide ion (Ln) and a surface functional group in a humic substance (HS):

$$\text{(2.4)} \qquad Ln^{3+} + HS^{-} = LnHS^{2+} \text{ with } K_{LnHS} = \frac{[LnHS^{2+}]}{[Ln^{3+}]\,[HS^{-}]}$$

Stern *et al.* (2007) found that different HS compositions resulted in a 2.7 log unit variation at pH 7 in log $K_{c\ LnHS}$ values. Suwannee River Fulvic Acid (SRFA) log $K_{c\ LnHS}$ was significantly lower than all other HS by around 2 orders of magnitude. The other HS analysed were 100-500 times more effective in binding REE than SRFA (Stern *et al.,* 2007). Amongst the HA analysed by Stern *et al.* (2007) (including soil, coal and peat HA), variability in log $K_{c\ LnHS}$ was relatively small (min and max average values were 12.15 and 12.60) by comparison with the effect of pH (Fig. 2.6b).

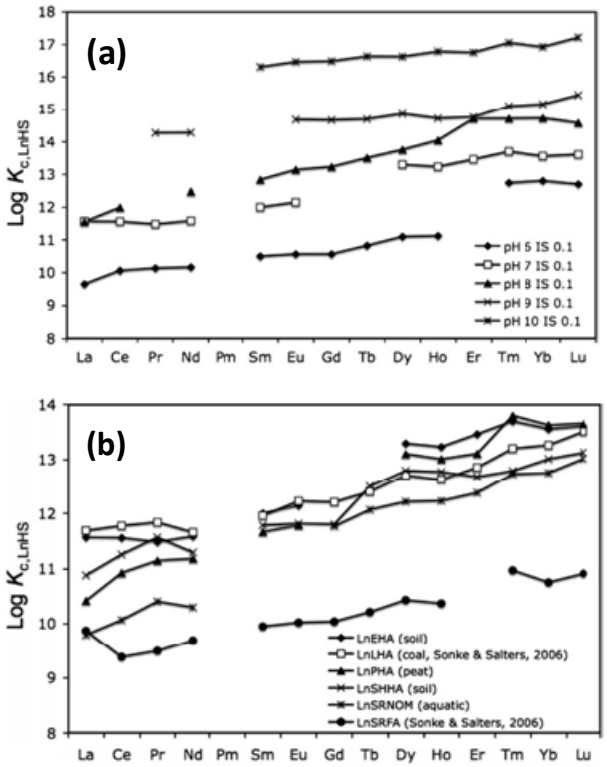

Figure 2.6 (a) LnEHA conditional binding constants at 0.1 *I* at pH 6, 7, 8, 9 and 10. (b) LnEHA conditional binding constants at pH 7 and 0.1 *I*, for EHA, PHA, SHHA, SRNOM, and LHA and SRFA (Sonke & Salters, 2006).

The pH dependency of binding capacity in HS is a result of several factors (Stern *et al.,* 2007) including the availability of stronger binding sites at high pH, including phenolic and carboxylic acids; deprotonation of acid functional groups resulting in higher overall negative charge on humic molecules, and the possible increasing importance of multi-denticity.

Geochemical variables (e.g. pH, *I*) are therefore of major significance when seeking to understand colloidal reactivity, mobility and fate. **Indeed, pH and *I* also strongly affect the competitive binding of metal ions by aquatic HS.** Metals partition between the dissolved phase and complexation sites in NOM based on their affinity for binding at available functional groups (Milne *et al*., 2003) and thus, certain groups of elements are in direct competition for binding sites in HS, e.g. Al vs. Pb (Kerndorff and Schnitzer, 1980; Alberts and Filip, 1998; Pinheiro *et al.,* 2000), whilst others are not: e.g. Ca vs. Pb (Tipping *et al.*, 1988; Pinheiro *et al.*, 1999).

Marang *et al.* (2009) examined the competition between Eu^{3+}, Ca^{2+} and Cu^{2+} for binding sites in a humic acid at pH 5.5 and found that Cu^{2+} and Eu^{3+} competed for the same classes of binding sites. Complexed Eu^{3+} was displaced at higher Cu^{2+} loadings, whereas Ca^{2+} induced only minor modifications in the Eu^{3+} coordinative environment (Marang *et al.,* 2009). Hence, colloidal binding of REE and lanthanides in karst aquifers may be limited by the presence of more reactive ions.

Other classes of NOM may be important in trace metal binding in soils and groundwaters, including: microbial exudates (Lamelas *et al.,* 2005a; 2005b); viruses (Daughney *et al.,* 2002) and bacteria (Boyanov *et al.,* 2003). The lack of information relating to trace element interactions with bio-colloids is largely related to difficulties in their characterisation rather than their scarcity (Lead & Wilkinson, 2006). Trace element binding by bacteria is likely to be pH-sensitive as with other biomolecules and organic ligands (Boyanov *et al.,* 2003; Lamelas *et al.,* 2005a).

2.2.4 Organo-mineral complexes

The preceding sections of this review form a basis for the further investigation of colloidal materials in karstic systems. In natural systems the classes of colloidal materials discussed here are rarely found in isolation, but rather are typically present as heterogeneous aggregates, referred to as organo-mineral complexes (OMCs) (Lead & Wilkinson, 2006). Organo-mineral complexes possess highly variable compositions, but three main components have been recognised to be present in such aggregates: fibrillar polysaccharides (1–10 nm wide and >100 nm long), small organic macromolecules (such as fulvic acids) and inorganic colloids (Buffle *et al.,* 1998; Fig. 2.7).

Under pH conditions typical of natural waters (i.e. >pH 6) functional groups (e.g. carboxylic) within organic acids are generally present as their conjugate base. Consequently, repulsive interactions dominate between organic polyanions and negatively charged mineral surfaces. Organo-mineral assemblage formation is hindered, therefore,

unless screened by electrolytes (Tombacz *et al.,* 1998). For example, clay-OM composites can build up through Ca^{2+} bridging between –COOH groups in HA and clay edges, faces, or lamellae (Ramos-Tejada *et al.,* 2001; Davis *et al.,* 2001).

Screening electrolytes such as Ca^{2+} may enable bridging reactions between fibrillar polysaccharides and small colloids, while small organic acids are thought to modify surface charge, possibly imparting enhanced solubility and reducing aggregation through charge stabilisation (Buffle *et al.,* 1998; Tipping *et al.,* 1998; Assemi *et al.,* 2004; Lead *et al.,* 2005). Coatings of small organic acids on inorganic colloids may also enhance or inhibit the metal binding properties of the mineral phase; binding studies include, Cu^{2+} binding to OM-goethite (Alachio *et al.,* 2001), Cd^{2+} binding to OM-goethite (Collins *et al.,* 1999), and Ni^{2+} binding to HA-kaolinite (Nachtegal & Sparks, 2003). Buerge-Weirich *et al.* (2002) concluded that adsorption of divalent transition metals (Cu^{2+}, Cd^{2+}, & Ni^{2+}) is inhibited by competition from NOM at the goethite surface at alkaline pH.

2.2.5 Summary

The preceding sections convey the complexity of natural colloid structure, stability and chemistry. In reality, natural aquatic colloids are rarely present as discrete organic or mineral particles, but instead exist in complex mixtures and aggregates within a continuum of sizes. The bulk of the colloidal pool exists below 100 nm (Galliard *et al.,* 2007), and small colloids are more stable and probably more reactive (Lead & Wilkinson, 2006). In the

following section the factors controlling their mobilisation from soils and into aquifers are discussed with reference to relevant aspects of karst geochemistry.

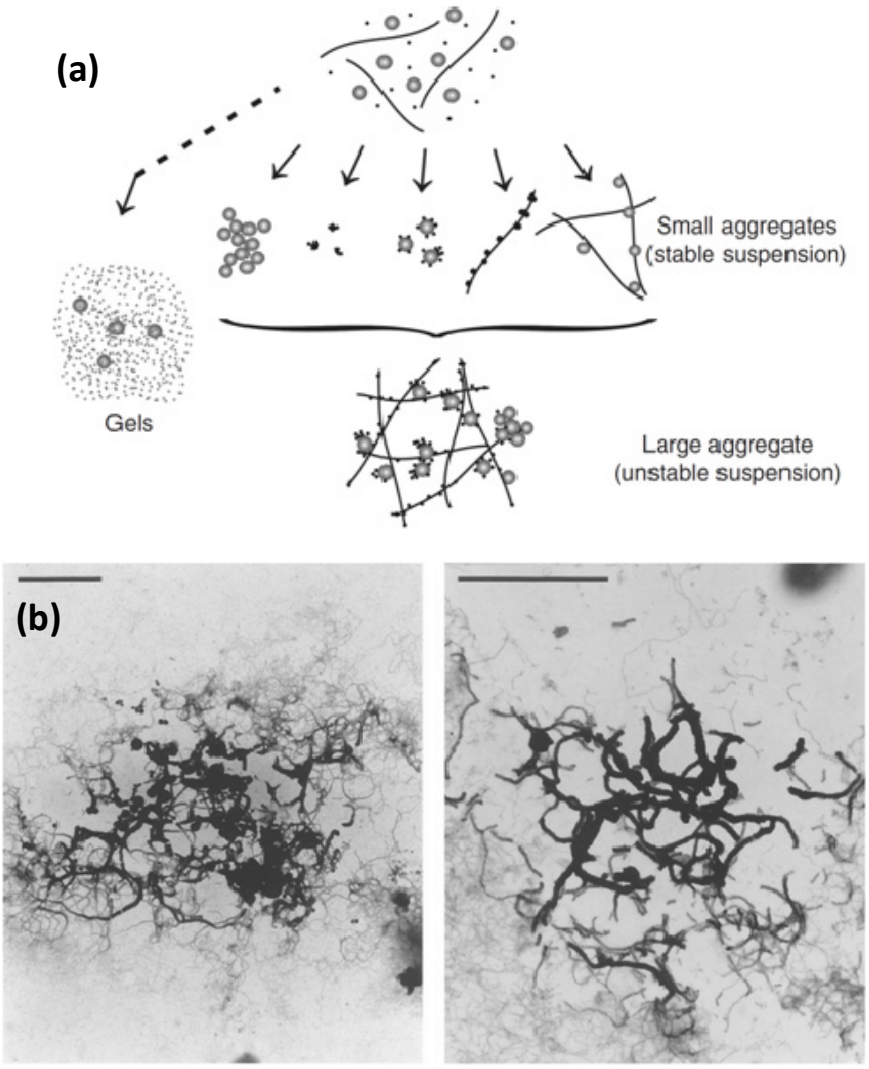

Figure 2.7 (a) Three component model of aquatic colloids relevant to aggregation processes. Small points are fulvic-type and other molecules such as sugars and amino acids, circles represent inorganic colloids and lines are biopolymers such as polysaccharide fibrils (Source: Buffle *et al.,* 1998). **(b)** TEM micrographs of lake water containing natural hydrous iron oxide aggregates with associated fibrils- probably polysaccharides of microbial origin (Source: Taillefert *et al.,* 2000).

2.3 COLLOID MOBILISATION AND TRANSMISSION

2.3.1 Factors controlling colloid mobilisation from soils

Mobilisation of colloids from soils can result from both changes in chemistry or flow (Shevenell & McCarthy, 2002; Sen & Khilar, 2006). The actual distance of separation between a fine colloid and the pore surface may be very small (around 10^{-1} nm), thus, at this scale, both short-range (London-van der Waals) and medium-range (electrostatic) forces act between bodies. The fine particle will also be subject to hydrodynamic forces exerted by the flowing liquid and if the overall net energy of interactions is repulsive, then release will take place (Sen & Khilar, 2006).

Chemically-mediated release of colloidal materials occurs where changes occur in the binding of colloids to pore surfaces (e.g. Ryan & Gschwend, 1994; Ryan & Elimelech, 1996; Seaman *et al.,* 1995; Kaplan *et al.,* 1996). Colloidal release is limited when a potential energy barrier exists, and is diffusion-limited when this barrier is removed by a change in solution chemistry (Rousseau *et al.,* 2004). **Chemical factors may be more important for the mobilisation of smaller colloids and are considered more common** (Sen & Khilar, 2006), **while larger particles are more strongly influenced by hydrodynamic factors** (Kaplan *et al.,* 1993; Shevenell & McCarthy, 2002).

Under high flow conditions, the hydrodynamic boundary layer thickness may be reduced, thereby diminishing the limits on diffusion of colloids into solution (Shevenell &

McCarthy, 2002); however, it is generally accepted that under flow rates typical of most natural systems (including karstic springs) hydrodynamic forces are less important than electrostatic adhesive/repulsive forces (Khilar & Fogler, 1984; Cerda, 1987; Atteia & Kozel, 1997; Atteia *et al.,* 1998; Sen & Khilar, 2006).

Decreases in ionic strength and changes in pH may promote colloid release from larger grains by reduction of the energy barriers to detachment (Kia *et al.,* 1987; Seaman *et al.,* 1995; Rousseau *et al.,* 2004). Indeed, mobilisation of small colloids and decreases in pH appear to be correlated (Atteia & Kozel, 1997; Atteia *et al.,* 1998), probably as a result of protonation of available binding sites at pore surfaces. Rousseau *et al.* (2004) also demonstrated that colloid leaching under steady flow varied with the boundary and initial conditions. The highest mobilisation of particles being achieved using deionised water, the highest infiltration rate and the highest initial soil moisture content (Rousseau *et al.,* 2004). Hence, colloid mobilisation from soils can be considered a complex function of several interacting factors:

1. **Atmospheric precipitation:** amount (Grant *et al.*, 1996), duration (Kaplan *et al.,* 1993) and nature and extent of pauses in precipitation (Schelde *et al.,* 2002). Although chemical and structural factors are of great importance, rainfall drives translocation of colloids and soil water.
2. **Initial water distribution within the soil:** in partially saturated soils, colloid mobilisation may be retarded by the presence of thin water films (Wan & Tokunaga, 1997).

3. **Soil structure:** primarily on the presence of vertical continuous macropores (Jacobsen *et al.,* 1997; Laegdsmand *et al.,* 1999).

4. **Ionic strength of the incoming solution:** sudden particle release has been shown to occur through reduction of the pore water salt concentration to below the critical salt concentration (CSC) (Seaman *et al.,* 1995; Rousseau *et al.,* 2004; Sen & Khilar, 2006). Divalent cations (Ca^{2+}, Mg^{2+}) enhance colloidal deposition through compression of the double-layer potential energy, whereas monovalent cations act as a dispersant (Rousseau *et al.,* 2004).

5. **pH of infiltrating solution:** although pH may be important in some instances, it may be less significant for permanently charged clay minerals (Sen & Khilar, 2006). The pH of rainfall in the majority of instances can be considered to be constant (ca. pH 5.5).

Initial soil moisture conditions appear to be of major importance to the subsequent release of colloids, which may be reflected in the timing of colloid transmission in cave dripwaters (Wan and Wilson, 1994). Processes such as freeze-thawing and drying-wetting may drive the replenishment of the available colloid pool in soils. This is supported by the findings of Schelde *et al.* (2002), who showed that peak colloid availability increased with increasing length of flow interruption, even after prolonged leaching.

2.3.2 Colloidal chemical composition in karstic waters

There is a paucity of physiochemical data on colloids and colloidal binding of trace components in karstic waters. However, available data confirm that colloidal composition is generally consistent with the local lithology (Atteia *et al.,* 1998; McCarthy & Shevenell, 1998). McCarthy & Shevenell (1998) showed that larger-size colloids and Ca- and Mg-containing colloids were more abundant in karstic lithologies. Colloid properties may change in systems with large gradients in redox potential, e.g. condensation of iron-rich globular colloids containing organic matter and significant amounts of calcium (Mavrocordatos *et al.,* 2000).

Recent data published in Hartland *et al*., (2010a) and Fairchild and Hartland (2010) point to the presence of colloids in a range of sizes in karst dripwaters. Complexes of mineral (e.g. Fe oxides and aluminosilicates) and organic colloids appear to be common, and smaller colloids with dimensions between 10 and 20 nm have also been identified (Hartland *et al*., 2010a).

2.3.3 Controls on colloidal stability in karstic aquifers

In general, colloidal abundance is greater in lower ionic strength groundwaters and hence in karstic systems, decreases in colloidal abundance have been attributed to increases in divalent cation concentrations associated with calcite dissolution (McCarthy & Shevenell, 1998; Atteia & Kozel, 1997; Atteia *et al.,* 1998). The presence of colloids in groundwater

implies stability: to remain in solution colloidal suspensions must be chemically stable (resistant to dissolution), physically stable (resistant to coagulation with other particulates), and have avoided filtration in immobile aquifer material (McCarthy & Shevenell, 1998).

Colloidal stability is determined by the balance between repulsion and attraction between particles and/or surfaces (McCarthy & Shevenell, 1998). In karst waters, the physical configuration, stability and reactivity of colloids may be affected by several factors:

- **Ionic strength (*I*):** through charge compression, *I* may induce coagulation of mineral colloids by van der Waals attraction, or induce changes in the physical configuration of organic compounds (e.g. coiling) (Tipping, 2001).
- **Solution pH:** with increasing pH, acidic functional groups in organic compounds deprotonate resulting in charge stabilisation and extended configurations (Mobed, 1996; Tipping, 2001). Variable charge associated with metal hydroxides and aluminosilicates may also enhance colloid stability at higher pH values.
- **Cation bridging reactions:** such as between negatively charged mineral surfaces and organic colloids- promoting coagulation (Ramos-Tejada *et al.,* 2001; Davis *et al.,* 2001).
- **Occlusion within, or adsorption onto precipitates up-flow of speleothem drip sites:** termed *prior calcite precipitation* (Fairchild *et al.,* 2000), this can occur for example due to aquifer drying. High Mg/Ca and Sr/Ca ratios are indicative of this process (Fairchild *et al.,* 2000).

- **Adsorption of OM to aquifer solids:** this is thought to readily occur (Lee *et al.,* 2005; Einsiedl *et al.,* 2007), but may be enhanced by high ionic strength conditions, e.g. where aquifer drying occurs. Epilithic biofilms and in situ microbial communities may also mineralise adsorbed OM (Einsiedl *et al.,* 2007), coincidentally producing a secondary source of CO_2 and further driving $CaCO_3$ dissolution.

Hence, within karstic aquifers colloid stability is affected by the competing factors of *I* and pH.

At concentrations representative of karstic aquifers (<15 mg L^{-1} TOC), Lee *et al.* (2005) found that adsorption of Suwannee River Humic Acid (SRHA) to $CaCO_3$ particles suspended in water was both rapid and largely irreversible (pH 8.25, pCO_2 $10^{-3.5}$). On the basis of these findings, Einsiedl *et al.* (2007) speculated that all available aquifer surfaces may become blocked by adsorbed HS, thus, enabling OM to remain in solution and explaining the utility of fulvic acids as conservative groundwater tracers (e.g. Ban *et al.,* 2008). However, the transmissivity of small, hydrophilic organic acids in karstic aquifers may owe more to the inherent stability of these compound classes than to the availability of binding sites. This remains an area for debate, but Einsiedl *et al.* (2007) did not address the generally observed dominance of fulvic-like materials over higher molecular weight OM in karstic aquifers (e.g. Baker & Genty, 1999).

2.3.4 Karst hydrogeology

The karstic aquifer system may be subdivided into two domains: the unsaturated and saturated zones. In an unconfined aquifer water descends under gravity until it reaches a point where the fluid pressure in the voids is equal to atmospheric pressure: the water table (Ford & Williams, 2007). The water table delimits the top of the saturated, (phreatic) zone where voids and fissures are filled with water, and the unsaturated (vadose) zone occurs where voids in rock are only partially occupied by water. The epikarst (subcutaneous zone) occupies the top of the vadose zone and usually consists of a particularly weathered zone of limestone that lies immediately beneath the soil (usually 3-10 m deep) (Ford & Williams, 2007). This gradually gives way to the main body of the vadose zone, comprising largely unweathered bedrock (Ford & Williams, 2007). In Fig. 2.8 the principal geochemical reaction associated with each hydrographic region is given.

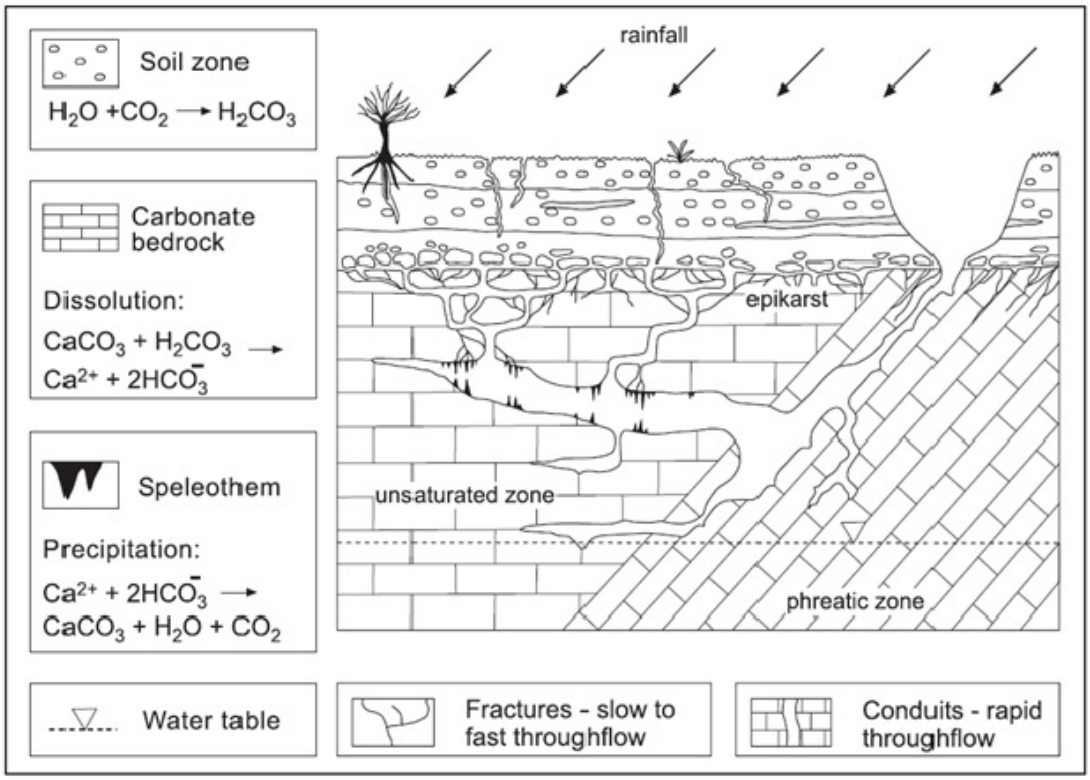

Figure 2.8 A conceptual model of the karst system with its physiology of water flow and CO_2 transport and release (Tooth, 2000) (reproduced from Fairchild *et al.,* 2007).

2.3.5 Transmission of colloids in karst groundwater

Water may be held in matrix, fracture and conduit porosity in the saturated and epiphreatic zones which feed cave dripwaters. The diverse range of flow paths available to infiltrating waters means that the transport of coarse particulate matter is characterised by deposition and resuspension phenomena (Atteia *et al.,* 1998 Massei *et al.,* 2002; 2003). Small colloids <1 μm are likely to be highly mobile in shallow fractured karst formations compared with unconsolidated porous media because of more rapid flow rates in fractures and cavities

(Shevenell & McCarthy, 2002). In Fig. 2.9, a conceptual model of possible flow pathways in a karstic soil-aquifer system is shown.

Experimental studies have demonstrated that colloids can migrate through fractured media more rapidly than solutes because the solutes are more strongly influenced by matrix diffusion (diffusion into micropores between fractures) (McKay *et al.*, 1993; 2000; McCarthy & McKay, 2004). In these studies, "colloidal tracers" (1 - 5 μm) arrived much earlier than non-reactive solute tracers (bromide, chloride, or fluorescent dye), typically by factors of 10 to 100 (McKay *et al.*, 1993; 2000; McCarthy & McKay, 2004).

2.3.6 Summary

The mobilisation of colloids from soils is likely to be driven by chemical factors and the degree of soil saturation (Wan & Wilson, 1994a; 1994b; Sen & Killar, 2006). Once mobilised, flow routing is likely to be of primary importance (McCarthy & McKay, 2004) since longer residence times will favour colloid deposition (McCarthy & Shevenell, 1998).

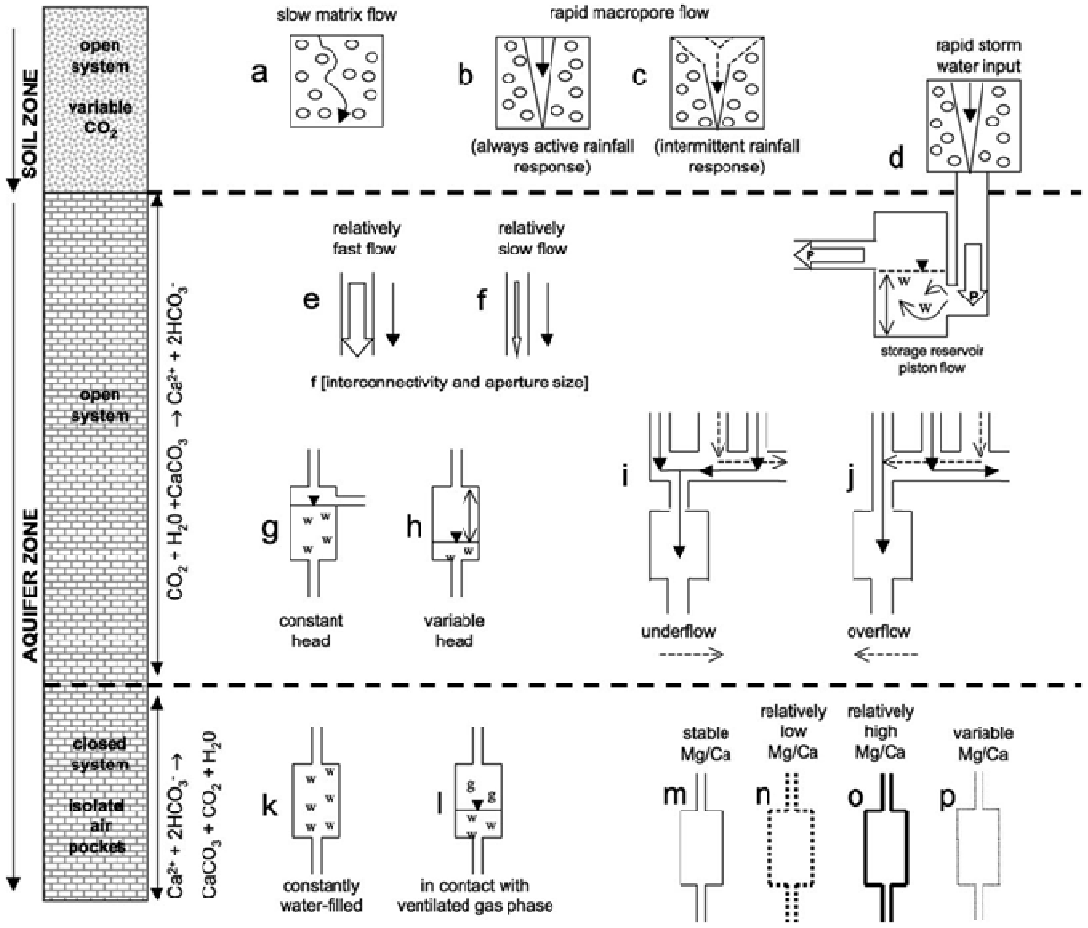

Figure 2.9 Model illustrating the potential soil and aquifer zone flow-paths and conditions which may control karst water evolution (Tooth & Fairchild, 2003).

2.4 IMPURITIES IN SPELEOTHEMS

2.4.1 Incorporation of trace impurities into speleothem calcite

Aside from isotopic studies the geochemical investigation of speleothems is based largely on the presence of trace impurities. The inclusion of trace components can occur via several mechanisms:

- Substitution for Ca^{2+} by divalent and monovalent cations
- Substitution for CO_3^{2-} by divalent and monovalent anions
- Adsorption at defect sites
- Fluid inclusions in porous regions
- Adsorption of organic matter and other solid phases to the crystal growth surface

Inclusion of trace elements present as free ions often display predictable enrichments based on their equilibrium partitioning between the solution and crystal. The main focus is on elements which form divalent cations in solution and substitute for Ca^{2+} in the calcium carbonate crystal lattice, primarily Mg^{2+}, Sr^{2+} and Ba^{2+} (including Mn^{2+} and Fe^{2+} in reducing waters) (Fairchild & Treble, 2009). The distribution of such elements between solution and crystal can be described as follows:

$$(2.5) \quad \left(\frac{Tr}{Ca}\right)_{CaCO_3} = K_d\left(\frac{Tr}{Ca}\right)_{solution}$$

where Tr is the trace ion and K_d is the distribution coefficient, which may vary to a lesser or greater extent with temperature, precipitation rate, crystal morphology, or other aspects of solution composition (e.g. complexation reactions between organic ligands and trace ions) (Morse & Bender, 1990; Fairchild & Treble, 2009).

Departures from equilibrium values for K_{Tr} can occur due to kinetic effects induced by changes in temperature or precipitation rate (Morse & Bender, 1990). Partitioning of trace elements can also be affected to varying degrees by changes in crystal morphology and solution composition (Fairchild & Treble, 2009). Partitioning differs between aragonite and calcite and hence it is important to carefully discriminate between these phases in studied samples (McMillan *et al.,* 2005). Equilibrium partitioning may also occur with respect to sulphate SO_4^{2-} and carbonate CO_3^{2-} (Busenberg & Plummer, 1985); hence variations in SO_4^{2-} in speleothems may reflect changes in solution composition and/or pH shifts driven by changes in pCO_2.

Trace elements may possibly be incorporated in association with co-precipitated colloidal species such as small organic colloids, metal hydroxides and aluminosilicates. Borsato *et al.* (2007) described coincidental variations between dark and UV-fluorescent laminae and

a suite of elements associated with colloidal transport (Y > Zn, Cu and Pb > P and Br) (Fig. 2.13). However, the coordination chemistry of these elements within the crystal lattice is unknown. This gap in knowledge is significant, since for interpretation of elemental variations in speleothems, the speciation of the elements of interest must be understood. Mason *et al.* (2007) using NMR spectroscopy demonstrated that P is present as both individual phosphate ions and as crystalline monetite ($CaHPO_4$), which probably grew simultaneously with the occluding calcite. Phosphate is also preferentially incorporated at defect sites within the crystal lattice (Meyer, 1984). A wider range of elements may be readily incorporated at defect sites, as opposed to lattice sites where only ions of suitable size and valence may be substituted. Elements readily incorporated at defect sites include Na^+ (Busenberg & Plummer, 1985) and REE^{3+} (Elzinga *et al.,* 2002). Singly and triply charged elements (e.g. Y^{3+}, Na^+, PO_4^{3-}, Br^-) may substitute as ion pairs, thereby, preserving charge balance (Fairchild & Treble, 2009); and enrichments at defects are likely to be greater in faster growing samples (Frisia *et al.,* 2000). Incorporation of ions can also occur by direct adsorption to the crystal surface, e.g. Si adsorbs directly from solution and is co-precipitated (Hu *et al.,* 2005).

2.4.2 Adsorption of NOM to calcium carbonate

The adsorption of organic matter and organo-mineral complexes at speleothem growth surfaces must be understood in order to properly interpret inclusion-rich laminae (IRL) in speleothems. Experimental studies suggest that adsorption of NOM to the calcite surface occurs rapidly and is mostly irreversible: possibly indicating that the accumulation of OM

at speleothem growth surfaces may be supply-limited (Murphy *et al.,* 1990; Lee *et al.,* 2005).

Lee *et al.* (2005) examined the adsorption of SRFA to synthetic calcite at concentrations within a natural range for karstic systems. They found that SRFA exhibited Langmuirian-type behaviour and its adsorption was followed by a shift in electrostatic charge to more negative zeta [electrokinetic] potential (Lee *et al.,* 2005). SRFA adsorption did not inhibit Cu^{2+} sorption (5 μM Cu^{2+}, pH 8.25, $_{P}CO_2$ $10^{-3.5}$) because Cu^{2+} adsorbed directly to calcite, showing a greater affinity for calcite than surface adsorbed SRFA (Lee *et al.,* 2005). More negative surface charge resulted in non-Langmuirian-type behaviour at concentrations above 15 mg L^{-1}; and importantly, such surface coatings of hydrophilic OM may enhance adsorption of more hydrophobic moieties to the calcite surface through provision of hydrophobic domains (Murphy *et al.,* 1990). Deposition of organic acids at the growth surface of speleothems is affected by several factors:

- **Diffusivity:** the hydrodynamic diameter of the hydrated compound or colloidal complex will determine its diffusivity within the thin water film at the surface of the speleothem. Diffusivity of polyaromatic OM may be affected by pH, i.e. because of conformational changes (Lead *et al.,* 2003).
- **Hydrophobicity:** hydrophobic moieties may preferentially adsorb to available surfaces because of intra- and inter-colloidal hydrophobic interactions.

- **Saturation Index:** as affects growth rate and ionic strength of solution. At higher *I*, OM may be increasingly prone to adsorption to calcite due increased aggregation. Higher growth rates may cause faster occlusion of OM.
- **Drip rate:** determines rate of supply of OM and also constrains the time available for diffusion to the crystal surface. At a certain distance from the crystal surface hydrodynamic influences on colloids will be non-significant. Also, at low drip rate, drying of the surface water film may be significant.

2.4.3 Enrichments in trace elements and NOM in speleothems

Coincident enrichments in UV-fluorescent NOM and trace elements, termed Impurity Pulse Laminae (IPL) (Fairchild *et al.,* 2007), provide evidence for colloid-facilitated metal transport in karst waters. IPL may be clearly visible in sections under transmitted light (Fairchild *et al.,* 2001; Frisia *et al.,* 2003), or primarily visible in this way. Several authors have reported enrichments characteristic of IPL (Roberts *et al.,* 1998; Huang *et al.,* 2001; Richter *et al.,* 2004; Borsato *et al.,* 2007; Zhou *et al.,* 2008). The first report by Roberts *et al.* (1998) described annual chemical variation coincident with fluorescent laminae in stalagmite SU-96-7 from Uamh an Tartair, Sutherland, NW Scotland. The stalagmite displayed a consistent pattern of antipathetic variation of Mg with Sr and Ba coinciding with fluorescent laminations (Roberts *et al.,* 1998). These variations may reflect inhibition of Sr and Ba by Mg or other factors, e.g. adsorption of NOM. The catchment area of Tartair drains through peat bogs rich in dissolved organic matter (DOM). UV-fluorescent laminae

in SU-96-7 (20-60 μm thickness) were demonstrated by Proctor *et al.* (2000) to be annual and the thickness of annual laminae were used as a proxy for rainfall over the last millennium.

Richter *et al.* (2004) reported periodic (mostly synchronous) enrichments in REE and Mn within the laminae of eight late glacial German stalagmites. REE and Mn were generally concentrated in the more pigmented autumnal layers within the annual laminae (Richter *et al.,* 2004). Richter *et al.* (2004) attributed these peaks to elevated soil CO_2 concentrations in the summer, driving more intense weathering of the host rock and allochthonous rock materials, but conceded that Mn and REE could be transported by organic complexes. Indeed, Zhou *et al.* (2008) provided evidence of the co-abundance of Al and Mn in dripwater from Songjia Cave, Central China and made the connection between enrichments in Mn, P and REE with wetter climatic periods.

IPL in speleothems from Grotta di Ernesto have been studied by several workers (Huang *et al.,* 2001; Fairchild *et al.,* 2001; Borsato *et al.,* 2007). Huang *et al.* (2001) showed that annual laminae in the ER76 stalagmite matched variations in Mg and Sr, likely to result from prior calcite precipitation or enhanced dolomite dissolution (Huang *et al.,* 2001; Fairchild *et al.,* 2001). Micro-analyses of a modern stalactite from Ernesto also showed antipathetic variations in magnesium and strontium within calcite (Huang *et al.,* 2001).

Trace element variability in Ernesto stalagmite ER78 was mapped by Borsato *et al.* (2007) using micrometer-resolution X-ray fluorescence (μXRF). Annual variability in drip water chemistry at Ernesto is well known (Fairchild *et al.,* 2001) and a significant proportion of rapid fracture-fed flow ensures rapid transmissivity into the cave (Frisia *et al.,* 2000; Borsato *et al.,* 2007). Monthly drip-rate monitoring data from spring 2002 to 2005 is shown in Fig. 2.10, showing distinct pulses during the winter and springtime.

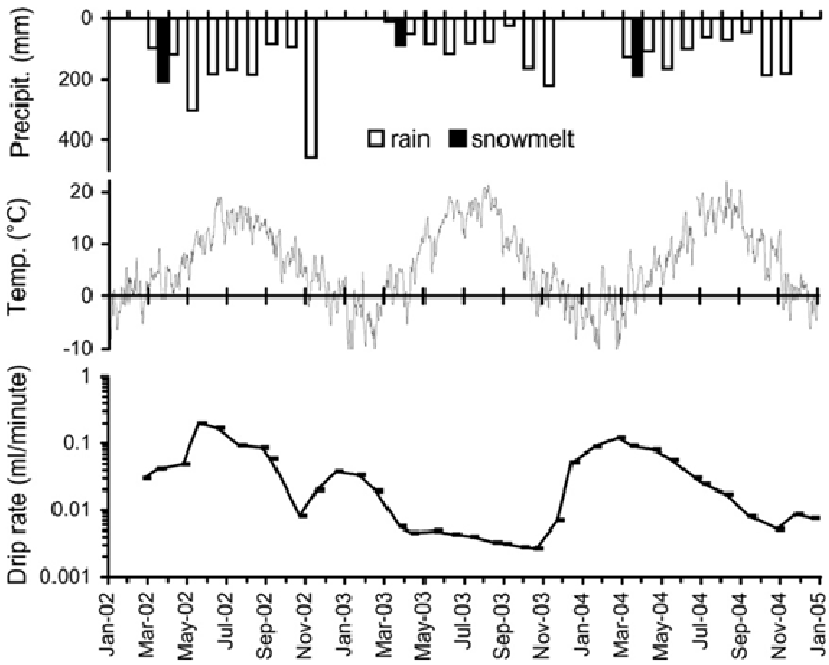

Figure 2.10 Mean monthly temperature, precipitation and infiltration data from Passo Vezzana weather station (1350 m a.s.l, 15 km west of Grotta di Ernesto), compared with the monthly drip rate of the stalactite feeding the ER78 stalagmite. Short-lived high drip rates during intense infiltration events could well be missed by monthly visits (Source: Borsato *et al.,* 2007).

Borsato *et al.* (2007) produced the first evidence from a stalagmite deposit of variation in a suite of elements commonly associated with colloidal transport, centred on IPL (Figure 2.11a). Peak concentrations were ordered Y > Zn, Cu and Pb > P and Br (Borsato *et al.,*

2007) (Figure 2.11b). They hypothesised that this hierarchy is due to the selectivity of element binding by organic colloids flushed from the soil zone during autumn infiltration. Borsato *et al.* (2007) also found that Sr troughs were associated with IPL corroborating the findings of Roberts *et al.* (1998) and Huang *et al.* (2001). They speculated that the Sr troughs were induced by competition with other elements (Borsato *et al.,* 2007). Peaks in the abundance of the trivalent metal Y (probably colloidally transported) and Br (possibly present as an organohalogen) were thought to have resulted from tree-felling in the early 20th century (Borsato *et al.,* 2007).

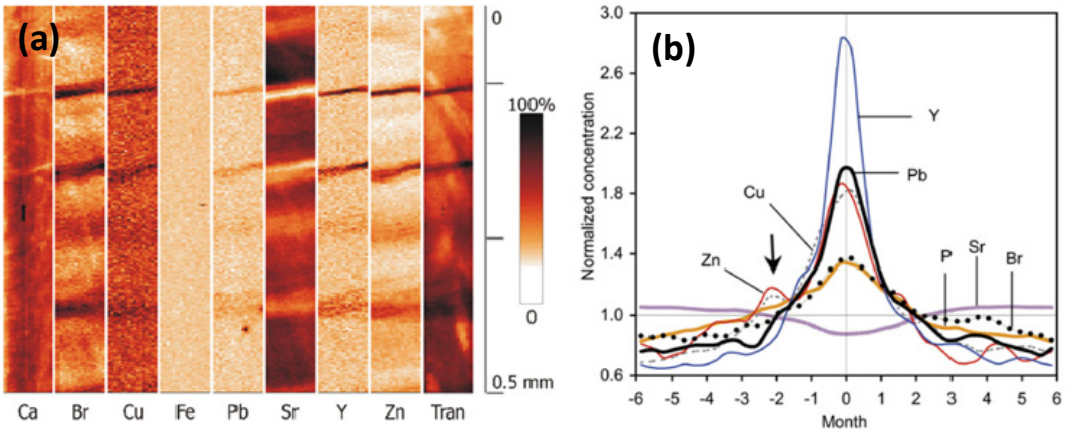

Figure 2.11 (a) μ-XRF maps (30 x 500 μm) between 5.5 and 6.0 mm below the sample top showing Ca, Br, Cu, Fe, Pb, Sr, Y, Zn concentration and transmissivity (Tran) distribution for a 5-year interval (5 laminae). **(b)** Composite diagram of the average "annual" signal for the 7 elements which show an annual structure obtained by stacking 10 successive cycles observed from 5.55 to 6.45 mm below the top, re-sampled over 81 points per cycle, and centred over the visible lamina, which marks "month" 0 (Source: Borsato *et al.,* 2007).

Enrichments in Y, Cu, Pb and Zn were not confined to the centre of dark laminae, but inhabited a broader zone encompassing the two months preceding and following the dark laminae (Borsato *et al.,* 2007), possibly indicating pronounced infiltration events during

mid-to-late summer (Fig. 2.11b). Changes in crystal morphology were also documented by Borsato *et al.* (2007); crystals grown on glass slides before autumnal flushing were characterised by well-developed rhombohedra, but those formed during autumn and early winter had developed complex surfaces with micrometer-sized holes between crystallites and a higher density of macrosteps, attributed to the presence of OM in dripwaters (Borsato *et al.,* 2007; Fig. 2.12).

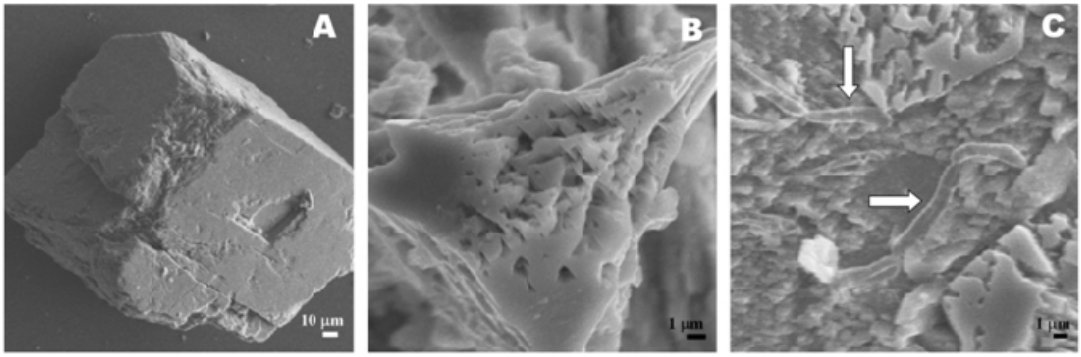

Figure 2.12 SEM micrographs of calcite crystals deposited on glass plates under the ER78 drip. (A) Typical calcite crystal grown throughout one hydrological year and removed in September, prior to the autumnal discharge peak. The rhombohedral crystal shows macro steps, where calcite growth likely occurs. (B) Composite crystal removed in November, after autumnal discharge peak. The composite crystal consists of smaller crystallites of ca. 1 µm in size that do not completely coalesce, and leaves voids between them. (C) Putative bacteria on the surface of calcite crystals removed after the autumnal discharge peak. No micro-pits or macro-steps on the calcite surface (Source: Borsato *et al.,* 2007).

Further to the work of Borsato *et al.* (2007), µ-XRF analyses of stalagmites from Obir Cave (Austrian Alps) have shown that changes in the abundance of certain elements (in this case Pb and Zn) may be dominated by fluctuations in supply as occurs following intense autumnal rainfall events, whereas other elements (e.g. Mg, Sr and Ba) are dominated by

crystallographic effects. Other elements (e.g. P) are intermediate, responding to both changes in supply and crystal structure (Fairchild *et al.,* 2010) (Figure 2.13).

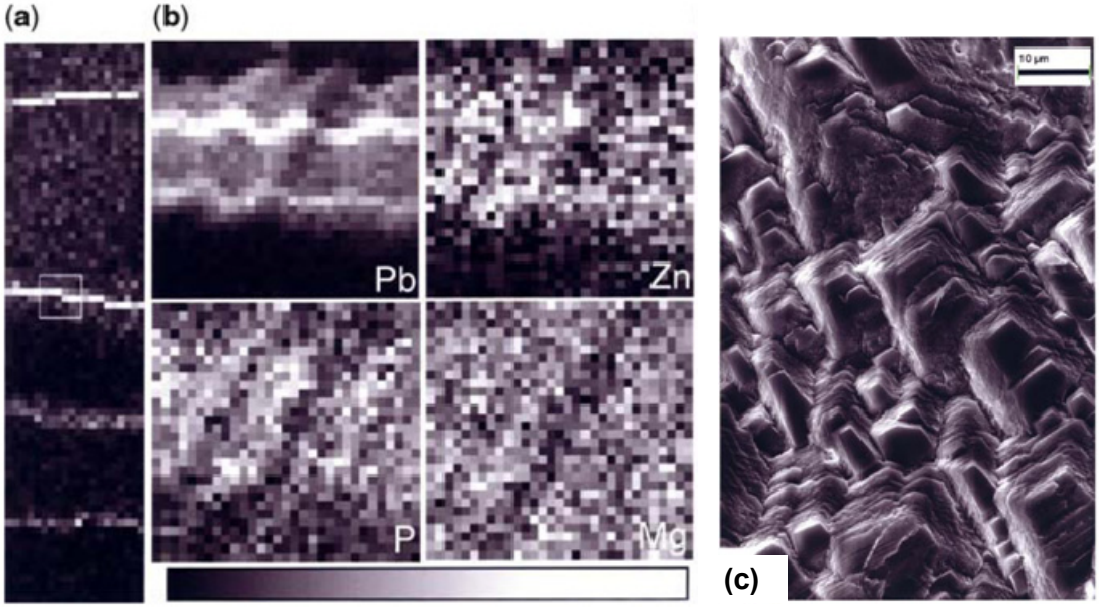

Figure 2.13 Obir84, level within the area of the EBSD map. X-ray elemental mapping at ultra-high resolution of sample Obi 84, induced by relatively low-energy synchrotron radiation. **(a)** a low-resolution map (400 _ 100 μm), showing the development of four annual laminae rich in Pb. **(b)** high-resolution maps, 30 _ 30 μm with 1 μm pixels of Pb, Zn, P and Mg. The Pb map displays a 15 μm-wide zone of enrichment with two 1–2 μm high-Pb zones within it. The enrichment zone is also displayed, but less prominently in the Zn and P maps. All maps show an oblique structure running from upper right to lower left, seen to correspond to crystallite development by the zigzag pattern of the Pb zones. The grey shade linear scale-bar below the image has the following upper and lower limits in counts: Pb (0–154), Zn (0–12), P (0–31) and Mg (0–22). **(c)** SEM of top surface of sample illustrating crystallites which display a mixture of flat smooth surfaces and rough surfaces representing stacked edges (Source: Fairchild *et al.,* 2010).

Further evidence that trace metals may be transmitted in colloidal or dissolved complexes with organic matter has been provided by Jo *et al.* (2010) who identified a strong relationship between excess ^{210}Pb in a soda-straw stalactite from Seopdong Cave, Korean

Republic, and rainfall amount (Fig. 2.14). In explaining the relationship, Jo *et al.* (2010) implicated colloidal carriers in transporting Pb following the wet (typhoon) season. The excellent correlation (R^2=0.9) derived between $^{210}Pb_{ex}$ and rainfall (Jo *et al.,* 2010) suggests that colloid-transported elements in speleothems may yield at least qualitative information on rainfall variations in palaeoclimates.

2.4.4 Summary

Impurity pulse laminae may provide a marker of the start of the hydrologic year (Borsato *et al.,* 2007), and hence, direct evidence of growth rate (Fairchild *et al.,* 2001). Where absent they may be correlated with a decrease in growth rate determined by other techniques (Baker *et al.,* 1997b), such as changes in crystal morphology and growth fabrics (Borsato *et al.,* 2007). IPL may potentially yield hydrological information, particularly in hydrologically sensitive settings or where climate displays a distinct seasonality (e.g. the two wet seasons observed in many sub-tropical climates), sub-annual responses can be detected (Shopov *et al.,* 1994; Baker *et al.,* 1999c).

The derivation of useful information from IPL remains a challenge that requires the integration of inorganic and organic geochemical studies, high resolution monitoring of natural organic tracers and trace elements, and quantitative models of cave-karst aquifer hydrology and hydrogeochemistry; thereby, enabling discrimination between climatic and cave-specific factors (Fairchild *et al.,* 2007). This thesis marks the first detailed

investigation of colloidal materials in cave dripwaters with the aim of quantifying their trace element binding properties, and determining their potential as a speleothem-proxy.

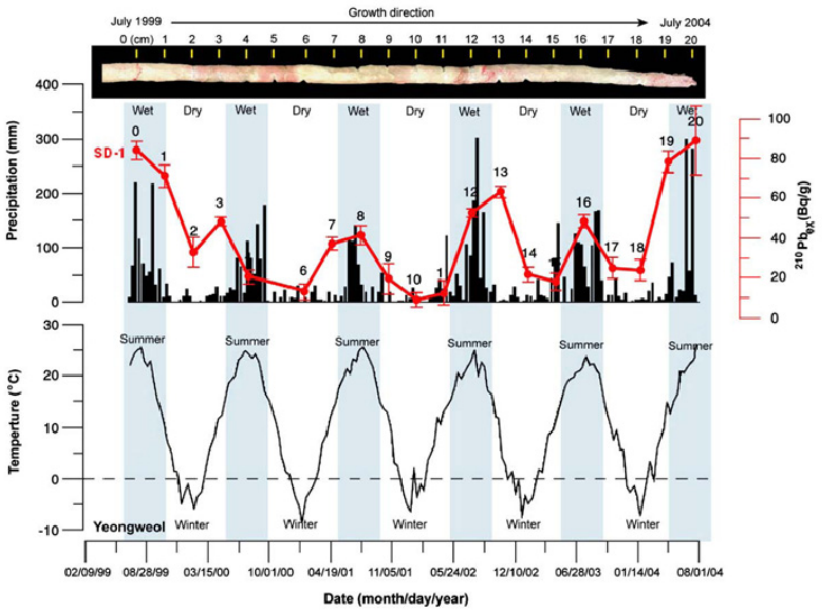

Figure 2.14 Annual precipitation and temperature variation in Yeongwol area corresponding to the growth of the soda straw (SD-1) with $^{210}Pb_{ex}$ activity concentrations from July 1999 to July 2004. Each black bar represents the cumulative amount of rainfall for 11 days (at Yeongweol meteorological station site). The red line denotes the simple step plot of the 210Pbex contents of SD-1 with error bars. Numbers above the red line are microdrilled sample numbers from 0 to 20 cm. Vertical blue bars represent the rainy periods, showing that the amount of rainfall is much higher in blue bar periods (Source: Jo *et al.,* 2010).

3. METHODOLOGY

3.1 INTRODUCTION

The following chapter details the methodologies employed in field and laboratory work and in later sections, the sites where fieldwork was conducted. Methodologies were developed and refined in order to obtain the most detailed and representative dataset from cave dripwater, soil and speleothem samples. Bulk and size-separated dripwater samples were analysed for inorganic (major ions, trace elements and stable isotopes) and organic geochemistry (total organic carbon (TOC), fluorescence). Specialised techniques were also employed to analyse colloidal characteristics, and the lability of trace element-colloidal complexes. Figure 3.1 details the range of techniques employed on water samples.

Monthly monitoring of cave dripwaters was carried out at Poole's Cavern, Buxton, UK, between June 2008 and August 2009. Samples of dripwater were also taken from Lower Balls Green Mine, Minchinhampton, UK, in September, October and November 2008 and Grotta di Ernesto, Trentino, Italy, in October 2007 and November 2008. Soil samples from all three sites were also studied in leaching studies and speleothem samples from each study site were analysed for their trace element and organic compositions (Fig. 3.2).

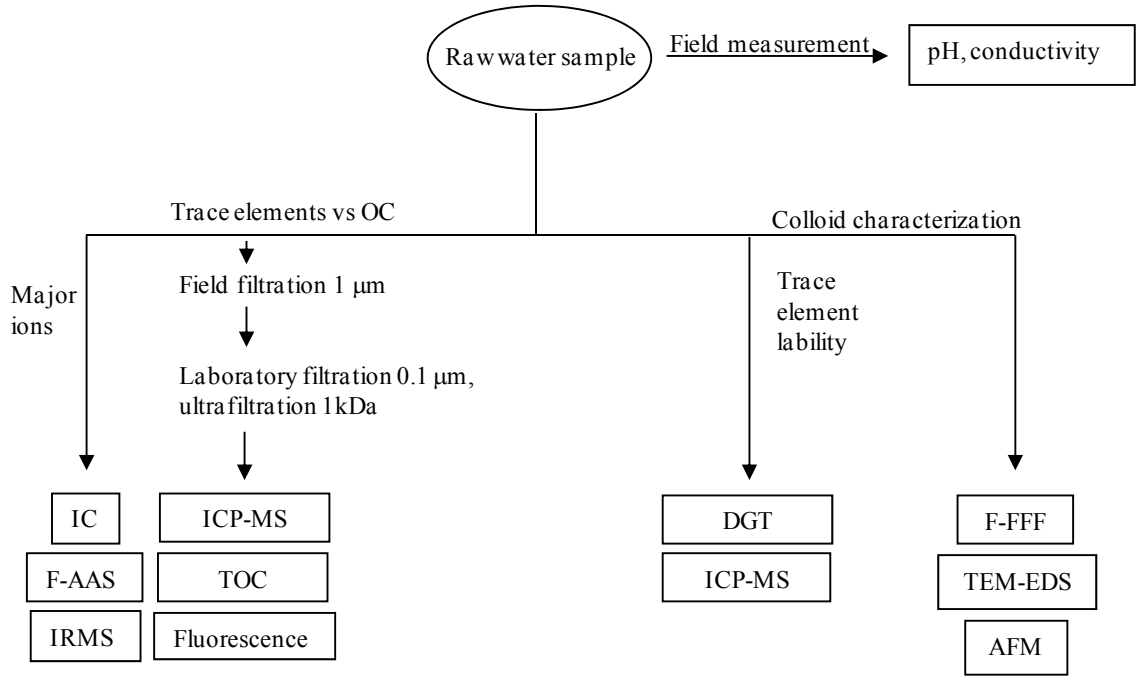

Figure 3.1 Multi-method approach adopted for the analysis of cave dripwater (full range of techniques employed on Poole's Cavern samples only). Acronym definitions are given on pages XXVII-XXIX.

3.2 SAMPLING AND ANALYSIS OF CAVE WATERS

Method development mainly involved the elimination of contaminant sources (trace elements and organic carbon) from the materials used in the sampling and fractionation of cave dripwater samples and much care was taken in devising a cleaning protocol for field and laboratory equipment and filters.

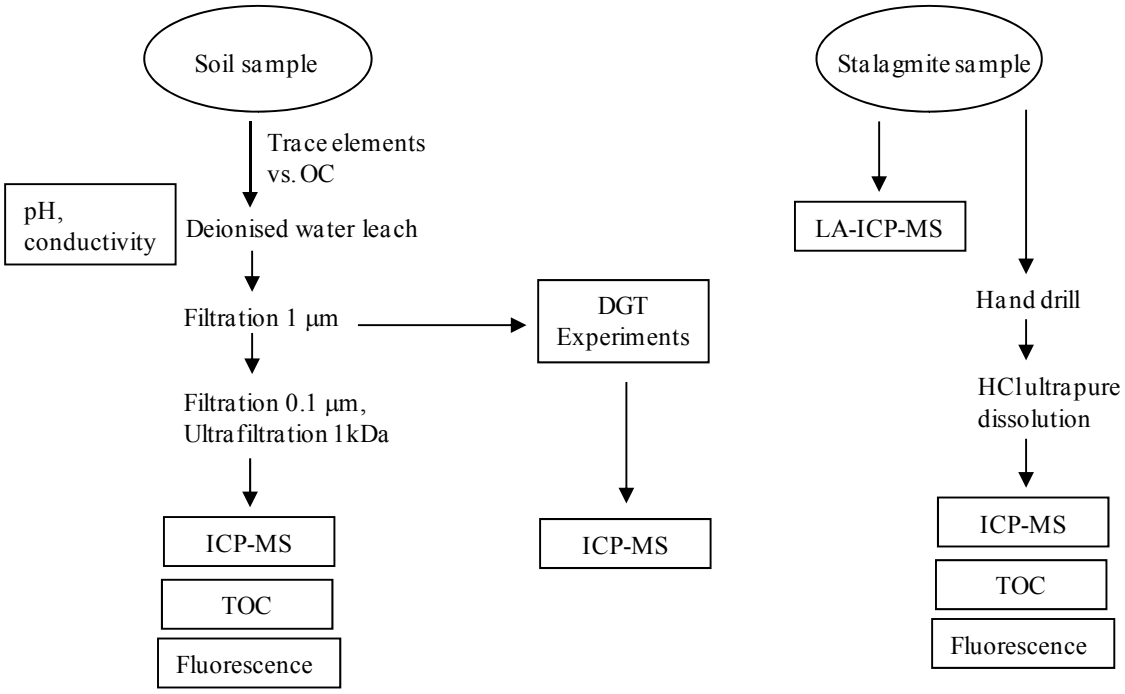

Figure 3.2 Multi-method approach adopted for the analysis of soil and stalagmite samples.

3.2.1 Sampling of colloids in dripwaters

3.2.1.1 Preparation for sampling of dripwaters

All materials coming in contact with water samples were pre-cleaned using 10% HNO_3 and deionised water, including brown glass sample vials (for organic carbon measurements), Millipore Sterifil™ filtration systems, Amicon ultrafiltration components, syringes and funnels. Items were soaked in 10% HNO_3 for at least 24 hrs, and then washed three times with distilled-deionised Barnstead Nanopure™ water (hereafter DIW). Brown glass vials

for organic carbon samples were then combusted at 550 °C in a muffle furnace for 5 hours. Items were stored and transported in new, sealed plastic bags, which had previously been subjected to the same washing procedure.

Filters used in sampling of colloidal fractions were pre-cleaned using 10% HNO_3 and DIW. Whatman GF/B and Whatman 0.1 μm (100 nm) cellulose nitrate filters were cleaned with 250 mL of 10% HNO_3 and 1.5 L DIW. Millipore 1 kDa cellulose ultra-filtration membranes were cleaned with 75 mL of 10% HNO_3 and 225 mL DIW. Whatman GF/B filters were oven-dried at 60°C and kept in clean tissue paper prior to use in the field. The cleaned Whatman 0.1 μm filters and Millipore 1 kDa membranes were kept in 2% HNO_3 during storage (1-3 days) and in DIW for 24 hrs prior to use.

3.2.1.2 Sampling of dripwaters

Samples for colloids were taken using new Nalgene HDPE 500 mL bottles and acid-washed HDPE funnels. Nitrile laboratory-grade gloves were worn throughout sample handling and were changed frequently. Sample bottles were left *in situ* for as long as necessary to collect a sufficient amount of water (typically <24 hours), 200 mL being the minimum amount required for all analyses. Samples of the raw water sample were then taken for TOC and fluorescence, stable isotopes, trace elements and major ions. Samples for TOC and fluorescence were taken in acid-washed, dark-brown glass vials which were rinsed with some of the sample prior to sample collection (see Fig. 3.3: sample collection at Poole's Cavern, Buxton).

Figure 3.3 Images of fieldwork at Poole's Cavern, Buxton, UK. Clockwise from top left: sampling of dripwater in Roman Chamber, "field-laboratory" setup, field supplies in clean plastic bags, the author during sampling.

Following collection, a sub-sample was taken for pH and conductivity measurement using a WTW pH/EC meter connected to a standard WTW EC probe and Hamilton Polyplast precision pH electrode. The pH electrode was calibrated in the field using fresh WTW pH standards at pH 7 and pH 10. Following measurement of pH and EC the sub-sample was immediately discarded. The raw water samples were then immediately filtered under

gravity through pre-acid-washed Whatman GF/B glass micro-fibre filters (nominal pore-size of 1 μm) using acid-washed Millipore Sterifil™ filter units. The first few mL of the sample permeating the GF/B filter was also discarded. Since particulates promote the aggregation of colloids this filter step was undertaken to reduce aggregation in the sample prior to further filtration in the laboratory. The sample was then returned to the Nalgene™ HDPE collection bottle after washing of the collection bottle with some of the 1 μm filtered sample. All samples were kept close to ambient cave temperature (<5°C) during transport to the laboratory.

Water samples for trace elements in the field and laboratory were taken using new Nalgene HPDE 8 mL sample bottles pre-acidified with 0.8 mL 20% Aristar HNO_3, therefore resulting in samples equivalent to 2% HNO_3 v/v (sample matrix for ICP-MS analysis) when the bottles were filled to their 8 mL capacity.

3.2.2 Fractionation of water samples using membrane filtration and ultrafiltration

Filtration of water samples at 0.1 μm and 1 kDa (ca. 1 nm) was carried out in all instances within 48 hours of sample filtration at 1 μm, and typically within 18 hours for samples from UK study sites. Filtration at 0.1 μm utilised a Millipore Sterifil™ system attached to an electric air pump. Ultrafiltration at 1 kDa was achieved using an Amicon stirred-cell ultrafiltration system at low-flow (4 bar N_2). All ultrafiltration and filtration components which came into contact with the sample had previously been acid-washed with 10% HNO_3

and DIW using the same approach previously outlined. These components were also cleaned thoroughly using 10% HNO_3 and DIW deionised water between sample filtrations.

New filter membranes were used for each sample and filtration rates were monitored at regular intervals to ensure that rates were consistent and that blocking of membrane pores was not occurring to a significant extent, thereby affecting the membrane pore size and size-based exclusion of colloids. This exercise demonstrated that the mean flow rate through the 0.1 μm membrane (over the time taken to filter 100 mL) was 0.77 mL s^{-1} with a SD of ± 0.02 mL s^{-1}. Ultra-filtration rates were measured by weighing the amount of water that permeated the 1 kDa membrane in 5 minutes (4 bar, 250 mL starting volume, DIW water collected in a weighing boat with hydrophobic coating and weighed on scales accurate to ± 0.001 mg). The average flow rate through the 1 kDa membrane was 23.2 μL s^{-1} with a SD of ± 0.5 μL s^{-1}.

3.2.3 Determination of total organic carbon in size-separated fractions

TOC concentration was determined using a Shimadzu TOC-V, high-temperature combustion analyser following the non-portable organic carbon (NPOC) method using a 3 minute spurge time and 2 washes between analyses. Samples were acidified with ultrapure HCl to produce carbon dioxide which is measured by infra-red detection, and then subtracted from TOC which was determined by oxidation of organic carbon by high-temperature combustion. Each reported measurement is the average of 4-10 injections, with

standard deviations reported as an estimate of error. DIW blanks produced following the same procedure used in sample collection and preparation, averaged 0.1 ± 0.1 mg L^{-1}. Instrumental drift and changes in analytical accuracy were addressed by the integration of check standards into the calibration on each run. R^2 values for calibration curves were typically better than 0.98.

Despite the previously-outlined filter cleaning procedure, sequential filtration of dripwater samples resulted in an accumulation of non-fluorescent organic carbon (cellulose from the filter membranes) in each successive permeate. Therefore, in order to quantify the TOC content of size-separated fractions, a blank correction procedure was applied to all TOC determinations of filtered dripwater. Procedural blanks were completed using DIW, following the same procedure used in sample collection and preparation. The TOC values presented in this thesis are blank-corrected mean values and error bars are the standard deviation of the replicated analyses. The limits of detection for each filter fraction are defined as three times the standard deviation of the procedural blanks. See Fig. 3.4 for the results of TOC procedural blanks (n = 6).

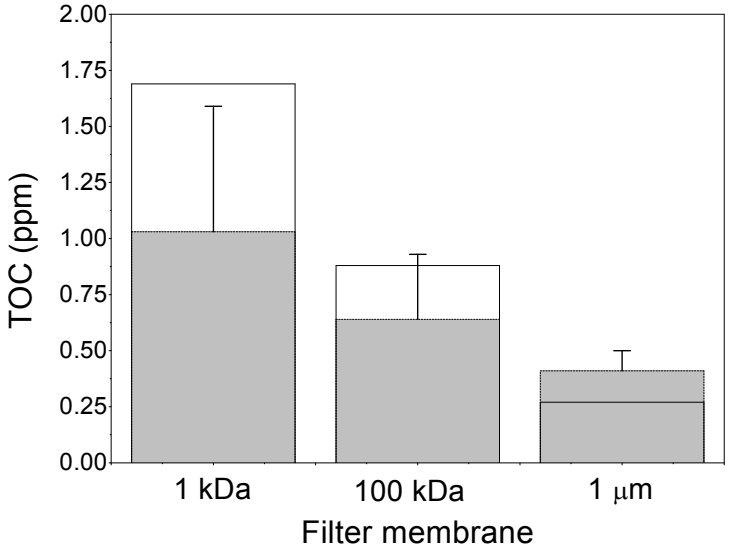

Figure 3.4 Total Organic Carbon concentration in procedural blanks of filter membranes (dotted line, grey fill), and the limits of detection for determining TOC in the permeate of each membrane (solid line). Limits of detection calculated as three times the standard deviation of the procedural blank. Error bars correspond to one standard deviation of the procedural blank.

3.2.4 Fluorescence spectroscopy of size-separated dripwater samples

Fluorescence spectra were obtained using a Varian Cary Eclipse™ fluorescence spectrophotometer equipped with a Peltier temperature controller using a 4 mL, 1 cm path length cuvette. Samples were analysed using methods previously published by Baker (2001), whereby fluorescence emission excitation matrices (EEMs) were generated by scanning and recording emission spectra from 300 to 500 nm at 0.5 nm steps with 5 nm increments of excitation wavelength between 280 and 400 nm. Excitation and emission slits were set to 5 nm and the analytical temperature and photomultiplier voltage were set to 20

± 0.1 °C and 770 V. Calibration of the spectrophotometer was performed via measurement of the Raman intensity at 395 nm emission using a sealed distilled water cell. Raman intensity was measured approximately every 15 analyses and averaged 26.7 ± 0.76 over the period August 2008 to August 2009. All fluorescence intensity values reported in this manuscript are corrected using the Raman peak intensity by the following formula:

(3.1) Corrected intensity = initial intensity x 20 / Raman intensity

Results from procedural blanks demonstrated that organic carbon leached from filter membranes was non-fluorescent and blank values were equivalent to DIW.

3.2.5 Measuring trace element concentrations in size-separated fractions by inductively Coupled Plasma Mass Spectrometry (ICP-MS)

Trace element concentrations in dripwaters were determined using an Agilent quadrupole ICP-MS. Dripwater samples (8 mL) were acidified using Aristar HNO_3 producing a sample matrix of 2% HNO_3. Calibration standards were run at concentrations of 1, 10, 20 and 50 μg L^{-1} and check standards were analysed at regular intervals during each run. Isotopes measured were ^{23}Na, ^{24}Mg, ^{27}Al, ^{29}Si, ^{47}Ti, ^{51}V, ^{52}Cr, ^{55}Mn, ^{56}Fe, ^{59}Co, ^{60}Ni, ^{63}Cu, ^{66}Zn, ^{79}Br, ^{88}Sr, ^{89}Y, ^{114}Cd, ^{137}Ba, and ^{208}Pb. Detection limits were 0.05 mg L^{-1} for major ions (Na, Mg, Si) and 0.1 μg L^{-1} for trace elements excepting Cr, Ti, Ni, Zn and Cu (0.2 μg L^{-1})

and Pb and Fe (0.5 μg L^{-1}). Results of ICP-MS analyses of procedural filter blanks are given in Table S1 (Appendix I).

Analyses of deionised water and acid blanks were below detection limits for all metals except Al (18.6 ± 4.9 μg L^{-1}). Internal (within-run) precision was better than 0.05 μg L^{-1} for all elements, and overall (external) precision is estimated at 0.1 μg L^{-1} for all elements except Al, Cr, V, Mn, Fe, Br, Cd, Pb (0.5 μg L^{-1}).

3.2.6 Determination of Ca and K concentrations by AAS

Concentrations of Ca and K were determined using a Perkin Elmer Analyst 300 Atomic Absorption Spectrometer (AAS). Samples were kept refrigerated below 5 °C prior to analysis in sealed, sterile HDPE plastic bottles. Cave water samples were diluted until the concentration in the measured solution was within the analytical range of 0 – 5 mg L^{-1} where the relationship between concentration and absorption is linear. Calibration curves prepared using Perkin Elmer AA standard solutions for Ca and K were better than 0.95 in all instances. Quoted values of Ca and K are the background-corrected means of three replicate analyses.

3.2.7 Determination of major anion concentrations by Ion Chromatography

The concentration of major anions in unfiltered dripwater samples (Cl^-, NO_3^-, SO_4^{2-} and PO_4^{3-}) was determined used a Dionex (ICS2000) Ion Chromatography system configured for injection of 0.5 mL sample aliquots. Samples were kept refrigerated below 5 °C and analysed within 2 weeks of sample collection. Calibration standards were prepared from BDH multi-element anion standards and analyses were background-corrected to DIW. Check standards at 5 and 10 mg L^{-1} were run at regular intervals and integrated into the final calibration curve.

3.2.8 Determination of alkalinity by colorimetric titration

Alkalinity in selected cave dripwater samples was calculated colorimetrically using a Hach digital titrator loaded with a 0.16 N H_2SO_4 cartridge. BCG-MR indicator powder was added to 100 mL of sample and the sample was stirred as the titration proceeded to the colorimetric end-point. Alkalinity (mg $CaCO_3$) was calculated by multiplication of the total digits of H_2SO_4 added by the appropriate digit multiplier, since meq acid = meq alkalinity. Alkalinity was determined on one full set of samples from each monitored drip point. This was then used as a guide for the calculation of alkalinity in samples based on the difference between the contribution of known ions to charge in the sample and the charge balance (Table 4.2), since:

$$\sum C_i z_i = 0 \qquad (3.2)$$

where, C_i is the concentration of each ion in solution and z_i is its charge. Because of this relationship it is also possible to predict the conductivity of the solution from its composition. The contribution of ions to conductivity it approximately their concentration times the square of the charge of the ion. A more accurate method by Rossum (1975) was used as an independent check on the accuracy of the difference method of alkalinity determination (Table 4.2).

3.2.9 Determination of stable isotope ratios by IRMS

Water stable isotopes were determined using a GV Instruments Isoprime isotope ratio mass spectrometer connected to a Eurovector Environmental Analyser. Stable isotope values are expressed using the δ convention:

$$\delta^{18}O = (^{18}O/^{16}O_{sample}) / (^{18}O/^{16}O_{standard}) \quad -1 \tag{3.3}$$

And similarly for hydrogen isotopes (δD) expressed as ‰ (parts per thousand) relative to Vienna Standard Mean Ocean Water (V-SMOW). Hydrogen isotope ratios were determined by reduction to hydrogen at 1050 °C in the presence of a chromium catalyst. For oxygen isotopes, reaction of water at 1250 °C with carbon dioxide from nickel plated carbon over glassy carbon, yielded carbon monoxide for oxygen isotope analysis. Results were duplicated to ensure reproducibility and in order to eliminate sample hangover effects for oxygen analysis, samples were first analyzed for δD, before arranging samples in order

of decreasing δD for determination of $\delta^{18}O$. Internal (within-run) precision is 0.3 ‰ for δD and 0.06 ‰ for $\delta^{18}O$, and overall (external) precision estimated at 0.5 ‰ for δD and 0.1 ‰ for $\delta^{18}O$.

3.3 TRACE ELEMENT LABILITY BY DGT

Speciation of trace elements in cave dripwaters was examined using the diffusive gradients in thin films (DGT) technique. DGT enables the lability of metal-ligand complexes to be determined, i.e. the extent to which metal ions are exchangeable between a binding phase (colloid) and bulk solution (free ion). The DGT technique has been validated by over 60 publications (e.g. Zhang & Davidson, 1995; 1999) and 10 PhD theses, and requires no calibration prior to deployment. DGT is based on a simple device that accumulates solutes on a binding agent after passage through a hydrogel which acts as a well defined diffusion layer (Fig. 3.5).

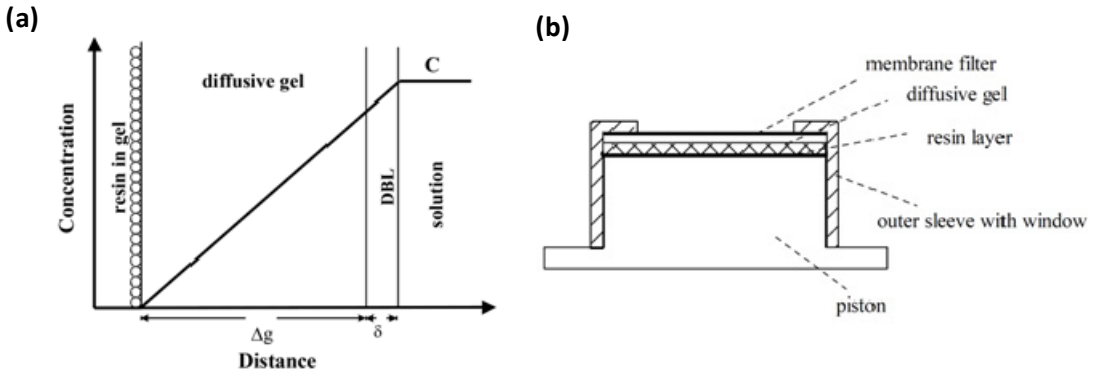

Figure 3.5 (a) Schematic cross-section through a DGT device in contact with solution, showing the steady-state concentration gradient. The diffusive layer is shown as a single layer of gel, but in practice includes a gel layer and filter. The thickness of the diffusive boundary layer (DBL) in solution depends on the rate of water movement. **(b)** Schematic representation of a section through the DGT assembly (Source: Zhang (2003)).

DGT metal depletion experiments involved the deployment of DGT units in 50 mL water samples in screw-capped PTFE jars. Each experiment consisted of DGT devices loaded with Chelex resins or FeO_x resins with 0.4 mm open pore hydrogels plus acidified and un-acidified control solutions. The samples were swirled daily to ensure the solution was well-mixed. Aliquots of 1.8 mL were taken for ICPMS analysis at 0 hrs, 6 hrs, 12 hrs, 1 day, 2 days, 4 days, 7 days and 9 days, and acidified with 0.2 mL 20% Aristar HNO_3 equalling 2% acid v/v. At the end of the experiment binding resins were retrieved and immersed in 5 mL 2 M Aristar HNO_3 in preparation for ICPMS analysis.

3.4 COLLOID CHARACTERISATION

The colloidal characteristics of cave dripwater samples were examined using two primary techniques: Flow Field-Flow Fractionation (Fl-FFF) and Transmission Electron Microscopy (TEM). Samples were taken from Poole's Cavern between May and June 2009 and were processed within 48 hours of sample collection.

3.4.1 Fractionation of karstic aquatic colloids by Fl-FFF

Because of the dilute nature of cave dripwaters, pre-concentration of the water samples was required before samples could be fractionated using Flow Field-Flow Fractionation (Fl-FFF). Samples of dripwater (500 mL) were concentrated 20 times using ultrafiltration at 1 kDa in an Amicon stirred-cell ultrafiltration system at low-flow (4 bar N_2) producing 20 mL of sample for Fl-FFF analysis. The product was then fractionated using a Postnova F1000 Universal Fractionator Fl-FFF system and particles were detected using a Perkin-Elmer UV-Vis detector scanning at 254 nm and a Jasco 821-FP Intelligent Spectrofluorimeter scanning at the excitation-emission couplet of 320:400 nm, an optical region characteristic of humic-like fluorescence. See Fig. 3.6 for details of the Fl-FFF system. The system eluent used in fractionation of hyperalkaline Poole's Cavern samples was 10 mmol KCl (Aristar grade), prepared using DIW and adjusted to pH 11 dropwise using 1 M Aristar grade NaOH and a Thermo Orion 3 Star bench-top pH meter.

Particle separation in Fl-FFF results from their interaction with a parabolic velocity gradient within the channel and a secondary cross-flow (friction coefficient) applied perpendicular to the channel flow (Fig. 3.7). Application of the field-flow results in accumulation of particles against the channel wall, the resulting concentration gradient results in the translational diffusion of particles back into the channel. The smallest, most-diffusive particles diffuse into the highest velocity flow and are eluted first (Fig. 3.7). Hence, by systematic manipulation of the cross-flow parameter, the fractionation of colloids based on their diffusion coefficients was achieved. Once suitable cross-flow conditions were identified, three replicate runs were carried out in order to verify the results and fractions were collected for further analysis by transmission electron microscopy. Fractions collected for TEM were prepared by direct ultracentrifugation as discussed in the following section.

Figure 3.6 Annotated photograph of the Flow-Field Flow Fractionation system and associated peripherals.

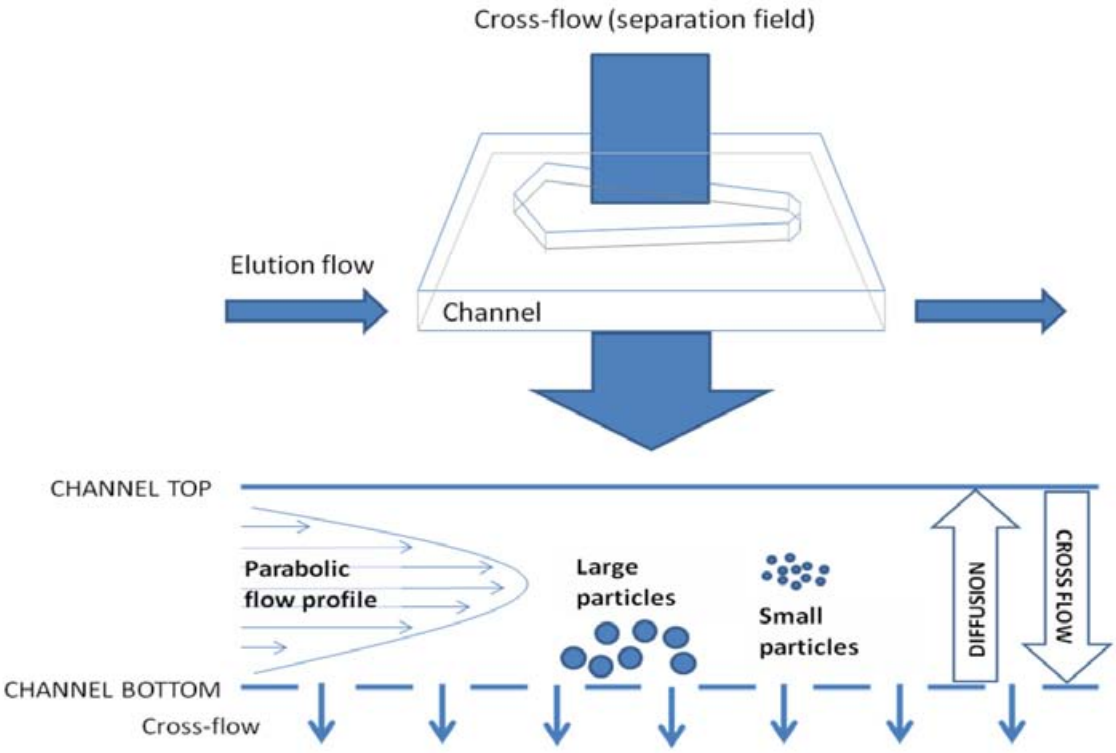

Figure 3.7 Representation of the principles behind Fl-FFF and the influence of the separation flow-field on particles within the Fl-FFF channel.

For a more detailed coverage of the specific system conditions used during Fl-FFF experiments and FFF theory see Chapter 5.

3.4.2 Transmission Electron Microscopy (TEM) of karstic colloids

Specimens for Transmission Electron Microscopy (TEM) from Poole's Cavern were prepared by direct ultracentrifugation onto TEM grids (Agar Scientific Cu 200 mesh Formvar carbon coated, 12 mL sample, 30,000 rpm, 60 minutes). TEM allows accurate morphological and compositional information to be obtained at the individual particle level.

Colloids were analysed using a Phillips Technai TEM in imaging mode coupled to an Energy Dispersive Spectroscopy (EDS) detector. Samples from Grotta di Ernesto were also prepared by the dropping method whereby 50 μL of sample was pipetted onto the TEM grid surface and allowed to dry whilst held in place with tweezers and covered to prevent atmospheric deposition. The grid was then rinsed with DIW to remove precipitated salts and then allowed to dry again.

3.4.3 Atomic Force Microscopy (AFM) of karstic colloids

A small number of samples were prepared for AFM analysis following the adsorption method. A freshly cleaved mica sheet surface of about 1 cm^2 was introduced into a new HDPE sample tube containing 3 mL of the sample. The mica sheet was then removed and rinsed with DIW for 30 s to remove non-adsorbed material, and dried under ambient conditions (relative humidity 60%) in a covered Petri dish, but with an opening at the side to allow drying whilst preventing airborne contamination. The measurements were carried out in the non-contact mode using Si cantilever with a spring constant of 42 (10 ~ 130) N m^{-1} (Nanosensors, 910 (U)-NCHR). All scans were carried out in air, at room temperature. Images were acquired in true non-contact mode and recorded in topography mode with a pixel size resolution of 256 × 256 and a scan rate of 0.5-1.0 Hz. Height measurements of adsorbed nanoparticles were made using the section analysis software of the microscope.

3.5 ANALYSIS OF SPELEOTHEMS

A major part of this thesis relates to the relationship between organic carbon (OC) and trace elements since it was expected that a significant component of colloidal materials in karstic dripwaters consist of organic compounds in various forms. Hence, a central objective of this study is to determine how the ratio of trace elements to OC varies between dripwaters and stalagmites, and how trace element variations in stalagmites change throughout annual hydrological cycles.

3.5.1 Measuring the trace element contents of speleothems using Laser Ablation Inductively Coupled Plasma Mass Spectrometry (LA-ICP-MS)

Samples selected for LA-ICP-MS analysis were sectioned and polished using only distilled water as a lubricant. Samples were then ultrasonicated for 5 minutes in methanol and 10 minutes in DIW. Analysis of speleothem samples was performed on a custom-built excimer 193 nm laser-ablation system with two-volume laser-ablation cell coupled to an Agilent quadrupole ICP-MS, at Royal Holloway University of London. The system combines rapid signal washout with full flexibility in sample size (50 x 50 x 25 mm) and high sensitivity (>10000 cps/ppm for mid-high m/z, 55 μm, 5 Hz). The system setup is described in detail in Müller *et al*. (2009). See Fig. 3.8 for a schematic of the laser-ablation cell and Fig. 3.9 for photos of the laser-ablation unit, laser-ablation cell holding the PC-08-1 stalagmite (re-

growth of PC-97-1 from Poole's Cavern (Baker *et al.*, 1999c)) sample and an on-screen view of the selected ablation path used on the PC-08-1 sample.

Samples were pre-ablated with two traverses in the growth direction as a cleaning step (50 Hz, 100 μm S^{-1}). Laser spot sizes and ICPMS acquisition times were optimised based on the analytical priorities for each sample, determined largely by the growth rate of the speleothem. Instrumental conditions of the LA-ICP-MS system can be stabilised over the course of an analytical session but are not precisely reproducible between sessions because of the large number of variables which affect sensitivity. The absolute efficiency of laser ablation (grams ablated per second) also varies between different materials and laser parameters (e.g. energy density and pulse rate). Because of these factors, absolute calibration of LA-ICP-MS analysis is impractical and hence calibration is achieved through external (STD, a material with known concentrations of all elements of interest) and internal standardisation (an internal reference element *r*) whose concentration is known independently in both the external standard and the sample specimen (Heinrich *et al.*, 2003). This leads to the basic relationship of LA-ICP-MS quantification (Longerich *et al.*, 1996):

$$\frac{C_i^{\mathrm{SAMP}}}{C_r^{\mathrm{SAMP}}} = \frac{C_i^{\mathrm{STD}}}{C_r^{\mathrm{STD}}} \cdot \frac{I_i^{\mathrm{SAMP}}\, I_r^{\mathrm{STD}}}{I_r^{\mathrm{SAMP}}\, I_i^{\mathrm{STD}}} \cdot \left\{ \frac{S_i^{\mathrm{SAMP}}\, S_r^{\mathrm{STD}}}{S_r^{\mathrm{SAMP}}\, S_i^{\mathrm{STD}}} \right\} = 1 \qquad (3.4)$$

where C refers to the concentration of the subscripted element (r is a reference element or internal standard, i is an unknown element) in the superscripted material, and I refers to the corresponding background-corrected signal intensity in counts per second (counts/s) (Heinrich *et al*., 2003).

In the absence of element-specific fractionation, the sensitivity ratios S_i SAMP/S_i STD, although numerically unknown, are identical for all elements including the reference element, such that the S terms cancel. This allows the solution of Eqn. 1 for all C_i SAMP, provided that C_r SAMP and the concentrations of all elements in the standard (STD) are known (Heinrich *et al*., 2003). In this instance, because the mass of Ca can be considered to be stoichiometrically constant in calcite this was used as the internal reference element r.

Internal calibration was thus achieved using the USGS MACS-3 carbonate standard which was ablated once per sample. No suitable, homogeneous carbonate standard was available for high resolution trace element measurements and so external calibration was achieved using a NIST 612 glass standard which was ablated once before and after sample ablation. Background counts measured at the beginning and the end of each transect were subtracted from the standard and sample counts. The trace element/Ca ratio in the unknown was then corrected using the known concentrations in NIST 612. The concentration of each trace element in the speleothem was then calculated by scaling to the known proportion of Ca in $CaCO_3$ (40%).

This quantification method was verified by the measurement of trace element concentrations in multiple Aristar HNO_3 (8 mL 5% HNO_3 to 2 mg $CaCO_3$) dissolutions of each sample by ICP-MS. ICP-MS analysis of carbonate dissolutions was performed at the University of Birmingham as previously outlined in section 3.2.5. Calibration standards were matrix-matched to 100 mg L^{-1} Ca and 10, 20 and 50 ppm check standards were analysed at regular intervals during each run.

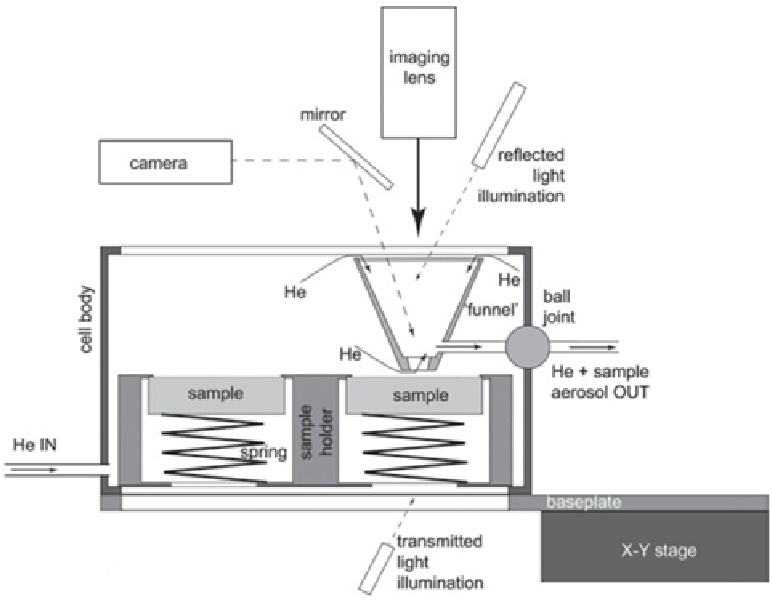

Figure 3.8 Highly schematic cross section of the Laurin two-volume laser-ablation cell (not to scale). Helium (He) enters the cell body at its bottom, and flows from both bottom and top through the funnel, where the He flow entrains the aerosol that condensed out from the laser-induced plasma. The funnel-shaped upper cell and tilted reflected light illumination improve the off-axis viewing system overall. Sample aerosol and He leave the LA cell for the ICPMS via an exit tube connected to the cell body via a ball joint, and Ar and N_2 (optional) are admixed downstream, in front of the 'squid' signal smoothing device. Source: Müller *et al*., (2009).

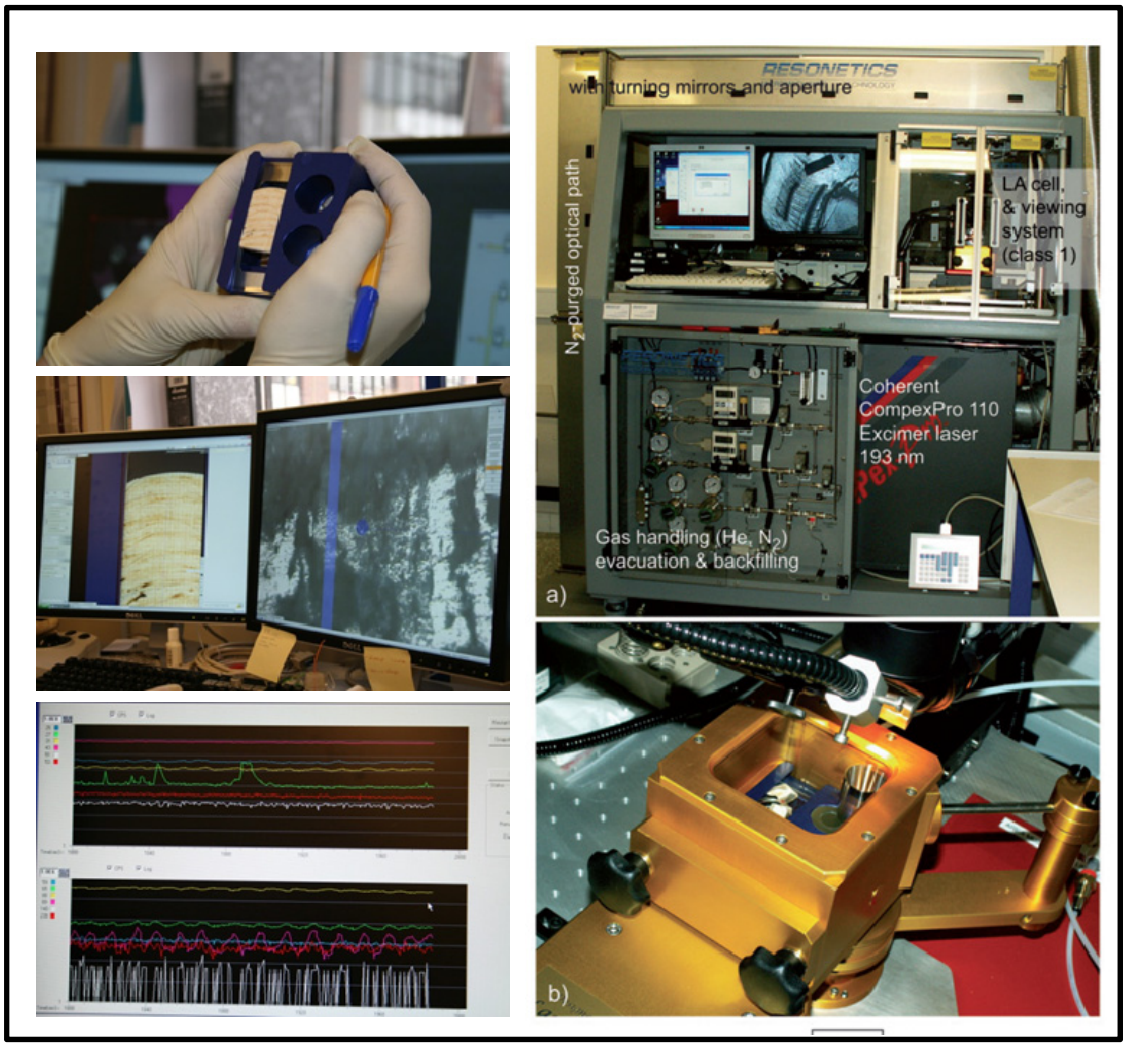

Figure 3.9 Photos of LA-ICP-MS system at Royal Holloway University of London. Left column from top to bottom: PC-08-1 sample being placed into Laurin laser ablation cell, on-screen view of programmed sample ablation track (left screen) and video of proceeding sample ablation (right screen), real-time monitoring of elemental counts for a suite of selected elements. Right column: (a) Photo of laser-ablation unit (ICPMS not visible) showing that the laser beam path is arranged around both excimer laser and ablation cell utilizing three turning mirrors contained in an N_2-purged beam path. (b) Laurin two-volume laser-ablation cell with sample holder and funnel-shaped inner cell. The off-axis camera and mirror as well as reflected light illumination are also visible.

3.5.2 Determining the bulk organic properties of speleothems

Extraction of organic carbon from speleothem samples was achieved following an unpublished method developed by Prof. Andy Baker (*pers. comm*.). Speleothem samples were sectioned, polished and cleaned as previously discussed. The samples were then milled using a jeweller's hand-drill and diamond-tipped drill bit. The powdered calcite was weighed (minimum sample weight 100 mg) and placed in pre-acid washed and combusted (500 °C, 5 hours) glass vials. Ultrapure HCl was then added drop-wise until CO_2 bubbles were no longer visible and sample dissolution was complete. The sample was then made up to 10 mL with DIW prior to TOC and fluorescence analysis. Sample fluorescence was measured following the previously outlined protocol. In samples containing high OC contents dilution with DIW was performed until peak intensities were within instrument detection limits. The TOC concentration of the acid dissolutions was determined by the NPOC method using a three minute sparge time; no further acid addition was required since all DIC had already been consumed by the previous acid digest. DIW blanks were analysed every three samples and no carry-over was evident between carbonate samples and DIW.

3.6 SAMPLING AND ANALYSIS OF SOILS

Soil samples were obtained from each study site, where an approximately 0.3 x 0.6 m wide soil pit was dug and a full 5 cm thick cross-section of the soil profile was removed in acid-washed, sealable plastic bags. Soil pit locations were selected so as to avoid disturbance of

soils directly above the subterranean study sites. Soil profiles were described, mapped and photographed before being in-filled following the sequence of removal.

Soil samples were refrigerated and representative subsamples were taken for batch DIW leaching in new 500 mL HDPE Nalgene bottles (20 g soil shaken with 500 mL DIW, 5 minutes). Leachates were immediately filtered at 1 μm to remove particulates and then subsequently filtered at 0.1 μm and 1 kDa. Equipment preparation and filter-cleaning steps followed the same protocol developed for the fractionation of water samples (see sections 3.2.1 and 3.2.2). Samples of each filter fraction were taken for ICP-MS, TOC and fluorescence. TOC and fluorescence analyses were completed with 24 hours (see sections 3.2.3 and 3.2.4 for details of instrumental analysis). A sub-sample of the 1 μm filter permeate was taken for pH and conductivity measurement using a WTW pH/EC meter connected to a standard WTW EC probe and a Hamilton Polyplast precision pH electrode. The pH electrode was calibrated at regular intervals during laboratory work using new WTW pH 7 and 10 standard solutions.

3.7 STUDY SITES

Most the data presented herein was obtained during 15 months of field work at Poole's Cavern (53°12′N 1°56′W), near Buxton, UK. The remainder of the field and experimental data was obtained from samples from Lower Balls Green Mine (LBGM), Minchinhampton, UK, and Grotta di Ernesto (ERN), Trentino, NE Italian Alps. Samples of dripwaters were

taken from LBGM in September, October and November 2008 and ERN in October 2007 and November 2008.

3.7.1 Poole's Cavern

Poole's Cavern (PC) was selected as the primary study site for mainly pragmatic reasons: the cave is readily accessible from Birmingham, it has been the subject of relevant cave science, and most importantly, the cavern owners and staff (PC is a working show cave) encourage the advancement of scientific understanding. The study of Baker *et al.* (1999c) is of particular relevance; Baker *et al.* described the occurrence of annual fluorescent banding within fast-growing hyperalkaline "Poached Egg" stalagmites and annual winter maxima in humic-like fluorescence intensity in the high pH dripwaters. The re-growth of the PC-97-1 stalagmite (Baker *et al.*, 1999c) was targeted for study of its organic carbon and trace element contents and following authorization from English Nature and the cavern owners (Buxton Civic Association), the re-growth (PC-08-1) was removed in June 2008. In Fig. 3.10, images of stalagmites PC-97-1 and PC-08-1 are shown.

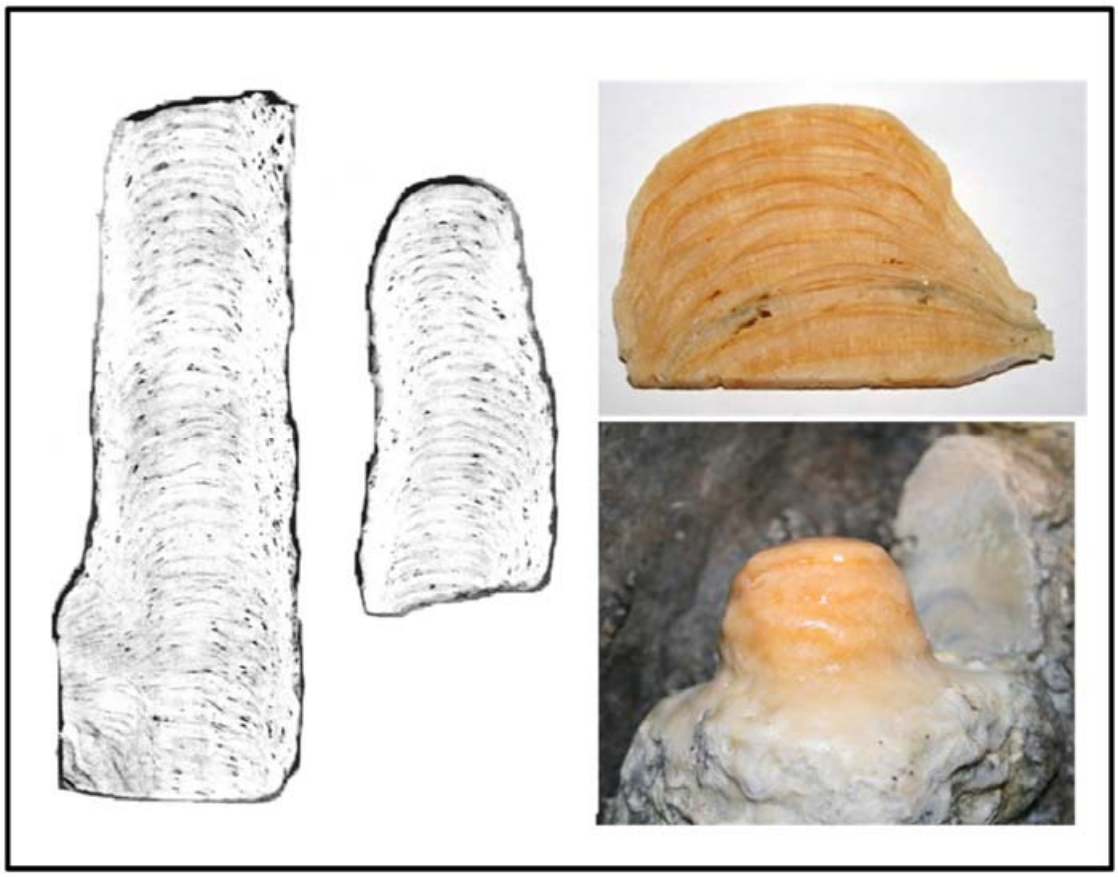

Figure 3.10 Stalagmite PC-97-1 under visible light illumination (left) (Baker *et al.*, 1999c) sample height is 30 cm and grew over the period 1910 – 1997; stalagmite PC-08-1 prior to (right below) and after sampling (right top) and sectioning. PC-08-1 is the re-growth of PC-97-1, sample height is 4 cm and grew between 1997 and June 2008; a dark region is visible in the polished section of PC-08-1 which corresponds to 2001-2002 when dripwater collections were suspended and drainage channels were dug into the overlying hillside (A. Walker, cave manager, *pers. comm.*).

The luminescent structure of PC "Poached Egg" stalagmites was found to follow a near sinusoidal shape with no structural variations with exception of certain laminae which exhibited a double band structure (Baker *et al.*, 1999c). Zones of high fluorescence intensity were found to correspond to the darker layers visible in PC-97-1 and PC-08-1 (Fig. 3.10).

Stalagmites PC-97-1 and PC-08-1 grew behind a large flowstone formation “The Cat” in the Poached Egg Chamber, 130 m from the cavern entrance. The Cat flowstone is decorated by multiple stalagmites and is accessible from the main path. Drip point PE1 (from which PC-97-1 and PC-08-1 precipitated) is located at the back of the flowstone at a lower level than the flowstone top and hence is obscured from view from the pathway.

PC dripwaters were surveyed in April 2008 and drip points BC1 and BC2 (normal pH), PE1 and RC1 (hyperalkaline) were selected for the monitoring of colloidal fractions. Drip point RC2 (hyperalkaline seasonal drip next to RC1) was included in the study in August 2008 when it began to flow. The locations of the monitored drip points are shown in Fig. 3.11 and in Table 3.1 the average electrical conductivity (EC) and pH values are given. As can be seen, the majority of the hyperalkaline dripwaters are located in the Poached Egg chamber. In the Roman chamber, several hyperalkaline drip points are located in close proximity to those of normal pH, demonstrating the complexity of flow routing between soil and drip.

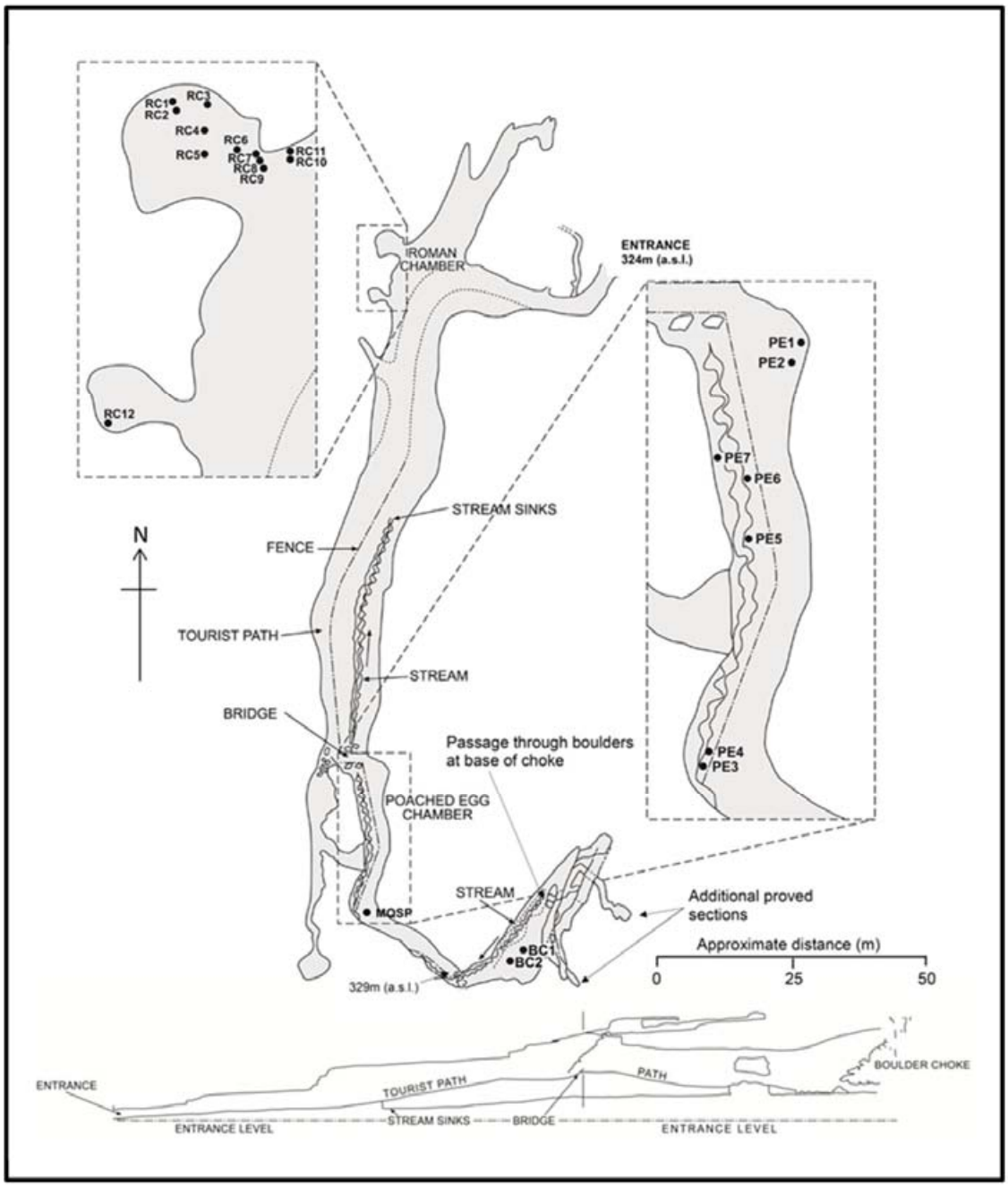

Figure 3.11 Schematic of Poole's Cavern with the locations of sampled drip points indicated. Drip points sampled for colloidal materials are shown **emboldened** in Table 3.1.

Drip point	pH	Electroconductivity (mS cm^{-1})
RC1	**12.3 ± 0.6**	**2.08 ± 1.38**
RC2	**12.4 ± 0.5**	**2.26 ± 1.25**
RC3	8.1	0.61
RC4	7.9	0.51
RC5	12.3	1.18
RC6	8.4	0.25
RC7	8.2	0.34
RC8	8.2	0.37
RC9	8.1	0.47
RC10	7.7	0.53
RC11	7.7	0.52
RC12	7.6	0.52
RC13	7.9	0.60
PE1	**11.7 ± 0.4**	**0.70 ± 0.24**
PE2	11.8	0.76
PE3	11.8	0.60
PE4	11.7	0.76
PE5	11.6	0.66
PE6	12.1	1.34
PE7	11.8	1.00
BC1	**7.9 ± 0.2**	**0.48 ± 0.04**
BC2	**7.9 ± 0.2**	**0.49 ± 0.04**
MQSP	7.8	0.45

Table 3.1 Summary pH and electroconductivity data from surveyed and monitored drip points. Data from drip points sampled for colloidal materials (emboldened) are the average and standard deviations of monthly measurements from June 2008-August 2009.

3.7.1.1 Geology of Poole's Cavern

Poole's Cavern is a shallow cave developed in Lower Carboniferous (Asbian) Limestone, Bee Low Limestone Formation, Peak Limestone Group. Strata within the Cavern are thick with well-developed cross-bedding, pale-brownish gray, fine to medium grained. Volcanic

horizons intervene locally within the Bee Low Limestone Formation, most notably the Upper Millers Dale Lava Member found on the eastern margin of Grin Low, around 750 m east of the Cavern entrance; although this is probably of greatest significance for the cavern stream (Fig. 3.13). Regionally, the limestone dips in a generally northward direction, inclining between 5-10 degrees at the northern edge of the outcrop (Pitty, 1996). Local variations in the angle of dip are exemplified within the Cavern; near the entrance the strata incline by 14 degrees northwards and level out in the main section, becoming horizontal at the inner end of the show section (Pitty, 1966).

3.7.1.2 Morphology of Poole's Cavern

Poole's Cavern is relatively large by comparison to other caves in the Buxton area; it is approximately 240 m long and in the largest (main) chamber it is around 15 m wide and 20 m high. Development of the main passage occurred through phreatic widening along closed joints with solutional undermining and collapse. Vadose erosion (solution of the floor, walls and ceiling by an underground stream) has caused a V-shaped cave floor to develop and has removed most of the fallen blocks. There is a massive bank of flowstone on the path-side of the cavern stream with large gour terraces and an impressive sequence of rim-stone pools. The flowstone originally extended to the present-day entrance and was largely broken and removed to allow access. The entrance passages contain thick Quaternary sediment sequences which have not been studied in detail.

At its base-level the Cavern varies little attitudinally, whereas the ground surface above rises continuously at an average of 13-15 degrees; hence, the limestone overburden progressively increases toward the end of the Cavern (Pitty, 1966). The public section of the cave ends at the foot of a boulder slope which can only be penetrated for a few metres at stream level. The boulder choke has also been penetrated at higher level to access two chambers one of which has roots from the surface (Gill & Beck, 1991).

3.7.1.3 Environmental setting of Poole's Cavern

Poole's Cavern and the wooded hillside (Grin Hill or "Low") above it form the bulk of Buxton Country Park, situated in Buxton's south-western suburbs. The hummocky topography of Grin Low preserves the artificial domes of former lime kilns (Fig. 3.12). Lime burning on Grin Low was still an active industry in 1815. At this time the hillside was covered in large heaps of refuse-lime called "lime ashes", which progressively solidified after being "slaked" by rains (Le Chevalier, 1977). By 1835 the northern hillside was afforested (Grin Plantation) (Le Chevalier, 1977) and this developed into the present-day mature, deciduous secondary-woodland composed chiefly of beech, ash and sycamore (Fig. 3.12).

Figure 3.12 Images of surface environment above Poole's Cavern (left) hummocky topography preserves the locations of spoil heaps under deciduous woodland canopy (right) exposed faces of limestone from quarrying.

Soils are 30-60 cm thick consisting of leaf litter and organic-rich top soil (Brown Ranker (Baker & Genty, 1999)) overlying lime waste and fragments of poorly-sorted limestone (Table 3.2; Figure 3.13). The soil profile at PC is typically characterised by deep, organic-rich A horizons but exhibits a high degree of variability across the site. Lime waste has a pervasive influence over the geochemistry of PC dripwaters, causing hyperalkality and distinct elemental compositions (notably elevated K^+ and SO_4^{2-}).

Horizon	Thickness	Description
O	1-5cm	Leaf litter mainly composed of beach, ash and sycamore leaves
A	10-30cm	Horizon rich in OM. Dark brown colouration. Lots of thin roots. Horizon thickness varies substantially laterally.
AE	<1 cm	Possible transitional A->E but not prominent
E	5 - 20cm	Medium brown clayey horizon. Penetrated by thick roots. Layer is interspersed by varying proportions of unconsolidated, angular to sub-angular, poorly sorted limestone fragments. Translocation of OM around roots is apparent.
C	0–20cm	Light brown. Mainly lime waste and limestone fragments, angular to sub-angular, poorly sorted.
R		Unconsolidated bedrock

OM = organic matter

Table 3.2 Indicative soil horizons characteristic of anthroposol overlying Poole's Cavern

Figure 3.13 Examples of soil profiles in soil pits dug at Poole's Cavern. Soils are characterised by a high degree of lateral variability with a wide range of intermediate compositions. Image on the left shows a soil profile, approximately 60 cm deep, principally light-brown clay rich soil 40-60 cm depth and a mixed horizon (0-20 cm) consisting of light-brown clays and darker organic-bearing soil interspersed by plant roots. Image on the right shows shallower section, approximately 40 cm deep, characterised by dark-brown organic-rich top soil (0-20 cm) and a mixture of organic-rich and clayey components (20-40 cm).

3.7.1.4 Climate and hydrology of Poole's Cavern

Buxton is located in the Peak District, an upland region in the northern Midlands (mean annual temperature and rainfall 9°C and 1300 mm, respectively). In Buxton, as in many upland areas in the UK, there is a pronounced maximum in effective rainfall in autumn to winter when Atlantic westerlies are at their most vigorous. The period June 2008 to August 2009 was climatically unusual in that the peak effective rainfall of 2008 occurred in late summer and early autumn.

The most prominent hydrological feature of Poole's Cavern is an intermittent stream which has been proven by tracing experiments to be fed by sinks close to the boundary between the limestone and overlying shale on Stanley Moor to the south of the Cavern (Fig. 3.14) (Ford & Gunn, 1992). The stream enters the cave from beneath the boulder choke and drains down-dip towards the dry entrance but sinks about 70 m before reaching it. The sinking water finally resurges at Wye Head, approximately 500 m due north (Ford & Gunn, 1992).

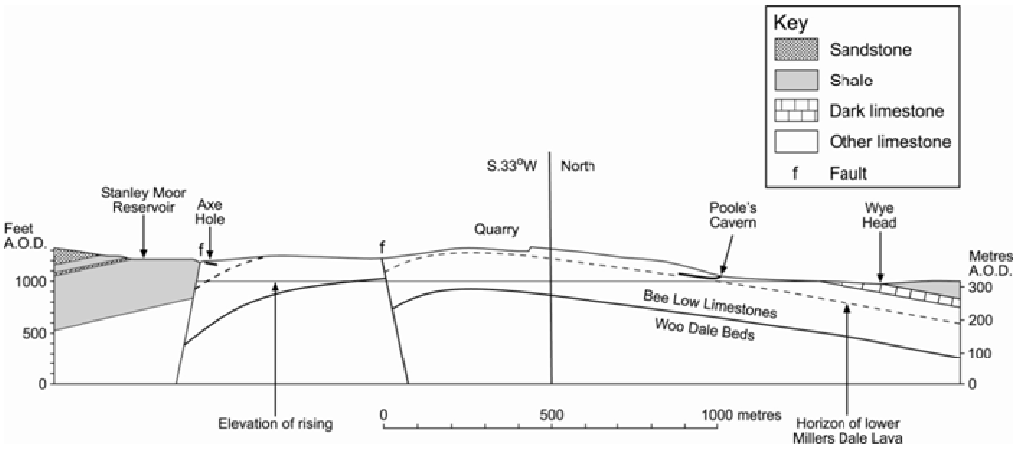

Figure 3.14 Section from the Stanley Moor swallets (sink holes) to Wye Head rising (resurgence) (after I.G.S. 1975).

3.7.1.5 Geochemistry of Poole's Cavern dripwaters and speleothems

Poole's Cavern is highly unusual because of the presence of hyperalkaline dripwaters in the Poached Egg and Roman chambers. At high pH (>9.5) calcium carbonate precipitation is accelerated by diffusion of CO_2 gas into solution where it combines with hydroxyl ions (OH^-) (hydroxylation) to form carbonate ions (CO_3^{2-}) which then react with Ca^{2+} to form $CaCO_3$.

(3.5) $CO_{2(g)} \rightarrow CO_{2(aq)}$

(3.6) $CO_{2(aq)} + OH^-_{(aq)} \rightarrow HCO_3^-{}_{(aq)}$

(3.7) $HCO_3^-{}_{(aq)} + OH^-_{(aq)} \rightarrow CO_3^{2-}{}_{(aq)} + H_2O_{(aq)}$

(3.8) $CO_3^{2-}{}_{(aq)} + Ca^{2+}{}_{(aq)} \rightarrow CaCO_{3(s)}$

The overall hydroxylation – precipitation reaction (equations 3.9 - 3.11) occurs more slowly than the rate at which CO_2 dissolves into solution. For $CO_{2(g)}$ to $CO_{2(aq)}$:

(3.9) Rate = ¼ n v,

where n = molar concentration (mol cm^{-3}) and v = molecular velocity

(3.10) $v = (kT/2\pi m)^{0.5}$,

where k = Boltzmann constant, and m = mass of CO_2

Therefore, for a pCO_2 of $10^{-2.36}$, rate = 4.6 x 10^{-4} mol cm^{-3} s^{-1}

For the hydroxylation-precipitation reaction (equations 3.5 - 3.8):

(3.11) $\text{Rate} = \Delta[CO_{2(aq)}] / \Delta t$

$= kOH^- [CO_{2(aq)}] [OH^-]$

So, at a pH of ~12, and a pCO_2 of $10^{-2.36}$, rate = 6.3 x 10^{-5} mol cm^{-3} s^{-1} (~100 mm/year) (Baker *et al.*, 1998). Although the latter rate is slower, carbonate precipitation proceeds much more quickly than conventional stalagmite growth which averages 1 x 10^{-11} mol cm^{-3} s^{-1} (~0.1 mm/year). In Poole's Cavern, actual growth rates of hyperalkaline stalagmites are much slower than are theoretically possible- rates of up to 1 cm/year have been calculated

(Hartland *et al.*, 2010a). This is probably because drip rates and fall-heights differ from those required for optimal carbonate precipitation.

During this study it was found that, in practice, the carbonate system in Poole's Cavern acted much too quickly for dripwater collections to be taken from hyperalkaline drips without prior calcite precipitation in the sample bottles. Baker *et al.* (1998) conducted experiments with a single-drop pH meter and found that the pH of hyperalkaline dripwater from the Poached Egg chamber dropped by ~2 pH units over 15 minutes. During dripwater sampling for this study it was found that calcite precipitated rapidly on collection funnels, but precipitation in the bottles was much less, presumably being limited by diffusion of CO_2 into solution. Hence, it was impossible to avoid some calcite precipitation because the methodological protocols employed here required a minimum of 200 mL for the suite of analyses on size-separated fractions.

3.7.2 Lower Balls Green Mine

The second UK study site for this study was Lower Balls Green Mine (LBGM), Minchinhampton, Gloucestershire (51°7′N -2°17′W). The mine was selected for study to provide data from a site analogous to the well-studied (e.g. Fairchild *et al*., 2006b), but inaccessible Brown's Folly Mine (BFM), Bath, Somerset, which has been closed due to safety concerns. The mine is located on the edge of the Cotswold escarpment and has not been the subject of previous scientific study.

3.7.2.1 Geology and mining activity

Mining at LBGM was in the Middle Jurassic Inferior Oolite group, Birdlip Limestone Formation, Cleeve Cloud Member. The beds dip gently eastwards and are characterised by well-developed cross-bedding (Fig. 3.15). This is overlain by a rubbly horizon of oolitic marl (Scottsquar member) which is not present 1 km to the west at Upper Balls Green Mine. Above the marl is a resistant bed (Harford Member) (Sumbler *et al*., 2000). Mining in the inferior oolite began around 1800 and by 1900 had extended well into the hillside (Fig. 3.16). Around this time a major roof collapse on top of the railway ultimately caused mining to be abandoned by around 1905.

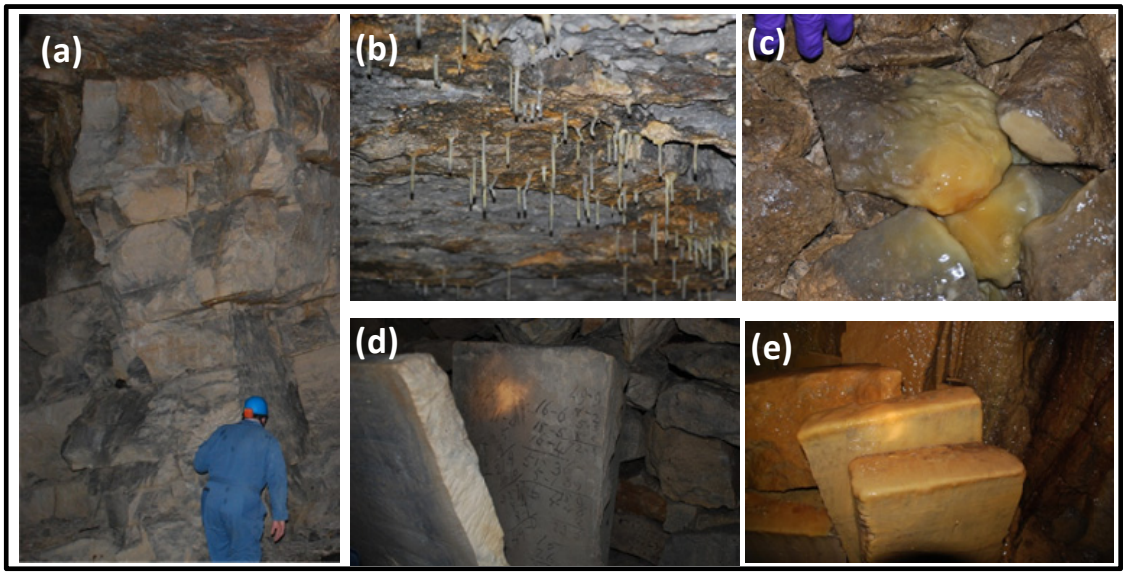

Figure 3.15 (a) Exposed faces of Inferior Oolite in Lower Balls Green Mine and examples of modern calcite precipitation since mining was abandoned around 1905 **(b)** soda straw stalactites **(c)** flowstone at drip point LB3 **(d)** sawn limestone slabs left by miners and **(e)** flowstone overgrowth over slabs.

3.7.2.2 Environmental setting of Lower Balls Green Mine

With the exception of a few houses near the mine entrance, land-use above the mine is given over to dairying and sheep grazing (Fig 3.17). The soil above the site appears undisturbed with no evidence of ploughing, and is characteristic of the slowly permeable, calcareous, clayey soils of the Evesham group, Sherborne component profile (NSRI, 2008) (Fig. 3.18; Table 3.3).

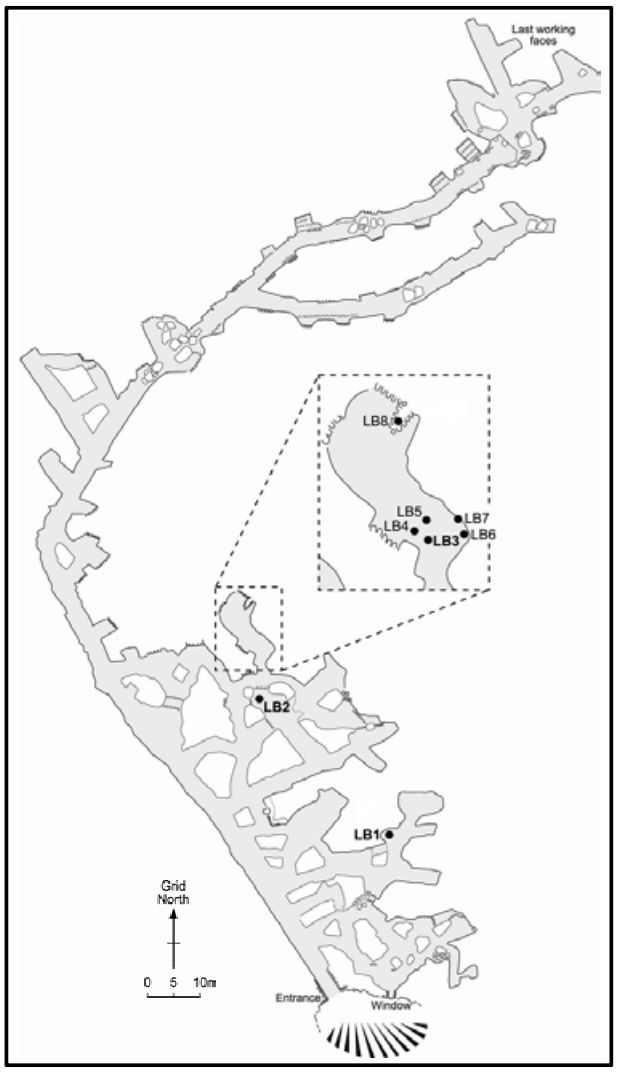

Figure 3.16 Schematic of Lower Balls Green Mine (1025 m long) with the locations of sampled drip points indicated (surveyed by A.J. Price and A.J. Dickinson)**.** TT = location of tiny tag temperature logger.

Figure 3.17 Land use above Lower Balls Green Mine. The mine extends into the hillside approximately right to left with respect to the photograph.

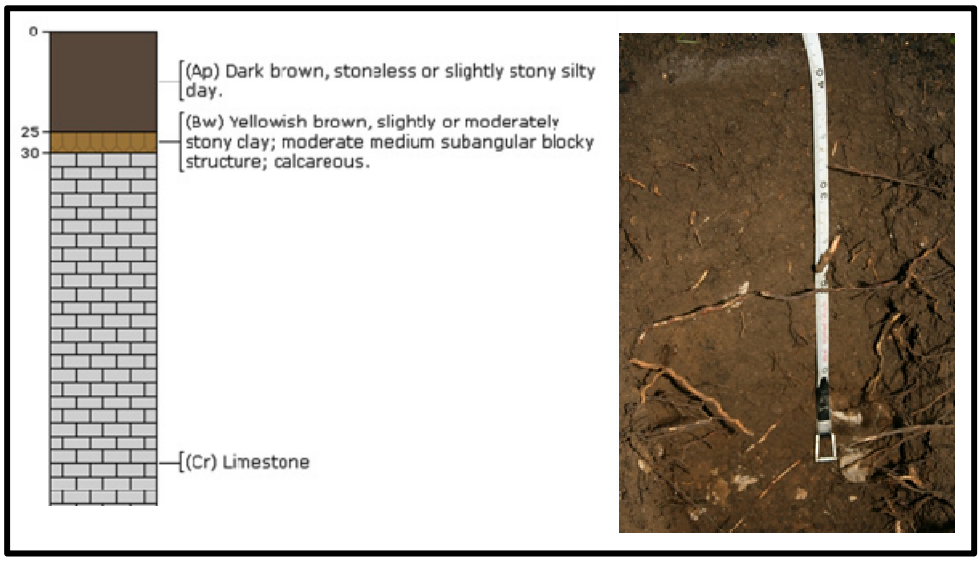

Figure 3.18 Evesham 1 Sherborne (Si) component series profile (NSRI, 2008) (left) and photograph of soil pit (~40 cm deep) dug above LBGM.

Horizon	Thickness	Description
A	10-15cm	Organic-bearing horizon. Dark brown silty clay.
AE	1-3 cm	Transitional A->E gradation from dark brown to light brown colouration.
E	<10cm	Medium, yellowish brown coloured horizon. Clay with few limestone fragments.
R		Unconsolidated bedrock

Table 3.3 Indicative soil horizons characteristic of clayey soils overlying LBGM

3.7.2.3 Climate and hydrology of Lower Balls Green Mine

Minchinhampton is located on the edge of the Cotswold escarpment, an upland limestone region in the south-west English Midlands. The Cotswolds is climatically similar to the Peak District in the north-eastern Midlands, being one of the wettest areas in the region. Rainfall is fairly evenly distributed throughout the year and unlike the Peak District (where Atlantic depressions play a major role) there is a less-pronounced increase in rainfall in the winter months.

The highly-permeable limestones of the Inferior Oolite and Great Oolite form major aquifers which feed a multitude of springs, including one which flows from the quarry face above the mine entrance and which forms a stream which extends a short distance into the mine before sinking again. Percolation flow within the mine occurs at numerous points with a range of different flow regimes present, from high-discharge cracks fed directly by spring water, to slow, seepage flow drips. Speleothem formation is prevalent throughout the mine and is particularly active in the Macaroni chamber where numerous small stalagmites and flowstones are actively forming (enlarged section on Fig. 3.16). Surveys of pH and EC of dripwaters in LBGM are consistent with the expected range for calcite precipitation (Table 3.4).

Monitoring of percolation sites in LBGM began in September 2008 when Stalagmate Plus™ driploggers were placed under drip points LB1, LB2 and LB3, and TinyTag™ temperature loggers were also installed at locations TT1 and TT2. Drip sites LB1 and LB2

were selected because they represent an extreme end-member for percolation flow in speleothem-forming karstic groundwaters. Drip site LB3 is a much slower, speleothem-forming drip, characteristic of more typical conditions found in cave systems.

Sample Site	pH range	Electroconductivity ($\mu S\ cm^{-1}$)	Temperature range (ºC)
LB1	7.9-8.3	501-533	11.4-12.5
LB2	7.7-8.1	250-549	10.7-12.4
LB3	8.0-8.2	494-571	11-11.7
LB4	7.7-7.8	547-564	10.8-11.1
LB5	7.8-8.0	550-627	10.6-12.3
LB6	7.7	481	11.8
LB7	7.6	504	12.3
LB8	7.6	558	12

Table 3.4 Reference pH and EC data from Lower Balls Green Mine (LBGM) dripwaters.

3.7.3 Grotta di Ernesto

Grotta di Ernesto is an alpine cave located slope of the Valsugana valley in the Northeast Italian Alps (45º58'37''N, 11º39'28''E, 1165 m a.s.l) (Fig. 3.19). Fieldwork was conducted in October 2007 and November 2008. However, much of the data collected in 2007 was not usable because methodological approaches weren't fully refined and trace element and organic contamination of filtered samples could not be corrected.

Grotta di Ernesto is one of the best studied caves in Europe. The cave was discovered in 1984 and since then it has been visited frequently, except during the winter. The research

which provided the impetus for the present study (Borsato *et al.*, 2007) was carried out on samples from Grotta di Ernesto, thus, making its study a major objective of this research program.

3.7.3.1 Geology of Grotta di Ernesto

Grotta di Ernesto lies ~20 m under the surface and is developed in Jurassic dolomites and limestones partly overlain by scree consisting of marls onto which a brown calcareous soil, 0.5-1.5 m thick developed. It consists of two connected cylindrical chambers, approximately 5 m wide with a total length of 72 m, developed along a NW trending sub-vertical fault. Numerous stalagmites and stalactites have formed within the cave.

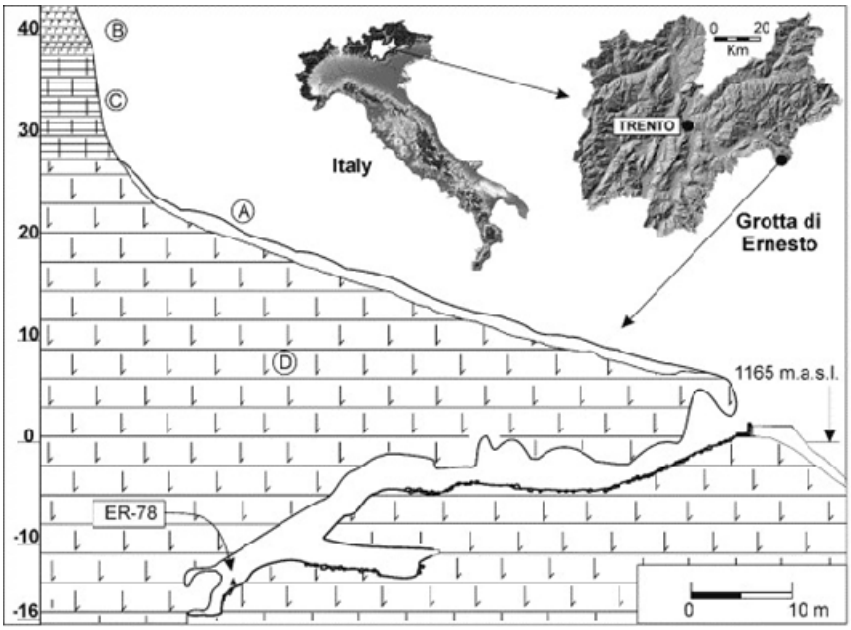

Figure 3.19 Cross section of Grotta di Ernesto with the location of stalagmite ER78. (A) soil; (B and C) marly limestones; (D) dolomite (Source: Borsato *et al*., 2007).

3.7.3.2 Environmental setting of Grotta di Ernesto

Vegetation above Grotta di Ernesto consists of semi-natural conifer vegetation mixed with beech (Fig. 3.19). The most common species are Norway Spruce (*Picea abies* (L.) Karst) and Silver Fir (*Abies alba* Miller). Beneath the thick layer of pine needles and leaf litter a thick calcareous soil has developed with an organic-rich A horizon (Table 3.5; Fig. 3.20) (Fairchild *et al*., 2009).

3.7.3.3 Climate and hydrology of Grotta di Ernesto

The yearly atmospheric precipitation at two nearby meteorological stations (Bieno, 806 m; and Lavarone, 1171 m) averaged over the period 1924-1996 are 1190 and 1300 mm, respectively, with two peaks, in May-June and October-November (Fig. 2.15). The effective precipitation, after subtraction of estimated evapotranspiration using the Thornthwaite method (Borsato *et al.*, 2007), shows a single peak in October-November, when infiltration is also aided by the reduced foliage cover and the concentrated nature of the rainstorms.

Annual changes in feeding drip water chemistry and drip rates are known (Fairchild *et al.*, 2000). A significant component of rapid fracture-fed flow ensures rapid transmissivity of the surface signal (e.g. isotopic properties of rainwater) to the cave (Borsato, 1997; Frisia *et al*., 2000; Miorandi *et al.*, 2010). Monthly drip-rate monitoring since spring 2002 of the drip feeding ER78 (Miorandi *et al.*, 2010), confirms maximum drip rate following high

rainfalls and in particular, autumnal rains and infiltration in the soil zone observed by Frisia *et al.* (2000).

Numerous stalagmites and stalactites have formed within the cave. There are no streams or rivulets, but several muddy and concretionary pools are present in the cave, some of which dry up in summer and fill during autumn and spring. The present day air temperature is constant year-round at 6.6 ± 0.1ºC. It has typically two months of winter snow cover and a summer soil moisture deficit.

Horizon	Thickness	Description
O	1-5cm	Leaf litter mainly composed of beach leaves, pine needles, cones
A	5-10cm	Horizon rich in OM. Dark brown colour. Lots of thin roots. Horizon thickness varies laterally.
AE	<1 cm	Possible transitional A->E but not prominent
E	>15cm	Medium brown coloured horizon. Mixed mineral and OM. Penetrated by thick roots. Layer is interspersed by unconsolidated, angular-subangular, poorly sorted limestone fragments. Translocation of OM around roots is apparent.
C	>30cm	Light brown. Mainly weathered limestone and dolomite. As above, lots of limestone fragments, angular to sub-angular, poorly sorted.
R		Unconsolidated bedrock

Table 3.5 Soil horizons characteristic of brown calcareous soil overlying Grotta di Ernesto.

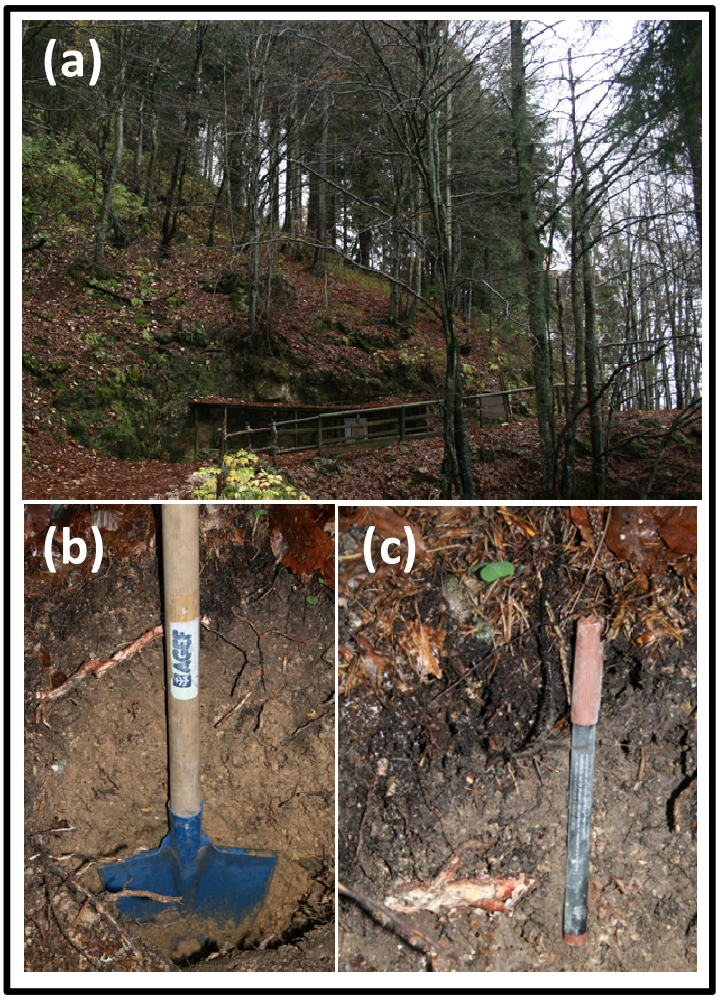

Figure 3.20 (a) View of the steep forested hillside above Grotta di Ernesto, (b) soil profile at Grotta di Ernesto and (c) enlargement of organic-rich A horizon with E horizon beneath.

4. FLUORESCENT PROPERTIES OF DRIPWATER NOM

4.1 INTRODUCTION

Groundwaters are characterised by generally low concentrations of organic matter (OM) (typically < 2 mg L^{-1} at depths > 5 m (Pabich *et al.,* 2001). In karst groundwaters, much of the OM which migrates into the phreatic zone is rapidly mineralised by epilithic [rock-attached] microbial communities (Einsiedl *et al.,* 2007), except for a presumably recalcitrant, hydrophilic (fulvic-like) fraction which remains in solution. It is unclear whether this residual OM avoids mineralisation because of a limited availability of suitable binding sites on aquifer surfaces, as proposed by Einsiedl *et al.* (2007), or whether its survival in solution is instead related to other factors, including composition (hydrophilicity vs. hydrophobicity), speciation (particulate, colloidal, dissolved) and hydrogeochemical processes (transport, coagulation-deposition, carbonate dissolution-precipitation).

Between its initial mobilisation from soils, and the end-points of respiration or export from the karst network, OM in its varied forms is subject to the effects of hydrogeochemical processes. In particular, the ionic strength of percolating groundwaters and the residence (reaction) time of OM in solution are important factors in the stability of OM in the colloidal size range. This is because at higher *I* the electric double layer of electrolytes,

through which electrostatic repulsion between negatively charged colloid surfaces is exerted, becomes compressed, enabling attractive London van der Waals interactions to occur, ultimately resulting in agglomeration and deposition of colloidal OM if attraction exceeds repulsion (Buffle and Leppard, 1995; Lead and Wilkinson, 2006).

High divalent cation concentrations also promote the formation of colloidal aggregates through cation-bridging reactions between dissolved and colloidal OM and inorganic phases such as metal oxides (Fe, Al, Mn) and aluminosilicates (Mavrocordatos *et al.,* 2000; Majzik and Tombacz, 2007). Dissolved organic carbon (DOC) is defined as those compounds below a cut-off of 0.45 μm, although this has long been recognised as a somewhat arbitrary, systematic definition (Thurman, 1985). In fact, aquatic colloidal materials exist down to 1 nm in size (Lead and Wilkinson, 2006), and in karst, OM is known to exist within colloidal aggregates with diameters well below 0.45 μm (Mavrocordatos *et al.,* 2000; Hartland *et al*., 2010a). In addition, the concentration of colloidal entities in fractured aquifer systems has been shown to be negatively correlated with the ionic strength of solution (McCarthy and Shevenell, 1998) and thus, destabilisation through charge-shielding is a potentially important process control affecting the transmission of OM in karstic networks.

Dissolved organic carbon concentration and UV-fluorescence have been widely applied as hydrologic tracers in cave studies (Baker *et al.,* 1997a; 1999b; Cruz *et al.,* 2005; Ban *et al.,* 2008). Peaks in luminescence intensity and organic matter in cave waters often occur

during hydrologically active periods in northern temperate (Baker *et al.,* 1999b), sub-tropical (Cruz *et al.,* 2005) and monsoonal climate zones (Tan *et al.,* 2006; Ban *et al.,* 2008). However, the transmission of NOM in dripwaters is often offset from rainfall maxima. Possible reasons for this include decoupling of the soil-aquifer system as a result of soil-moisture deficit (Baker *et al.,* 1997a, 2000; Cruz *et al.,* 2005), aquifer drying (Baker *et al.,* 2000), and differential hydrological routing between drips (Tooth and Fairchild, 2003). However, it is not know to what extent fluorescence intensity and DOC concentration reflect the transmission of colloidal organics and whether the migration rates of different organic species are affected by differences in drip discharge and routing.

Detailed spatial and temporal studies of the composition and physical speciation of NOM in cave waters are needed to better understand the processes controlling the transmission of NOM in karstic networks. Such information is of relevance for the interpretation of NOM in speleothems (Borsato *et al.,* 2007; Blyth *et al.,* 2008; Fairchild and Treble, 2009), to the turnover of OM by phreatic microbial communities (Farnleitner *et al.,* 2005; Einsiedl *et al.,* 2007) and hence for the development of epigenic karstic systems and speleogenesis through microbial CO_2 production (Gabrovšek *et al.,* 2000; Engel *et al*., 2004).

Fluorescence is a suitable technique for the rapid characterisation of NOM in a range of sizes (Seredyńska-Sobecka *et al.,* 2007). This chapter reports on studies conducted into the effects of pH, temperature, dilution and filtration on the fluorescent properties of NOM in Poole's Cavern (PC) dripwater samples. Experimental manipulation of these variables was

exploited in order to obtain a more detailed understanding of the properties of fluorescent NOM in karst dripwater.

4.2 MATERIALS AND METHODS

Five drip points at Poole's Cavern were selected for the investigation of the fluorescent properties of colloidal fractions (see Fig. 3.11 for locations). Each drip point was sampled on a monthly basis between August 2008 and August 2009. Bulk samples from drip point PE1 were also taken more frequently during the summer, autumn and winter of 2008 to provide additional information to aid the interpretation of the PC-08-1 stalagmite (Chapter 7), which was removed from beneath the PE1 drip in June 2008. In Tables 4.1 and 4.2, relevant geochemical and hydrological details for each drip site are given.

Details of the sampling strategy, laboratory protocols and instrumental methods are available in Chapter 3. In addition to the routine analysis of size-fractionated water samples, experiments were also conducted into the effects of temperature, dilution and pH on the emission wavelength and intensity of fluorescence in selected samples. In the pH-adjustment experiments, the pH of samples was modified by drop-wise addition of Ultrapure 0.1 M HCl and Aristar 0.1 M NaOH using an Orion 3 Star bench top pH meter (Thermo Electron Corp) and VWR pH probe. Thermal quenching of fluorescence intensity was conducted at temperatures between 10 and 45 ºC at 5 ºC increments using a Peltier temperature controller attached to a Varian Cary Eclipse spectrophotometer.

4.3 RESULTS AND DISCUSSION

4.3.1 Fluorescence characterisation of NOM

Fluorescence 3D Emission Excitation Matrices (EEMs) (maps of organic matter fluorescence intensity in optical space; Fig. 4.1) were applied to the study of NOM in cave dripwaters. Fluorescence signatures in Poole's Cavern dripwaters corresponded to humic-like (peak C) fluorescence at the excitation-emission pair of 290-340:395-430 nm and fulvic-like fluorescence (peak A) at the excitation-emission pair of 265-280:300-370 (Fig. 4.1; peak centres indicated on PE1 plot). Protein-like fluorescence (peak T) which is correlated with microbial breakdown of OM (Baker *et al.,* 2008) was generally absent in all dripwater samples with the exception of a prominent, transient signal in RC1 dripwater during a period of low flow in July 2009.

In the mildly-alkaline drips (pH 7.5-8, BC1 and BC2) the fluorescence signal was typically weak, consistent with the low OC concentrations measured in these drips and comparable to fluorescence intensity values from other cave studies (e.g. Baker and Genty, 1999). Low fluorescence intensities and OC concentrations (i.e. < 2 mg L^{-1}) were also measured in dripwaters sampled during surveys of other cave systems in the region (Blue John Cavern, Peak District; White Scar, Yorkshire) and elsewhere in the UK (Gough's Cavern, Cheddar Gorge; Kent's Cavern, Torquay). Contrastingly, the high pH drips studied at Poole's Cavern (RC1, RC2 and PE1) were characterised by elevated TOC concentrations 2-3 times that in the BC1 and BC2 drip points, and exceptionally high fluorescence intensities (Table

4.1; Fig. 4.1). Peak fluorescence in the high pH drips was also shifted to shorter wavelengths relative to that measured in BC1 and BC2, in particular with respect to the peak C fluorophore (Fig. 4.2).

4.3.2 Hydrochemical controls on fluorescence attributes

The relationship between fluorescence, TOC and hydrochemical variables was investigated using principal components analysis (PCA) (Fig. 4.3). PC1 explains ~50% of the variability in the data, and separates high and low pH waters. High pH waters had high raw fluorescence intensity, low raw fluorescence emission wavelengths, high K^+, high peak A fluorescence intensities (<100 nm), higher EC, and greater Ca^{2+}, SO_4^{2+} and TOC concentrations. PC2 only explains ~10% of the variability and comprises all inorganic elements except K^+. It is notable is that discharge loads equally on PC1 and PC2, and that the <100 nm fraction fluorescence properties do not fall in the same scores as raw values.

Elevated potassium concentrations (1 – 10 mg L^{-1}) were found in all hyperalkaline drip points compared to the lower pH drip sites (BC1 and BC2; K^+ <1 mg L^{-1}). Potassium is expected to originate from ash deposits associated with lime waste. Elevated SO_4^{2-} concentrations (1 – 50 mg L^{-1}) were also associated with the hyperalkaline dripwaters and probably also originate from ashes given that SO_4^{2-} is no more soluble at high pH (SO_4^{2-} concentrations in BC1 and BC2 were generally <10 mg L^{-1}).

Organic carbon concentration in Poole's Cavern dripwaters was dominated by the high pH conditions, with little association with drip discharge (Fig. 4.3). Higher pH conditions in the hyperalkaline dripwater samples (PE1, RC1 and RC2) were associated with higher TOC concentrations (Table 1), although PCA revealed that this association was strongest between pH and TOC in the PE1 dripwater- which had a consistently lower *I* than RC1 and RC2 (Fig. 4.3). The higher TOC content of PE1 is thought to relate to charge-stabilisation of colloidal NOM in the PE1 dripwater (Table 1), indicating that NOM was less stable at equivalent pH and higher *I* in RC1 and RC2 dripwater. Charge stabilisation occurs at elevated pH values because functional groups associated with organic compounds, colloid and particle surfaces, deprotonate, causing the development of increased electrostatic charge and therefore repulsion (Tipping, 2001); whereas at higher *I* (and equivalent pH) aggregation-deposition may be enhanced due to charge shielding (Buffle and Leppard, 1995).

The emission wavelength of peak A and C fluorescence (in raw and filtered samples) was best correlated with peak C fluorescence intensity <100 nm in the BC1 and BC2 samples; indicating compositional shifts in OM coinciding with higher fluorescence intensity. The geochemical variables (Cl^-, NO_3^-) were not significantly associated with OC concentration or fluorescence. The concentration of these anions instead varied according to other processes, being independent of the effects of high pH, e.g. Cl^- being largely derived from marine aerosol. The overall impact of minor ions (e.g. K^+, Cl^-, NO_3^-, SO_4^{2-}) on fluorescence is expected to be subordinate to the overall effect of *I* on the conformation of OC and associated fluorophores (i.e. through charge shielding).

	TOC contents of filtered dripwater samples (mg L^{-1})			Fluorescent properties of raw samples						
Sample point	**Raw**	**<1 μm**	**<100 nm**	**<1 nm**	**Peak A Ex (nm)**	**Peak A Em (nm)**	**Peak A Int (units)**	**Peak C Ex (nm)**	**Peak C Em (nm)**	**Peak C Int (units)**
RC1	4.1 ± 1.1	3.1 ± 1.0	2.3 ± 1.2	2.1 ± 0.6	239.4 ± 4.5	407.9 ± 7.1	414.29 ± 93.2	319.7 ± 13.8	400.0 ± 6.7	302.0 ± 74.3
RC2	3.7 ± 0.9	3.0 ± 0.8	2.5 ± 0.8	2.0 ± 0.9	238.1 ± 5.0	406.0 ± 6.9	435.5 ± 80.9	317.2 ± 2.5	394.6 ± 17.5	310.8 ± 57.9
PE1	4.0 ± 2.1	2.1 ± 1.0	1.8 ± 1.1	1.4 ± 1.3	225.4 ± 57.5	415.1 ± 6.4	245.2 ± 52.1	297.7 ± 80.7	401.3 ± 21.1	140.9 ± 34.8
BC1	1.7 ± 0.7	1.6 ± 1.2	1.6 ± 0.6	< LD	231.4 ± 48.7	422.6 ± 9.3	38.4 ± 15.2	320.4 ± 65.2	416.5 ± 8.0	23.2 ± 10.9
BC2	1.6 ± 0.8	1.6 ± 1.1	1.1 ± 0.3	< LD	217.5 ± 69.6	417.0 ± 9.4	34.1 ± 7.6	305.6 ± 92.3	419.4 ± 8.7	19.7 ± 6.6

Table 4.1 Summary fluorescence and total organic carbon (TOC) data from Poole's Cavern, June 2008 – August 2009

Data presented above are averages and standard deviations from monthly dripwater collections. LD = limit of detection for blank-corrected TOC values in filter permeates (see Chapter 3 for details of methodology). Ex = excitation, Em = emission, Int = intensity.

		Physicochemical properties			Major cations (mmol L^{-1})				Major anions (mmol L^{-1})						Estimated EC (Rossum)	% actual EC
Drip point	**n**	**EC (mS cm^{-1})**	**pH**	**Temp (°C)**	**Ca^{2+}**	**Mg^{2+}**	**Na^{2+}**	**K^{+}**	**HCO_3^-**	**CO_3^{2-}**	**OH^-**	**SO_4^{2-}**	**NO_3^-**	**Cl^-**	**EC (mS cm^{-1})**	**%**
PE1	5	0.69 ± 0.24	11.7 ± 0.4	9.2 ± 1.0	1.86 ± 0.71	nd	0.15 ± 0.01	0.12 ± 0.02	nd	nd	4.02 ± 1.83	0.36 ± 0.20	0.12 ± 0.02	0.18 ± 0.06	0.54 ± 0.61	80 ± 35
BC1	6	0.49 ± 0.06	8.0 ± 0.1	9.1 ± 1.3	2.34 ± 0.27	0.03 ± 0.00	0.14 ± 0.01	0.03 ± 0.01	4.03 ± 0.61	0.02 ± 0.01	nd	0.07 ± 0.04	0.14 ± 0.07	0.14 ± 0.10	0.51 ± 0.05	106 ± 13
BC2	5	0.51 ± 0.05	8.0 ± 0.1	8.9 ± 0.8	2.34 ± 0.40	0.04 ± 0.00	0.15 ± 0.01	0.03 ± 0.01	3.95 ± 1.20	0.02 ± 0.00	nd	0.08 ± 0.03	0.17 ± 0.10	0.17 ± 0.06	0.53 ± 0.06	107 ± 14
RC1	4	2.08 ± 1.24	12.1 ± 0.6	8.4 ± 0.7	3.61 ± 2.56	nd	0.17 ± 0.01	0.15 ± 0.04	nd	nd	12.8 ± 9.92	0.25 ± 0.13	0.16 ± 0.07	0.21 ± 0.07	0.89 ± 0.47	45 ± 24
RC2	3	2.32 ± 1.43	12.4 ± 0.5	8.6 ± 0.8	2.96 ± 1.20	nd	0.18 ± 0.01	0.16 ± 0.12	nd	nd	11.2 ± 5.72	0.16 ± 0.17	0.12 ± 0.06	0.12 ± 0.10	0.76 ± 0.30	35 ± 14

Table 4.2 Mean physiochemical and geochemical data from Poole's Cavern, June 2008 – August 2009

Alkalinity estimated by difference from charge balance, proportions of HCO_3^-, CO_3^{2-} and OH^- predicted from solution pH. Predicted conductance calculated by the method of Rossum (1975). Modification of dripwater composition by calcite precipitation before collection may be indicated by the disparity between the measured conductance and that predicted by the Rossum calculation. EC= electrical conductivity; Nd= not determinable.

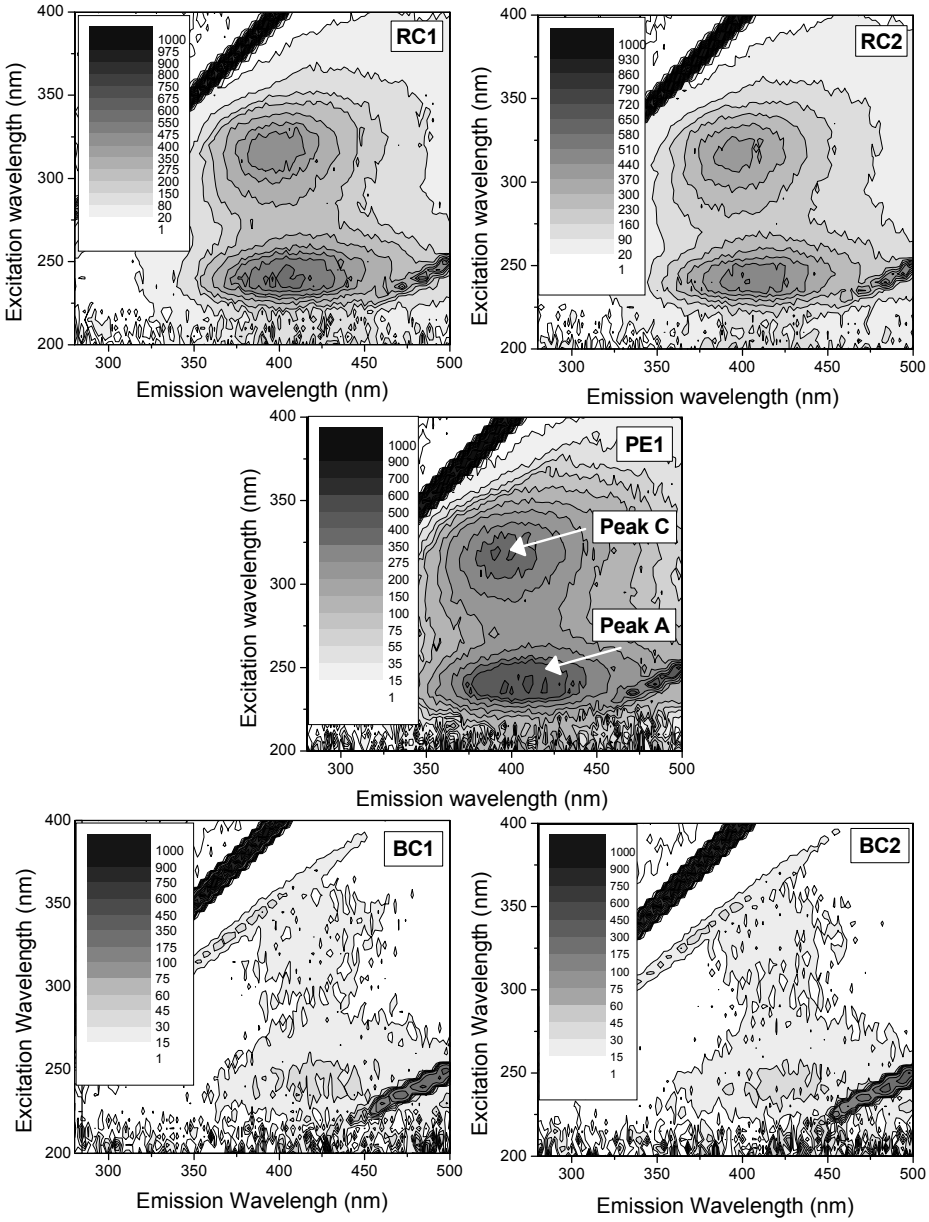

Figure 4.1 Fluorescence Emission-Excitation Matrices (EEMs) of dripwaters sampled at Poole's Cavern in December 2008. Peak A and C fluorophores are indicated on the PE1 plot (centre). Fluorescence intensities (arbitrary units) in EEMs shown by shaded contours. Diagonal lines in EEMs correspond to first- and second-order Raleigh scatter of incoming light by water molecules.

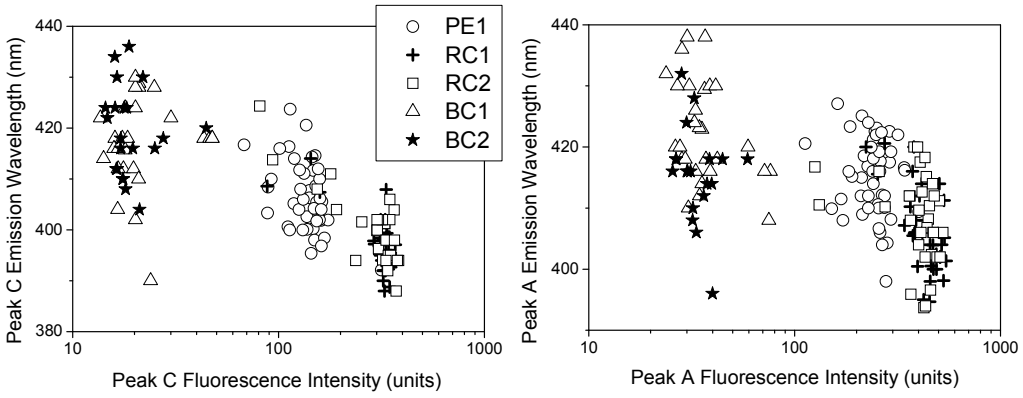

Figure 4.2 The peak A and peak C emission wavelength to intensity relationship in Poole's Cavern dripwater samples. Samples from high-pH drips PE1, RC1 and RC2 exhibited abnormally high fluorescence intensities for the range of TOC concentrations measured. Peak fluorescence emission wavelengths were consistently shifted to shorter wavelengths relative to drip points in the normal range of pH (BC1 and BC2).

4.3.3 Effects of filtration and dilution

Fluorescence intensities typically increased following filtration. Deionised water (DIW) filter blanks were found to be equivalent to the DIW blank (i.e. zero detectable fluorescence) and hence the phenomenon was attributed to the reduction of inner-filtering of incoming light by solids. The phenomenon of inner-filtering was first recognised in strongly absorbing samples (high TOC) and occurs when the incoming light is unable to fully penetrate the sample (Bashford and Harris, 1987; Mobed *et al.,* 1996). Hence, at a given concentration of organic carbon the fluorescence-TOC relationship departs from linearity (Mobed *et al.,* 1996). Indeed, Hudson *et al.* (2007) recognised that with respect to peak A fluorescence intensity there is no point at which inner-filtering is completely negated by dilution.

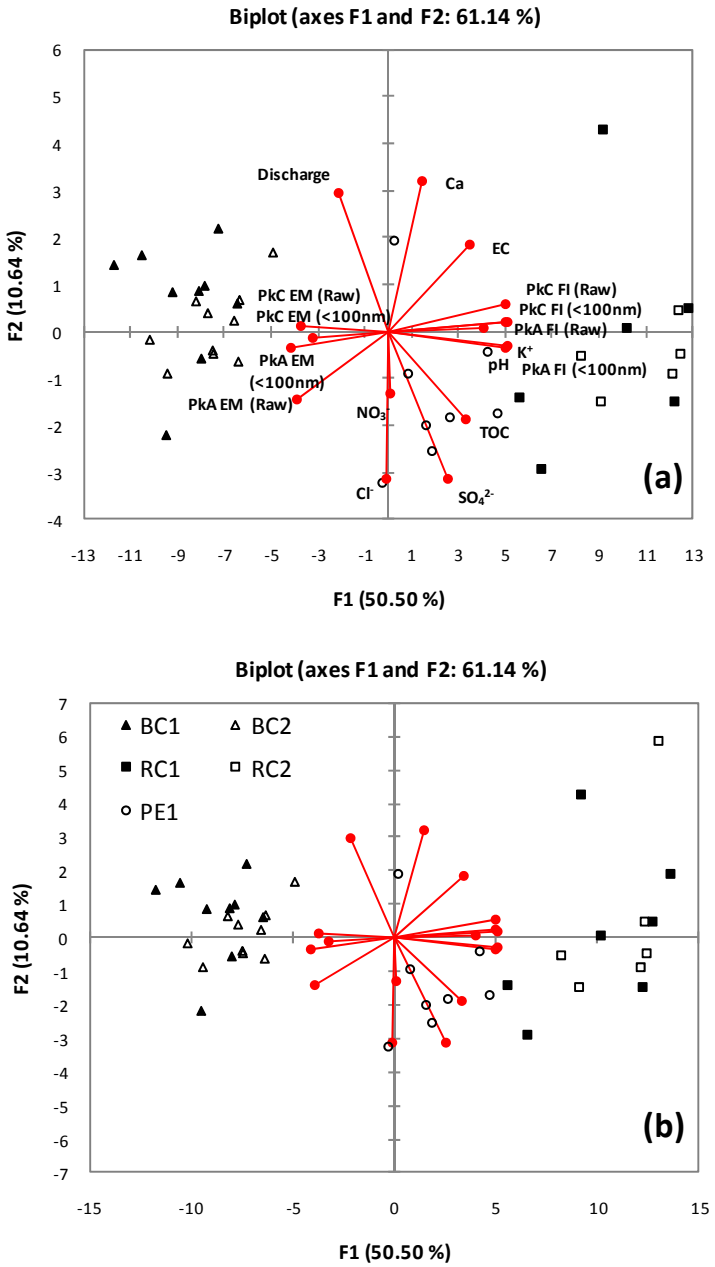

Figure 4.3 Principal components analysis of Poole's Cavern dripwater hydrochemical variables and fluorescence characteristics (a) bi-plot of variables and factors showing data distribution from each location (b) correlations between variables and factors. PC1 explains ~50% of the variability in the data, and separates high and low pH waters. PC2 explains ~10% of the variability and comprises all inorganic elements except K^+. PkC= peak C, PkA= peak A, EM= emission, TOC= total organic carbon.

Increases in fluorescence following filtration have been observed by previous authors, but these authors did not explicitly attribute the phenomenon to reduced inner-filtering (Patel-Sorrentino *et al.,* 2002; Seredyńska-Sobecka *et al.,* 2007; Liu *et al.,* 2007). In order to investigate this process, a series of dilution experiments were conducted with size-separated dripwater samples collected in November-December 2008 and May-June 2009. The results of this exercise demonstrated that the fluorescence intensity of both fluorophores in raw and filtered dripwaters was generally sub-optimal and hence, fluorescence was quenched to some extent by inner-filtration. Inner-filter effects were strongest with respect to peak A, with fluorescence intensities in the 2:1 diluted samples ranging between 51-113% of that in the undiluted samples, peak C fluorescence intensities ranged between 50-81%. Thus, the fluorescence of NOM in both normal and high-pH cave dripwaters was found to be quenched by inner-filtering even at low concentrations and after removal of colloids (i.e. following ultrafiltration at ca. 1 nm).

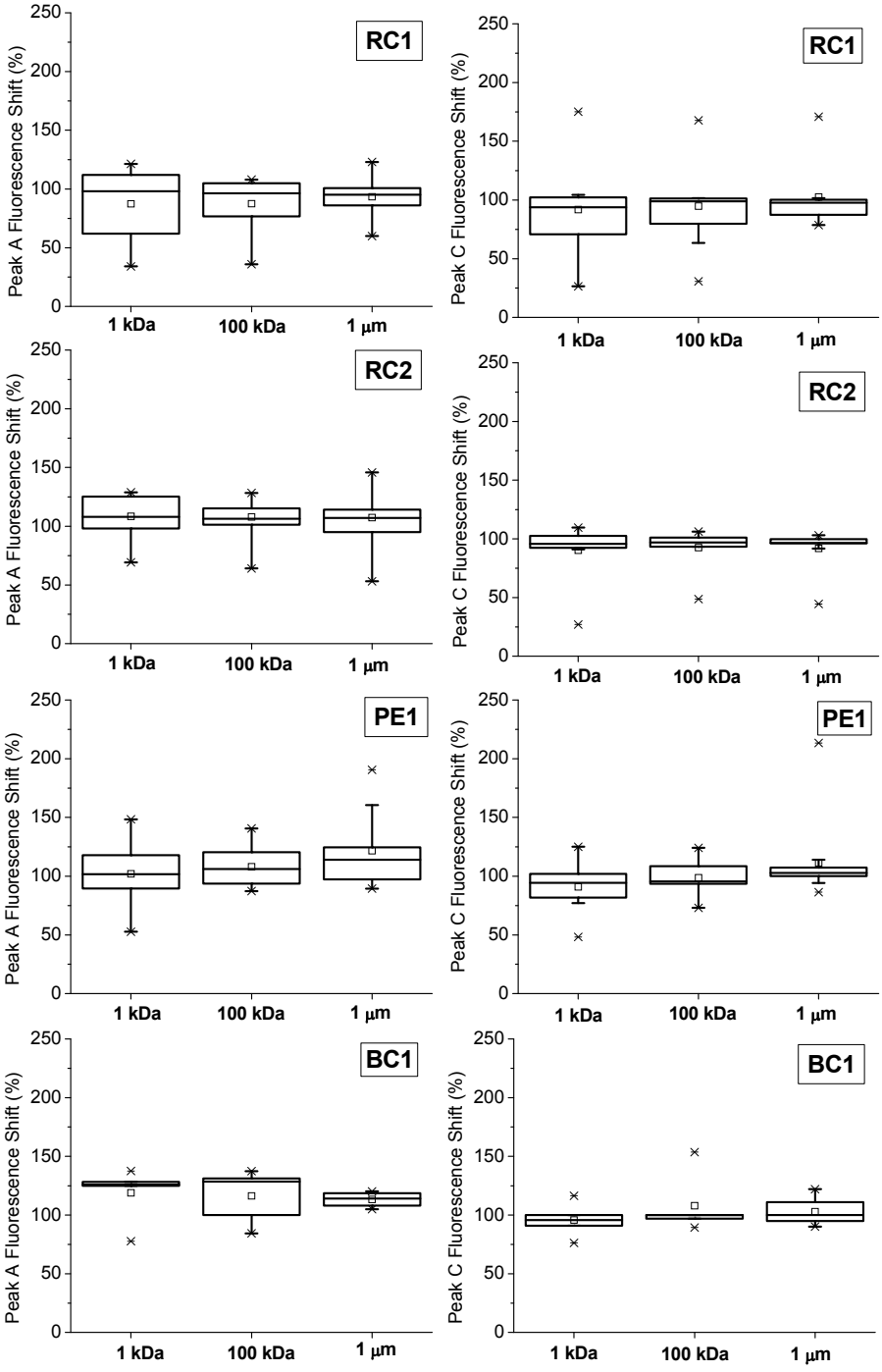

Figure 4.4 Box plots of the fluorescence intensity (%) in the permeates of sequentially filtered Poole's Cavern dripwater samples relative to that in the raw (unfiltered) sample.

The fluorescence intensities in sequential filter permeates are plotted as a percentage of the fluorescence measured in the raw sample in Figure 4.4. As in the dilution experiments, peak A fluorescence was generally more sensitive to filtration. In RC1, RC2 and BC1 samples, median peak C fluorescence was slightly reduced between filter permeates, while peak A fluorescence increased strongly in the <0.1 μm and <1 nm fractions. But, in PE1, the median peak C fluorescence was slightly reduced by each successive filtration, reflecting the removal of a sub-fraction of fluorescent OM by each filter step. Increases in peak A fluorescence intensity below ca. 100 nm in the BC1, RC1 and RC2 dripwater samples may be consistent with the removal of largely non-fluorescent light scattering colloids in these samples. However, the results from all the dripwaters show that *fluorescent* OM was concentrated in the finest fraction, i.e. ≤ ca. 1 nm.

The impact of filtration on fluorescence intensity and OC concentration is summarised in Fig. 4.5. Overall, fluorescence intensity at peak C was associated with colloidal OM to a greater extent than peak A- peak C fluorescence intensity was generally reduced by sequential filtration between 1 μm and 1 nm (following an initial increase between the raw sample and the 1 μm filter permeate) (Fig. 4.5). Contrastingly, peak A fluorescence increased with each successive filtration, confirming that this fluorophore is much more sensitive to IFE (Hudson *et al.*, 2007) and less specifically associated with colloids than peak C. Overall, coarse colloidal materials contributed a disproportionally small amount of the total fluorescence in the studied samples, relative to the substantial amount of organic carbon resident in the colloidal phase in hyperalkaline dripwater (Table 4.1).

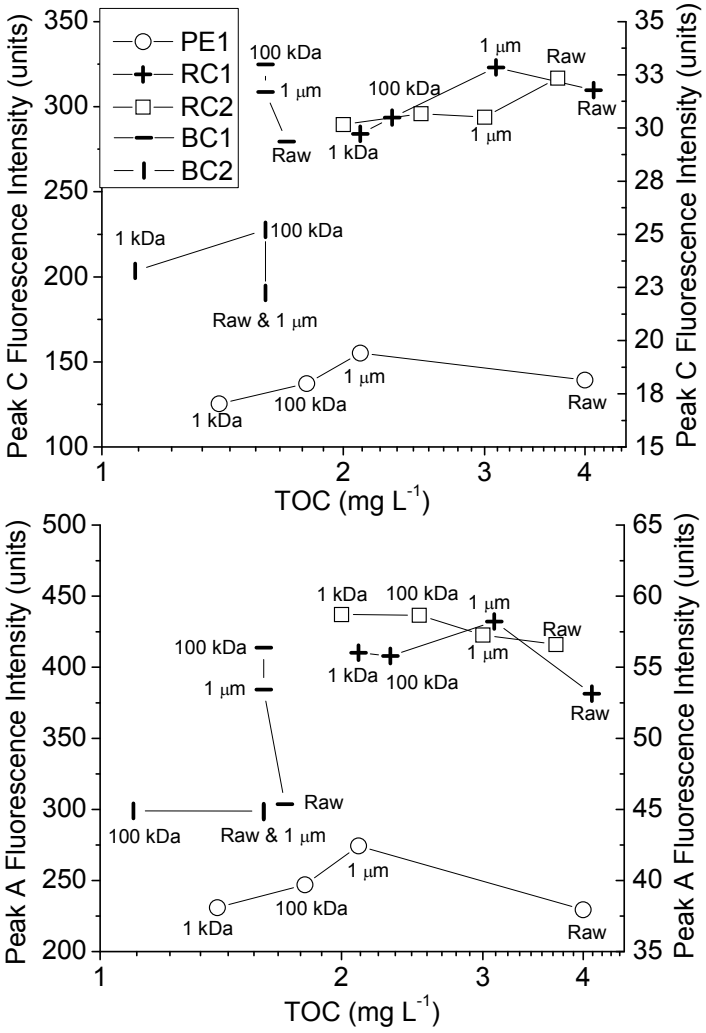

Figure 4.5 Summary of the interrelationship between total organic carbon (TOC) concentration and Peak A and Peak C fluorescence intensity in raw and sequentially filtered Poole's Cavern dripwaters. Colloidal fluorescence at Peak A is entirely quenched by inner-filtering of light. Peak C fluorescence of colloids is strongly quenched by coarse colloids and particulates.

Thus, even though the coarse colloids and particulates exhibited some intrinsic fluorescence, this was typically less than or equivalent to their quenching effect; so that when these components were removed by filtration, the net result was that the fluorescence

signal in the filtered sample was either not substantially altered, or enhanced. This process is summarised as follows:

$$(4.1) \qquad \text{PkA } FI_{coll} + (\text{PkA } FI_{diss} - \text{PkA } IFE_{coll}) \leq \text{PkA } FI_{diss}$$

$$(4.2) \qquad \text{PkC } FI_{coll} + (\text{PkC } FI_{diss} - \text{PkC } IFE_{coll}) \geq \text{PkC } FI_{diss}$$

Where FI_{coll} and FI_{diss} are the intrinsic fluorescence intensities of the colloidal and dissolved organic fractions, and IFE_{coll} is the fluorescence intensity of the dissolved fraction that is quenched by inner filtering by coarse colloids (>100 nm) and particulates.

In Fig. 4.6, the relationship between fluorescence and TOC concentration is shown with respect to the high pH samples: it is apparent that fluorescence intensity in the unfiltered samples does not reflect the concentration of OC, but fluorescence intensity at <100 nm is correlated with OC concentration, reflecting the importance of IFE in these samples.

4.3.4 Thermal quenching of fluorescence

Thermal quenching of fluorescence is a novel technique that is based on the fact that fluorescence intensity is quenched in response to changes in temperature in proportion to the exposure of the fluorophore to the energy source (Baker, 2005). Thermal quenching has only yet been applied in the characterisation of aquatic NOM in a few cases (Baker, 2005; Elliot *et al.,* 2006; Seredyńska-Sobecka *et al.,* 2007), and has not been previously applied with cave dripwater samples.

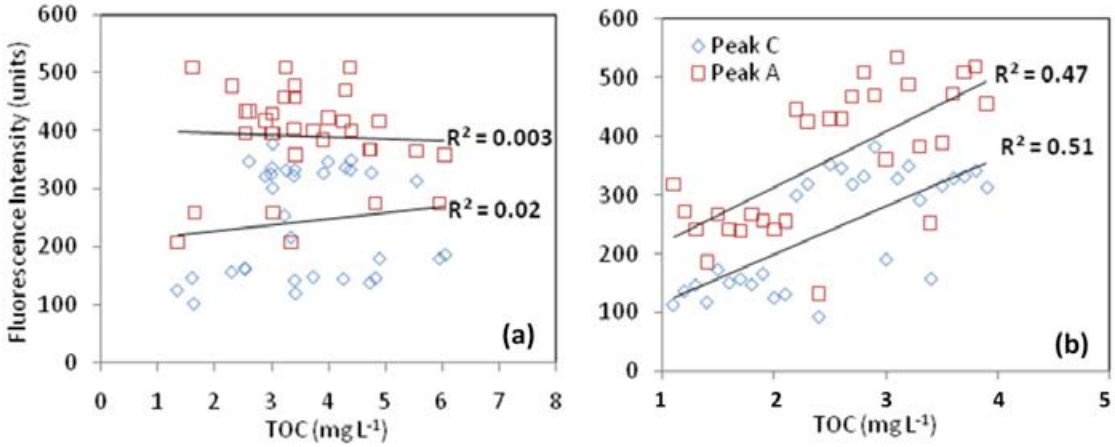

Figure 4.6 Relationship between TOC concentration and peak C and peak A fluorescence intensity in the raw (a) and permeate of the 0.1 μm (ca. 100 nm) membrane (b) in Poole's Cavern high pH drips (combined data). TOC and fluorescence intensity values in the filtered samples are correlated demonstrating that the coarse colloidal (>100 nm) fraction of TOC did not contribute substantively to bulk fluorescence properties of dripwater samples and that fluorescence intensity variations in Poole's Cavern dripwaters are representative of predominantly dissolved compounds. It was not possible to test this relationship with TOC in the 1 kDa ultrafilter permeates because TOC in the majority of samples was below the limit of detection.

Thermal quenching of fluorescence was conducted on size-separated dripwater samples taken in October and December 2008 and March 2009, from drip points PE1, RC1 and RC2. Thermal quenching experiments were also conducted using size-separated samples from the BC1 drip, sampled in March, June and August 2009. Because the absolute fluorescence intensities varied both spatially and temporally, fluorescence intensities in each sample were normalised by expressing the intensities as a percentage of the total fluorescence detected between 10 ºC and 45 ºC, for each fluorophore. In order to evaluate the nature of the fluorescent response to temperature without introducing bias, the data points from each size fraction were linearly regressed against temperature. The gradient

from the regression equation and the correlation coefficient were then used in further statistical analysis.

In Fig. 4.7, the thermal quenching behaviour of size-separated OM from each drip point is shown. Linear regressions of the amassed data show that the nature of the thermal response of OM in each drip point did not vary, either between size-separated fractions or between months. In fact, at the 0.05 level no statistically significant shift in the thermal response was found between the population means of the RC1, RC2 and PE1 drip points (2-way ANOVA, Bonferroni test). However, the thermal quenching of peak C fluorescence in OM from the BC1 drip was found to be significantly different at the 0.05 level from that of the high pH drips. Indeed, OM in the BC1 drip was significantly less sensitive to temperature, but with more scatter in the data, which is probably the result of a lower signal-to-noise ratio in fluorescence from BC1.

Thermal quenching of peak A fluorescence intensity in the BC1 samples was also found to be significantly different to the RC1 and RC2 samples, but not with respect to those from the PE1 drip point. Overall, there was no difference between size fractions in any of the drips in terms of thermal response. Hence, the conclusion can be drawn that fluorophores in organic compounds from the high pH drips were exposed to the incoming light to a similar extent, and that fluorophores in the BC1 drip were less exposed to the incoming light. Because the BC1 samples were not pH-adjusted prior to the thermal quenching experiments it is not possible to determine whether this difference originates from compositional factors or simply because of the lower pH of the BC1 samples (Section 4.3.5).

It is important to emphasise that although the absolute fluorescence intensity values did vary between size fractions, and were typically enhanced in filtered samples as found by (Liu *et al.,* 2007), no statistically significant difference between the thermal sensitivity of size-separated fractions was detected; i.e. the extent to which fluorophores in were exposed to incoming light did not vary between size-separated fractions. This is considered to reflect that the colloidal fraction of organic carbon in the samples was not compositionally distinct from NOM in the finest size range (i.e. ≤ 1 nm). Increases in the absolute fluorescence intensity values between size-separated fractions are not apparent in Fig. 4.7a and 4.7b because of the aforementioned normalisation procedure.

Hence, this finding is indicative of the consistent presence of OM in a continuum between >1 μm and <1 nm. Colloidal NOM exhibited a small but detectable proportion of total fluorescence in PE1 dripwater samples. The observed increases in peak A fluorescence intensity below 100 nm in the BC1, RC1 and RC2 dripwater samples are consistent with the presence of largely non-fluorescent light scattering colloids in these samples. The results from the BC1, RC1 and RC2 dripwaters suggest that fluorescent OM was concentrated in the finest fraction, whereas, in the PE1 dripwater, a small proportion of fluorescent OM was present with diameters >1 nm (Fig. 4.4). This interpretation is consistent with the findings reported in the following section and Chapter 5. The distribution of colloids and particulates in Poole's Cavern dripwaters may therefore be related to the ionic strength and pH of the drip waters. This inference is based on the fact that the PE1 drip was the only drip with an ionic strength in the normal karstic range, but

with a consistently high pH, providing conditions under which colloids may have been preferentially charge-stabilised.

4.3.5 The pH-fluorescence relationship

Exceptionally high fluorescence intensities and shorter peak emission wavelengths (relative to ca. pH 8 samples) were detected in the high pH drips (PE1, RC1 and RC2). In order to examine the effect of pH on the fluorescence characteristics of OM in these dripwaters, a subset of drip water samples were pH-adjusted and analysed using fluorescence EEMs. The TOC concentration in the pH-adjusted samples was also measured to ensure that variations in fluorescence were independent of TOC content. Experiments were repeated on consecutive months (July and August 2009) with the exception of water sampled from RC2 (sampled in November 2008 and August 2009). Both raw (unfiltered) samples and those filtered at 100 nm were used in order to evaluate whether pH effects were size-specific. In Fig. 4.8, the fluorescence intensity in the pH-adjusted samples is plotted as the percentage deviation relative to Suwannee River Fulvic Acid (SRFA) standard prepared at 5 mg L^{-1} and equivalent pH ± 0.1 pH units. The SRFA standard was used for comparison because it is a small hydrophilic compound which responds to elevated pH in a predictable and consistent manner, and comparable to aquatic dissolved NOM in general, i.e. an increase in fluorescence intensity between pH 1 to 11 and a slight decrease at pH 12 (Patel-Sorrentino *et al.,* 2002; Spencer *et al.,* 2007).

Changes in fluorescence characteristics with pH are the result of changes in the coordination or neighbouring environment of fluorescent acidic functional groups (e.g. phenols and other aromatic acids) which occur due to deprotonation, indicating enhanced intra-molecular repulsion between negatively charged functionalities (Tipping, 2001). Therefore, at high pH, conformational changes in the organic molecules may occur (e.g. uncoiling), changing their exposure to incoming light (Miano *et al.*, 1988; Senesi *et al.*, 1991a; 1991b).

By comparing the pH-sensitivity of fluorescence in different samples it is possible to derive information relating to the physical configuration of the OM. Relatively greater increases in fluorescence intensity at high pH may be indicative of the presence of higher molecular weight, conjugated compounds; or alternatively of the expansion of OM present in colloidal aggregates (at lower pH values). Pronounced pH-sensitivity in organic compounds is possibly indicative of a greater proportion of functional groups possessing higher activation energies, which may in turn result in stronger binding of trace metals (Stern *et al.,* 2007).

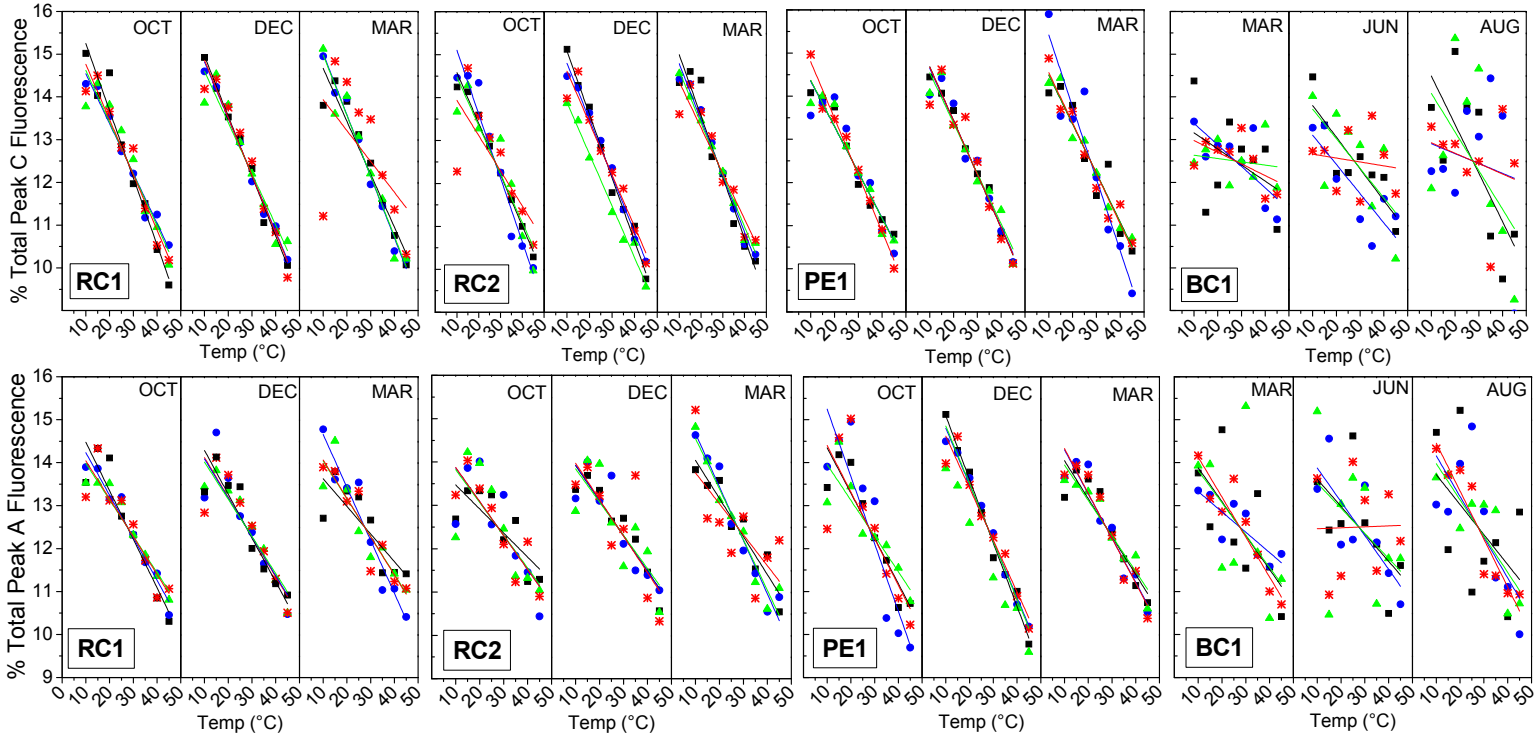

Figure 4.7 Thermal quenching of fluorescence intensity in size-fractionated Poole's Cavern dripwater samples from different months (■ = raw, ▲ = ≤100 nm ● = ≤1 μm, * = ≤1 nm). Top row = Peak C fluorescence intensity, bottom row = Peak A fluorescence intensity. Fluorescence intensity values were Raman-corrected and normalised by expressing fluorescence intensities as a percentage of the total fluorescence detected between 10 and 45 °C.

The fluorescence intensity of OM from BC1 displayed little change between pH 8 and 12 (relative to SRFA) and thus, the pH sensitivity of OM in the normal pH dripwater (BC1) is consistent with a low molecular weight (LMW) aquatic fulvic acid (Fig. 4.8). At high pH, emission wavelengths in the BC1 dripwater were found to increase marginally (red-shift) at longer wavelength fluorescence (peak C) and decrease (blue-shift) by a similar amount at shorter wavelengths (peak A). Spectral shifts resulting from pH changes may reflect the type of OM present (Mobed *et al.,* 1996), but inconsistencies between published studies make it difficult to use such information as a reliable diagnostic tool (Tam and Sposito, 1993; Patel-Sorrentino *et al.,* 2002). Differential behaviour in the pH sensitivity of peak A and C is indicative of their association with structurally distinct classes of OM (Patel-Sorrentino *et al.,* 2002).

Unlike the BC1 samples, those from the high pH sites (PE1 and RC2) were found to be highly sensitive to increases in pH with respect to the peak C fluorophore (Fig. 4.8). In particular, RC2 dripwater sampled in November 2008 exhibited by far the greatest relative increase in peak C fluorescence at high pH. This is thought to reflect the presence of high molecular weight (HMW), poly-aromatic OM in the RC2 dripwater at this time. The peak C emission wavelengths in fractionated RC1 and RC2 dripwaters were elevated in winter 2008, consistent with transmission of HMW OM during this time (Appendix V).

In the PE1 dripwater samples the results for peak A fluorescence were markedly different between consecutive months. In July, the peak A fluorescence response to pH increase was small but positive, whereas in August the peak A fluorescence response

was strongly negative, characterised by a sharp decline at pH 9 followed by a partial recovery above pH 10.

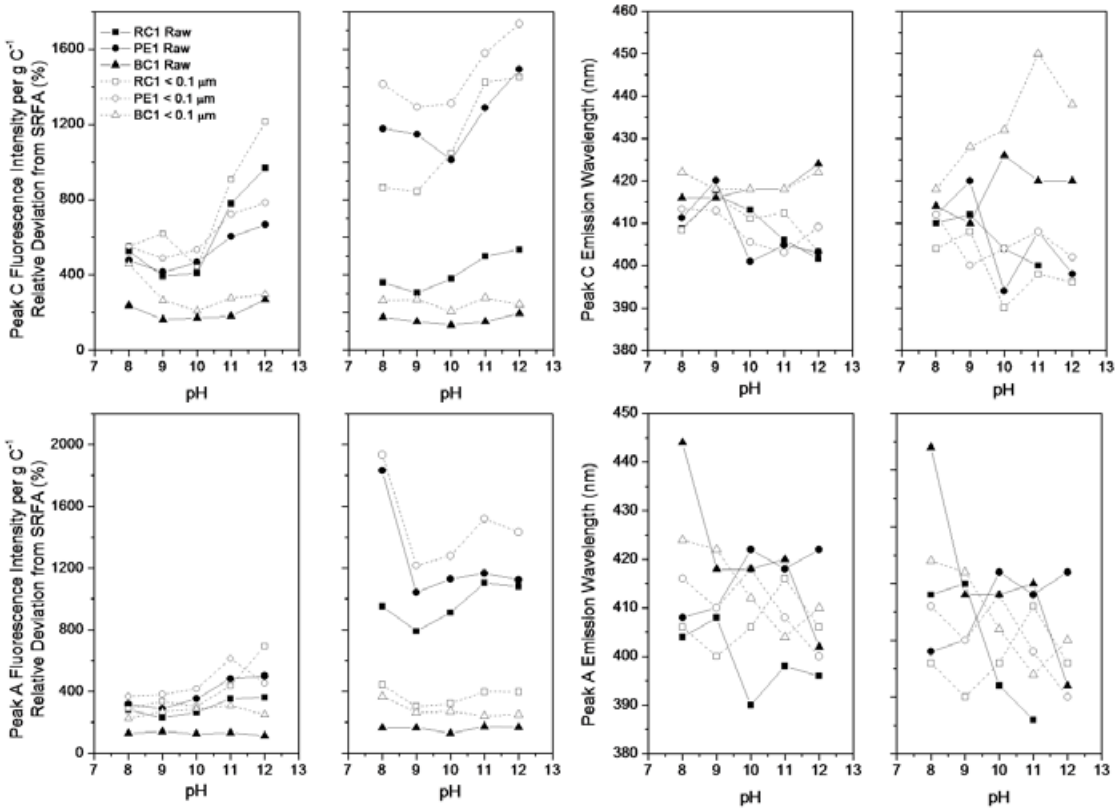

Figure 4.8 Effects of pH adjustment on the intensity and emission wavelength of peak C and peak A fluorescence in Poole's Cavern dripwater samples. Emission intensities are expressed as the percentage intensity per gram of carbon relative to Suwannee River Fulvic Acid (SRFA) (International Humic Substances Society) at equivalent pH (100 equals the intensity of SRFA). Exp = experiment.

All samples from hyperalkaline drips displayed spectral shifts into shorter wavelengths at both peak C and peak A. This behaviour is distinct from the BC1 samples and is consistent with the overall trend towards shorter emission wavelengths and higher fluorescence intensities in samples from the high-pH drip sites (Fig. 4.2). Peak C fluorescence in the high-pH drip waters increased significantly above pH 10, whereas the BC1 sample exhibited a comparatively muted increase. Enhanced fluorescence with increasing pH in the samples obtained from the hyperalkaline drip points is indicative of

substantial conformational changes in the structure of the organic matter. This hyper-sensitivity to pH changes is highly unusual[1], and is indicative of the presence of higher molecular weight, poly-aromatic compounds in RC2 and PE1 drips. It must be emphasised, however, that the observed fluorescence intensities, and the magnitude of fluorescence sensitivity at high pH in the PE1 and RC2 samples, far exceeds that known for natural soil or aquatic compounds in the published literature.

In general, the pH-induced fluorescence intensity shifts were comparable between the raw and 100 nm filtered samples, with the exception that intensities were typically higher in the filtered samples (Fig. 4.8). This difference between the unfiltered and filtered samples is essentially an artefact arising from the method of data representation: TOC concentration in the 100 nm permeates was reduced compared to that in the raw sample, but fluorescence intensity in the 100 nm permeates was generally not substantially altered and hence, the fluorescence intensity per gram of carbon is shown to increase substantially (Fig. 4.8). This does not reflect an increase in the fluorescence sensitivity of OM following filtration, but rather, it reflects the fact that the majority of the coarse colloidal OM removed by the filtration step did not contribute substantially to the total fluorescence of the raw sample, *i.e. coarse colloidal OM in the drip water samples exhibited little intrinsic fluorescence.*

[1] For example, Spencer *et al*. (2007) examined the pH sensitivity of fluorescence in samples from a diverse range of UK waterways. Peak C fluorescence per g C^{-1} expressed as a percentage of that exhibited by SRFA between pH 8 and 10 was 70-85% in waters draining an upland peat area (A11 Chirdon Burn) and 145-150% in river water from a predominantly rural/agricultural catchment (A4 River Taw). Patel-Sorrentino *et al*. (2002) examined the pH sensitivity of OM in rivers of the Amazon Basin between pH 2 and pH 12. Fluorescence intensity at both peak C and peak A did not increase between pH 10 and 12 in any sample studied and in some samples was found to decrease by around 10 – 20%.

4.4 SUMMARY

Charge substantially stabilises colloidal OC, especially at high pH (pH 9 - 13) drip points; organic-bearing colloids in typical (pH 7.5 - 8.1) karstic drips, are less stable as they are expected to have a lower charge. Removal is most likely by coagulation-deposition or adsorption onto aquifer surfaces although it is possible that higher concentrations of OM are mobilised in soils where this occurs coincidentally with dissolution of CaO in lime waste. Given that fulvic-like compounds are, by definition, soluble at all pH values, high pH conditions in Poole's Cavern dripwaters may stabilise a greater proportion of more hydrophobic, humic-like compounds in the colloidal size range, possibly associated with the peak C fluorophore.

Fluorescence intensity (both at peak A and C) is strongly affected by fluorescence inhibitors in the coarse colloidal and particulate size-range. This process is important for the interpretation of fluorescence signals in raw water samples and implies that fractionation of OM is necessary to obtain a true fluorescence signal which correlates with OC concentration.

The fluorescent response of fractionated OM to changes in temperature was no different to that observed for dissolved compounds (with a dimension ≤1 nm). This most probably reflects that organic fluorescence in colloidal fractions was substantially quenched by one or a combination of several processes, including:

- compressed conformation of fluorophores within colloidal aggregates

- complexation, adsorption and aggregation with other colloidal entities
- surface precipitation of $CaCO_3$

Thus, the measured response of fluorescence to experimentally manipulated variables was dominated by OM in the 1 kDa permeate (i.e. ≤ ca. 1 nm), and this was the case for samples from both normal- and high-pH drips. At high pH (pH 10 - 12), fluorescence intensities in samples from hyperalkaline dripwaters increased substantially, probably reflecting both conformational and chemical changes.

5. SIZE, SPECIATION AND LABILITY OF NOM-METAL COMPLEXES IN HYPERALKALINE CAVE DRIPWATER

5.1 INTRODUCTION

This chapter seeks to determine the relationship between natural organic matter (NOM) and trace metals in cave dripwaters to enable the interpretation of NOM-transported metals in speleothems. Trace metal transport by organic colloids may be captured by speleothems (Borsato *et al*., 2007; Fairchild *et al*., 2010), potentially encoding important palaeoclimatic information (Richter *et al*., 2004; Zhou *et al*., 2008; Jo *et al*., 2010); however, there is currently no information on colloid-metal interactions from these systems.

It is widely accepted that NOM is a dominant complexant of trace metals in natural systems including soils and groundwaters (Filella, 2008) and encompasses a range of heterogeneous polymeric substances, generally subdivided into polysaccharides, humic and fulvic acids. Fulvic acids (FA) are considered the dominant class of aquatic NOM in freshwaters (40-80%) (Tipping & Hurley, 1992; Tang & Johannesson, 2003); they have low molar masses (~1000 Da), and high charge density at neutral and alkaline pH, whereas humic acids (HA) are less abundant (< 5-20%) and have higher molar masses and lower charge densities than FA (Buffle *et al.*, 1998; Tipping, 2001). In reality, binding phases in environmental systems are rarely present in isolation, and above the

level of simple molecules, NOM and inorganic solids are generally present as composites (Lead and Wilkinson, 2006).

Natural aquatic colloids are ubiquitous and are numerically the most abundant particles in natural waters (e.g. 10^6 times more 10 nm colloids than the equivalent number of 1 μm particulates; Doucet *et al.,* 2007). Colloids have a pervasive influence over the binding and transport of trace elements in soils and groundwaters (McCarthy *et al.*, 1998; McGechan *et al.,* 2002) to the extent that for many metals, only a tiny fraction is free, i.e. hydrated (Lead and Wilkinson, 2006). Colloids have been extensively studied in other systems, yet their precise function remains poorly defined, largely because of their inherent heterogeneity and differences between analytical techniques (Lead and Wilkinson, 2006). Certain aspects of colloid-metal interactions are however well established, such as the importance of colloid size in trace element binding and transport (Baalousha *et al.,* 2006; Dai *et al.,* 1995; Waeles *et al.,* 2008). The fine colloidal fraction (<25 nm) may often dominate trace element partitioning (Lyvén *et al.,* 2003; Stolpe *et al.,* 2005), presumably because of the greater specific surface area of smaller colloids (Buffle *et al.,* 1995). This is consistent with studies of the coarse colloidal fraction (>50 nm) in surface waters which suggest that trace element binding is weaker at larger sizes (Lead *et al.,* 1999; Lyvén *et al.,* 2003), although this effect is limited (Lead *et al.,* 1999), possibly because of the complex morphology of aquatic colloids and the presence of surface coatings which may enhance the binding affinity of inorganic colloids (Lead *et al.,* 2005).

In karstic systems, attention has primarily focused on aquatic colloids and particulates in quickflow conduits and springs (Atteia *et al.,* 1998; McCarthy and Shevenell, 1998; Mavrocordatos *et al*., 2000), and no detailed studies of colloids have yet been conducted in seepage-flow cave dripwaters, although evidence from speleothems indicates that colloid-facilitated transport of certain trace elements may occur (Borsato *et al.,* 2007; Fairchild *et al*., 2010; Jo *et al*., 2010). Most compellingly, Borsato *et al*., (2007) demonstrated an association between trace metals (Y, Zn, Cu and Pb) known to preferentially coordinate with oxygen-containing groups at colloid surfaces, and annual fluorescent (organic-bearing) laminae in stalagmite ER78, Grotta di Ernesto, NE Italian Alps.

It is becoming clear that NOM extends a pervasive influence over speleothem compositions including their trace element chemistry and crystallographic properties (Borsato *et al*., 2007; Fairchild & Treble, 2009; Fairchild *et al*., 2010). An understanding of the size, speciation and metal binding properties of NOM in karst dripwaters is needed to assess the mechanisms and rates of metal incorporation in speleothems, and hence the relationship between trace metal variations and hydroclimatological processes (Fairchild & Treble, 2010). For example, at the growing stalagmite surface, the timescales involved in transport (i.e. diffusion of the complex within the thin water film) and the degree to which metals are labile (i.e. exchangeable from complexes), are expected to be determining factors in the incorporation of NOM and metals in speleothems, and therefore must be quantified (Fairchild & Treble, 2009; Fairchild *et al*., 2010).

It is accepted that a multi-method approach must be adopted in the characterisation of natural aquatic colloids (Lead and Wilkinson, 2006). In this chapter, the use of three prominent techniques to characterise the colloidal fraction of NOM in cave dripwater samples is reported: flow field-flow fractionation (Fl-FFF) coupled to UV-Vis and fluorescence detectors, transmission electron microscopy (TEM) coupled to x-ray energy dispersive spectroscopy (X-EDS), and diffusive gradients in thin films (DGT). A hyperalkaline (pH > 10) cave environment (Poole's Cavern, UK) was targeted because the ratio of Tr to organic carbon (OC) increases in high pH dripwaters at this site, indicative of enhanced complexation by NOM, e.g. Ni/OC and Cu/OC (in raw and 100 nm filtered samples) increase from ca. 0.1 to 1.5 ‰ between pH 8 and pH 12, respectively (Fairchild & Hartland, 2010). Thus, this study addresses the lack of information on colloid-metal interactions in cave waters, and the lack of high-pH data in natural systems in general.

5.2 MATERIALS AND METHODS

Water samples were taken from drip point PE1 in Poole's Cavern, Buxton, UK (53°12′N 1°56′W) (Fig. 3.11). The dripwater samples were studied both by the aforementioned techniques and were size-fractionated by sequential membrane filtration at nominal pore sizes of 1 μm, 0.1 μm (100 nm) and 1 kDa (≈ 0.001 μm or 1 nm), and were analysed for total organic carbon (TOC), fluorescence and trace elements.

Water samples were collected in new Nalgene HDPE bottles which were pre-rinsed with DIW and the sample water (from within the first 30 minutes of collection). The pH

and conductivity of the water samples was measured at the time of sampling and mean values are included in Table 4.2 along with mean major ion geochemical data from a year of monitoring. Samples for Fl-FFF analysis were collected over the minimum logistically feasible time period (<12 hours) and filtered at 1 μm, prior to transport to the laboratory at <10 ºC. This filtration step was undertaken in order to stabilise the colloidal pool by removal of particulates which enhance aggregation (Lead *et al*., 1999). A separate sample of the raw dripwater was retained for TEM analysis and aliquots from monthly samples were also routinely taken for ICP-MS, TOC, and fluorescence analyses.

Samples of PE1 dripwater collected in June 2009 for Fl-FFF analysis were pre-concentrated (10x) in the laboratory using an Amicon stirred-cell ultrafiltration system and Millipore (Billerica, MA, USA) 1 kDa regenerated cellulose membrane (90% retention efficiency) at low-flow (4 bar N_2, 23.2 μL s^{-1} ± 0.5 μL s^{-1}). Injection of the dripwater samples into the Fl-FFF was performed within 12 hours of the start of sample pre-concentration.

5.2.1 Flow-Field Flow Fractionation (Fl-FFF)

The size distributions of UV-absorbing and fluorescent colloids in PE1 dripwater was examined by conversion of Fl-FFF-Fluorescence into a number particle size distribution (Section 5.3.1). Fl-FFF separates colloids strictly by differences in their diffusion coefficients (D) (Beckett & Schimpf, 2000). The parameter D can be related hydrodynamic diameter (d_H) through the Stokes-Einstein equation:

(5.1) $$\lambda = \frac{V^0}{V_c w^2}\ D = \frac{kTV^0}{3\pi\eta V_c w^2}\ d_{\mathrm{H}}^{-1}\ \text{Flow FFF}$$

Where, V^0 is the channel void volume, V_c is the volumetric rate of cross-flow, w is the channel thickness, ŋ is the solvent viscosity, k is Boltzmann's constant, and T is the temperature. Thus, either D or d_{H} can be calculated from retention measurements through rearrangement of Eqn. 1 to:

(5.2) $$D = \frac{\lambda V_c w^2}{V^0}$$

(5.3) $$d_{\mathrm{H}} = \frac{kTV^0}{3\pi\eta V_c w^2 \lambda}$$

Equations 5.2 and 5.3 were used to calculate D and d_{H} respectively, corresponding to a given slice of the elution profile (Beckett & Schimpf, 2000).

A F1000 model Universal Fractionator (Postnova Analytics Europe, Landsberg, Germany; Fig. S5) was employed with a channel 29 cm long, 2.5 cm wide and 254 μm thick. The system was fitted with a 1 kDa regenerated cellulose membrane (Postnova Analytics Europe, Landsberg, Germany) which acted as the accumulation wall. The carrier solution was Barnstead nanopure deionised water (R = 18.2 MΩ cm^{-1}) with 2 mmol KCl and was degassed before delivery to the Fl-FFF by a PN 7505 vacuum degasser (Postnova Analytics Europe, Landsberg, Germany). Cross-flow was maintained using a PN 1121 double piston pump and the carrier solution was delivered

via a 515 HPLC isocratic pump (methods previously used in Baalousha and Lead (2007) and Baalousha *et al*., (2008)).

Fl-FFF channel conditions were 1 mL min^{-1} channel flow (this was checked independently during fractionation experiments and was found to vary by <0.01 mL min^{-1}) and cross-flows between 0.2 and 0.75 mL min^{-1}. Relative colloid abundance (weight hydrodynamic diameter distribution) was measured using a UV-vis detector at 254 nm and a fluorescence spectrophotometer at the excitation-emission couplet of 320:400 nm corresponding to peak C (humic-like) fluorescence. The eluted fraction corresponding to the 1-10 nm size fraction (i.e. 0-1.2 mL) was collected after fractionation for further analysis by TEM.

UV-vis and fluorescence intensity signals were collected using Flow 21 software (Postnova Analytics Europe, Landsberg, Germany). Nanospherical polystyrene standards of 20 nm ± 0.1 nm and 100 nm ± 0.1 nm hydrodynamic diameters (Duke Scientific, Palo Alto, CA) were used in Fl-FFF calibration to ensure that separation was consistent with FFF theory. Standards were supplied at dispersion of 10 g L^{-1} and were injected at 250 mg L^{-1} concentration. The calculated channel dimensions were 214 μm channel thickness and 1.19 mL channel volume.

Humic-like fluorescence intensity at peak C (Fig. 5.1b) was targeted because it has been shown to be positively correlated with UV absorbance at 254 nm (Carstea *et al.,* 2009). Increases in UV absorbance at 254 nm and fluorescence at peak C thus reflect higher concentrations of chromophoric, humic-like organic matter. Fluorescence at peak A

(Fig. 5.1b), although of humic character, is not well correlated with humic NOM concentration and is prone to signal disruption (Hudson *et al*., 2007). A stable baseline for peak A fluorescence from the Fl-FFF was not obtained, but signal detection in the peak C fluorescence region was both stable and reproducible.

5.2.2 Transmission Electron Microscopy (TEM)

TEM is a complementary technique to Fl-FFF and allows the determination of colloid size, structure and morphology on a particle-by-particle basis (Leppard *et al.,* 1990; Wilkinson *et al.,* 1999). TEM samples were prepared onto copper TEM grids (Agar Scientific, Stansted, United Kingdom) using direct ultracentrifugation at 150000g on a Beckman L7-65 ultracentrifuge (Brea, CA, USA) with a swing-out rotor SW40Ti (Wilkinson *et al.,* 1999a; Baalousha *et al*., 2010) within six hours of sample collection. Samples were analysed within two weeks of preparation using a TECNAIF20 Field Emission gun (FEG) transmission electron microscope coupled with an x-ray Energy Dispersive Spectrometer (X-EDS) from Oxford Instruments. The microscope was operating at an accelerating voltage of 200 keV, a field emission gun at emission 3, gun lens 3 and extraction voltage of 4400 eV and spot size 2-3, second condenser lens aperture of nominally 200 μm and objective aperture of nominally 50 μm. The spatial resolution (point to point) was better than 0.2 nm. Contrasted Bright Field (CBF) was collected by a Gatan camera (Gatan, Inc, Pleasanton, CA, USA) for particle imaging (Rouzaud and Oberlin, 1989; Williams and Carter, 1996). Qualitative X-EDS analysis was performed to determine particle elemental composition. TEM micrographs were analysed and size measurements on 150 particles (equivalent circular diameter) were

performed using Digital Micrograph software (Gatan Inc, Pleasanton, CA, USA). The measured sizes were classified into intervals of 5 nm to construct particle size distribution histograms (number particle-size distribution). The number-average diameters and hydrodynamic diameters $N(z)$ of the observed particles by TEM and the eluted particles from Fl-FFF were calculated using Eqn. 5.4.

$$N(z) = (\sum_i n_i \times z_i) / (\sum_i n_i) \quad (5.4)$$

where n_i is the number of particles or the UV-absorption/fluorescence intensity and z_i is the equivalent circular diameter of each observed particle by TEM or the hydrodynamic diameter measured by Fl-FFF.

Potential artefacts (i.e. through particle drying) were not accounted for in the preparation method (e.g. use of hydrophilic resins to stabilise against shrinkage), however the potential for artefacts was mitigated by the adoption of a multi-method approach.

5.2.3 Diffusive Gradients in Thin-Films (DGT)

Lability of trace elements in hyperalkaline cave dripwaters was examined using the diffusive gradients in thin films (DGT) technique (Davison & Zhang, 1994; Zhang & Davidson., 1995; Zhang & Davison, 2000; Zhang, 2004). DGT is based on a simple device that accumulates solutes on a binding resin after passage through a hydrogel which acts as a well defined diffusive boundary layer (DBL) in which the movement of

ions occurs only by molecular diffusion. The binding resin immobilises free ions, thus preventing re-formation of NOM-metal complexes after their dissociation via reactions of the form:

$$(5.5) \quad ML^{(n-z)} \leftrightarrow \quad M^{z+} + L^{n-}$$

where ML is the metal-ligand complex and M^{z+} and L^{n-} are the free metal and ligand ions formed following dissociation.

DGT units equipped with Chelex resins (metal-binding) and FeO_x resins (vanadium-binding) were deployed in PE1 dripwater samples in two sets of laboratory-based metal depletion experiments conducted in June 2009 and July 2010. Samples were taken in the summer, a hydrologically quiescent period, when coarse colloids were less abundant (Chapter 6), and hence trace metal speciation was less complex than in the autumn-winter period which coincides with elevated NOM fluorescence intensity (Baker *et al*., 1999c). The experiments were designed to quantify the total mass and proportion of labile metal ions in the samples. The experimental setup consisted of 50 mL sample solution in a screw-capped PTFE jar in the presence of a DGT sampler (0.4 mm open-pore hydrogel). An un-acidified control (a jar lacking a DGT device) allowed estimation of losses from solution occurring due to aggregation/deposition during the experiments and a second control (acidified to 2% HNO_3) was used to check the reproducibility of the analysis allowing for identical sample manipulations. By comparing the mass of metal in the control solutions to the mass eluted from DGT Chelex resins it was possible

to verify the mass of metal available to DGT and thus the relative lability of trace metal complexes.

Experiments were initiated within six hours of sample collection/preparation and lasted between 168 and 216 hours. The experimental solutions were mixed thoroughly on a daily basis by swirling the solution within the PTFE jar. Aliquots (1.9 mL + 0.1 mL 40% Aristar HNO_3) were taken at regular intervals and at the end of the experiments the resins from the DGT units were recovered and eluted in Aristar grade 2 M HNO_3 (Chelex resins) or Ultrapure 2 M HCl (FeO_x resins).

5.3 RESULTS

5.3.1 Hydrodynamic diameter distribution of humic-like NOM by Fl-FFF

Fig. 5.1 presents the emission-excitation matrix plot (EEM) of the original sample (Fig. 5.1a), and the EEM (Fig. 5.1b) and UV-vis absorbance spectra (Fig. 5.1c) corresponding to the concentrated PE1 dripwater sample fed into the Fl-FFF. Fig. 5.2 shows the Fl-FFF fractograms of PE1 dripwater fractionated at cross-flows of 0.2 mL min^{-1} (Fig. 5.2a) and 0.75 mL min^{-1} (Fig. 5.2b). Both the UV and fluorescence detectors measured optical regions characteristic of humic-like compounds, 254 nm-absorption and the (Peak C) excitation-emission couplet 320:400 nm, respectively. The results from both detectors showed similar overall trends (Fig. 5.2), but the fluorescence results were more reproducible than the noisier UV results. Fluorescence signals had higher signal-to-noise ratios than UV-Vis signals because NOM in Poole's Cavern's

hyperalkaline dripwaters fluoresce very strongly in the (humic-like) optical regions targeted (Chapter 4). Fluorescence and UV signals peaked following elution of the smallest colloids from the Fl-FFF channel (Fig. 5.2). Signals from both detectors were slow to decline to baseline values demonstrating that UV-sensitive chromophores and fluorophores followed similar distributions and were present in the concentrated sample in a range of sizes.

In Fig. 5.3, the abscissa of the plot in (a) shows the retention volume (V_R) from which the diffusion coefficient (D) (abscissa in b) and hydrodynamic diameter (d_H) (abscissa in c) were calculated by applying FFF theory (Beckett & Schimpf, 2000). The data used in calculations of V_R, D and d_H was derived from experiments using cross-flows of 0.75 mL min^{-1} (Fig. 5.2a). Fl-FFF coupled to a fluorescence detector (as with UV signals) measures a volume-weighted particle size distribution (VPSD; Baalousha and Lead, 2007). The number-average and standard deviations of the calculated diffusion coefficient and hydrodynamic diameters (VPSD) respectively were $0.06 \pm 0.12 \times 10^{-6}$ cm^2 min^{-1} and 84.4 ± 90.3 nm, and the median values were 0.12×10^{-6} cm^2 min^{-1} and 41.6 nm. Thus, Fl-FFF VPSD results indicate that by particle weight, larger organic colloids were more abundant than small, UV-absorbing and fluorescent (humic-like) colloids (Fig. 5.3c). When the Fl-FFF-Fluorescence data were converted a number-weighted particle size distribution (NPSD) by applying Eqn. 5.6 (Fl-FFF cumulative distribution given by dotted line in Fig. 5.5) the number-average and standard deviations of the calculated diffusion coefficient and hydrodynamic diameter (NPSD) were respectively, $0.18 \pm 0.12 \times 10^{-6}$ cm^2 min^{-1} and 26.8 ± 49.5, and the median values were 0.67×10^{-6} cm^2 min^{-1} and 7.15 nm. Thus, the Fl-FFF data indicate that small

organic colloids were numerically much more abundant than larger organic colloids, although these were not well resolved from the void peak at the Fl-FFF fractionation conditions used.

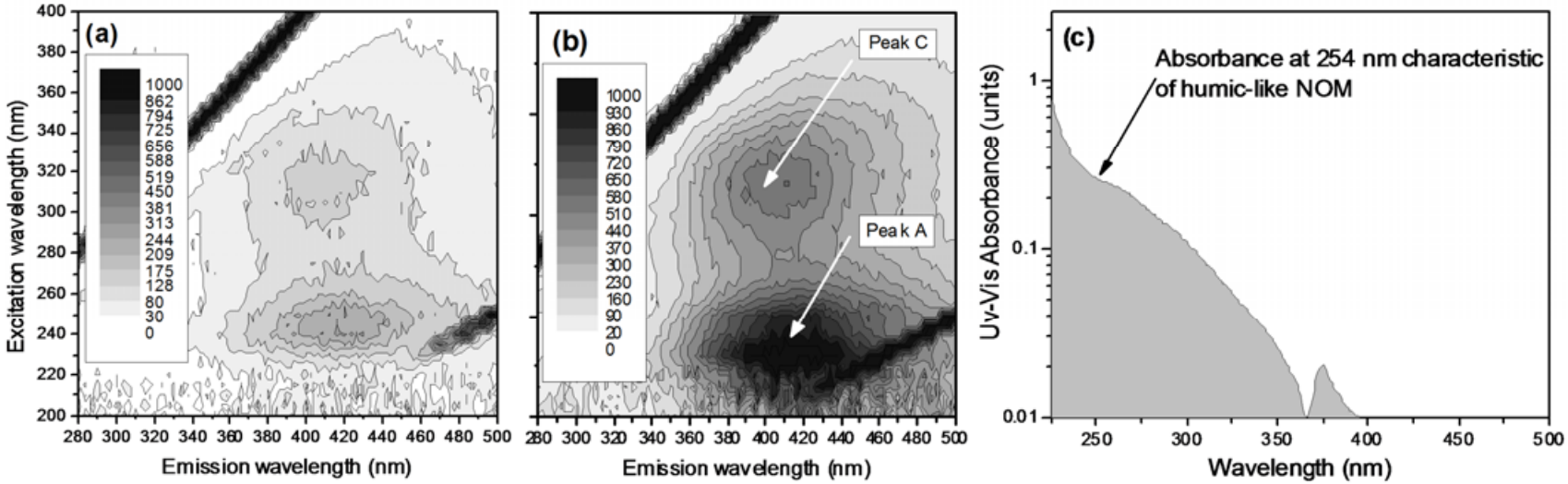

Figure 5.1 Summary fluorescence and UV-Vis absorbance spectra for the original and concentrated PE1 dripwater (June 2009) sample prior to characterisation by Fl-FFF-UV-Flu; (a) EEM of original sample, (b) EEM of the concentrated sample showing humic-like Peak C and Peak A fluorescence centres, (c) UV-Vis absorbance spectra of concentrated sample. Fluorescence intensities (arbitrary units) in EEMs shown by shaded contours. Diagonal lines in EEMs correspond to first- and second-order Raleigh scatter of incoming light by water molecules. Sample concentrated by ultrafiltration at 1 kDa in a stirred cell at 4 bar N_2.

$$\% \text{ NPSD} = \frac{\left(\frac{\text{Fluorescence signal}}{\text{particle volume}}\right)}{\sum \frac{\text{Fluorescence signal}}{\text{particle volume}}} \times 100 \quad (5.6)$$

where particle volume in Eqn. 5.6 corresponds to the particle volume in each slice of the Fl-FFF fractogram ($V = \frac{3}{4}\pi h^3$ where h is the particle radius). This conversion is based on the simplification that all the particles within this range have the same density (Baalousha and Lead, 2007).

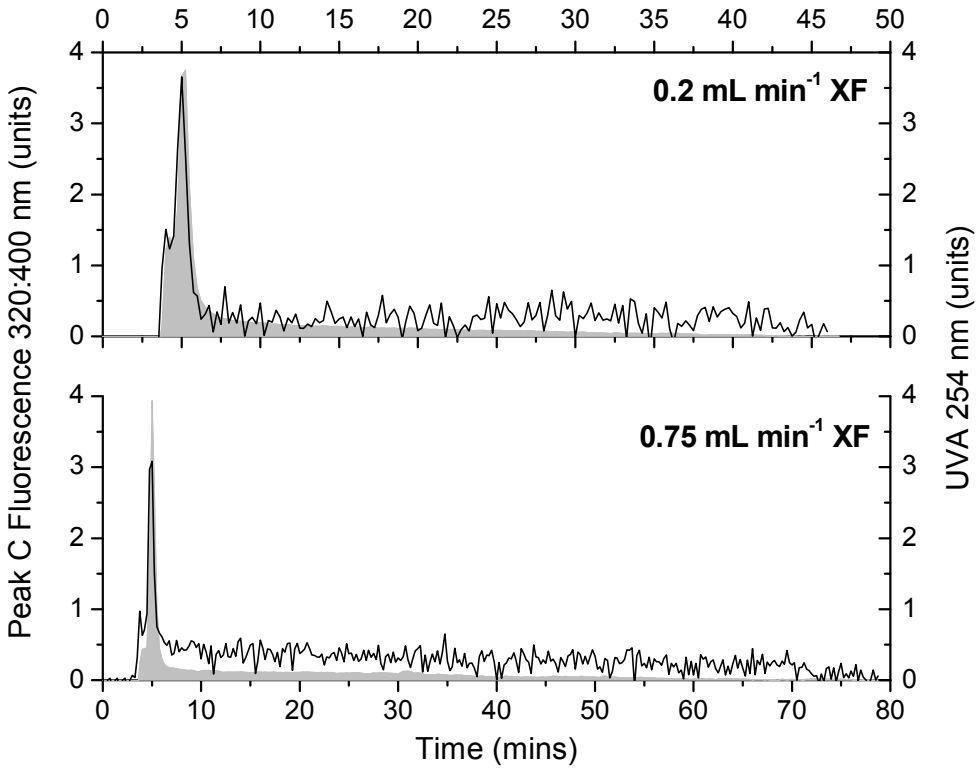

Figure 5.2 Plots of Peak C humic-like fluorescence intensity at the 320:400 nm excitation-emission couplet (grey-filled spectra) and UV absorbance (UVA) at 254 nm (black lines) in response to colloids eluted from the Fl-FFF system at cross-flows (XF) of 0.2 and 0.75 mL min^{-1}. Plots are averages of triplicate analyses at each cross-flow.

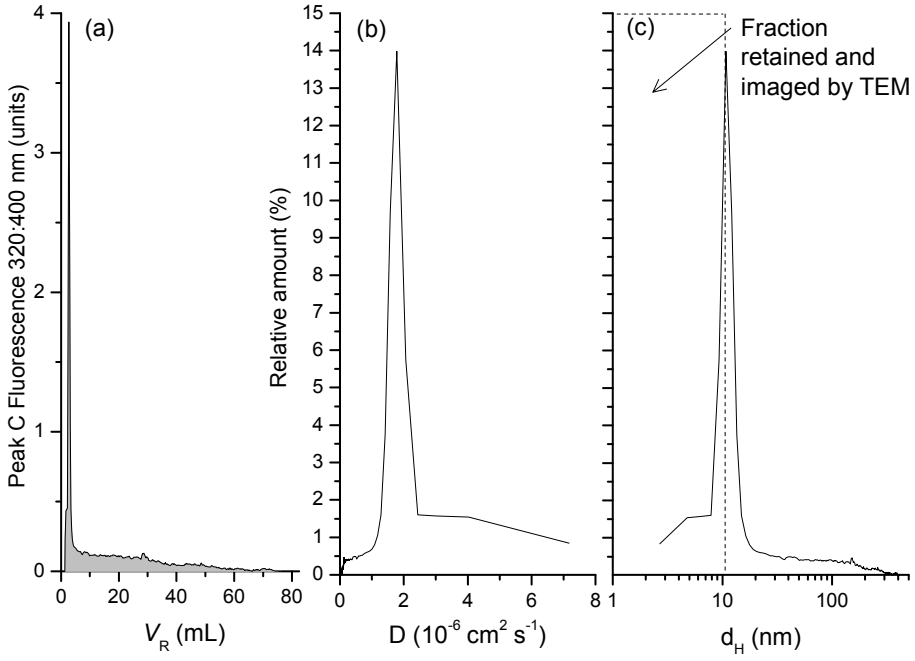

Figure 5.3 Fl-FFF-Flu fractograms: (a) retention volume V_R (b) diffusion coefficient D and (c) hydrodynamic diameter d_H, measured by Fl-FFF-Flu following pre-concentration by ultrafiltration at 1 kDa in a stirred cell at 4 bar N_2. Fl-FFF parameters: channel flow = 1.0 mL min^{-1}, cross flow = 0.75 mL min^{-1}, channel thickness = 206 μm, and channel volume = 1.07 mL. Humic-like fluorescence signal at 320:400 nm excitation-emission couplet normalised to area under the fractograms.

5.3.2 Particle size distribution, morphology and qualitative elemental composition by TEM-X-EDS

Representative images of colloids and aggregates in PE1 dripwater sampled in June 2009 are presented in Fig. 5.4. Analyses of colloidal and particulate aggregates (e.g. Fig. 5.4a) by X-EDS (see adjacent spectra) were consistent with complexes of organic compounds aggregated around colloidal aluminosilicates, iron and titanium oxides. In Fig. 5.4(b), a multitude of approximately spherical nanoparticles are visible and these are shown in (c) at higher magnification. X-EDS spectra of the nanoparticles in PE1

dripwater confirmed that they did not contain substantial amounts of inorganic materials (C, O and Cu peaks detected). Size analysis (equivalent circular diameter) of TEM micrographs showed that colloids and particles in PE1 dripwater occupied a continuum of sizes between ca. 1 nm to 4 μm, but the vast majority of colloids (by number) were found to reside in the nanoparticulate range between ca. 1 and 5 nm (Fig. 5.4 and 5.5). TEM size analysis of the 1 to 10 nm Fl-FFF fraction (Fig. 5.4d) confirmed that the Fl-FFF accurately fractionated the fine colloidal fraction with no diameters measured > ca. 5 nm.

The TEM particle-size distribution (Fig. 5.5) is largely consistent with the findings of Fl-FFF NPSD which showed the greatest number of UV-fluorescent and absorbing colloids were present below 10 nm and TEM analyses also confirmed the poly-dispersity of the colloidal pool as indicated by Fl-FFF fluorescence data (Fig. 5.5a). The number-average particle diameter in the TEM number particle size distribution (NPSD) (in the range measured by Fl-FFF) was 28.8 ± 2.8 nm and the median was 3.38 nm. Thus, the Fl-FFF NPSD data are in agreement with the TEM NPSD (Fl-FFF NPSD number-average was 26.8 nm) and gross drying artefacts resulting from TEM sample preparation can therefore be discounted because the colloid sizes obtained by Fl-FFF NPSD and TEM were similar. Baalousha and Lead (2007) found that the ratio of the number average size obtained from AFM and Fl-FFF-UV was between 1 and 2.1 for different samples; this compares well to the ratio of TEM/Fl-FFF number-average diameters from this study of 1.1.

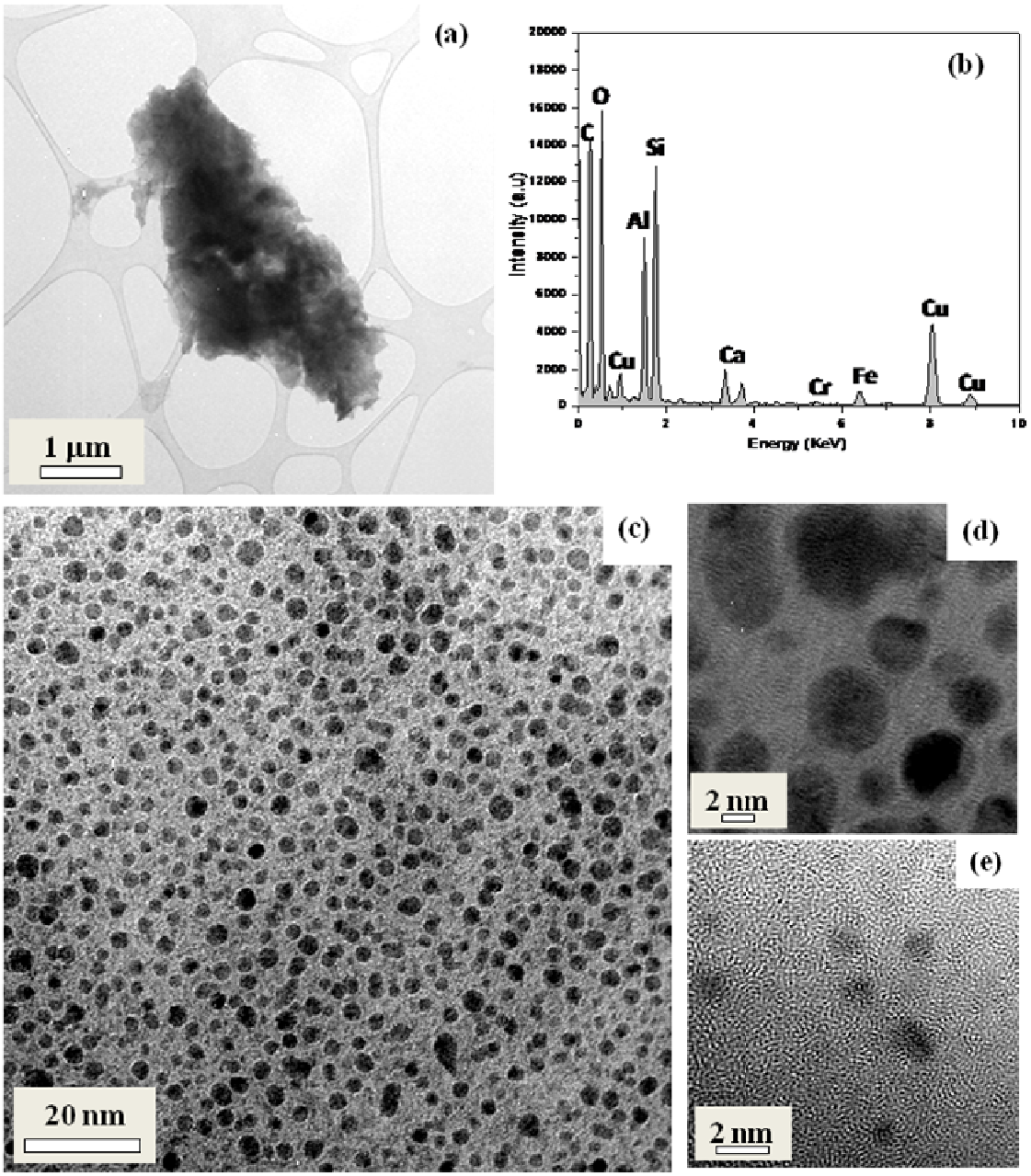

Figure 5.4 Representative TEM images of PE1 dripwater (images a-c raw water sampled in June 2009) (a) particulate aggregate containing aluminosilicates and Fe oxides (elemental composition from adjacent X-EDS spectrum; Cu peaks in spectrum originate from supporting grid and C peaks originate from grid and analysed particles), (b and c) globular nanoparticles with diameters between ca. 1 and 5 nm. Image (d) obtained from 1 to 10 nm Fl-FFF fraction of PE1 dripwater fractionated at cross-flow of 0.75 mL min^{-1}. Samples prepared by direct ultracentrifugation onto copper TEM grid without pre-concentration following collection/fractionation (TEM images produced in collaboration with M. Baalousha).

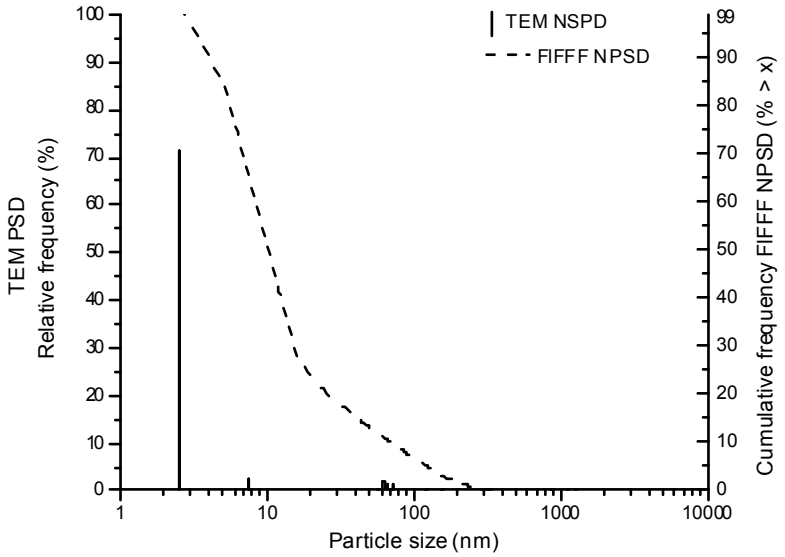

Figure 5.5 Particle size distributions (PSD) in PE1 dripwater on the basis of equivalent circular diameter (point by point) determined by analysis of TEM images (left y-axis) and by Fl-FFF (right y-axis). Fl-FFF-Flu volume-weighted size distribution was converted to a number weighted size distribution following Baalousha and Lead (2007). TEM sample prepared without pre-concentration. Relative frequency of particle counts calculated for 5 nm bins between 1 and 5000 nm plotted with respect to bin centre. The vast majority (71%) of particles measured (n=150) fell between 0 and 5 nm in size. Particles with dimensions >1 μm are not shown.

5.3.3 Distribution of organic carbon and trace elements with size

PE1 dripwater sampled in June 2009 was analysed for organic carbon and trace elements in sequentially filtered subsamples (Raw, 1 μm, 100 nm and 1 nm membrane permeates; Fig. 5.6). Data from TOC, fluorescence and ICP-MS bulk analyses of sequentially filtered PE1 dripwater were deconvolved to yield the proportions of NOM, fluorescence and trace elements in size fractions. Calculation of the concentration of metals and organic carbon in each fraction (Table 5.1) was achieved by iteratively subtracting the concentration in filter permeates from those in the preceding permeate (or original sample) (Table 5.1).

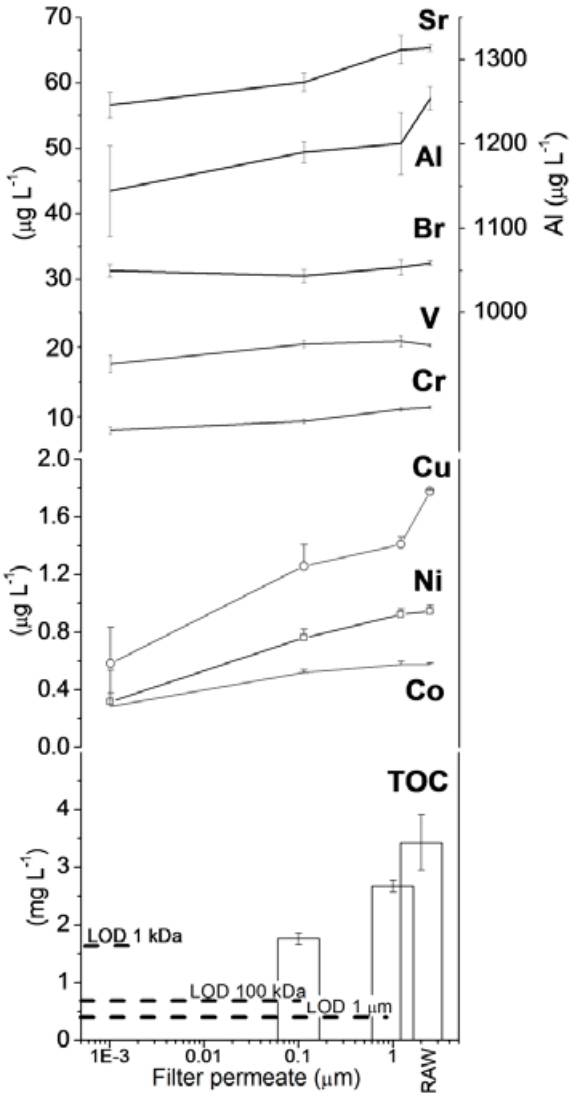

Figure 5.6 Trace element and blank-corrected TOC concentrations in permeates of sequentially filtered PE1 dripwater sampled in June 2009. LD = limit of detection. Error bars are the standard deviation of triplicate analyses.

Concentrations of organic carbon in sequentially-filtered subsamples were consistent with the presence of NOM in a range of sizes and support the findings of TEM and Fl-FFF analyses (Sections 5.3.1 – 5.3.2) (Fig. 5.3 and Table 5.1). However, determination of TOC in the <1 nm fraction was not possible because of high OC blanks (Chapter 3). TOC analyses indicate that organic carbon was distributed evenly between the particulate/coarse-colloidal and fine-colloidal/nominally dissolved size fractions (Table

5.1). However, the distribution of humic-like fluorescence intensity at the peak C fluorophore was weighted to the finest materials with ca. 86% originating from the nominally dissolved size fraction, i.e. ≤1 nm (Table 5.1), indicating that humic-like fluorescence principally originated from small colloids or dissolved NOM. Negative fluorescence in the coarse and particulate fractions reflects inner-filtering (quenching) of fluorescence by solids in these size fractions (Chapter 4). The distribution of fluorescence in the sample was calculated by treating the fluorescence intensity in the 100 nm permeate as the true maximum (or starting) intensity. NOM-bearing particles and colloids above 100 nm probably fluoresce (as indicated by Fl-FFF-Fluorescence data), but their signal is largely masked by their inner-filtering effect (Chapter 4).

The concentrations of most elements were reduced to some extent by filtration (Table 5.1), but Sr, V and Ti were only reduced slightly, and were concentrated in the finest size fraction. In contrast, large changes in the concentrations of Cu, Ni and Co were observed (Fig. 5.6), particularly following ultrafiltration at 1 kDa, indicating that ca. 50% of Co and ca. 65-70% of Cu and Ni were adsorbed to colloid and particle surfaces with dimensions ≥ ca. 1 nm (Table 5.1).

In Fig. 5.7 a-c, the concentrations of Cu vs. Ni, Cu vs. Co and Co vs. V in sequentially-filtered monthly PE1 dripwater samples from one year of monitoring are given. High (and significant) correlations between metals were identified, indicating a common provenance amongst Cu, Ni, Co and V. The correlation between Cu and Ni was strongest (R^2 = 0.8; Fig. 5.7a) and total metal concentrations decreased linearly with each filtration step, probably indicating that both Cu and Ni partitioned consistently

between carrier phases below ca. 100 nm and below ca. 1 nm, characteristic of the competitive nature of metal binding (Tipping, 2001). In contrast, cross-plots of Sr vs. Co, Sr vs. Cu and Sr vs. Ba (Fig. 7d-f) demonstrate that the changing abundances of alkaline earth metals (derived from bedrock dissolution) were not linked to the same process responsible for co-variation in transition metals, i.e. Sr and Ba showed no colloidal association being concentrated in the dissolved fraction.

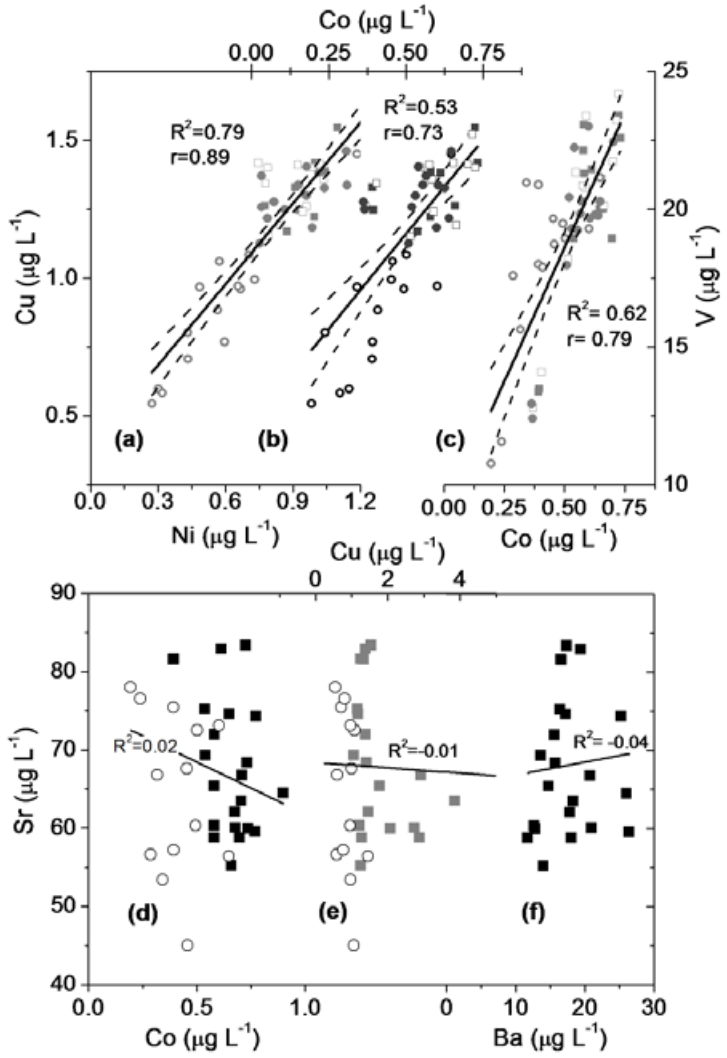

Figure 5.7 Total metal concentrations in PE1 dripwater sampled over a hydrologic year for (a) Cu vs. Ni, (b) Cu vs. Co, (c) Co vs. V, (d) Sr vs. Co, (e) Sr vs. Cu, and (f) Sr vs. Ba. ■ = raw, □ = ≤1 µm, ● = ≤100 nm, ○ = ≤1 nm. Release of Ba from filter membranes was too variable to allow blank correction in sequentially filtered samples. Solid lines are linear regression trend lines and dashed lines are 95% confidence bands.

					Proportion of element in size-separated fraction (%)						
Sample	**Size class**	**Nominal size**	**TOC (mg L^{-1})**	**Peak C Fl (%)**	**Ti**	**V**	**Cr**	**Co**	**Ni**	**Cu**	**Sr**
June 2009	Particulate	≥ 1 μm	0.7 ± 0.5	-6.1	6.6	0	3	0	2	21	0
June 2009	Coarse colloidal	1 μm – 100 nm	0.9 ± 0.1	-3.0	7.5	2.1	15	10	17	9	8
June 2009	Fine colloidal	100 nm – 1 nm	1.8 ± 0.2	13.7	9.2	13.6	12	40	47	38	5
June 2009	ND	≤1 nm		86.3	76.7	84.3	71	50	34	33	87

Table 5.1 Partitioning of trace elements between particulate (>1 μm), coarse colloidal (1 μm – 100 nm), fine colloidal (100 nm – 1 nm) and nominally dissolved (ND) (≤1 nm) size fractions in PE1 dripwater sampled in June 2009 based on the nominal pore size cut-offs of filter membranes. The concentrations of Cd, Y and Pb were below detection limits. Procedural blanks for elements shown were below detection limits.

5.3.4 Metal binding to NOM in dripwater

5.3.4.1 Modelling metal binding to humic acid

Metal speciation in PE1 dripwater was modelled using the Windermere Humic Aqueous Model (WHAM) 6.0, which incorporates Model IV (Tipping, 1998), and visual MINTEQ 3.0, which incorporates the NICA-Donnan model (Benedetti *et al*., 1995; Kinniburgh *et al*., 1999). Modelling of metal binding in PE1 dripwater was simplified by treating all OC below 100 nm as HA (2.7 mg L^{-1} HA; 8 °C; pCO_2 3.16 x 10^{-4}). This simplification is partially justified by the strong pH sensitivity of NOM in the hyperalkaline dripwaters at this site (relative to lower pH drips) which is consistent with substantial conformational changes at high pH, possibly indicative more highly aromatic NOM than found in pH 8 dripwaters (Chapter 4). The other common metal binding phases (colloidal Mn and Fe oxides) can be discounted because of the very low concentration of Mn and Fe (<0.1 and 2.7 μg L^{-1}, respectively). Models were run at pH 11 and pH 8 to provide information on the estimated metal speciation in the June 2009 sample and the expected speciation at the normal pH of karst waters.

Estimates of Cu binding with HA were very similar for the two models (ca. 100%), but distinctly different estimates of humic binding were obtained for other transition metals including Cr, Fe, Ni and Zn (Table 5.2). Neither model predicted strong binding of Ca, Al, Co or Ba at either pH, whereas estimates for humic binding of Sr and Ni at pH 8 and 11 were inconsistent between models, with WHAM predicting increased Sr binding (15.5%) at pH 11 and MINTEQ predicting greater Ni (55%) binding at pH 8.

For the transition metals predicted not to be dominantly complexed by HA at pH 11 (e.g. Al, Cr, Ni and Co), both models predicted the formation of ion pairs with carbonate or hydroxyl (Table 5.2). The MINTEQ model was re-run with PE1 June 2009 solution data (pH 11) and the metal hydroxides and carbonates were added as potential solid phases. Potential solids do not influence the equilibrium problem, unless the solution becomes oversaturated with respect to a particular possible solid; in which case the model precipitates the solid, depleting the aqueous phase accordingly. MINTEQ did not predict precipitation of any metal hydroxide or carbonate species except $Ni(OH)_2^{(0)}$ (10.9% of Ni precipitated; Table 5.2), indicating that a small proportion of Ni in the PE1 dripwater may have been present as an inert solid. The stability of inorganic complexes in PE1 dripwater at pH 11 was supported by further modelling with PHREEQC which showed that the metal hydroxides of Cu and Zn were well below their solubility product (Ni, Co not included in standard database). The composition of PE1 dripwater in the presence of HA was also modelled at lower pCO_2 values (10^{-4} and 10^{-5}), representative of the possible range for karst waters (Appendix IX; Table S31). This exercise indicated that humic binding of less reactive metals (e.g. Ni and Co) is favoured at lower pCO_2 values because of reduced competition from CO_3^{2-} and OH^-. The modelling also showed that metal hydroxides are unlikely to precipitate at lower pCO_2.

Ion	r_{ion}	z/r	n_1	PE1 ($\mu g\ L^{-1}$)	WHAM Output						MINTEQ Output							
					M-HA (%)	Inorg (%)	Main inorganic form	M-HA (%)	Inorg (%)	Main inorganic form	M-HA (%)	Inorg (%)	Main inorganic form	Precip (%)	M-HA (%)	Inorg (%)	Main inorganic form	Precip (%)
					pH 8			pH 11			pH 8				pH 11			
Al^{3+}	0.5	6	0.42	1200	0.94	99.1	$Al(OH)_4^-$	0.05	99.9	$Al(OH)_4^-$	3.15	96.8	$Al(OH)_4^-$	0	0.01	100	$Al(OH)_4^-$	0
Cr^{3+}	0.69	4.3	-	11.3	98.3	1.7	$Cr(OH)_2^+$	24.0	76.0	$Cr(OH)_4^-$	1.16	98.8	$Cr(OH)3^{(0)}$	0	0.57	99.4	$Cr(OH)3^{(0)}$	0
V^{3+}	0.74	4.1	-	20.3	-	-	-	-	-	-	0.00	98.9	$V(OH)_2^+$	0	0.00	98.9	$V(OH)_2^+$	0
Cu^{2+}	0.69	2.9	0.53	1.78	93.5	6.5	$CuCO_3^{(0)}$	100	0.0	$Cu(OH)_2^{(0)}$	100	0.00	$CuCO_3^{(0)}$	0	99.9	0.10	$Cu(OH)_3^-$	0
Ni^{2+}	0.72	2.8	0.65	0.95	1.26	98.7	$NiCO_3^{(0)}$	0.53	99.5	$NiCO_3^{(0)}$	44.9	55.0	Ni^{2+}	0	6.98	82.1	$Ni(OH)_3^-$	10.9
Zn^{2+}	0.74	2.7	0.67	0.49	32.0	68.0	Zn^{2+}	7.93	92.1	$Zn(OH)_2^{(0)}$	100	0.04	Zn^{2+}	0	99.9	0.15	$Zn(OH)_2^{(0)}$	0
Co^{2+}	0.74	2.7	0.71	0.58	0.92	99.1	$CoCO_3^{(0)}$	0.32	99.7	$CoCO_3^{(0)}$	16.4	83.6	Co^{2+}	0	1.84	98.2	$Co(OH)_2^{(0)}$	0
Fe^{2+}	0.76	2.6	0.3	2.71	5.23	94.8	$FeCO_3^{(0)}$ / Fe^{2+}	6.60	93.4	$FeCO_3^{(0)}$	100	0.02	Fe^{2+}	0	99.9	0.09	$FeOH^+$	0
Ca^{2+}	0.99	2	0.85	74493	0.25	99.8	Ca^{2+}	0.34	99.7	Ca^{2+}	0.49	99.5	Ca^{2+}	0	0.71	99.3	Ca^{2+}	0
Sr^{2+}	1.13	1.8	0.85	65.4	1.83	98.2	Sr^{2+}	15.5	84.5	Sr^{2+}	1.06	98.9	Sr^{2+}	0	6.61	93.4	Sr^{2+}	0
Ba^{2+}	1.35	1.5	0.9	14.7	0.11	99.9	Ba^{2+}	0.15	99.9	Ba^{2+}	0.92	99.1	Ba^{2+}	0	4.56	95.4	Ba^{2+}	0

Table 5.2 The ionic radii (r_{ion}), ionic potentials (z/r) and the NICA-Donnan binding parameters (n_1) of cationic elements studied and predicted metal speciation in PE1 dripwater in the presence of humic acid (2.7 mg L^{-1}) using the Windermere Humic Aqueous Model (WHAM) and visual MINTEQ. Values of z/r and n_1 are included as indicative measures of the relative binding affinity of metal ions for binding with humic-like NOM (n_1 values are from Milne *et al*., 2003). M-HA= percentage of metal in complexes with humic acid; Inorg= percentage inorganic fraction of metal; Precip= percentage of metal precipitated as inorganic solids.

5.3.4.2 Lability of NOM-metal complexes by DGT

DGT depletion experiments were conducted with PE1 dripwater samples taken in June 2009 and July 2010. The objective was to determine the concentration of DGT labile metal in the samples. Implicit in the DGT technique is that the Chelex binding resin is an essentially infinite sink for metal ions: Zhang and Davison (1995) determined the capacity of the normal Chelex DGT to be equivalent to 0.65 mg Cd. Depletion of elements in solution (i.e. accumulation in the Chelex resin) was expected to reflect their availability for the binding phase, any residual metal ions in solution being retained in complexes. Thus, in principle, the shape of the metal depletion curve allows for three forms of metals to be distinguished:

- Free ions, simple inorganic complexes and weakly bound metals: depleted rapidly in the first stages of the experiment.
- Strongly bound metals: metal complexes with NOM may dissociate more slowly leading to a steady decline in solution concentration.
- Inert metals: NOM-metal complexes which do not dissociate and thus are not available to DGT. In this case the total dissolved metal concentration does not change (no depletion).

These experiments focused on the transition metals Cu, Ni, Co, V, and the alkaline earth metals Sr and Ba. Other metals were monitored during these experiments, including Al, Fe and Zn, but these data are not given because of substantial depletion observed in control solutions. The chromium concentration was also monitored but this did not

change during the experiment, suggesting that it was probably present mostly as chromate, as indicated WHAM (Table 5.2). In Fig. 5.8 the concentration of metals (Ni, Cu, Co, V (FeOx DGT), Ba, Sr) in each solution over time are shown in relation to the concentrations in the control solutions. Figure 5.8 demonstrates that the concentration of all the studied metals declined to some extent over the course of the experiments. Total metal concentrations in PE1 dripwater sampled in 2009 and 2010 were similar with the exception of Cu and Ni which were around 30% higher in 2009 (Table 5.3). Marked differences were apparent in metal depletion trends between years, but overall, trends in the transition metals (Cu, Ni and Co) and alkaline earth metals (Sr and Ba) were internally consistent in each year. Large differences in depletion behaviour were evident between each group, most notably the alkaline earth metals were most rapidly depleted in the early stages of each experiment, whereas depletion of the transition metals occurred more slowly (Fig. 5.8; outliers shown as crossed symbols).

Metal lability in PE1 dripwater samples was assessed using two approaches, firstly by examining the initial 24 hr of solution depletion for each metal (ΔC_{24} (%); Table 5.3), and secondly by comparing the concentration of available metal in solution (C_A) to the concentration of metal sampled by DGT (C_S) (see below). Where necessary, anomalous values were excluded from the calculations by using the next valid data point in the sequence (e.g. final Sr value in 2010), or where depletion trends were linear (e.g. Ni, Cu, Co in 2009) anomalous values were corrected by using the equation of the regression line (e.g. Ni and Cu initial concentrations in 2009).

The first approach yields information on the initial availability of metals (ΔC_{24}; Table 5.3) rather than their overall availability, and therefore is of the greatest interest for understanding the extent to which metals transported in complexes with NOM are likely to co-adsorb (i.e. form "ternary" mineral-ligand-metal complexes), or dissociate and bind directly to the calcite surface (Fein, 2002). This analysis reveals that depletion of Cu and Ni occurred more quickly in 2009 (ΔC_{24}; Table 5.3) than in 2010 when their starting concentrations were ca. 30% lower. The concentrations of Cu and Ni essentially remained static in the first 48 hrs of the 2010 experiment, whereas Co was comparatively more labile than in 2009, although Co depletion was minimal in absolute terms (≤8% of the initial concentration in the first 24 hrs). The averages and standard deviations in metal depletion rates from the first 24 hr of deployment (Average ΔC_{24}; Table 5.3) show that overall, depletion was most rapid for Ba (15 ± 6%) and Sr (14 ± 6%), and slowest for Cu and Ni (5 ± 3%) and Co (5 ± 4%), following the overall order Ba and Sr >> Co, Ni and Cu (Table 5.3).

Vanadium shows a high degree of specificity for binding with DGT Fe oxide resins (Stockdale *et al*., 2008) and a DGT-FeO_x (0.4 mm OP) sampler was used to measure all V species in the July 2010 sample. Allowing for outliers, depletion of V was linear (Fig. 5.8), demonstrating that the rate of supply of V remained constant throughout the experiment. Depletion of V in the first 24 hours was comparable to the other transition metals at ca. 3% of the starting concentration (Table 5.3). Thus, the depletion trend in V (2010) and the rate of supply to FeOx DGT was comparable to that seen in the other transition metals in the 2009 experiment, and contrasts markedly with the depletion

trends in Ba and Sr, which showed an initially rapid reduction, followed by a steady decline (Ba) or levelling off in concentration (Sr).

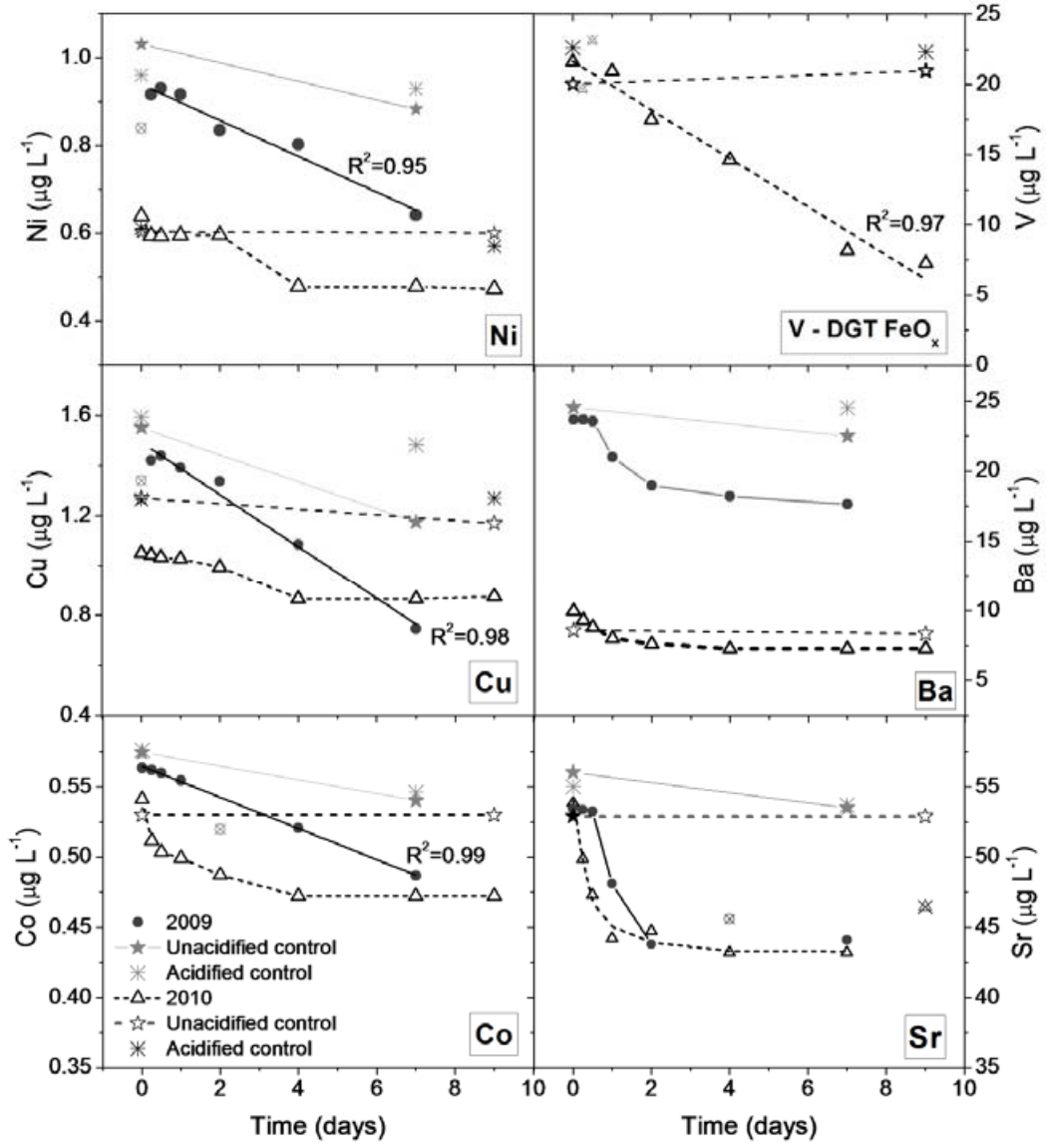

Figure 5.8 DGT depletion experiments on PE1 dripwater from June 2009 (filled circles) and July 2010 (open triangles) for the metals Ni, Cu, Co, V, Ba and Sr. DGT samplers were fitted with Chelex ion exchange resins except for 2010 V depletion experiment (FeO_x resin). The change in concentration in the un-acidified and acidified controls reflects destabilisation of colloid-metal complexes. Crossed circles and crossed triangles denote outliers in solution aliquots from DGT experiments. Some data points from acidified controls are not shown for clarity where control concentration equalled the initial solution concentration or plotted over the un-acidified control (excluded outlier in acidified control for Sr in 2010 exp (45 ppb)). Discrepancies between initial concentrations in DGT solutions and controls (e.g. Cu and Ni) are attributed to inhomogeneities between separate aliquots. Experimental conditions: June 2009, pH = 11.0, EC = 402 µS cm^{-1}, T = 4 °C.

Metal lability in PE1 dripwaters was also assessed by comparing the calculated concentration of available metal (C_A) in μg L^{-1} (Eqn. 5.7) to the DGT sampled concentration (DGT C_S) determined from the DGT sampled mass (M_{DGT}; Eqn. 5.8) using Eqn. 5.9. The calculation of C_A allows for estimation of losses of metal occurring through colloid destabilisation (e.g. coagulation-sedimentation) and minor potential adsorption to the vessel walls.

$$(5.7) \quad C_A = C_i - C_f - ((100/C_i) \times \Delta C_{\%ctrl})$$

where C_i is the total dissolved concentration of metal (μg L^{-1}) in solution at T=0, C_f is the total dissolved concentration of metal (μg L^{-1}) in solution at the end of the experiment, and $\Delta C_{\%ctrl}$ is the percentage change in concentration of metal in the un-acidified control. Calculation of the percentage change in concentration in the control solution was necessary because of small differences in concentration between DGT-deployed solutions and controls (attributed to inhomogeneities between aliquots).

$$(5.8) \quad M_{DGT} = C_e \times (V_{acid} + V_{gel})/fe$$

where C_e is the elution solution measured by ICP-MS, V_{acid} is the volume of acid added to the resin, V_{gel} is the volume of the resin gel (0.16) and *fe* is the elution factor and has a value of 0.8. The elution factor takes into account the ratio of eluted to bound metal obtained when the DGT Chelex resin is immersed in acid.

Eqn. 5.9 gives the DGT calculated labile solution concentration in μg L^{-1}.

(5.9) DGT $C_S = M_{DGT}/V$

where M_{DGT} is the mass accumulated by DGT and V is the initial solution volume (Eqn. 5.7).

The results of these calculations are given in Table 5.3. Calculations of DGT C_S were generally comparable to the C_A concentration (Table 5.3) and in the main, observed metal depletion in solution can be attributed to removal by DGT (Table 5.3), with the small disparities in C_A or DGT C_S representing the analytical uncertainty plus the non-systematic error associated with different aliquots used in the DGT deployment and control solutions.

Results of metal availability integrated over the entire DGT deployment (DGT C_S (%); Table 5.3) show that overall the most labile metals were Ni, Cu, Sr and Ba. The metal pairs Cu and Ni, and Sr and Ba showed substantially similar depletion trends in both years and the proportions of DGT sampled metal were also similar for each pair (DGT C_S (%); Table 5.3), but with a comparatively greater disparity between C_A and DGT C_S for Sr and Ba in the 2010 experiment. Results for Co were the most consistent, being the least DGT-labile metal with a maximum of ca. 4% Co being sampled by DGT in both years (Table 5.3).

The DGT sampled concentration of each metal in 2009 and 2010 was ranked and the sum of ranks of Chelex DGT-available metals (Table 5.3) was of the order Ni > Cu >>

Ba > Sr >> Co. These experiments demonstrate that the concentration of total DGT-available species in PE1 dripwater was much less than the total solution concentration (Table 5.3), indicating that inert species, possibly colloidal complexes (Table 5.1), were the dominant metal species of Ni, Cu and Co.

Sample		**Co**	**Ni**	**Cu**	**Sr**	**Ba**	
PE1 2009	C_i (μg L^{-1})	0.56	0.94	1.49	53.4	23.7	
	ΔC_{24} (%)	2	3	7	10	11	
	C_A (μg L^{-1})	0.04	0.17	0.38	6.9	4.1	
	DGT C_S (μg L^{-1})	0.02	0.26	0.35	9	5	
	DGT C_S (%)	4 ± 4	29 ± 13	25 ± 2	16 ± 3	20 ± 3	
	DGT C_S rank	5	1	2	4	3	
							V (FeOx)
PE1 2010	C_i (μg L^{-1})	0.54	0.64	1.05	53.9	10.0	21.6
	ΔC_{24} (%)	8	7	2	18	20	3
	C_A (μg L^{-1})	0.07	0.16	0.09	7.40	2.39	13.4
	DGT C_S (μg L^{-1})	0.02	0.13	0.12	3.77	0.81	12.6
	DGT C_S (%)	3 ± 10	20 ± 6	12 ± 3	7 ± 7	8 ± 16	59 ± 3
	DGT C_S rank	5	1	2	4	3	
	Sum of ranks	10	2	4	8	6	
	Average ΔC_{24} (%)	5 ± 4	5 ± 3	5 ± 3	14 ± 6	15 ± 6	3

Table 5.3 Trace metal availability for sampling by DGT in depletion experiments with samples of PE1 dripwater from June 2009 and July 2010 using DGT samplers equipped with 0.4 mm open pore hydrogels and Chelex binding resins. In 2010 a second sampler equipped with a FeO_x binding resin was also deployed to measure vanadium. C_i = initial concentration; ΔC_{24} = change in solution concentration in first 24 hr of the depletion experiment; C_A = available concentration for binding by DGT samplers; C_S = concentration sampled by DGT samplers. Error in DGT C_s is calculated from the difference from C_A.

5.4 DISCUSSION

5.4.1 Size, speciation and composition of colloidal NOM in cave dripwater

The combined data from Fl-FFF and TEM demonstrate that the 1 to 10 nm fraction of PE1 dripwater sampled in June 2009 was dominated by globular nanoparticles which exhibited strong UV absorbance and fluorescence intensity in optical regions characteristic of humic substances. This result is consistent with findings from river waters that the 1 to 5 nm size range is dominated by organic-rich, humic-like materials (Benedetti *et al*., 2003; Lyvén *et al*., 2003; Allard *et al*., 2004; Baalousha and Lead, 2007). The potential for the introduction of artefacts (Lead *et al*., 1997) in size fractionation and speciation such as dehydration and aggregation in TEM preparation was mitigated by a multi-method approach (Lead and Wilkinson, 2006) which showed excellent agreement between TEM and Fl-FFF.

In Fl-FFF, size (hydrodynamic diameter) is calculated from measurement of particle diffusion coefficient using the Stokes-Einstein (SE) relationship (Eqn. 5.1) which assumes that the particles are small, spherical and compact, i.e. not open and penetrable by solute molecules (Baalousha and Lead, 2007). Because TEM and Fl-FFF gave similar results, deviations between techniques either reflect fundamental differences in measured properties between techniques, or between particle composition and morphology (i.e. sphericity, permeability), and the assumptions of the SE relationship (Baalousha and Lead, 2007). As proposed by Baalousha and Lead (2007), where the ratio of Fl-FFF D* (number average diffusion coefficient) to particle diameter (d) is not

1, this implies that particles are either not spherical, or permeable. Baalousha and Lead (2007) reported values of D* / h (h = particle height measured by AFM) for humic substances in lake and river water between 1 and 2.10, comparable to results of the analyses from this study which gave a value of D* / d (d = equivalent spherical diameter by TEM) of between 1.1. Since the particles were shown to be spherical in TEM analyses, this result indicates that the nanoparticles were permeable and therefore provides further evidence of their humic-like characteristics (Duval *et al*., 2005).

5.4.2 Metal binding to NOM in cave dripwater

The DGT depletion experiments with PE1 dripwater demonstrated that the initial availability of Sr and Ba for binding by DGT was greater than for the transition metals, consistent with stronger binding of transition metals by NOM. Overall, the depletion curves in (Fig. 5.8) together with the results of ΔC_{24} (%) in Table 5.3 and the metal size-distribution results in Table 5.1, suggest that:

i) A larger proportion of Sr and Ba were present as free ions (faster diffusion in DGT gel) and/or weaker binding species (faster dissociation);

ii) most V, Ni, Cu and Co were bound to large molecules such as NOM. The minor initial depletion was probably due to the slow diffusion of large complexes;

iii) incomplete depletion curves of V, Co, Ni and Cu indicate that the actual DGT labile concentration could be higher than results obtained.

The DGT C_S results in Table 5.3 show that:

i) Metal-ligand complexes for V, Ni and Cu were more labile compared to Co complexes. It is reasonable to assume that Ni and Cu were mainly present in complexes with NOM which were labile for DGT, as shown in previous studies (Warnken *et al*., 2007; 2009).

ii) Sr and Ba may mainly have formed inorganic complexes which are not labile to DGT, or more probably, were present as free ions but were out-competed for binding sites by Ca (around 2000 times more abundant) which was much more concentrated in the sample (Ca does not compete with the transition metals (Tipping *et al.*, 1988; Pinheiro *et al.*, 1999; Marang *et al*., 2009)). This is supported by the plateau in Na concentration (Appendix IX; Fig. S6) in the DGT experiments coinciding with the plateau in the Sr and Ba depletion curves.

iii) Both WHAM and visual MINTEQ underestimated Ni, V and Co binding with NOM at very high pH.

The result for Co is surprising given that complexation of Co by NOM is normally weaker than for Cu and Ni (e.g. Warnken *et al*., 2007). The behavior of Co may represent an unusually strong form of complexation by NOM at very high pH. It is difficult to interpret the findings for Co because the depletion in solution was very small. However, the consistency of the depletion trends for Co (Fig. 8; analytical uncertainty ± 0.01 μg L^{-1}) and agreement between the depletion in solution and the concentration sampled by DGT indicate that the data are valid.

Modelling of Cu speciation with WHAM and MINTEQ showed good agreement with the DGT results, which showed that between 70-100% of Cu was in aqueous complexes with NOM (filtration data indicate ca. 70% being bound by colloids), compared to ca. 95-100% of Cu bound to HA predicted by both models. Given the strong correlations between Cu and Ni, and Co and V in fractionated PE1 samples and the similarities in the DGT depletion trends for these metals, it seems likely that all these metals were predominantly complexed by NOM, but did not necessarily share similar complexation patterns, i.e. all metals did not necessarily compete for the same NOM binding sites (Marang *et al*., 2009).

It is widely recognised that pH is perhaps the most important parameter determining the binding of metals to NOM (Tipping, 2001; Bradl, 2004; Stern *et al.,* 2007). However, the order of initial metal availability to DGT (ΔC_{24}) was not consistent with the published data on the pH-dependant binding of metals with humic substances which suggest stronger binding by Cu over Ni and Co (Milne *et al*., 2003). Indeed, the elevated V/OC, Ni/OC and Cu/OC (compared to Co/OC) in hyperalkaline dripwaters at this site (Fairchild & Hartland, 2010) supports the enhanced complexation of these metals by NOM at high pH. Thus, the very strong complexation of Co by NOM in PE1 dripwater may be pH-independent, and is probably anomalous in the wider environmental context.

The results of DGT experiments for V are difficult to interpret because binding between V and NOM is poorly studied. The speciation of V is complex, being affected by multiple factors including redox potential, oxidation state, pH, competing cations and

complexing agents (Martin and Kaplan, 1998; Bradl, 2004). It is recognised that binding with NOM does occur (Wehrli and Stumm, 1989), and the results of the DGT experiments indicate that V binds strongly to dissolved or nanoparticulate NOM at elevated pH. Adsorption of V to colloidal iron oxides (which may be stabilised by humics (Tipping & Higgins, 1982)) may have occurred to a small extent, but colloidal iron oxides could not be a significant binding phase in the samples studied, since the total Fe concentration in raw samples was <2 μg L^{-1}, and V was not substantially reduced by filtrations at either 100 nm or at 1 kDa, indicating that V was mainly present in the nominally dissolved fraction.

Under hyperalkaline conditions, the bulk of the metal in solution was found to be inert, with only a small proportion being DGT-labile. The residual transition metals in solution were unlikely to be present as aqueous ions or small inorganic complexes and the low Fe concentration indicates the most likely other phase was not important. Thus, overall, these findings point to the dominant role of NOM in binding metal ions in hyperalkaline cave dripwaters. This result highlights the difficulty of modelling metal speciation at very high pH, since models must extrapolate away from their calibrated range, i.e. between pH 4 and 8 (Milne *et al*., 2003).

These results have significant implications for our understanding of metal partitioning into speleothems. Empirical distribution coefficients (Eqn. 2.5) of <<1 for Cu have been calculated between dripwaters and stalagmites from Obir cave, Austrian Alps (Fairchild *et al.*, 2010), consistent with retention of Cu in aqueous complexes. Dissociation of Cu and other complexed metals from aqueous complexes is likely to be rate-limiting, i.e. by

reducing the available proportion of free metal capable of substituting for Ca in $CaCO_3$ lattice sites. These results also suggest that variations in the abundance of transition metals in cave waters (and speleothems) over time may be linked to the abundance of NOM in a range of sizes.

5.4.3 Implications for the study of speleothem archives

Fl-FFF-Fluorescence and TEM characterisation experiments have demonstrated that small humic-like colloids were the most numerous colloid class in the studied samples. Size-fractionation and DGT experiments and strong correlations between metals (Cu, Ni, Co and V) point to the dominant role of NOM in metal binding and transmission to the cave.

Diffusion coefficients for humic-like nanoparticles in PE1 dripwater were obtained from the Fl-FFF analyses. Diffusion rates of the smallest colloids ($D = 7 \times 10^{-6}$ cm^2 s^{-1}; equal to 100 μm in 30 min) are therefore fast compared to the rate of metal dissociation measured by DGT. In reality, colloids occupy a homogeneous distribution in solution and thus those colloids in closest proximity to the crystal surfaces are expected to adsorb rapidly (Lee *et al*., 2005). Therefore, dissociation rates of (strongly bound) NOM-metal complexes at speleothem growth surfaces are likely to be of secondary importance to the speed of NOM adsorption (Lee *et al*., 2005), indicating that ternary (mineral-ligand-metal) complex formation may be initially favoured. Subsequent dissociation is probable for all but the most stable $CaCO_3$-NOM-metal complexes and

further work is needed so that trace metal concentrations in speleothems can be properly interpreted.

The findings of this study appear to confirm the hypothesis of Borsato *et al*. (2007) who suggested that the coincidence of trace metal enrichments in stalagmites with fluorescent organic-bearing laminae demonstrated the occurrence of colloid-facilitated transport in cave dripwaters. The hierarchy of trace element enrichment in laminae was of the order Y > Zn, Cu and Pb > P and Br, and this was suggested to reflect the strength of trace metal binding by colloids at this site (Borsato *et al*., 2007). However, this belies the true complexities involved, such as the affinity of metals for binding sites in NOM, the size, speciation and lability of NOM-metal complexes, the nature of surface complex formation at the calcite surface (Fein, 2002), and the timing of the transmission of NOM-metal complexes as determined by the interaction between climate, soils, and cave hydrology (Chapter 6).

Clearly, specific structural and chemical properties of NOM and its effect on NOM-metal complexation may be unique to the Poole's Cavern's hyperalkaline environments. Further work is needed to characterise NOM-metal binding and transport in a range of cave environments with different characteristics, but this study has shown that humic-like NOM is abundant in cave waters and that NOM-metal complexes dominate metal speciation at very high pH. As in other systems (Filella, 2008), NOM is likely to be an important complexant of trace metals in the normal pH range of dripwaters (ca. pH 7.5-8.5) given that humic-metal complexes are predicted to be the dominant species in

surface waters at pH 5 to 8 (Tipping & Hurley, 1992; Tang & Johannesson, 2003) although binding is likely to be weaker than at ca. pH 12 (Tipping, 2001).

5.5 SUMMARY

A multi-analytical approach to the study of NOM-metal complexes in dripwater PE1 from Poole's Cavern reveals, for the first time, associations between metals (V, Cu, Ni and Co) and NOM in cave dripwater. The application of colloid characterisation techniques (Fl-FFF and TEM X-EDS) and DGT have shown

(1) The abundant presence of fluorescent, globular nanoparticles in cave dripwater with diameters between 1 and 10 nm, consistent with humic- and fulvic compounds. Fluorescence in the studied samples predominantly originated from materials with diameters between 1 and 10 nm, but coarse colloids in the PE1 dripwater samples also fluoresced possibly indicating the presence of organic carbon in a range of colloidal solids. Conversion of the Fl-FFF fluorescence volume particle size distribution (VPSD) to a number particle size distribution (NPSD) produced an improved agreement between Fl-FFF and TEM results and suggest that the nanoparticles studied were partially soft i.e. permeable.

(2) DGT has been applied for the first time to measure metal lability in cave dripwaters. A DGT experiment using the high pH dripwater PE1 from Poole's Cavern demonstrated that a large proportion of transition metal ions were non-exchangeable and held in inert aqueous complexes with either colloidal or dissolved NOM.

These findings are of importance for the interpretation of trace metals in speleothem archives. Until now the partitioning of trace metals into calcite has generally been interpreted based on the assumption that they are present as free ions. This work shows that the partitioning of metals between dripwaters and speleothems is likely to be restricted by binding with colloidal or dissolved NOM. The strength of binding, size and speciation of NOM-metal complexes are likely to impact on the partitioning of aqueous complexes into calcite.

6. NOM-FACILITATED TRANSPORT OF TRACE METALS IN CAVE DRIPWATERS

6.1 INTRODUCTION

This chapter addresses the hydrogeochemical role of aqueous NOM in trace metal binding and transport in speleothem-forming dripwaters. The "NOM" term is used here generically to encompass the particulate (solids with a dimension >1 μm), colloidal (solids with a dimension between 1 nm and 1 μm), and dissolved organic matter (DOM; <1 nm) in cave waters, unless otherwise specified.

In soils and groundwaters, aqueous particulates, colloids, and DOM compete to bind trace metals (Pedrot *et al*., 2008). Particulates may be more readily removed from percolating solutions by pore blockage, permitting colloids and DOM to dominate the transport of complexed (i.e. chemically bound) cationic species (McCarthy and McKay, 2004). This process is well known from field and column studies, but there have been few published studies of naturally-occurring trace element transport by these agents in karstic groundwaters (McCarthy and Shevenell, 1998; Mavrocordatos *et al.*, 2000), and none in cave percolation waters that feed speleothems. The process has however, been modelled extensively in relation to groundwater systems (Bekhit *et al.*, 2009) and used to explain enhanced transport of metals (Chen *et al.*, 2005; Hartland *et al.*, 2010a), radionuclides (Kersting *et al*., 1999) and pollutants in general (White *et al.*, 2005).

Transport of trace elements by NOM in karst systems is of specific interest to studies of the elemental composition of speleothems (Fairchild *et al.*, 2006a; Fairchild and Treble, 2009), and has been identified as a potentially important vector for a suite of surface-reactive metals (Hartland *et al*., 2010a). This process may become manifest in speleothems as annual, to sub-annual, synchronous variations in organic fluorescence and trace metals (e.g. Cu, Ni, Zn, Pb, Y, REE) (Borsato *et al.*, 2007), and where strong seasonal variations in effective rainfall occur, NOM-mobilised trace metals in speleothems may be quantitatively linked to rainfall amount (Jo *et al.*, 2010).

Temporal studies have shown that pronounced increases in NOM concentration and fluorescence occur in cave waters during hydrologically active periods in northern temperate (Baker *et al.*, 1997a; 1999b; Fairchild *et al*., 2006b), sub-tropical (Cruz *et al*., 2005) and monsoonal climates (Tan *et al.*, 2006; Ban *et al*., 2008). However, the transmission of fluorescent NOM in percolation waters is often temporally offset from rainfall maxima. Possible mechanisms for this delay include decoupling of the soil-aquifer system as a result of soil-moisture deficit (Baker *et al.*, 1997a; 2000; Cruz *et al.*, 2005), aquifer drying (Baker *et al.*, 2000), and differential hydrological routing between drips (Tooth & Fairchild, 2003). However, the breakthrough times of particulate, colloidal, and dissolved NOM in dripwaters have not been examined and because coarse colloids (>100 nm) and particulates (>1 μm) may be less prone to matrix diffusion (diffusion into micropores and fractures) than fine colloids (1-100 nm) and solutes (<1 nm), they may be transmitted more quickly (McCarthy & McKay, 2004).

Variations in NOM may be usefully applied as a conservative tracer of groundwater hydrology, and UV-fluorescence has been used in numerous studies to identify temporal variations in NOM amount and composition (Baker *et al*., 1997a; Baker & Genty, 1999; Tan *et al*., 2006). However, NOM fluorescence is susceptible to disruption by inner-filtering (i.e. self-absorption, Hudson *et al*., 2007) and where present, the coarse fraction masks fluorescence in finer fractions (Chapter 4). Fluorescence attributes of NOM may also be quantitatively related to its functional properties (Baker *et al.*, 2008). For example, humic-like (Peak C) fluorescence emission wavelengths in the typical range of cave waters (ca. 400-420 nm) correlate with weaker metal binding, whereas longer Peak C emission wavelengths, characteristic of more aromatic/hydrophobic NOM, correlate with stronger binding (Baker *et al.*, 2008).

Detailed spatial and temporal studies of the interaction between NOM and trace metals in cave waters are needed to better understand the processes behind the incorporation of NOM (Blyth *et al.*, 2008) and associated inorganic constituents of speleothems (Borsato *et al*., 2007; Fairchild & Treble, 2009).

This chapter provides an analysis of NOM and trace metal partitioning between size classes in sequentially-filtered soil leachates and cave dripwaters. Variations in the intensity of fluorescence, total organic carbon (TOC) and trace element contents of sequentially-filtered cave dripwater samples from three contrasting sites are presented and compared to leached soil samples. In essence, this work seeks to identify the particulate, colloidal and dissolved components in dripwaters that are responsible for

trace element transport; examine how these differ from soils, whether these differ significantly between sites, and whether differences with time reflect hydrology.

The distinction between aqueous phases (e.g. colloidal vs. dissolved) is often blurred and is largely method dependant (Lead and Wilkinson, 2006). Throughout the text reference is made to size classes derived from sequential membrane filtrations, the distinction between which should not be interpreted too rigidly.

6.2 MATERIALS AND METHODS

Three contrasting study sites were targeted: Poole's Cavern (PC), near Buxton, UK; Lower Balls Green Mine (LBGM), Minchinhampton, UK; and Grotta di Ernesto (ERN), Trentino, NE Italian Alps (site diagrams and descriptions are in Chapter 3). Hydrologic and hydrogeochemical information on the drip points studied is summarised in Table 6.1 and their average geochemistry is given in Table 3.2 and Table 6.2. Methodologies used in sample collection, fractionation and analysis are detailed in Chapter 3.

Drip rates of PC dripwaters (PE1 and BC1) and LBGM drips (LB1-3) were monitored at 30 second intervals using Driptych Stalagmate-Plus^{TM} (Egham, UK) drip rate loggers from June 2008 to August 2010 and September 2008 to August 2009, at PC and LBGM, respectively. The hydrology and hydrochemistry of ERN dripwaters has been well characterised by long-term monthly dripwater and soil water monitoring over the period 1995-2008 (Miorandi *et al.*, 2010).

6.2.1 Evapotranspiration calculations

Potential evapotranspiration was calculated for Buxton (PC) and Gloucestershire (LBGM) from January 2008 to August 2009, using the Penman-Monteith equation which is the favoured method for temperate forested environments (Shaw, 1994). Subtraction of potential evapotranspiration (E) from measured rainfall (P) gives an estimate of effective infiltrating precipitation (P-E). Weekly averaged temperature, wind speed, relative humidity and daylight hours were used in the calculations.

6.2.2 Classification of operationally-derived size classes

In Chapter 5, colloids and particles in dripwater samples from Poole's Cavern drip point PE1 were subjected to a detailed characterisation of their size, morphology, and composition. Analysis of PE1 dripwater samples (June 2009) using Flow Field Flow Fractionation (Fl-FFF) and Transmission Electron Microscopy (TEM) coupled to X-ray Energy Dispersive Spectroscopy (X-EDS) revealed both the heterogeneous composition, and poly-disperse distribution of NOM-bearing materials with dimensions between 20 nm and >1 μm. The numerically most abundant colloid class were fluorescent, UV-absorbing globular nanoparticles with diameters ranging from 1 - 4 nm, consistent with fulvic- and humic-like macromolecules characterised in other freshwater environments (e.g. Baalousha and Lead, 2007).

Data on colloid size and morphology in dripwaters have also been presented in Fairchild and Hartland (2010) and Hartland *et al.*, (2010a), and reconnaissance TEM and Atomic

Force Microscopy (AFM) analyses of colloid size and morphology in ERN and LBGM (AFM only) waters were found to be consistent with these previous studies (Appendix VI). Generalised colloid classes in dripwaters were therefore delineated on the basis of size from sequential filtrations at nominal pore sizes of 1 μm, 100 nm and 1 kDa:

- **Particulate**: >1 μm to ca. 1 μm (heterogeneous particles)
- **Coarse colloidal**: ca. 1 μm to ca. 100 nm (large aggregates and globular colloids)
- **Fine colloidal**: ca. 100 nm to ca. 1 nm (small aggregates, humic and fulvic macromolecules)
- **Nominally dissolved**: ≤ ca. 1 nm (fulvic macromolecules and organic solutes)

Membrane filters exhibit variable efficiencies and allow a proportion of material to pass with diameters exceeding the assigned 'cut-off' (Lead *et al.*, 1997). Therefore, it is not appropriate to assign sharp boundaries to the size-classes defined. For example, it is expected that fulvic colloids with diameters around 1-2 nm may permeate a 1 kDa ultrafilter membrane (Liu and Lead, 2006), and hence no "truly dissolved" size class is defined here because the finest colloids have been characterised by Fl-FFF and TEM and have been shown to have diameters of ca. 1-4 nm (Chapter 5).

6.3 HYDROLOGY AND HYDROCHEMISTRY OF DRIPWATERS

6.3.1 Poole's Cavern

Ratios of Ca to Sr and Mg did not show any variation with drip rate in Poole's Cavern dripwaters, but modification by precipitation of $CaCO_3$ during collection was evident in drips RC1 and RC2 and data from these drips has been excluded (Appendix II) because calcite precipitation is likely to have substantially altered their composition for those elements which preferentially partition into calcite (Fairchild *et al.*, 2010). Some calcite precipitation also occurred during collection of PE1 dripwater but this was negligible by comparison (Table 3.2). Major cations did not respond coherently to discharge variations in PE1 or BC1.

Flow at drip point BC1 was less variable than PE1, had a higher mean discharge (Table 6.1), and was weakly correlated with 30-day antecedent rainfall at Buxton (Fig. 6.1a). Subsequent monitoring of drip point BC2 over the period September 2009- December 2010, demonstrated that discharge at BC1 and BC2 is characterised by an underflow-overflow relationship (Tooth and Fairchild, 2003), i.e. rainfall inputs followed preferential flow routes feeding BC1, leading to reduction in flow at BC2 and thus when flow at BC1 reduced, flow at BC2 increased (Appendix VIII).

Site	RSD of discharge (%)	Max discharge (μL s^{-1})	Mean discharge (μL s^{-1})	Drip classification*	pH	Electro conductivity (μS cm^{-1})	High Mg/Ca or Sr/Ca at low flow? (PCP)	Drip point type	Speleothem morphology (modern precipitate) at impact point
Poole's Cavern									
BC1	27	87	58.4	Seepage flow	7.91 ± 0.22	496 ± 42.1	no/no	Crack in ceiling	Active flowstone
BC2	32	42	27.7	Seepage flow	7.88 ± 0.17	501 ± 41.7	no/no	Crack in ceiling	Active flowstone
PE1[a]	75	49	8.7	Seasonal (fast)	11.50 ± 0.73	703 ± 257	no/no	Short soda straw	Incipient cone-shaped stalagmite
RC1	149	35	5.4	Seasonal (slow)	11.77 ± 1.46	1878 ± 1413	no/no	Long soda straw	Cone-shaped stalagmite
RC2	114	95	27.8	Seasonal (fast)	12.71 ± 0.10	1946 ± 1547	no/no	Short soda straw	Incipient candle-shaped stalagmite
Lower Balls Green Mine									
LB1	58	501	195	Vadose flow	8.07 ± 0.14	520 ± 11.1	?/?	Crack in ceiling	Active flowstone
LB2	20	539	401	Percolation stream	8.08 ± 0.12	498 ± 94.4	?/?	Crack in ceiling	Active flowstone
LB3	76	366	27.3	Vadose flow	8.12 ± 0.07	521 ± 31.7	?/?	Short soda straw	Active flowstone/incipient stalagmite
Grotta di Ernesto									
St-1[b]	88	390	207	Seasonal (fast)	7.87 ± 0.05	284 ± 3.9	yes/no (negligible)	Stalactite	Active flowstone
St-2[c]	78	600	41.7	Seasonal (fast)	7.86 ± 0.07	282 ± 10.5	yes/yes (minor)	Short soda straw	Cone-shaped stalagmite
St-ER77	32	3.1	2.4	Seepage flow	8.04 ± 0.13	287 ± 0.8	?/?	Soda straw	Cone-shaped stalagmite
St-ER78	115	1.1	0.5	Seasonal (slow)	7.81 ± 0.05	281 ± 0.1	?/?	Thick stalactite pendant	Incipient cone-shaped stalagmite

Table 6.1 Summary dripwater hydrology, indicative hydrochemical properties and drip point characteristics.

* Drip classification after Smart & Freidrich (1986) as modified by Baker *et al.* (1997); [a] Named PC-96-7 in Baker *et al.* (1999c); [b] named G1 and [c] named G2 in Borsato (1997) and Fairchild *et al.* (2000); St= stalactite; designation of Grotta di Ernesto drip locations follows Miorandi *et al.* (2010). Drip discharges estimated assuming an average drip volume of 0.15 mL.

			Physicochemical properties			Major cations (mmol L^{-1})				Major anions (mmol L^{-1})						Estimated EC (Rossum)	% actual EC
Site	**Drip point**	**n**	**EC (mS cm^{-1})**	**pH**	**Temp (°C)**	**Ca^{2+}**	**Mg^{2+}**	**Na^{2+}**	**K^{+}**	**HCO_3^-**	**CO_3^{2-}**	**OH^-**	**SO_4^{2-}**	**NO_3^-**	**Cl^-**	**EC (mS cm^{-1})**	**%**
LBGM	LB1	3	0.52 ± 0.01	8.1 ± 0.2	11.8 ± 0.4	1.69 ± 0.19	0.11 ± 0.01	0.33 ± 0.05	0.48 ± 0.09	2.85 ± 0.35	0.02 ± 0.01	nd	0.24 ± 0.02	0.17 ± 0.02	0.32 ± 0.02	0.56 ± 0.02	112 ± 5
LBGM	LB2	3	0.52 ± 0.01	8.1 ± 0.1	11.3 ± 0.6	1.70 ± 0.15	0.10 ± 0.01	0.29 ± 0.03	0.50 ± 0.15	3.28 ± 0.14	0.02 ± 0.00	nd	0.19 ± 0.10	0.15 ± 0.01	0.25 ± 0.11	0.57 ± 0.06	114 ± 15
LBGM	LB3	2	0.46 ± 0.06	8.2 ± 0.0	11.3 ± 0.3	1.73 ± 0.09	0.10 ± 0.00	0.27 ± 0.01	0.29 ± 0.01	2.61 ± 0.32	0.02 ± 0.00	nd	0.29 ± 0.01	0.14 ± 0.04	0.33 ± 0.01	0.55 ± 0.01	126 ± 13
ERN	St-1	1	0.28 ± 0.00	7.9 ± 0.1	8.1 ± 0.5	0.96	0.19	0.02	0.09	2.12	0.01	nd	nd	0.04	0.01	0.33	120
ERN	St-2	1	0.28 ± 0.01	7.9 ± 0.1	8.2 ± 0.6	1.00	0.18	0.02	0.07	2.15	0.01	nd	nd	0.06	0.01	0.33	165
ERN	St-ER77	1	0.29 ± 0.00	8.0 ± 0.1	7.9 ± 0.4	0.97	0.17	0.02	0.05	2.00	0.01	nd	nd	0.04	0.01	0.32	121
ERN	St-ER78	1	0.28 ± 0.00	7.9 ± 0.1	7.4 ± 0.7	0.98	0.24	0.02	0.09	2.21	0.01	nd	nd	0.04	0.01	0.34	127

Table 6.2 Average geochemical composition of dripwaters from Lower Balls Green Mine (LBGM), and data from individual samples from Grotta di Ernesto (ERN)

Alkalinity estimated by difference from charge balance, proportions of HCO_3^-, CO_3^{2-} and OH^- predicted from solution pH. Predicted conductance calculated by the method of Rossum (1975). Modification of dripwater composition by calcite precipitation before collection may be indicated by the disparity between the measured conductance and that predicted by the Rossum calculation. EC= electrical conductivity; Nd= not determinable.

Discharge at drip PE1 (Fig. 6.1c) did not vary coherently with rainfall patterns, and was not correlated with antecedent rainfall (Fig. 6.1b). Over much of the monitoring period the discharge of PE1 was indicative of long-term matrix-fed flow, showing only small fluctuations between 0.1-0.2 mL min^{-1} (Fig. 6.1a). In the study of Baker *et al.* (1999c) the same drip point (feeding stalagmite PC-96-7) was suggested to be fed by both matrix porosity and a more responsive flow component, and this may account for the increased discharge of PE1 over autumn and winter 2008. However, PE1 discharge also displayed complex non-linear behaviour; in spring 2009 discharge sharply decreased before increasing by an order of magnitude (Fig. 6.1c), discharge then declined exponentially and returned to the previous range. This was consistent with subsequent discharge behaviour of PE1 during the period August 2009 to June 2010, and may represent the formation of air-locks (decline in discharge) that when released produced increased flows. However, this discharge pattern did not measurably impact on PE1 geochemistry e.g. Sr/Ca, OC concentration, or trace metals.

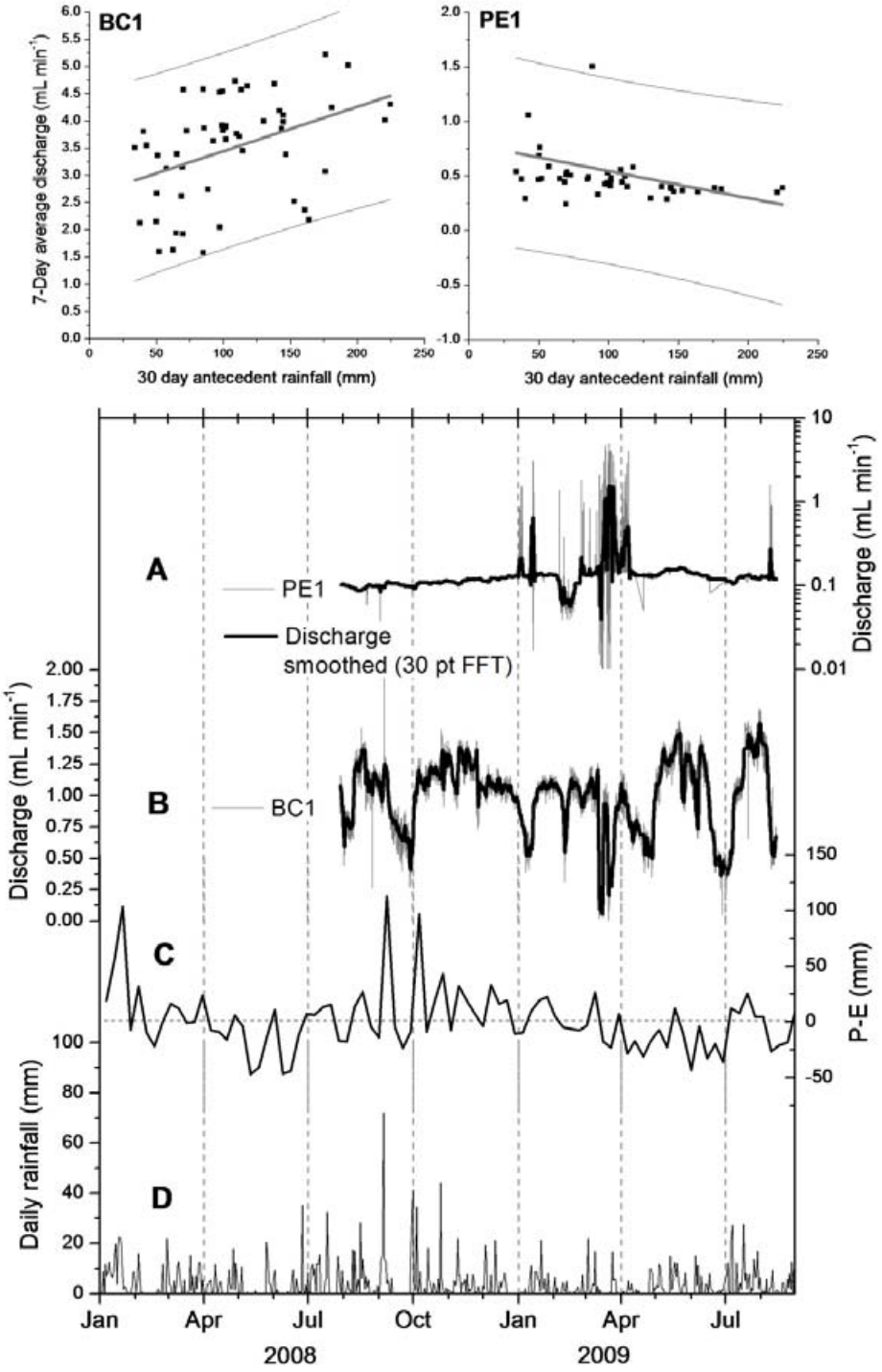

Figure 6.1 Hydrology of Poole's Cavern drip points BC1 and PE1 monitored between July 2008 and August 2009. Top: cross-plots of average weekly discharge vs. antecedent rainfall. Grey lines are linear regression trend lines and black lines are 95% prediction bands. Middle: monitored drip rates of PE1 (A) and BC1 (B) drip points plotted against weekly effective precipitation (C) and daily rainfall (D)**.** P-E= Precipitation Evapotranspiration (Penman method), FFT= Fast Fourier Transform. Discharge estimated based on average drop volume of 0.15 mL.

6.3.2 Lower Balls Green Mine

The dripwaters of Lower Balls Green Mine represent the extreme hydrological end-member for the range of non-turbulent percolation flows found in karst systems (Table 6.1). The mean discharge of drip points LB1 (Fig. 6.2a) and LB2 (Fig. 6.2b) were very high, but LB1 was best correlated with variations in antecedent rainfall (Fig. S4; Appendix VIII). Drip point LB3 (Fig. 6.2c) was the most variable drip and at maximum flow LB3 discharge was comparable to LB1-2 (Table 6.1). But, on average LB3 had the lowest discharge, indicating that LB3 was fed by both seepage-flow and rapid, fracture-flow components (Fig. 6.2c).

The discharge of all three drips at LBGM was correlated to some extent with variations in 60 day antecedent rainfall. However, the discharge of drip point LB3 between July 2009 and August 2009 departed from the previous range (Fig. 6.2c). Separate linear regression of the LB3 data from July and August 2009 (Fig. S4d; Appendix VIII) demonstrated that discharge at this time was correlated with 14 day antecedent rainfall, indicating that rapid (preferential) vadose recharge routes were decoupled from the LB3 drip point during the sampling period. Ratios of Ca to Mg and Sr in samples from LBGM did not indicate prior calcite precipitation had occurred in any of the drips.

6.3.3 Grotta di Ernesto

Drip points sampled in November 2008 encompassed both responsive fracture-fed drips (St-1 and St-2) and slower drips (St-ER77 and St-ER78) dominated by matrix porosity

with minor modification by prior calcite precipitation (Miorandi *et al.*, 2010). Drip rates and dripwater electroconductivity and pH values were representative of the normal range (Miorandi *et al.,* 2010). The average drip discharges observed between 4/11/08–08/11/08 are shown in Fig. 6.3 in relation to drip discharges plotted against antecedent rainfall from the dataset of Miorandi *et al.* (2010). ERN dripwater samples taken in November 2008 were obtained at close to upper end of their hydrological range.

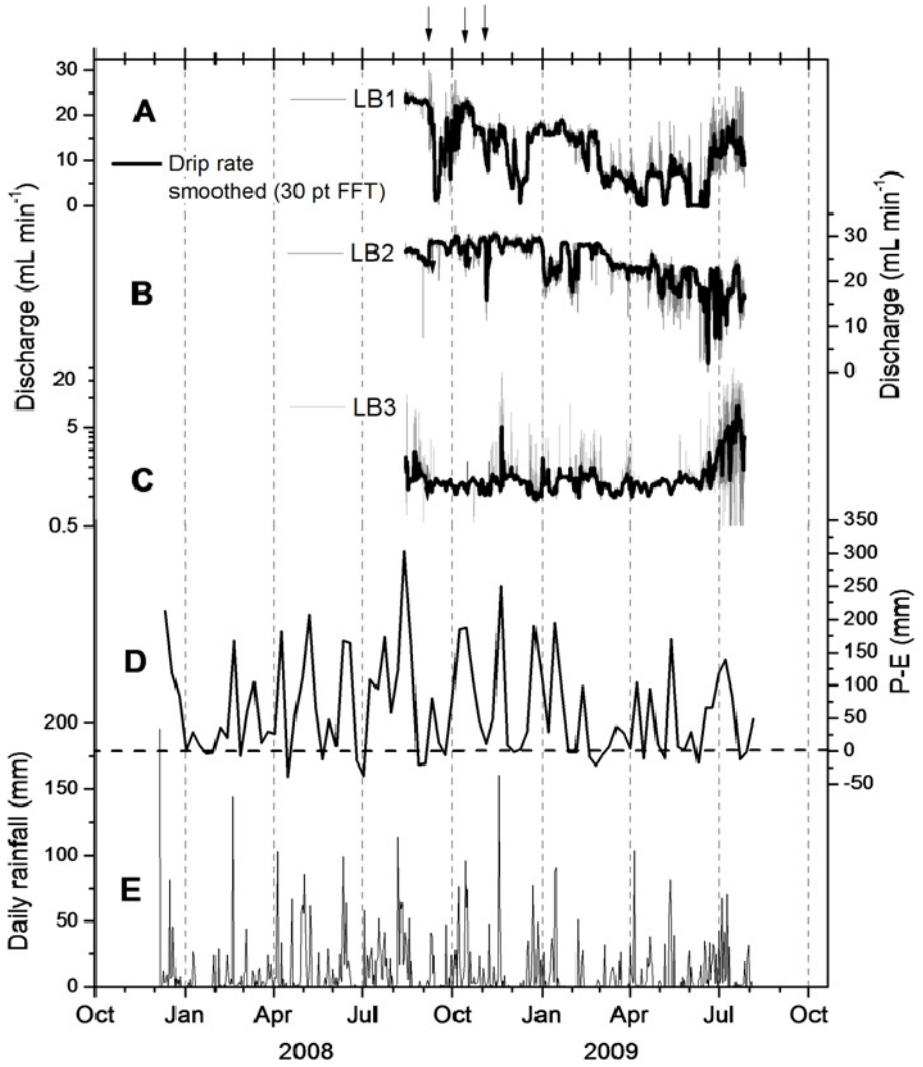

Figure 6.2 Monitored discharges of drip points LB1 (a), LB2 (b) and LB3 (c) in Lower Balls Green Mine between July 2008 and August 2009; (d) weekly effective precipitation (P-E) and (e) daily rainfall. P-E= Precipitation-Evapotranspiration (Penman method), FFT= Fast Fourier Transform. **Arrows at top denote timing of dripwater sampling**. Discharge estimated based on average drop volume of 0.15 mL.

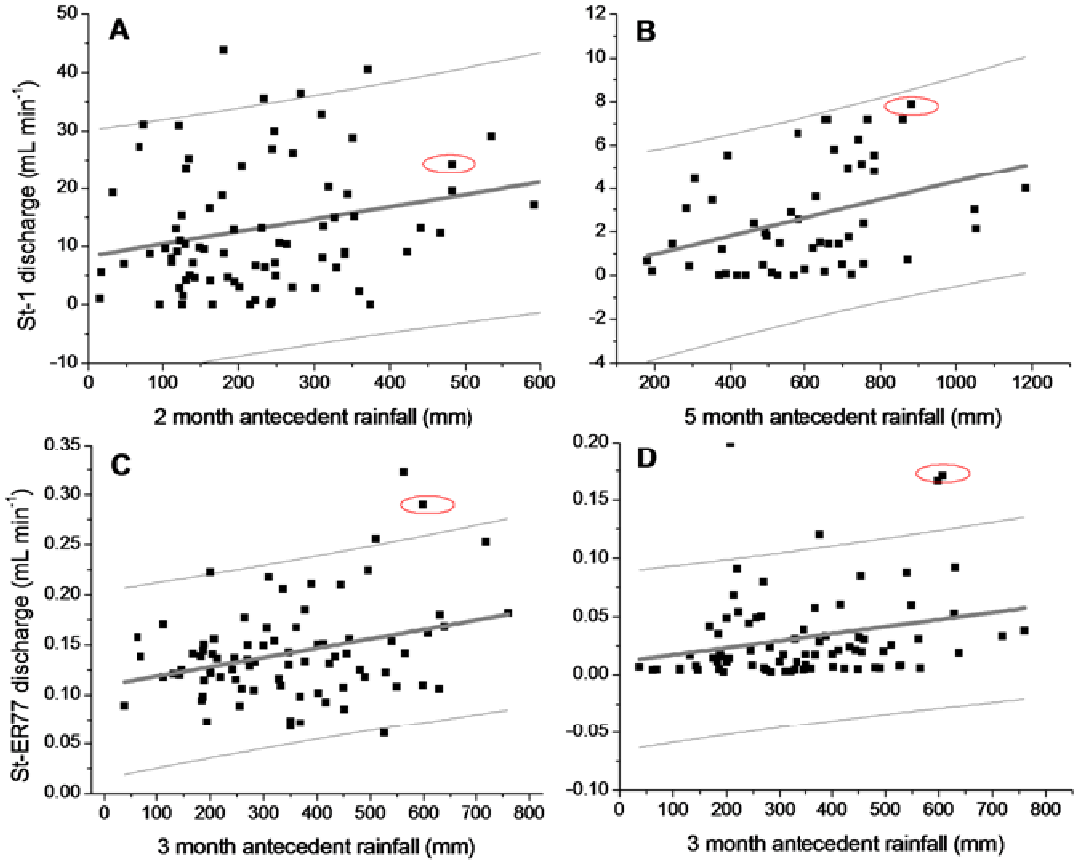

Figure 6.3 Cross-plots of discharge vs. antecedent rainfall for Grotta di Ernesto drip points St-1 (a), St-2 (b), St-ER77 (c) and St-ER78 (d) corresponding to the period August 2001 to November 2008 (data source: Miorandi *et al.*, (2010)). Circled values are the discharge and antecedent rainfall values corresponding to sampling in November 2008. Grey lines are linear regression trend lines and black lines are 95% prediction bands. Discharge estimated based on average drop volume of 0.15 mL.

6.4. RESULTS

6.4.1 Size-based partitioning of trace elements in aqueous soil leachates and cave dripwaters

6.4.1.1 Trace element partitioning in soils

The elemental compositions of soil leachates between sites were found to be highly similar. One-way analysis of variance (ANOVA Bonferroni means comparison) found no significant differences at the 0.05 level between the population means of each element between sites. Trace elements in the three soils were concentrated in the coarse colloidal fraction, with residual metal being located in the nominally dissolved fraction and little being associated with fine colloids (Table 6.3). When the proportions of metal associated with the coarse and nominally dissolved size classes in soils were ranked, the following hierarchy of trace metal concentration in the coarse soil fraction (opposite of concentration in nominally dissolved fraction) was derived: Fe & Y > Ti > Mn > Pb > Co > Al > Zn > Cr > Si > Ni > Cu > V >> Br > Mg >> Sr >> Na (Table 6.3).

6.4.1.2 Trace element partitioning in dripwaters

The distribution of trace elements, major ions and organic carbon in sequentially-filtered dripwaters from the three study sites also revealed a high degree of uniformity. In Table 6.4, a representative subset of the size-fractionated dripwater data is presented (remaining data is given Table S2; Appendix II). Two-way ANOVA (Bonferroni means

comparison) found no significant difference at the 0.05 level between the population means of each study site, but significant differences were detected (at the 0.05 level) between the population means of Cu, Ni, Co, V and Al in the hyperalkaline PE1 dripwater (PC), and the other studied dripwaters. Trace metals were generally concentrated in the finest size fraction (Table 6.4), but Co, Cu, and Ni were more evenly distributed between both fine and nominally dissolved size fractions, possibly indicating a colloidal association.

6.4.1.3 Comparison between the composition of soils and dripwaters

In essence, the size distribution of metals in the soils (Table 6.3) was totally different from that found in the dripwaters (Table 6.4). Results indicate that metals associated with the coarse fraction of soils (e.g. Fe, Y, Mn, Pb) were largely below detection limits in fractionated dripwaters, possibly indicating removal of large colloids and particles by filtration through pore blockage (McCarthy and McKay, 2004).

The alkaline earth metals Na, Mg, and Sr generally show a low affinity for binding at colloid and particle surfaces, although trace amounts are expected to form structural components in aggregates in karstic waters (Shevenell and McCarthy, 2002). For example, the divalent cations Ca and Mg enable the formation of gels through cation-bridging reactions between negatively charged moieties (Verdugo *et al.*, 2005), possibly explaining the relatively greater partitioning of Mg into the coarser classes over Sr.

In natural waters, small colloids are typically present in numbers which are orders of magnitude greater than particulates (e.g. 10^6 times more 10 nm colloids than the equivalent number of 1 μm particles) (Doucet *et al.,* 2007). Preferential partitioning of surface-reactive trace metals into the finest size-fraction may be predicted based on the greater available surface area for sorption (Buffle *et al*., 1998) and this is consistent with the data from fractionated dripwaters (Table 6.4).

6.4.2 Competitive binding of metals by NOM in soils and dripwaters

Trace metal binding by NOM in dripwaters was modelled using the Windermere Humic Aqueous Model (WHAM) 6.1 which incorporates Model VI (Tipping, 1998), and visual MINTEQ 3.0 which incorporates the NICA-Donnan model (Kinniburgh *et al*., 1999). Modelling of metal binding to NOM in natural water samples is challenging because of the extreme heterogeneity of the OM present which encompasses a complex mixture of compounds with variable binding affinities and physiochemical properties, including variable charge and binding site distributions (Filella, 2008). This is further complicated by the variable stoichiometry of the reaction and competition between metals for binding sites (Unsworth *et al*., 2006). Model VI is based on a discrete set of sites (Tipping, 1998), whereas the NICA-Donnan model employs a bimodal, continuous distribution for protons and metal ions (Kinniburgh *et al*., 1999).

		Concentration ----- in size class (mg L^{-1})-----				----------Element concentration in size class (μg L^{-1})----------													
Site	Size class	TOC	Si	Na	Mg	Al	Ti	V	Cr	Mn	Fe	Ni	Co	Cu	Zn	Br	Sr	Y	Pb
Lower Balls Green Mine (n=3)	Coarse	**2.2** ± 0.2	**1.8** ± 1.2	0.0 ± 2.8	**0.2** ± 0.1	**975** ± 354	**16** ± 14	**2.7** ± 1.2	**1.8** ± 0.8	**9.7** ± 0.5	**944** ± 453	**0.7** ± 0.2	**0.2** ± 0.0	**1.4** ± 0.1	**54** ± 18	**2.7** ± 1.0	**1.9** ± 1.4	**2.2** ± 0.6	**2.9** ± 0.8
	Fine	**0.4** ± 0.1	0.0± 0.1	**0.1** ± 0.6	0.0 ± 0.1	**5.0** ± 15	0.0± 0.0	0.0± 0.9	**0.1** ± 0.2	0.0± 0.1	**6.4** ± 6.8	0.0± 0.1	0.0± 0.0	**0.1** ± 0.1	**1.5** ± 4.1	**0.7** ± 1.6	**0.1** ± 1.1	0.0± 0.0	0.0± 0.4
	ND	**3.0** ± 0.1	**0.4** ± 0.1	**4.0** ± 0.5	**0.2** ± 0.1	**27** ± 14.3	**0.1** ± 0.0	**0.7** ± 0.8	**0.2** ± 0.1	**0.1** ± 0.1	**1.2** ± 1.5	**0.1** ± 0.0	0.0± 0.0	**0.2** ± 0.0	**0.2** ± 4.1	**1.3** ± 1.2	**7.1** ± 0.4	0.0± 0.0	**0.3** ± 0.4
Poole's Cavern (n=1)	Coarse	-	0.3	0.2	0.0	129	2.1	0.5	0.2	5.6	111	0.1	-	0.5	33	0.0	0.4	0.3	1.4
	Fine	-	0.0	0.2	0.0	10	0.1	0.2	0.1	0.5	5.7	0.0	-	0.4	1.4	0.7	1.0	0.0	0.0
	ND	-	0.2	1.8	0.1	18	0.2	1.1	0.2	0.1	2.8	0.2	-	0.2	0.2	1.2	3.9	0.0	0.0
Grotta di Ernesto (n=3)	Coarse	**0.2** ± 0.5	**1.2** ± 2.2	0.0± 4.9	**0.1** ± 0.3	**511** ± 467	**6.5** ± 9.5	**0.8** ± 0.8	**3.6** ± 13	**13** ± 19	**318** ± 329	**2.3** ± 5.3	**0.3** ± 0.3	**1.3** ± 1.2	**54** ± 78	**3.3** ± 6.2	**0.9** ± 8.1	**0.8** ± 1.3	**1.5** ± 1.0
	Fine	**3.8** ± 0.5	0.0± 0.4	**0.4** ± 3.9	0.0± 0.3	**8.1** ± 43	**0.1** ± 0.7	0.0± 0.6	0.0± 0.7	**0.9** ± 2.8	**7.8** ± 20	0.0± 1.8	0.0± 0.1	0.0± 5.1	**24** ± 36	**0.4** ± 2.5	**0.5** ± 8.8	**0.1** ± 0.1	**0.1** ± 0.4
	ND	**1.7** ± 0.5	**0.3** ± 0.3	**6.7** ± 2.9	**0.1** ± 0.2	**32** ± 39	**0.3** ± 0.4	**0.4** ± 0.5	**0.4** ± 0.5	**0.6** ± 0.6	**4.2** ± 4.1	**0.2** ± 1.8	0.0± 0.0	**0.7** ± 5.0	**10** ± 6.8	**1.2** ± 1.2	**4.3** ± 6.0	0.0± 0.0	**0.2** ± 0.3
	% Coarse		73	3	41	91	93	58	74	93	96	70	92	64	84	42	15	94	92
	Coarse Rank		**10**	**17**	**15**	**7**	**3**	**13**	**9**	**4**	**1**	**11**	**6**	**12**	**8**	**14**	**16**	**2**	**5**
	% ND		27	92	52	7	5	39	20	2	1	28	5	22	4	38	76	1	6
	ND Rank		**7**	**1**	**3**	**10**	**13**	**4**	**9**	**15**	**16**	**6**	**12**	**8**	**14**	**5**	**2**	**17**	**11**

Table 6.3 Summary organic and trace metal composition of sequentially filtered aqueous soil leachates from Lower Balls Green Mine, Grotta di Ernesto and Poole's Cavern. ND = nominally dissolved.

		------Concentration in size class (mg L^{-1})------				----------Element concentration in size class (μg L^{-1})----------								
Site	Size class	TOC	Si	Na	Mg	Al	Ti	V	Cr	Ni	Co	Cu	Br	Sr
LB1 Lower Balls Green Mine (n=3)	Particulate	**1.6** ± 0.2	0.0± 0.2	0.0± 0.4	0.0± 0.1	0.0± 3.0	**0.1** ± 0.1	0.0± 0.1	-	-	0.0± 0.0	0.0± 0.1	0.0± 2.0	0.0± 7.3
	Coarse	**1.1** ± 0.2	**0.22** ± 0.2	**0.7** ± 0.4	**0.2** ± 0.2	0.0± 6.5	0.0± 0.1	0.0± 0.1	-	-	0.0± 0.0	**0.1** ± 0.0	**4.1** ± 2.2	**12** ± 7.1
	Fine	**0.1** ± 0.2	0.0± 0.1	**0.1** ± 0.3	0.0± 0.1	**2.7** ± 5.9	0.0± 0.1	0.0± 0.1	-	-	0.0± 0.0	0.0± 0.1	0.0± 1.6	0.0± 4.4
	ND	**1.7** ± 0.1	**3.0** ± 0.2	**7.4** ± 0.2	**2.6** ± 0.1	**30** ± 0.6	**0.7** ± 0.1	**0.2** ± 0.0	-	-	**0.3** ± 0.0	**0.6** ± 0.1	**40** ± 1.2	**138** ± 3.5
LB3 Lower Balls Green Mine (n=3)	Particulate	**1.9** ± 0.2	**0.1** ± 0.2	**0.1** ± 0.3	0.0± 0.1	**0.6** ± 0.8	0.0± 0.1	0.0± 0.0	-	-	0.0± 0.0	0.0± 0.0	0.0± 2.0	**3.2** ± 7.8
	Coarse	**1.3** ± 0.1	0.0± 0.3	**0.1** ± 0.5	0.0± 0.2	0.0± 2.5	0.0± 0.1	0.0± 0.0	-	-	0.0± 0.0	0.0± 0.1	**0.3** ± 3.5	0.0± 11
	Fine	**1.2** ± 0.2	0.0± 0.3	0.0± 0.6	0.0± 0.2	0.0± 3.2	0.0± 0.1	0.0± 0.0	-	-	0.0± 0.0	0.0± 0.1	0.0± 3.9	**2.0** ± 11
	ND		**3.0** ± 0.1	**7.3** ± 0.2	**2.8** ± 0.1	**31** ± 2.1	**0.6** ± 0.1	**0.1** ± 0.0	-	-	**0.3** ± 0.0	**0.3** ± 0.1	**43** ± 2.2	**149** ± 3.0
BC1 Poole's Cavern (n=3)	Particulate	**0.8** ± 0.3	0.0± 0.1	0.0± 0.1	0.0± 0.1	0.0± 0.9	0.0± 0.1	0.0± 0.1	**0.2** ± 0.2	-	0.0± 0.0	0.0± 0.6	**1.2** ± 1.4	**1.7** ± 2.1
	Coarse	**0.4** ± 0.3	**0.2** ± 0.1	**0.6** ± 0.1	**1.1** ± 0.0	**0.4** ± 1.0	0.0± 0.1	0.0± 0.0	0.0± 0.0	-	0.0± 0.0	**0.3** ± 0.6	**1.6** ± 1.8	**1.1** ± 1.9
	Fine /	**0.7** ± 0.4	0.0± 0.0	0.0± 0.1	0.0± 0.0	**0.3** ± 1.3	0.0± 0.1	0.0± 0.0	0.0± 0.0	-	0.0± 0.0	**0.1** ± 0.0	**1.0** ± 1.6	**0.9** ± 1.8
	ND		**2.7** ± 0.0	**3.1** ± 0.0	**0.9** ± 0.0	**5.3** ± 1.0	**0.7** ± 0.1	**0.4** ± 0.0	**0.2** ± 0.0	-	**0.3** ± 0.0	**0.2** ± 0.0	**40** ± 0.8	**56** ± 1.0
PE1 Poole's Cavern (n=3)	Particulate	**1.5** ± 0.3	0.0± 0.1	0.0± 0.1	-	**124** ± 39	**0.8** ± 0.1	0.0± 0.8	0.0± 0.3	**0.1** ± 0.1	0.0± 0.0	**0.4** ± 0.1	**0** ± 1.2	**0** ± 2.2
	Coarse	**0.3** ± 0.3	**0.4** ± 0.1	**0.2** ± 0.1	-	**325** ± 39	**0.1** ± 0.1	**1.7** ± 0.9	**0.2** ± 0.4	0.0± 0.1	**0.1** ± 0.0	0.0± 0.2	**0.6** ± 1.5	**6.4** ± 2.6
	Fine	**0.5** ± 0.2	**3.3** ± 0.2	**0.1** ± 0.2	-	**26** ± 55	0.0± 0.1	**0.9** ± 1.4	**0.7** ± 0.6	**0.1** ± 0.2	**0.1** ± 0.1	**0.4** ± 0.3	**1.3** ± 1.4	**0.9** ± 2.4
	ND	**1.4** ± 0.1	**3.2** ± 0.2	**3.7** ± 0.2	-	**808** ± 54	**0.8** ± 0.1	**20** ± 1.3	**8.9** ± 0.5	**0.8** ± 0.2	**0.5** ± 0.1	**1.2** ± 0.3	**32** ± 1.0	**54** ± 2.0
St-1 Grotta di Ernesto (n=1)	Particulate	**1.2** ± 0.2	**0.1** ± 0.4	0.0± 0.0	**0.1** ± 0.1	**1.6** ± 1.5	0.0± 0.1	0.0± 0.1	0.01 ± 0.0	0.0± 0.0	0.0± 0.0	0.0± 0.0	**0.3** ± 0.5	**0.3** ± 0.2
	Coarse	**0.5** ± 0.6	0.0± 0.1	**0.1** ± 0.0	**0.1** ± 0.1	0.0± 1.5	0.0± 0.0	0.0± 0.0	0.0± 0.0	0.0± 0.0	0.0± 0.0	0.0± 0.1	**0.1** ± 0.5	**0** ± 0.5
	Fine	**0.5** ± 0.6	**0.1** ± 0.1	0.0± 0.0	**0.1** ± 0.2	**1.8** ± 1.4	0.0± 0.1	0.0± 0.0	0.0± 0.0	0.0± 0.0	0.0± 0.0	**0.1** ± 0.1	**0.9** ± 0.4	**0.2** ± 0.6
	ND	**1.6** ± 0.1	**2.4** ± 0.7	**0.4** ± 0.0	**4.3** ± 0.1	**6.2** ± 0.7	**0.6** ± 0.0	**0.1** ± 0.0	**0.1** ± 0.0	**0.1** ± 0.0	**0.1** ± 0.0	**0.2** ± 0.1	**4.8** ± 0.2	**19** ± 0.5
St-ER78 Grotta di Ernesto (n=1)	Particulate	**0.4** ± 0.3	0.0± 0.1	0.0± 0.0	**0.2** ± 0.2	0.0± 1.3	0.0± 0.0	0.0± 0.0	0.0± 0.0	-	0.0± 0.0	0.0± 0.0	**0.3** ± 0.4	0.0± 0.8
	Coarse	**0.8** ± 0.3	**0.1** ± 0.1	0.0± 0.0	**0.2** ± 0.1	**2.3** ± 1.2	0.0± 0.0	0.0± 0.0	0.0± 0.0	-	0.0± 0.0	0.0± 0.0	**0.3** ± 0.3	**1.1** ± 0.2
	Fine	**0.5** ± 0.6	0.0± 0.1	0.0± 0.0	0.0± 0.1	0.0± 1.9	0.0± 0.0	0.0± 0.0	0.0± 0.0	-	0.0± 0.0	0.0± 0.0	**0.8** ± 0.2	0.0± 0.5
	ND	**2.1** ± 0.6	**2.1** ± 0.0	**0.4** ± 0.0	**5.3** ± 0.1	**7.7** ± 0.7	**0.6** ± 0.0	**0.1** ± 0.0	**0.1** ± 0.0	-	**0.1** ± 0.0	**0.2** ± 0.0	**6.3** ± 0.2	**17** ± 0.1
	% Coarse		5	7	11	33	21	8	4	7	9	21	5	6
	Coarse Rank		**10**	**7**	**4**	**1**	**3**	**6**	**12**	**8**	5	**2**	**11**	**9**
	% ND		79	92	88	65	78	88	89	78	84	65	93	94
	ND Rank		**8**	**3**	**6**	**11**	**9**	**5**	**4**	**9**	**7**	**10**	**2**	**1**

Table 6.4 Summary organic and trace metal composition of representative sequentially filtered dripwater samples from Lower Balls Green Mine, Grotta di Ernesto and Poole's Cavern. Data are averages of triplicate analyses of sequentially filtered dripwater samples. Nd = not determinable. Remaining data in Table S5 (Appendix II). ND = nominally dissolved.

Four representative drip points were chosen and the samples with the lowest recorded OC concentrations were selected. For the purposes of the modelling exercise all OC in the sample was presumed to be colloidal humic acid (HA) and the range of metals were reduced down to the most ubiquitous species Al(III), Cr(III), Fe(II), Co(II), Ni(II), Cu(II) and Zn(II) (Fig. 6.4). Inorganic colloidal phases were not included because during most of the monitoring, Fe and Mn were below detection limits (0.5 μg L^{-1} and 0.2 μg L^{-1}, respectively) and colloid characterisation by TEM-X-EDS did not identify abundant inorganic colloids in the studied samples (Appendix VI).

As shown elsewhere (Unsworth *et al*., 2006), estimations of HA-metal binding between the models were quite variable, but both models predicted that a proportion of each metal would be bound to HA under the given conditions (except where no metal was measured-marked by *; Fig. 6.4). Model predictions were most consistent for Cu(II), the speciation of which was predicted to be dominated by binding to HA. In general, WHAM predicted higher proportions of Al(III) bound to HA, while MINTEQ predicted higher HA binding of Fe, Ni, Co and Zn (Fig. 6.4).

Since the predicted binding of Cu(II) was most uniform between models and across study sites, a direct comparison was made between the concentration of Cu and the other, ubiquitous metals, Co and Ni, in the fractionated cave dripwaters and aqueous soil leachates. The affinity of these metals for functional groups in NOM is considered to be of the order: Cu > Ni > Co, and this is expected to be enhanced at pH 8, with Cu out-

competing other metals for suitable binding sites (Milne *et al*., 2003; Marang *et al*., 2009). This hierarchy of binding affinity is particularly well characterised for purified humic extracts and is considered to be essentially uniform between humic and fulvic acids (Milne *et al*., 2003).

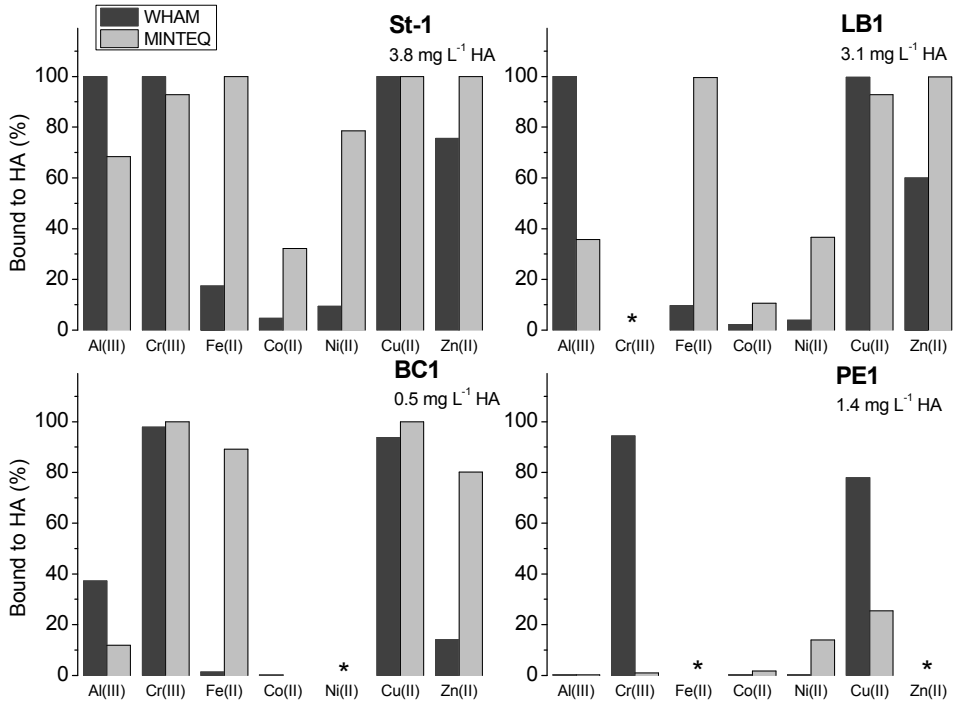

Figure 6.4 Results of equilibrium speciation modelling using WHAM 6.1 and MINTEQ 3.0 based on the simplification that 100% of natural organic matter (NOM) was colloidal humic acid. Samples from four representative drip points were modelled (BC1 and PE1, PC; LB1, LBGM; and St-1, ERN). Samples selected were those with the lowest recorded total organic carbon (TOC) concentration.

Concentrations of Cu, Ni and Co were well-correlated, both in samples from individual drip sites and between study sites (Fig. 6.5a and 6.5b). This consistency in the ratios of Cu:Ni and Cu:Co may indicate a common mechanism driving their changing abundance in dripwaters. Model predictions of Ni and Co binding to HA indicated that only a minor

fraction of the Ni and Co in dripwaters would be complexed with HA (Fig. 6.4). However, it is well documented that uncertainties in model predictions increase for metals with lower binding affinities for NOM (e.g. NICA-Donnan; Groenenberg *et al*., 2010), and that these uncertainties primarily originate from the considerable compositional differences between purified humic extracts used to calibrate equilibrium models (Milne *et al*., 2003) and NOM found in environmental samples (Unsworth *et al*., 2006; Filella, 2008; Groenenberg *et al*., 2010).

Equilibrium binding models rely on our poorly developed understanding of NOM composition and function (Filella, 2008). However, the *relative* binding affinity of metal ions for humic and fulvic acids is better defined (Milne *et al*., 2003). Since metal binding with NOM is governed by a competitive hierarchy of binding affinity (Kinniburgh *et al*., 1999; Marang *et al*., 2009), it is reasonable to expect (assuming that metal is present mainly in complexes with NOM) that the relative abundance of metals will reflect this hierarchy. Total Cu vs. Ni and Cu vs. Co concentrations in dripwaters were consistent with the order of binding strength Cu > Ni > Co (Fig. 6.5a and 6.5b).

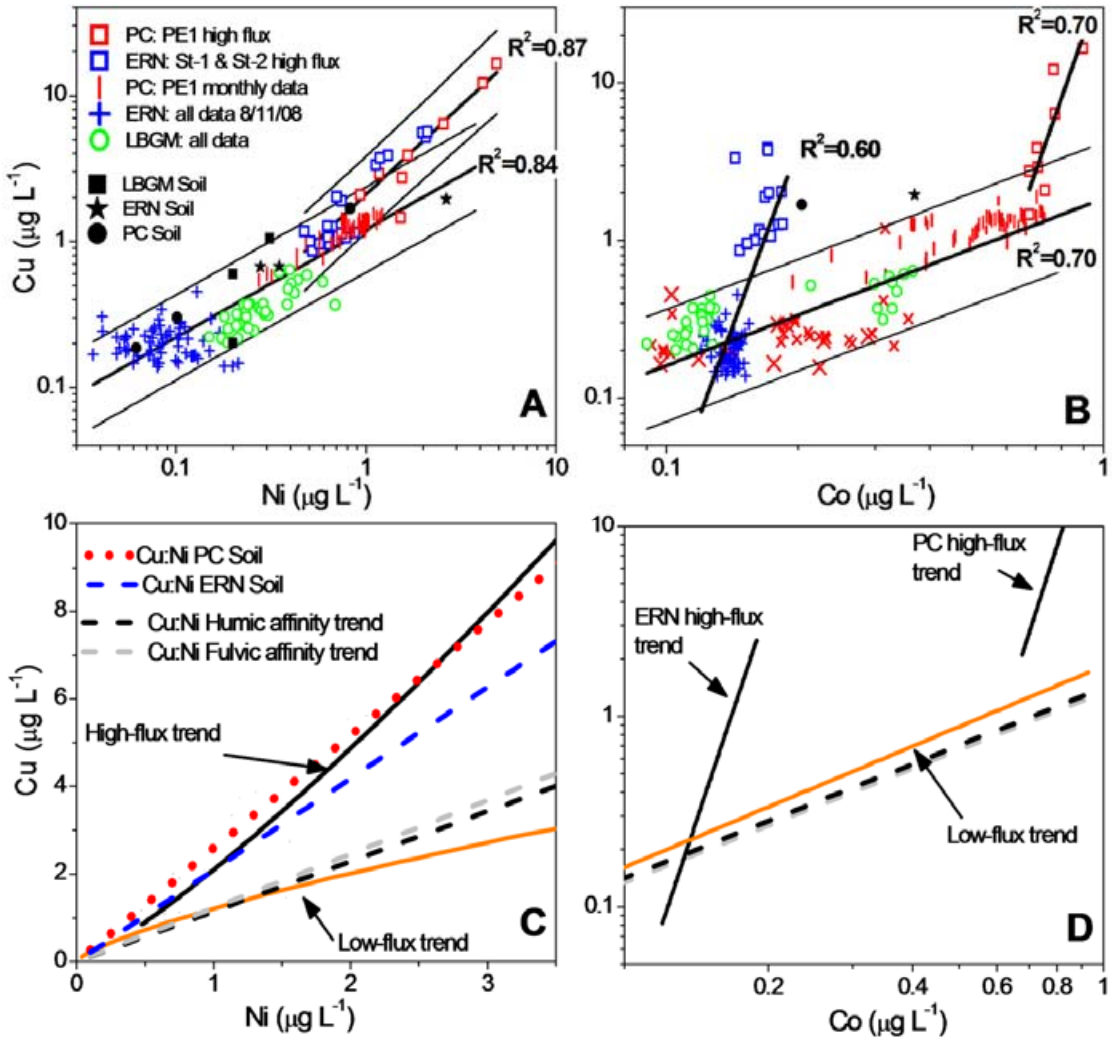

Figure 6.5 Inferred competitive binding of Cu, Ni and Co by humic-like natural organic matter (NOM) and coarse soil organic matter (SOM) in cave dripwaters. Plots show linear regressions of metal concentrations in dripwaters (a) Cu vs. Ni, and (b) Cu vs. Co. Plots in (c) and (d) show predicted metal ratios (c) Cu:Ni, and (d) Cu:Co, based on the equivalent n_1 NICA-Donnan humic and fulvic binding affinity ratio (n_1 values from Milne *et al*., 2003). Plot (c) also shows the equivalent Cu:Ni trend lines calculated using from average Cu:Ni in the Poole's Cavern (PC) and Grotta di Ernesto (ERN) soil leachates. Ratios of Cu to Ni in dripwaters show increased similarity to ratios in soils at times of high organic carbon and trace metal flux, indicative of qualitative changes in NOM composition (i.e., more aromatic/hydrophobic SOM). Thin lines in (A) and (B) are 95% confidence bands from linear regressions.

In Fig. 6.5c and 6.5d, the Cu vs. Ni and Cu vs. Co linear regression trend lines are plotted with the predicted Cu vs. Ni and Cu vs. Co trends derived from the equivalent ratios of n_1 binding affinity parameters for humic acid (HA) and fulvic acid (FA) from the study of Milne *et al*. (2003). The n_1 value is a generic parameter which describes the variation in hydrolysis behaviour of metals as an indicator of their potential for binding to humic substances; it is derived as a function of the formation of the first hydrolysis complex ($MOH^{(z-1)+}$) for a given metal ion (M^{z+}) and does not differ between humic and fulvic acids (Milne *et al*., 2003). Humic and fulvic affinity trend lines were derived by taking the equivalent n_1 ratio, e.g. Co/Cu = 0.71/0.53 = 1.34, and iteratively calculating the proportion of Cu expected for a given amount of Co, i.e. Cu ($\mu g\ L^{-1}$) = Co ($\mu g\ L^{-1}$) x 1.34 (Fig. 6.5d). The advantage of this approach is that it requires no prior knowledge of the proportions of HA/FA in NOM or of the NOM concentration, since the *relative* amount of each metal (which are presumed to be in direct competition for binding sites) is a function of their competitive interaction (binding affinity) which is uniform for metal binding to both HA and FA (Milne *et al*., 2003).

Interestingly, during periods of high infiltration, metal ratios in samples taken from ERN drips St-1 and St-2 and PC drip PE1 showed marked shifts toward higher values of Cu:Ni and Cu:Co. These shifts coincided with elevated TOC concentrations and increases in the concentration of metals (Fe, Al, Ti, and Y) which showed an association with the coarse fraction of soils (Section 6.4.1). During these higher fluxes of NOM and metals, Cu:Ni and Cu:Co departed from the characteristic range for binding to humic and fulvic acids (Fig.

6.5c and 6.5d), but remained well correlated. In particular, Cu:Ni at both ERN and PC were very similar (Fig. 6.5a) and were close to the Cu:Ni measured in the soil leachates from these sites (Fig. 6.5c).

Soil Cu:Ni trend lines were derived in the same way as humic and fulvic affinity lines (see above), but were calculated based on the average Cu:Ni in the PC and ERN soil leachates (Fig. 6.5c). It is clear that Cu:Ni ratios in dripwaters at times of elevated NOM and metal flux show increased similarity to the ratio measured in the soils (Fig. 6.5c). Thus, during periods of high NOM flux, increases in Cu:Ni are argued to reflect changes in the competitive interaction between Cu^{2+} and Ni^{2+} ions, i.e. Cu shows an increased affinity for binding at sites in SOM, compared to Cu vs. Ni binding with humic-like NOM (Fig. 6.5c). This is considered to be indicative of a qualitative change in NOM composition to relative higher aromaticity/hydrophobicity and is consistent with the strongly competitive nature of Cu(II) binding (Marang *et al*., 2009).

6.4.3 Relation between hydrology and NOM-metal transport

In the following section, results of temporal monitoring of NOM and metal concentrations in cave dripwaters are presented. However, because of the large amount of data acquired only those results considered to be of the greatest hydrogeochemical significance are presented and discussed (full dataset in Appendix II).

During the sampling campaigns at ERN and PC, additional non-fractionated samples were taken during the most hydroclimatologically active periods. At ERN, logistical constraints meant that collection and size-fractionation of dripwaters could only be performed at the end of the sampling campaign (to limit the potential for aggregation of colloids) and so additional raw dripwater samples were collected from the high discharge drips St-1 and St-2 between 4/11/08 and 7/11/08. At PC, additional unfiltered samples were also taken from drip PE1 on an approximately weekly basis through the period June 2008 to November 2008 in addition to the monthly size-fractionated samples. Thus, the PE1 drip was studied in the greatest detail and is given the most attention here.

6.4.3.1 Lower Balls Green Mine, September 2008-December 2008

The drip waters of LBGM were characterised by very high mean discharges, but quite low coefficients of variation (Table 6.1). An analysis of the discharge-rainfall relationship in drips LB1-3 showed that drip point LB1 was best correlated with antecedent rainfall (Fig. S4a; Appendix VIII). Size fractionated samples were obtained from LBGM drip points in September, October, and November 2008 and analysed for TOC, fluorescence and trace elements. Effective rainfall during the preceding July and August was high, but this was followed by a dry September and wet October and November (Fig. 6.2d). Over this time, the discharge of drip points LB1 and LB2 was higher than at any other time between January 2008 and August 2009, but drip point LB3 showed little variation in response to rainfall (Fig. 6.2).

Between September and December 2008, organic carbon in LBGM dripwaters was most variable in drips LB1 and LB3, fluctuating between 3.06 and 7.40 mg L^{-1}, and 2.50 and 6.40 mg L^{-1}, respectively. Organic carbon (OC) concentration in LB2 dripwater varied in the range 2.70 to 5.60 mg L^{-1} with most OC being present in the particulate (36%) and coarse colloidal (31%) size classes, the remainder being split evenly between the fine (17%) and nominally dissolved fractions (16%). Similarly, OC in LB3 dripwater was found predominantly in the particulate (39%) and coarse colloidal (39%) size range with only 22% in the nominally dissolved size class.

Despite the large proportions of OC in the particulate and coarse colloidal size classes in LB2 and LB3 samples, the transition metals Co, Cu and Ni did not partition into the larger size-classes, being concentrated in the nominally dissolved fraction and showing no temporal variability. In contrast to drips LB2 and LB3, the partitioning of OC and trace metals at LB1 revealed large changes between months (Fig. 6.6). The concentration of organic carbon and metals (Cu, Ni, Co) in the nominally dissolved size class declined steadily between September and November 2008. This decline was matched by an increase in the concentration of OC and Cu, Ni and Co in the coarse colloidal and particulate size classes in the wetter period (Fig. 6.6). In particular, Co and Ni showed strong shifts into the particulate size range in October and November 2008.

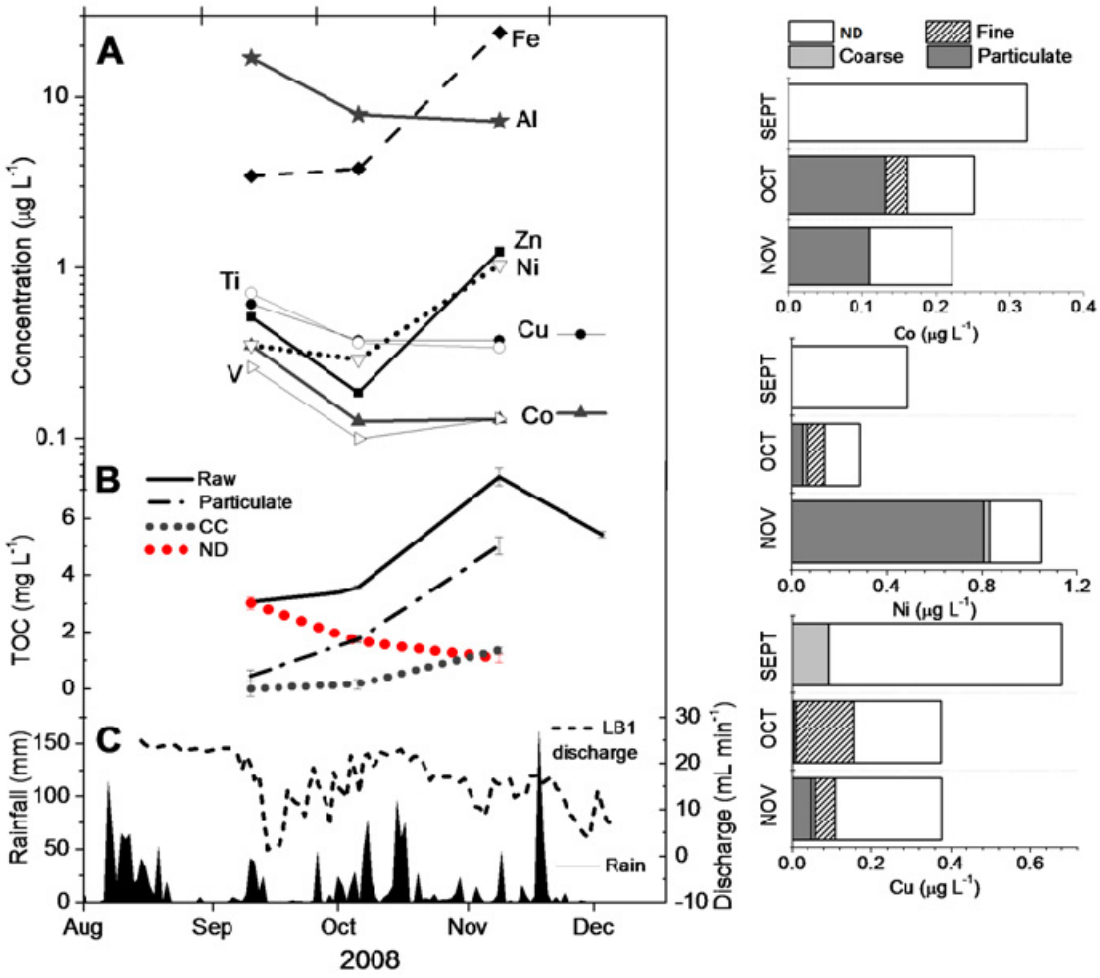

Figure 6.6 Time series of (A) trace metal concentrations in raw samples plotted against Total Organic Carbon (TOC) concentration in colloidal size classes (B) and daily rainfall and drip discharge for Lower Balls Green Mine drip LB1 (C). Stacked bars show metal distribution between colloidal size classes in September, October and November 2008 for the metals Cu, Ni and Co. ND = nominally dissolved.

These changes in metal and NOM partitioning coincided with increases in the concentration of Zn and Fe in November 2008. The proportions of Fe and Zn in each size class could not be determined because of variable release of these metals from filters (Appendix I), but based on the strong tendency of Fe to partition into the coarse size class in soils (Table 6.2),

and the similarity of Zn binding affinity to Cd and Cu (Companys *et al*., 2009; Warnken *et al*., 2007), this arguably represents an increase in metal transport by coarse colloids and particulates. Hence, these results indicate that NOM and trace metals in LB1 dripwater in the nominally dissolved and coarse colloidal/particulate size classes displayed divergent hydrological behaviour in response to increased infiltration and that metal transport by particles occurred preferentially to fine colloids.

6.4.3.2 Grotta di Ernesto, 3/11/2008-8/11/2008

Fieldwork was carried out at ERN in both October 2007 and November 2008. The 2007 field campaign was conducted before the first winter rains of that year and raw concentrations of Cu, Al and Mn (2.67, 2.99 and 0.28 μg L^{-1}, respectively (other metals were not measured)) in dripwater samples were substantially lower than in November 2008 (Fig. 6.7). Drip rates, pH and electrical conductivity (EC) values at Grotta di Ernesto were monitored on a daily basis over the period 4/11/08–8/11/08. The first heavy rainfalls of the winter occurred on 28/10/08 and were followed by a larger storm lasting from 1/11/08-4/11/08 (Fig. 6.7d). Variations in drip rate, EC and pH were consistent with discharge of stored waters and mixing (dilution) with lower EC rainwater in the days following the peak rainfall event (Tooth & Fairchild, 2003) (Fig. 6.7b). The response was quickest in drip points St-1 and St-2, consistent with the greater proportion of fracture-fed flow in these drips (Miorandi *et al.*, 2010). Drip points St-ER78 and St-ER77 were slower to respond,

signifying a piston-flow (or, pressure pulse) response characteristic of the flow-routing of these drips (Miorandi *et al.*, 2010).

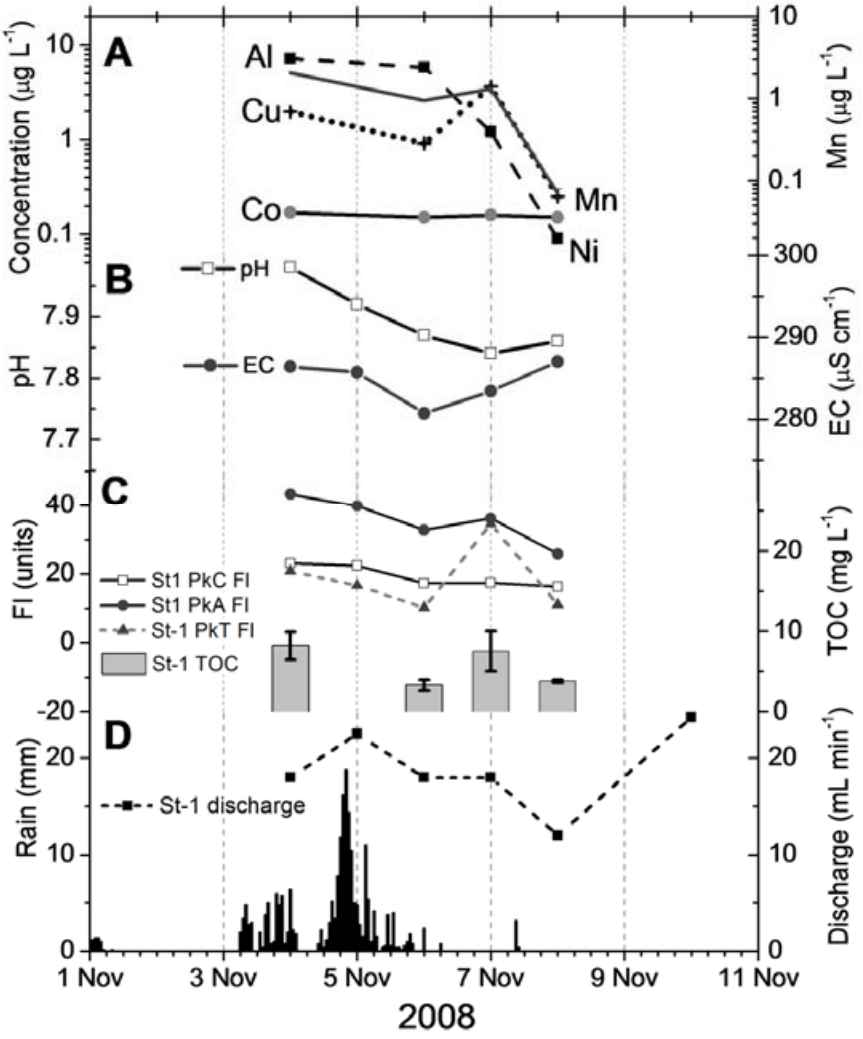

Figure 6.7 Time series of Grotta di Ernesto drip St-1 from fieldwork conducted in November 2008. Plot (a) elemental concentrations in raw samples, (b) variations in pH and electroconductivity, (c) Total Organic Carbon (TOC) concentration and fluorescence intensities and (d) daily rainfall and drip discharge. PkC FI = Peak C fluorescence intensity (excitation 300–350 nm; emission 400–460 nm); PkA FI = Peak A fluorescence intensity (excitation 230-260 nm; emission 400-460 nm); PkT FI = Peak T fluorescence intensity (excitation 220–235 nm; emission 330–370 nm).

In Fig. 6.7 the concentrations of trace metals (Al, Mn, Ni, Cu, and Co) and OC in drip St-1 are plotted against rainfall and drip rate variations between 1/11/08-11/11/08. Organic carbon, fluorescence and metals (Al, Mn, Ni, and Cu) in St-1 dripwater peaked in concentration on 4/11/08 and declined thereafter. Higher humic- and fulvic-like fluorescence intensities were also accompanied by transient peaks in tryptophan-like (peak T) fluorescence intensity. Thus, the coincidence of elevated concentrations of transition metals with higher NOM concentrations and fluorescence intensities (which originate mainly from the ca. 1 nm fraction (Chapter 4)) are indicative of simultaneous transmission of particulates, fine colloids and DOM.

6.4.3.3 Poole's Cavern, June 2008- August 2009

The dripwaters of Poole's Cavern were monitored on a monthly basis from summer 2008 to summer 2009. Data from the normal-pH drips BC1 and BC2 showed strong co-variation in Co, Ti and V over this period, consistent with correlations between these metals (Co and Ti, R^2= 0.67; Co and V, R^2= 0.69). Organic carbon and trace metals (Co, Ti and V) in BC1-2 samples fluctuated in the range of 1-4 mg L^{-1} and 0.1-1 μg L^{-1}, respectively. As found in LBGM drips LB2 and LB3, a greater proportion of NOM was present in the particulate size class during the wetter months, but no pronounced differences in trace metal partitioning between size classes were observed between seasons.

Analysis of variance of the elemental composition of size-fractionated BC1 and BC2 samples found no statistically significant difference at the 0.05 level (ANOVA, Bonferroni test) between August-December 2008 compared to January-August 2009. Indeed, the distribution of V, Co and Ti between size classes in BC1-2 samples was remarkably consistent. All three metals were predominantly associated with the nominally dissolved size class (V ca. 75%, Ti ca. 87-95% and Co ca. 81-83%) with small proportions associated with the fine colloidal and coarse fractions. Size-based partitioning of Co, Ti and V in the alkaline drips BC1-2 was substantially similar to that found in the hyperalkaline dripwater PE1, possibly pointing to their common complexation by NOM in the nominally dissolved size class.

Of all the dripwaters studied, those of hyperalkaline drip point PE1 were studied in the greatest detail. As discussed in Fairchild and Hartland (2010), competitive binding of Cu and Ni > Co at high pH values (pH 9-13) in PC dripwaters is reflected in elevated metal:OC compared to lower pH drips (e.g. BC1-2); Cu:OC and Ni:OC increase from ca. 0.1 to 1.5 ‰ at between pH 8 and 12 at this site (Fairchild and Hartland, 2010).

Detailed characterisation of colloids and particles in PE1 dripwater sampled in June 2009 showed that globular organic colloids with diameters between ca.1-4 nm were the most abundant colloid class, and NOM in this size range was shown to fluoresce strongly at 320 nm excitation, characteristic of humic-like compounds (Chapter 5). Furthermore, the fluorescence signal in PC dripwater samples is strongest in the nominally dissolved fraction, supporting the interpretation that the smallest fulvic-like colloids readily

penetrated the 1 kDa ultrafilter membrane (Chapter 4). In Fig. 6.8, the concentration and fluorescence attributes of NOM in size-fractionated PE1 samples are plotted against variations in rainfall and effective precipitation over the study period.

During peak effective rainfall in August and September 2008, organic carbon concentration in raw PE1 samples was substantially elevated (Fig. 6.8d) but because of colloidal and particulate inner-filtering (Chapter 4), fluorescence was not similarly elevated in raw samples (Fig. 6.8a-b). Peak C emission wavelengths were also substantially altered following filtration, consistent with disruption of peak C fluorescence by the coarse fraction. The mean peak C emission wavelength in fractionated samples is given (Fig. 6.8c) as an indicative measure of NOM composition since peak C emission wavelength is correlated with aromaticity/hydrophobicity (Senesi *et al.*, 1991a; Baker *et al.*, 2008). Thus, the data indicate that NOM in PE1 dripwater during August-October 2008 was relatively more aromatic/hydrophobic than in later months.

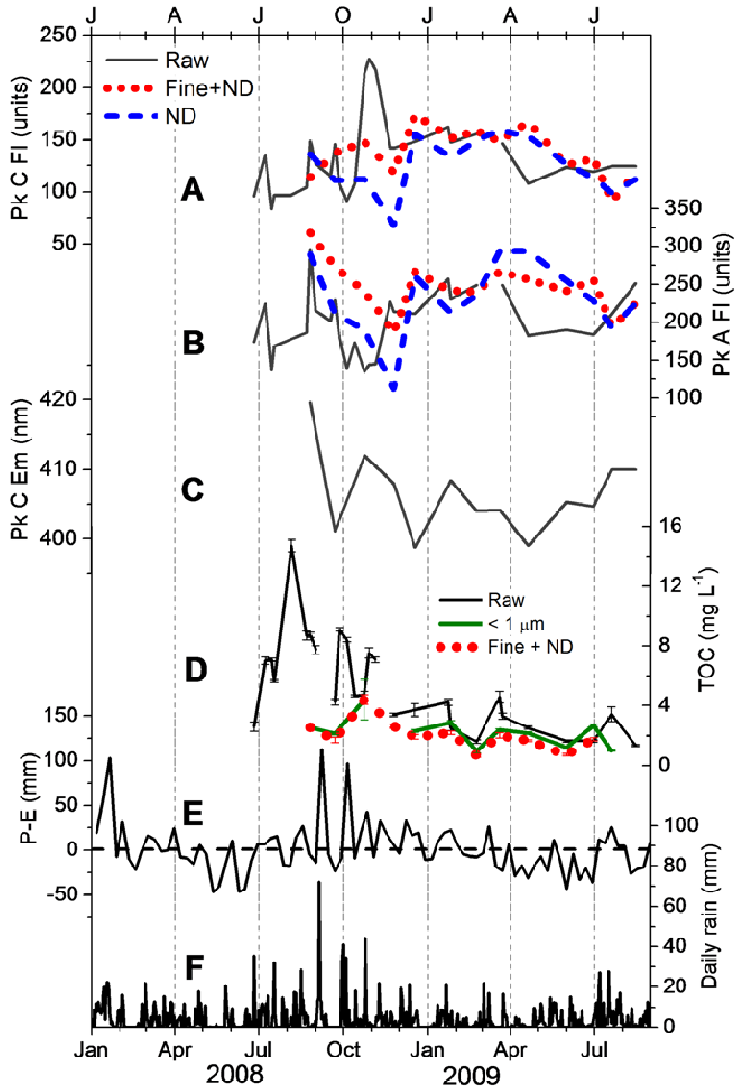

Figure 6.8 Time series of NOM fluorescence attributes and organic carbon concentrations in size-fractionated PE1 dripwater samples collected between June 2008 and August 2009. FI= Fluorescence Intensity (Raman-corrected), EM= Emission Wavelength, TOC= Total Organic Carbon, P-E= actual Precipitation minus Estimated precipitation (Penman).

Relative to the changes in TOC concentration, fluorescence intensities in the fine and nominally dissolved size range were slower to increase following infiltration events, only increasing as particulate TOC concentration, and peak C emission wavelengths declined (Fig. 6.8). In Fig. 6.9, the concentration of trace metals in raw samples, fine and nominally

dissolved size classes is shown. Concentrations of Ti, Fe, Ni and Cu, as well as Mn and Zn in raw samples were markedly elevated in the period July-November 2008 (Fig. 6.9c-g) and showed three distinct spikes in concentration. The concentration of Cu, Ni and Ti in the fine and nominally dissolved size classes meanwhile was essentially unaltered, indicating that Cu, Ni and Ti were mobilised in association with particulate NOM. This inference is supported by higher Cu:Ni in these samples (Fig. 6.5a and 6.5c), consistent with transmission of highly aromatic, coarse, soil organic matter (SOM). Increases in the concentration of Zn, and the transient presence of Mn and Fe in PE1 dripwater, provide further evidence for the ephemeral transmission of particulate SOM in pulses in response to peaks and troughs in effective precipitation (Fig. 6.9d and 6.9g).

Strongly contrasting with the behaviour of Cu, Ni, Ti, Zn, Mn and Fe, the concentration of Co was largely unchanged during the period of high NOM and trace metal flux, whilst marked depletions in V occurred antipathetically to spikes in Cu, Ni and Ti (Fig. 6.9a-e). In the following months the concentration of both Co and V slowly declined reaching a minimum between February and April 2009 after which their concentrations gradually increased (Fig. 6.9a-b). This decline was matched by a similar trend in the concentration of Ti, Ni and Cu in the fine and nominally dissolved size classes, although this trend was less pronounced than for Co and V (Fig. 6.9).

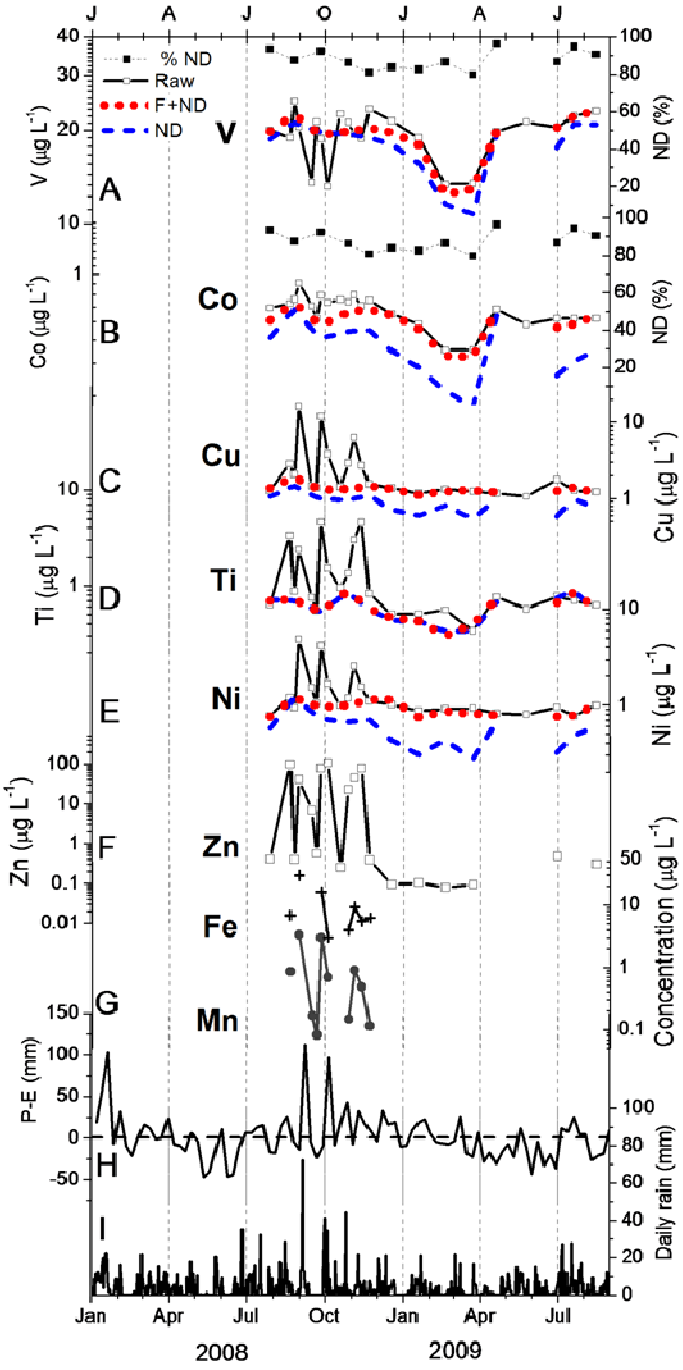

Figure 6.9 Time series of trace metal concentrations in sequentially-filtered PE1 dripwater samples collected between June 2008 and August 2009; (a) V (b) Co (c) Cu (d) Ti (e) Ni (f) Fe & Mn and (g) Zn; (h) weekly effective rainfall (P-E); and (i) daily rainfall. ND = nominally dissolved.

Both Co and V were concentrated in nominally dissolved size fraction (ca. 90% and 80%, respectively) with the remainder residing in the fine colloidal size range (Fig. 6.9a-b). Changes in the concentration of Co and V in both classes occurred synchronously, indicating that changes in the abundance of trace metal carriers in the fine and nominally dissolved size classes were controlled by similar processes. Most probably, this relates to the similar hydrodynamic properties of trace metal carriers in both the nominally dissolved and fine colloidal classes.

6.5 DISCUSSION

6.5.1 High-flux and low-flux, NOM-metal transport in cave dripwaters

The accumulated data indicate that two prominent modes of NOM-facilitated trace metal transport occur in karst percolation waters: high-flux and low-flux. In PE1 dripwater the first mode (high-flux) occurred in rapid, transient pulses in short order following peak infiltration events. Under high-flux conditions, Ti, Fe, Cu and Ni were mobilised by coarse colloids and particulates. Ratios of Cu:Ni between low- and high-flux events were distinctly different, indicating that binding to coarse (ca. >100 nm) SOM by Cu and Ni occurs preferentially, probably because of a higher degree of aromaticity when compared to small, humic-like colloids (Tipping, 2001). The second mode (low-flux) encompassed materials present in the fine colloidal and nominally dissolved size classes and was probably dominated by globular, humic- and fulvic-like colloids with diameters around 1-4 nm (Chapter 5). This is supported by the good agreement between measured Cu:Ni and

Cu:Co at low-flux and the predicted affinity ratios calculated from the equivalent n_1 values for metal binding humic substances (Milne *et al*., 2003).

The low-flux mode was characterised by its own trace element signature, and variously included V, Co and Ti, typically concentrated in the nominally dissolved size class. However, a degree of crossover occurred and some Cu and Ni were also associated with this mode of transport. The extent to which each mode is important appears to vary between sites and drips, probably mediated by flow-routing. In LBGM drips LB2-3 and PC drips BC1-2, large changes in trace metal partitioning between size classes were not detected. Despite substantial proportions of OC being detected in the particulate, coarse colloidal and fine colloidal size ranges, the surface-reactive metals Cu, Ni, and Co were uniformly concentrated in the nominally dissolved size range. Thus, because shifts in the ratio of these metals did not occur in these drips, changes in the size-distribution of NOM did not appear to coincide with changes in NOM composition (i.e. transmission of coarse SOM) and may instead reflect aggregation processes.

In LBGM drip LB1, ERN drips St-1 and St-2 and PC drip point PE1, Al, Ti, Fe, Ni, and Cu, as well as NOM (LB1 and PE1) revealed strong partitioning into the particulate size range during wetter periods. Experimental studies of the hydrodynamic behaviour of particles, colloids and solutes in fractured aquifer systems provide further insight into the results presented.

6.5.2 Hydrologic controls on NOM transmission

At Poole's Cavern, under slow, seepage-flow conditions in PE1 dripwater, fluorescent NOM in the fine and nominally dissolved size range showed an attenuated response to infiltration events. Rather than being transmitted in short pulses with particles, transmission of fine and nominally dissolved NOM was stretched out across several months. But, under fracture-fed flow conditions it is reasonable to suppose that fine organic colloids and DOM are transmitted much more rapidly.

These rationalisations fit within our understanding of the behaviour of artificial colloidal tracers in fractured-rock aquifers under various flow conditions. Most studies conducted to date have employed latex microspheres with diameters between 1 and 5 μm as surrogates for colloids (e.g. McKay *et al.*, 1993; 2000). These studies show that under low-flow conditions, the breakthrough times of particles are faster than solutes (Cl^-, fluorescent dyes), but at high-flow this difference becomes less pronounced (McCarthy and Shevenell, 1998; Goppert and Goldschieder, 2008). Solutes migrate more slowly than small particles and coarse colloids at low-flow because of their tendency to diffuse into pore spaces and micro-fractures (McCarthy and McKay, 2004); and thus, the results of this study indicate that at low-flow, fulvic- and humic-like colloids with diameters between ca. 1-4 nm (Chapter 5) behave similarly to dissolved tracers (e.g. Rhodamine, which has a similar molar mass (ca. 500) to the smallest FA).

These findings have important implications for our understandings of the behaviour of NOM in karst and shed new light on the results of previous studies which show that increases in DOC concentration and fluorescence in cave dripwaters are often offset from rainfall events by several months (Baker *et al.*, 1997a; 2000; Cruz *et al*., 2005). Indeed, variations in fluorescence and DOC often are not related to variations in rainfall (Cruz *et al*., 2005), and where correlations occur, they improve at elevated discharge (Baker *et al*., 1997a; Cruz *et al*., 2005) and in the most responsive drips (Ban *et al*., 2008).

From a survey of the literature it is evident that previous studies of NOM in cave dripwaters have focused on OC concentration below 0.45 μm (i.e., "Dissolved Organic Carbon" (DOC)) and fluorescence (e.g. Baker *et al*., 1997a; Ban *et al*., 2008). However, because of the role of coarse colloids (>100 nm) and particulates (>1 μm) in disruption of fluorescence signals it is not possible to determine whether fluorescence in these studies was disrupted by coarse colloids and particles (Chapter 4). Furthermore, because all materials with a dimension >0.45 μm were traditionally removed, it cannot be determined whether coarse colloidal/particulate NOM (> ca. 100 nm) and fine/nominally dissolved fluorescent NOM (< ca. 100 nm) decoupled as a result of the divergent hydrodynamic properties of each component.

6.5.3 Controls on colloid and particle release from soils

Divergence in hydrological behaviour and the timing of breakthrough in dripwaters between particles and small colloids can be understood in terms of their hydrodynamic properties in fractured-rock aquifers. However, the processes affecting the release of these components from soils must also be considered. Colloids and particles are affected by changes in both solution chemistry and flow (Shevenell & McCarthy, 2002; Sen & Khilar, 2006), but because the distance of separation between fine colloids and pore surfaces may be very small (~10^{-1} nm), both van der Waals (short range) and electrostatic (medium range) forces act more strongly on fine colloids (Rosseau *et al*., 2004).

Physiochemical processes at the interface between soil and aquifer solids and bulk solution are therefore central to understanding colloid retention and release. Small colloids including HA, FA, iron and manganese oxides, bind to soil and aquifer solids, forming films (Hering, 1995; Mayer and Xing, 2001), on which discrete, small colloids (1–5 nm) may be discerned (Gibson *et al*., 2007). Humic substances also form films on mineral colloids such as iron oxides, enhancing their surface charge and enabling their disaggregation and dispersion in solution (Baalousha, 2009).

The surface charge of fine colloids and nanoparticles and whether they have a surface NOM film are dominant controls on their release from surface sites and dispersion into solution. Release is favoured when the energy barrier on detachment is overcome by an

increase in surface charge caused by a change in solution chemistry (Sen and Khilar, 2006) such as a change in the pH or reduction in ionic strength of solution (Rosseau *et al.*, 2004).

Larger particles are more strongly affected by hydrodynamic factors (Kaplan *et al.,* 1993; Shevenell and McCarthy, 2002), but it is generally accepted that under flow rates typical of most natural systems (including karstic springs) hydrodynamic forces are less important than electrostatic adhesive/repulsive forces (Atteia *et al.,* 1998; Sen and Kilhar, 2006). Indeed, mobilisation of small colloids and decreases in pH appear to be correlated (Atteia & Kozel, 1997; Atteia *et al.,* 1998). Thus, changes in soil pH, mediated by biogenic CO_2 production, may lead to enhanced mobilisation of colloids from soils in summer and there is evidence indicating that dripwater DOC and reducing conditions in soils are correlated, allowing for offsets (Cruz *et al*., 2005).

In addition to these factors, it has been shown that colloid release is also affected by initial soil moisture content (Rosseau *et al*., 2004) and the extent of delays between infiltration events (Schelde *et al*., 2002). Particle and colloid release is greatest during initial irrigation (El-Farhan *et al*., 2000), but may be enhanced by delays, allowing replenishment of the colloidal pool in soil water by diffusion (Schelde *et al*., 2002). This makes sense in the context of the PE1 dripwater results, which showed peak NOM mobilised during the first effective rainfall of early summer, and particle-associated trace metals being transmitted in discrete pulses, possibly reflecting the depletion and replenishment of colloids and particles in soil water by wetting and drying processes.

NOM mobilised from soils at peak infiltration may correlate with rainfall intensity and this has been observed in cave waters in monsoonal regions where infiltration exceeds 50 mm d^{-1} (Ban *et al*., 2008). However, despite numerous column studies, the relation between colloid/particle mobilisation and flow remains ambiguous (Sen and Killar, 2006). What is clear is that most mobilisation occurs during the upward and downward limbs of the infiltration hydrograph (El-Farhan *et al*., 2000; Cheng and Saiers, 2010), and larger particles experience the greatest hydrodynamic drag (Sen and Killar, 2006). Thus, particle- or coarse colloid-transported metals (e.g. Fe, Y, REE, Pb) in dripwaters and speleothems may be more likely to correlate with infiltration intensity than metals transported by fine/nominally dissolved NOM.

6.5.4 Implications for the study of trace elements in speleothems

Evidence from speleothems points to NOM-mediated transport of transition metals, e.g. Y, Pb, Zn, Cu (Borsato *et al*., 2007); Pb and Zn (Fairchild *et al*., 2010); and Pb (Jo *et al*., 2010). For example, stalagmite ER78 from Grotta di Ernesto (corresponding to drip St-ER78) is characterised by annual fluorescent laminae which coincide with enrichments in a suite of elements including Y, Cu, Zn and Pb (Borsato *et al*., 2007). Of these elements, Y was most concentrated in the fluorescent zone, rapidly declining in concentration in the zone of growth corresponding to ±2 months (Borsato *et al*., 2007). In the soil samples studied here, Y was distinguished from the other metals because it was present exclusively in the coarse fraction. However, the pattern of Y enrichment in ER78 is similar to that of Cu and Zn, possibly reflecting the fact that effective rainfall at ERN is limited to the

autumn and winter (Borsato *et al*., 2007) and hydrological differences between sites, e.g. greater proportions of fracture-fed flow (ERN) vs. more matrix-flow (PC).

Variations of trace elements that show specific affinities for high-flux or low-flux transport in cave dripwaters may be captured in speleothems and thus may provide information on the timing and magnitude of rainfalls. This is particularly relevant in regions with large extremes in seasonally effective rainfall where particulate NOM and associated metals (e.g. Fe, Y, Th, REE, Pb) may potentially be mobilised by the kinetic energy of flow. For example, Jo *et al*. (2010) demonstrated a strong correlation between $^{210}Pb_{ex}$ (excess, or unsupported ^{210}Pb) in a modern stalactite from Korea and rainfall amount in a region where summer typhoons dominate the annual rainfall distribution. Thus, under suitable conditions the mobilisation and transmission of metals associated with coarse NOM may occur in proportion to the magnitude of infiltration events.

The speciation of specific organic constituents in cave dripwaters is yet to be examined in detail, but it is expected that lipids, DNA, spores, pollen and other materials are mobilised and transmitted in cave dripwaters during high NOM flux. Hence, changes in the ratio of metals (which directly compete for binding sites in NOM, e.g. Cu:Ni) in speleothems may indicate qualitative shifts in NOM composition, potentially aiding in the targeting of compound-specific, and other investigations of the organic fraction of speleothems (Blyth *et al*., 2008).

NOM-facilitated trace metal transport may be of central importance for the incorporation of 'detrital' ^{230}Th, in speleothems (Whitehead *et al*., 1999; Richter *et al*., 2004). Because trace metals display specific binding affinities for NOM in a range of sizes, resulting in a competitive hierarchy of trace element binding, it is reasonable to speculate that a range of other metals including Th may partition in a predictable manner, possibly enabling quantification of the excess 'colloidal' Th in speleothems. Thus, this study of colloid-facilitated trace metal transport points to a potential new dimension in speleothem-based palaeoenvironmental analysis.

6.6 SUMMARY

This study demonstrated for the first time that colloid- and particle-facilitated transport of trace metals occurs commonly in speleothem-forming groundwaters. Competitive binding of metals to NOM in cave waters leads to characteristic shifts in trace metal ratios. Particulate SOM probably contains a larger proportion of high-energy binding sites than small fulvic-like colloids and thus at high particulate SOM flux, shifts to higher Cu:Ni and Cu:Co occur because of the stronger competitive binding of Cu compared to Ni and Co. In contrast, during periods of low NOM flux, humic- and fulvic-like compounds appear to dominate trace metal binding in cave waters with little metal partitioning into coarse colloids and particles, consistent with weaker trace metal binding by aggregates. Under slow-flow conditions the migration of small fluorescent (humic- or fulvic-like) colloids occurs much more slowly than for coarse colloids and particles, possibly leading to the temporally-offset capture of both high-, and low-flux metal transport in speleothems.

7. NOM-METAL COMPLEXES IN A HYPER-ALKALINE STALAGMITE

7.1 INTRODUCTION

Cave systems in humid and temperate climates are typically characterised by a distinct seasonality in both external temperature (affecting ventilation processes) and infiltrating precipitation (affecting hydrogeochemical processes) (Fig. 7.1), and this seasonality is reflected in the chemical, isotopic and optical compositions of speleothems (Fairchild *et al.* 2001; Frisia *et al.* 2005; Tan *et al.* 2006; Baker *et al.* 2008; Frisia *et al*., 2011). The role of infiltrating precipitation in affecting speleothem trace element chemistry has been a recent focus of research (Borsato *et al*., 2007; Fairchild *et al.*, 2010) and is of particular interest because of the potential for metals transported by colloidal or particulate NOM to encode information on rainfall amount (Jo *et al*,. 2010). However, no information is currently available on the extent to which NOM-metal complexes partition between solution and speleothem.

Indicative data on metal partitioning into speleothems suggests that heavy metals (e.g. Y, Cu, Zn, Pb) behave differently to hydrolysing alkaline earth metals (e.g. Sr, Mg), but that partitioning can be substantially different between metal ions (Fairchild *et al*., 2010) with

similar binding affinities for aquatic NOM (Milne *et al*., 2003). For example, empirical distribution coefficients of <<1 for Cu and Y, and >>1 for Zn and Pb have been calculated between dripwaters and stalagmites from Obir cave, Austrian Alps (Fairchild *et al.*, 2010). One possibility is that such differences in partitioning between solution and speleothem reflect variable kinetics of metal dissociation from complexes with NOM, i.e. Cu and Y being more strongly retained in complexes with aquatic NOM.

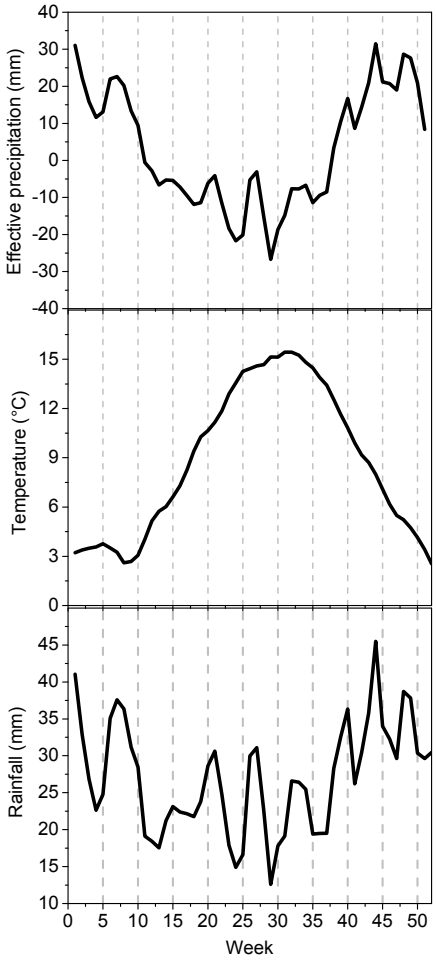

Figure 7.1 Stacked rainfall, air temperature and effective precipitation (rainfall–potential evapotranspiration) for Buxton, UK, over the period 1999–2008. Potential evapotranspiration calculated using the Penman equation. Stacked values have been smoothed using a 5 point fast Fourier transform algorithm.

Experimental data indicate that NOM-complexed metals may be incorporated in speleothems, but not necessarily in conjunction with the colloids or particulates which accelerated their migration to the growth surface. For example, Cu(II) and fulvic acid adsorption on calcite occurs rapidly at mmol Cu(II) concentrations and OC concentrations between 1 and 15 mg L^{-1}, but dissociation and adsorption of Cu(II) onto calcite occurs preferentially over complex formation with surface-adsorbed fulvic acid (Lee *et al.*, 2005). Importantly, surface-adsorbed fulvic acid does not appear to limit Cu(II) uptake

because Cu(II) displays a greater affinity for calcite surface sites in the concentration range examined by Lee *et al*. (2005). Similarly, Pb(II) and Zn(II) also display a strong affinity for calcite surfaces, forming inner-sphere complexes (Zachara *et al.*, 1991; Godelitsas *et al.*, 2003, Chada *et al.*, 2005) that are stable over long timeframes (Elzinga *et al*., 2006). Hence, competitive interactions between metals for binding sites at the calcite surface (following dissociation from NOM ligands) may be an important determinant of the incorporation of colloid-transported metals and other elements in speleothems.

The partitioning of NOM-metal complexes between solution and mineral is a function of the interaction between the aqueous complex and the adsorbed complex at the mineral surface (Fein, 2002). Incorporation of NOM-complexed metals can occur via two mechanisms: Type A (mineral-metal-ligand) and Type B or 'Ternary' (mineral-ligand-metal) complexes. Type B complexes correspond to co-adsorption and thus for aqueous complexes which exclusively form Type B surface complexes, NOM-metal incorporation in the mineral occurs in stoichiometric unity. Hence, for Type B complexes a linear correlation exists between the log stability constant of the ternary surface complex (Eqn. 7.1) and the sum of the log stability constants of the NOM-metal aqueous complex (Eqn. 7.2) and the NOM-surface complex (Eqn. 7.3) (Fein, 2002). It follows therefore that ternary complexation will be favoured for metals which form the most stable aqueous complexes with ligands that also form stable surface complexes with calcite, such as fulvic acids for which adsorption is both rapid and mostly irreversible (Lee *et al*., 2005).

$$(7.1) \quad \equiv SOH^{0}_{(s)} + M^{m+}_{(aq)} + L^{-L}_{(aq)} + H^{+}_{(aq)} \quad \leftrightarrow \quad \equiv S\text{–}L\text{-}M^{(m-L+1)}_{(s)} + H_2O_{(aq)}$$

$$(7.2) \quad \equiv SOH^{0}_{(aq)} + L^{-L}_{(aq)} + H^{+}_{(aq)} \quad \leftrightarrow \quad \equiv S\text{-}L^{(1-L)}_{(s)} + H_2O_{(aq)}$$

$$(7.3) \quad M^{m+}_{(aq)} + L^{-L}_{(aq)} \leftrightarrow ML^{(m-L)}_{(aq)}$$

where ≡ *S* represents a generic, crystalographically bound metal cation, *S*, at the surface-water interface, M^{m+} represents the metal cation, and L^{-L} represents the fully deprotonated organic acid anion.

Additional complexities inevitably arise for minerals formed in caves and other natural systems because of the heterogeneous speciation and size distribution of aqueous NOM and metals (Lead and Wilkinson, 2006). One major consideration is the variability in NOM-metal transport in caves that arises from the interaction between infiltration, flow routing, and the hydrodynamic properties of the fine and coarse NOM fractions (Chapter 6). As shown in Chapter 6, competitive binding of metals for sites in NOM gives rise to characteristic metal partitioning between NOM classes. Metal distributions in the coarse fraction of soils (>100 nm) displayed a clear hierarchy of concentration dominated by metals with high ionic potentials (Al, Cr, Y, Fe, Mn), whereas the divalent transition metals (Cu, Ni and Co) had an intermediate distribution, partitioning into both coarse and fine (1 – 100 nm) colloidal fractions of soils. Data from size-fractionated PE1 dripwater samples demonstrated that Cu, Ni and Co also bind with NOM in the fine and nominally dissolved (ca. ≤1 nm) size range. Monitoring of PE1 dripwaters indicated that the divergent hydrodynamic behaviour of the different NOM-metal species in seepage-flow dripwater (i.e. particulates vs. fine and nominally dissolved NOM) result in different breakthrough

times following peak infiltration events. Preferential transport of particulates and associated metals (Fe, Mn, Cu, Ni and Zn) occurred much more rapidly than for Co and V, presumably because fine (< ca. 100 nm) and nominally dissolved NOM (≤ ca. 1 nm) is much slower to migrate through the porous matrix than coarse colloids (> ca. 100 nm) and particulates (> ca. 1 μm) (Chapter 6).

Furthermore, each metal NOM-metal complex has different dissociation kinetics (Chapter 5) and thus incorporation in speleothem calcite will be a function of:

1) The size and composition (i.e. hydrophilicity/hydrophobicity) of the NOM ligand, affecting adsorption and stability at the calcite surface;
2) The lability (i.e. exchangeability) of the complexed metal and its binding affinity for the calcite surface;
3) The concentration of aqueous complexes.

In PE1 dripwater analysed in June 2009 and July 2010 the most stable (least labile) complexes were formed by Co, which was predominantly bound to the finest, fulvic-like fraction of NOM (Chapters 5 and 6). DGT depletion experiments demonstrated that Co was essentially inert, being retained in aqueous complexes. Thus, Co is the least complicated element in this system because it was transported exclusively by fine/ nominally dissolved fulvic-like NOM (Chapter 6) and was shown to be essentially non-exchangeable over the timescales involved in speleothem deposition (Chapter 5).

We currently lack the detailed understanding of calcite surfaces and the adsorption/desorption mechanisms for NOM-metal species in cave dripwaters needed to properly model surface complexation reactions in speleothems. However, initial data is available on NOM speciation and the relative strength of NOM-metal binding in dripwaters from drip PE1 (Chapter 5). In the following chapter the extent of NOM-metal partitioning between PE1 dripwater and daughter stalagmite PC-08-1 is examined. This study seeks to make the first quantitative connection between the organic and inorganic compositions of speleothems and thus determine the potential for speleothems to quantitatively encode fluctuations in NOM-facilitated trace metal transport in groundwaters.

7.2 MATERIALS AND METHODS

7.2.1 Study site

The data for this study were obtained from samples collected from Poole's Cavern (53°12′N 1°56′W), near Buxton, UK. The cave is described in detail in Chapter 3 and the geochemical composition of monitored dripwaters is given in Table 4.2. Data from the PE1 drip point are compared here to trace element and total organic carbon (TOC) data from the PC-08-1 stalagmite (re-growth of PC-97-1; Fig. 3.10 (Baker *et al.*, 1999c)).

7.2.2 PC-08-1 stalagmite

The PC-08-1 stalagmite (Fig. 7.2a) is a hyperalkaline speleothem which grew during the period 1997 to June 2008. The stalagmite was sampled in June 2008 and sectioned using distilled water without additional lubricants. The sectioned sample was then polished and cleaned by ultrasonication in methanol and deionised water to remove contaminants (Fig. 7.2b).

In PC-08-1, nine pale/dark lamina couplets were discernable comprising the period 1999 to 2008 (Fig. 7.2b). Some disruption of growth may have occurred during early growth (1997-1999) because of regular sampling by previous workers (Hartland *et al*., 2010a). At the time of collection (June 2008) the newly-deposited fabric was pale, porous calcite, overlying a darker, dense band, thus confirming that pale laminae in the sample correspond to summer growth and darker laminae correspond to winter growth. The boundary between pale and dark layers is not a sharp feature, however, and there is considerable lateral variation in lamina colour. Thus, the designation of layer colour is somewhat uncertain, although petrographic seasonality between pale porous calcite and dark dense calcite is obvious (Fig. 7.2b-c).

From measurement of the thickness of successive lamina couplets the average growth rate is estimated at ca. 4 mm yr^{-1}. Average pH and EC values measured in collected PE1 dripwater between June 2008 and August 2009 were 11.7 ± 0.4 and 0.7 ± 0.24 mS cm^{-1},

respectively. Above a pH of around 9, the mechanism of carbonate precipitation is overturned and gaseous CO_2 becomes a reactant, driving precipitation at an accelerated rate. The estimated annual growth rate of the PC-08-1 stalagmite is comparable to that of the PC-97-1 stalagmite (~5 mm yr^{-1}), which grew under the PE1 drip point between 1927 and 1997 (Baker *et al*., 1999c). However, intra-annual variations in growth rate, potentially driven by changes in drip rate and cave air pCO_2, are of significant importance to the interpretation of the PC-08-1 sample, and this issue is examined in section 7.3.

The fluorescent properties of the PC-97-1 stalagmite and its parent waters were studied by Baker *et al*. (1999c), who identified the occurrence of autumn/winter fluorescence maxima with respect to the humic-like peak C fluorophore. Both the PC-97-1 stalagmite and its re-growth (PC-08-1) are characterised by annual lamina couplets consisting of a porous pale layer and a dense fluorescent layer. Fluorescence in the PC-97-1 stalagmite displayed a marked sinusoidal pattern with 10% of laminae exhibiting a double band structure.

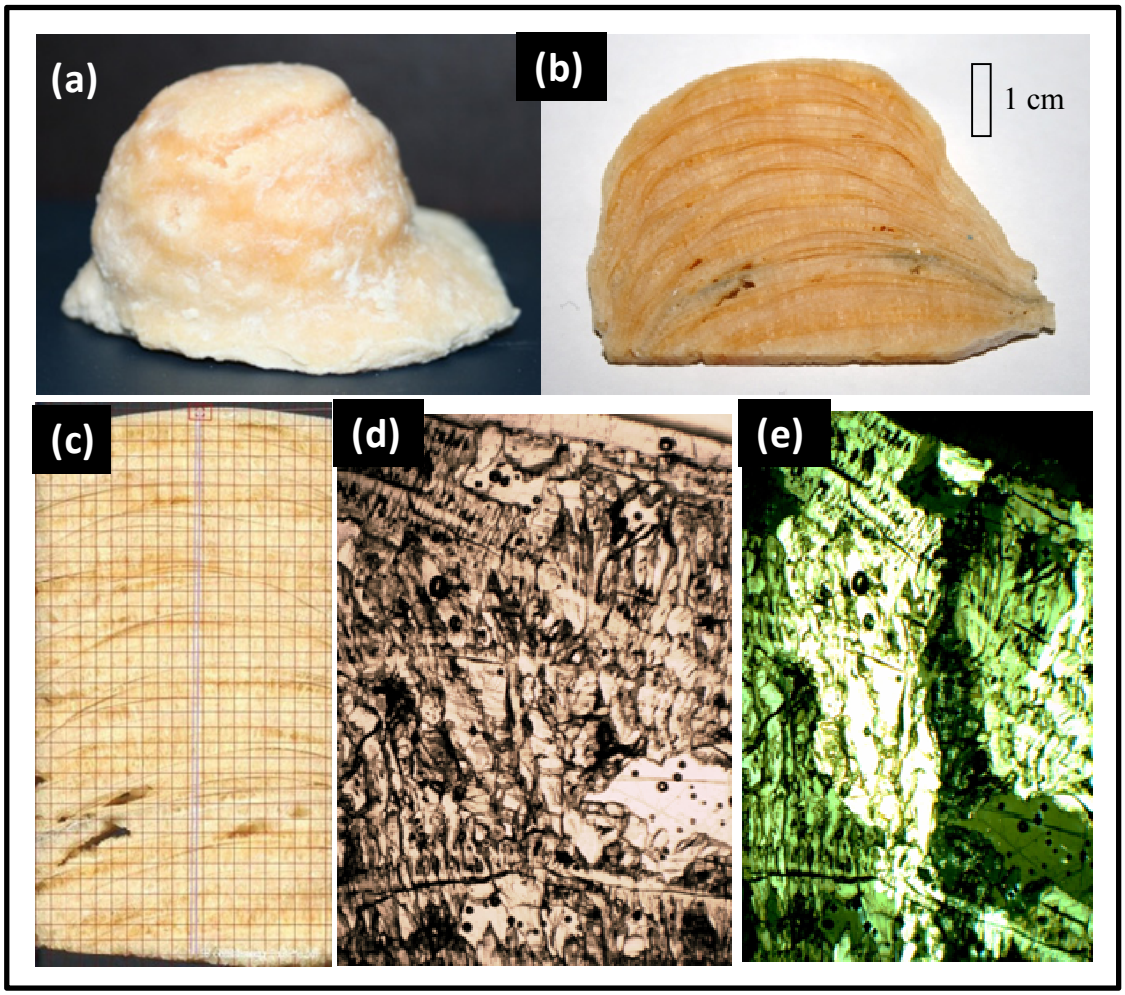

Figure 7.2 Images of the PC-08-1 stalagmite (a) prior to sectioning (b) 5 mm thick polished section showing successive pale and dark layers (c) sample mounted for LA-ICP-MS analysis with position of ablation tracks (300 μm apart) marked (d) microscope image (2.5 x magnification) of PE1 growth fabric under transmitted light and (e) under crossed polarisers showing columnar calcite nucleating in convex arcs which intersect the growth layers (Source d & e: I J Fairchild). At around 10-11 mm from the base of the sample there is a highly porous, detritus-rich zone which appears to correspond to a period of surface disturbance between 2001 and 2002 when drainage ditches were dug above the cave.

Annual lamina couplets in the PC-08-1 sample (formed approximately parallel to the stalagmite growth surface) are intersected by arcs of columnar calcite which are often more

convex than the pale-fluorescent lamina couplets (Figure 7.2c). Although the arcs intersect growth layers their elemental compositions were not found to be divergent from the surrounding fabric.

7.2.3 Chemical analysis of PE1 dripwater and PC-08-1 stalagmite

7.2.3.1 TOC in dripwater and calcite

TOC concentrations were determined using a Shimadzu (Kyoto, Japan) TOC-V, high-temperature combustion analyzer following the non-purgable organic carbon (NPOC) method. All glassware was cleaned by soaking in 10% HNO_3 and deionised water (DIW) and all organic carbon (OC) was removed by combustion at 500°C for 5 hours. Concentrations in size-fractionated dripwater samples were determined by taking the average of between 3 and 8 injections (2 washes, 3 min sparge). Stalagmite powders were obtained using a diamond-tipped hand drill. Samples from alternating pale and dark layers (~100 mg) were dissolved in 1 mL 2 M Ultrapure HCl and diluted 10 times with deionised water prior to analysis using between 3 and 5 injections. Carbonate samples were sparged with O_2 for 5 minutes to remove any residual DIC. Carbonate TOC procedural blanks were also prepared using Aristar $CaCO_3$ and had average TOC contents of 0.02 ± 0.02 mg g^{-1}. Reported values for TOC in the PC-08-1 stalagmite are blank corrected using this value.

7.2.3.2 Trace element composition of the PC-08-1 stalagmite

ICP-MS analysis of dripwaters and PC-08-1 dissolutions was performed at the University of Birmingham on an Agilent quadrupole ICP-MS. Powdered stalagmite samples (ca. 2 mg) were dissolved in 1.6 mL 10% Aristar HNO_3 and then diluted with 6.4 mL DIW (producing a sample matrix of 2% HNO_3 and 100 mg L^{-1} Ca). Calibration standards were matrix matched to 100 mg L^{-1} Ca and 10, 20 and 50 mg L^{-1} check standards were analysed at regular intervals during each run. Isotopes measured were ^{23}Na, ^{24}Mg, ^{27}Al, ^{29}Si, ^{47}Ti, ^{51}V, ^{52}Cr, ^{55}Mn, ^{56}Fe, ^{59}Co, ^{60}Ni, ^{63}Cu, ^{66}Zn, ^{79}Br, ^{88}Sr, ^{89}Y, ^{114}Cd, ^{137}Ba, and ^{208}Pb. Concentrations of Cd and Y in stalagmite dissolutions were below detection limits (<0.2 ug L^{-1}).

Trace metal concentrations in the PC-08-1 stalagmite were also measured in two parallel transects through the sample using Laser Ablation ICP-MS (LA-ICP-MS). Analysis was performed at Royal Holloway University of London on a custom-built excimer 193 nm laser-ablation system with two-volume laser-ablation cell coupled to an Agilent quadrupole ICP-MS (described in detail in Müller *et al.*, 2009). The sample was pre-ablated with two traverses in the growth direction as a cleaning step (96 μm spot, 50 Hz at 500 μm s^{-1}). Laser spot size during acquisition was 76 μm. Traverses were in the direction of growth at a rate of 33 μm s^{-1}.

Quantification of LA-ICP-MS data by external standardisation to USGS NIST-612 standards was compared with concentrations in the stalagmite determined by conventional solution ICP-MS analyses. The elemental concentrations determined by each method were found to vary depending on the element in question. Of the nine elements for which direct comparison was possible, agreement was best for Sr, Ba, Pb, Al and V, whereas Ni, Cu, Zn, Al, and Br determinations by LA-ICP-MS standardisation were generally lower by a factor of around 3.

It was found that concentrations determined by the two methods diverged because of an increase in Ca counts during each ablation transect in the direction of growth (Fig. 7.3). Given that the two transects show good reproducibility and analyses of standards revealed no such variations, the increase in Ca concentration is considered to reflect a reduction in the porosity of PC-08-1 in the direction of growth.

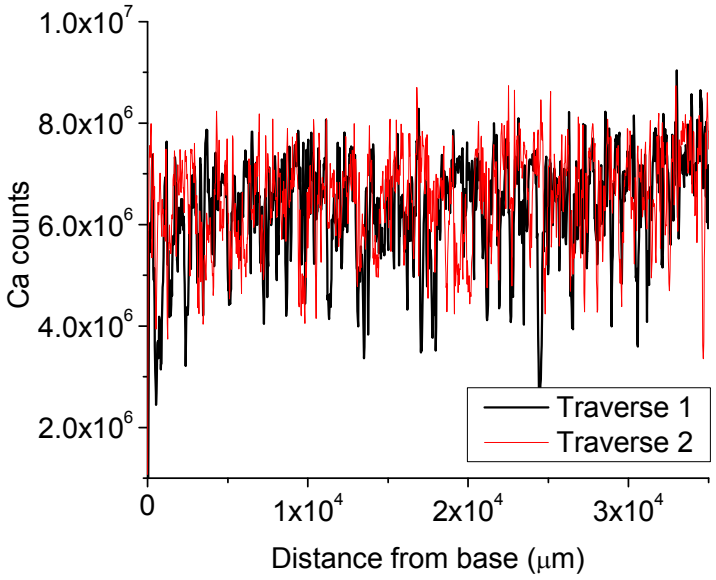

Figure 7.3 Variations in Ca counts in direction of growth in sample PC-08-1 as measured by LA-ICP-MS reflect the variable porosity of the sample. Ca counts in both transects are shown and reveal reasonable reproducibility.

Quantification of LA-ICP-MS data was thus achieved by scaling between known concentrations in PC-08-1 dissolutions and internal standardisation (using an internal reference element *r*). Because the mass of Ca can be considered to be stoichiometrically constant in calcite this was used as the internal reference element *r*. Internal calibration was achieved using the USGS MACS-3 carbonate standard which was ablated once. Average background counts measured at the beginning and the end of each transect were subtracted from the standard and sample counts. The trace element (Tr) to Ca ratio was then corrected using the known ratio in the corresponding layer of stalagmite (Eqn. 7.4). The concentration of each trace element in the speleothem was then calculated by scaling to the known proportion of Ca in $CaCO_3$ (40%).

(7.4) $$\text{Scaling factor} = \frac{\text{Tr}_{cc}}{\text{Ca}_{cc}} / \frac{\text{Tr}_{la}}{\text{Ca}_{la}}$$

Where Tr_{la} and Ca_{la} are the counts of a given trace element and calcium measured by LA-ICP-MS, and Tr_{cc} is the concentration of the trace element in the lamina determined by solution ICP-MS. Ca_{cc} is the concentration of Ca in the sample (40.08%).

7.2.4 Fluorescence analysis of PC-08-1

Dissolution samples of PC-08-1 were analysed using fluorescence EEMs constructed by the standard methods outlined in Chapter 3. Fluorescence intensity in the sectioned PC-08-1 sample was also analysed using a fibre-optic extension (1 mm beam width) mounted on a moving stage (1 mm step) and connected to a Varian Cary Eclipse spectrophotometer (instrument described in Chapter 3). The sample was traversed in the direction of growth along the LA-ICP-MS ablation path and fluorescence intensities were measured at 3 nm increments in excitation wavelength and 2 nm increments in emission wavelength between excitation and emission wavelengths of 300-390 and 314-476 nm, respectively (corresponding to the Peak C fluorescence region). Scanning fluorescence data were obtained by J. Dredge.

7.3 CAVE AIR pCO_2, GROWTH RATE AND ISOTOPE FRACTIONATION

In this section, the results of collaborative work on CO_2 sources in Poole's Cavern cave air and isotopic fractionation in hyperalkaline speleothems is introduced. Interpretation of stable isotope and pCO_2 data was led by I. J. Fairchild and an extended abstract on initial results of this work is given in Hartland *et al.* (2010a). This section draws predominantly upon this interpretation; as will be seen in the following sections, these factors are central to the interpretation of variations in trace elements in the PC-08-1 stalagmite.

It has been previously noted that above pH 9.5, the conventional mechanism of carbonate precipitation is overturned and $CaCO_3$ precipitates via the overall reaction:

$$(7.5) \qquad Ca^{2+}_{(aq)} + CO_{2(g)} + OH^{-}_{(aq)} \rightarrow CaCO_{3(s)} + H^{+}_{(aq)}$$

Because the dissolved carbonate load in hyperalkaline dripwater is typically too low to allow equilibration with respect to pCO_2 of cave air, $CO_{2(g)}$ is sequestered and combines with OH^- via hydroxylation to HCO_3^-, which following the loss of H^+, then combines with Ca^{2+} to form $CaCO_3$.

During the essentially irreversible hydroxylation reaction ($CO_2 + OH^- \rightarrow HCO_3^-$) carbon isotopes are strongly negatively fractionated (depletion in ^{13}C) (Clark *et al.*, 1992); this coupled with the strong isotope depletion of ^{18}O associated with the reactant OH^- (40‰ lighter than water) results in very light oxygen and carbon isotope ratios in hyperalkaline

carbonates. Both $\delta^{13}C$ and $\delta^{18}O$ were found to be much lighter in the pale PC-08-1 laminae (Fig. 7.4). This can be explained by a combination of light CO_2 sources in cave air and strong kinetic fractionation resulting from higher growth rates at high cave air pCO_2. High cave air pCO_2 values (Fig. 7.5) were observed in the summer and autumn (peaking in August) indicating that the (isotopically depleted) pale calcite probably corresponds to faster growth in summer resulting from faster CO_2 ingress into solution (and faster reaction kinetics). It has already been demonstrated that fluorescent OC is most abundant during the winter, when the darker (fluorescent) laminae form. This has yet to be tested by measurement of deposition rates and cave air CO_2 $\delta^{13}C$ values. Preliminary results for calcite deposition rates under the PE1 drip between June and September 2010 indicate that growth rates are highest when cave air pCO_2 concentrations peak.

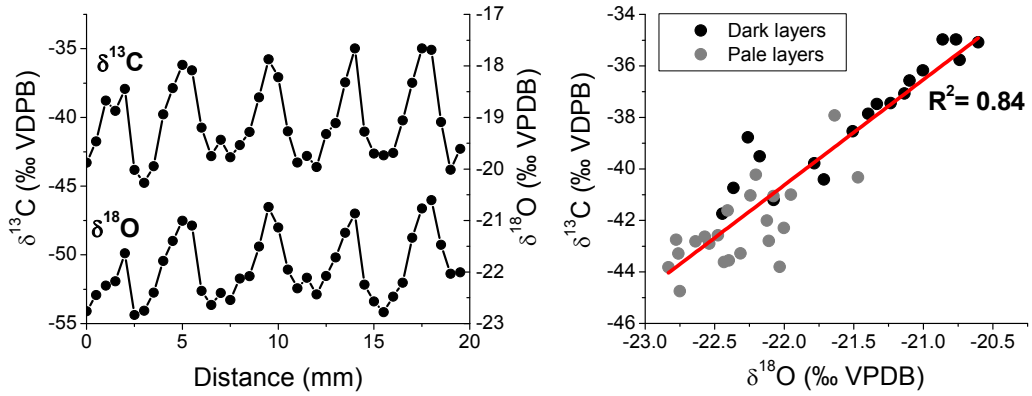

Figure 7.4 Summary of $\delta^{13}C$ and $\delta^{18}O$ ratios in PE1 stalagmite sampled at ~0.5 mm resolution with a diamond-tipped dental drill bit (Data obtained by David Dominguez Villar).

The stable isotopic composition of PC-08-1 is shown in Fig. 7.4. Due to friability and variations in the porosity/density of the sample a certain overlap was expected from

contiguous samples. The petrographic seasonality between pale porous calcite and dark dense calcite is matched by variations in both carbon and oxygen isotopes which are well correlated. Isotopic compositions are heavier in dark layers and lighter in pale porous layers reflecting kinetic fractionation at high extension rates when the pCO_2 of cave air is seasonally high in summer (Fig. 7.5). Uncertainties for stable isotope analyses are 0.04 and 0.13 for $\delta^{18}O$ and $\delta^{13}C$, respectively.

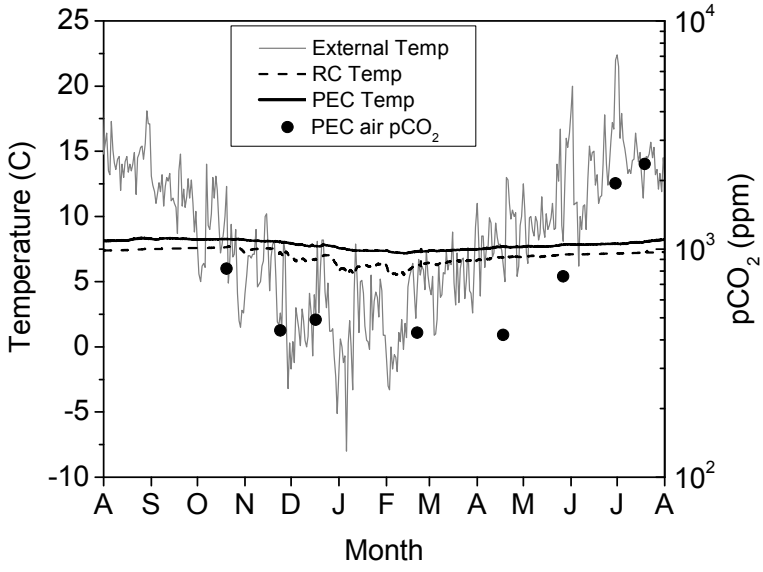

Figure 7.5 Variations in external and within-cave air temperature at Poole's Cavern between August 2008 and August 2009, and cave air pCO_2 values recorded in the Poached Egg chamber using a Vaisala CO_2 meter and probe over the period October 2008 to August 2009.

In Fig. 7.5, variations in external and within-cave air temperature between August 2008 and August 2009 at Poole's Cavern are plotted with cave air pCO_2 values recorded at intervals in the Poached Egg chamber over this period. These data confirm that when external air temperature drops below 7°C external air penetration into the Roman chamber is enhanced,

whereas temperature in the upper, interior part of the cave (Poached Egg chamber) is more stable. In the Poached Egg chamber, air temperature had a small annual range of around 1°C, whereas in the Roman chamber temperatures were in-phase with the exterior but were strongly damped. From November to April, cave air CO_2 concentration in the Poached Egg chamber was between 400-500 ppm- not much greater than atmospheric values (380 ppm). In the summer months CO_2 concentrations were higher, peaking in August. Variations in pCO_2 appear to be largely in phase with external air temperature.

7.4 PC-08-1 CHRONOLOGY

Counting back from June 2008, nine pale/dark lamina couplets are visible corresponding to the period summer/winter 1999/2000 to 2007/2008. Uncertainties relating to intra-annual growth rate variations over this period mean that it is difficult derive a precise chronology. Certain assumptions and simplifications must therefore be made. Because stable isotopes were most strongly kinetically fractionated in pale laminae, the assumption was made that higher growth rates during deposition of pale laminae corresponded to higher cave air pCO_2 values between May and October of each year. This is based on measurements of cave air pCO_2 in the Poached Egg chamber between October 2008 and August 2009 (Fig. 7.5). Variations in PC-08-1 extension rate within pale/dark laminae are not accounted for because of uncertainties in the relation between cave air pCO_2, drip hydrology and extension rate. However, the difference between the extension rate of dark and pale laminae is considered to be most important because intra-lamina $\delta^{13}C$ and $\delta^{18}O$ variability

(reflecting kinetic fractionation) is of a much lower order than inter-lamina variability (Fig. 7.3). This simplification does not allow for variations in drip rate above the baseline of 2-3 drips per minute, mainly because the recorded excursions from the baseline discharge were non-linear and did not coherently relate to variations in infiltration (Chapter 6).

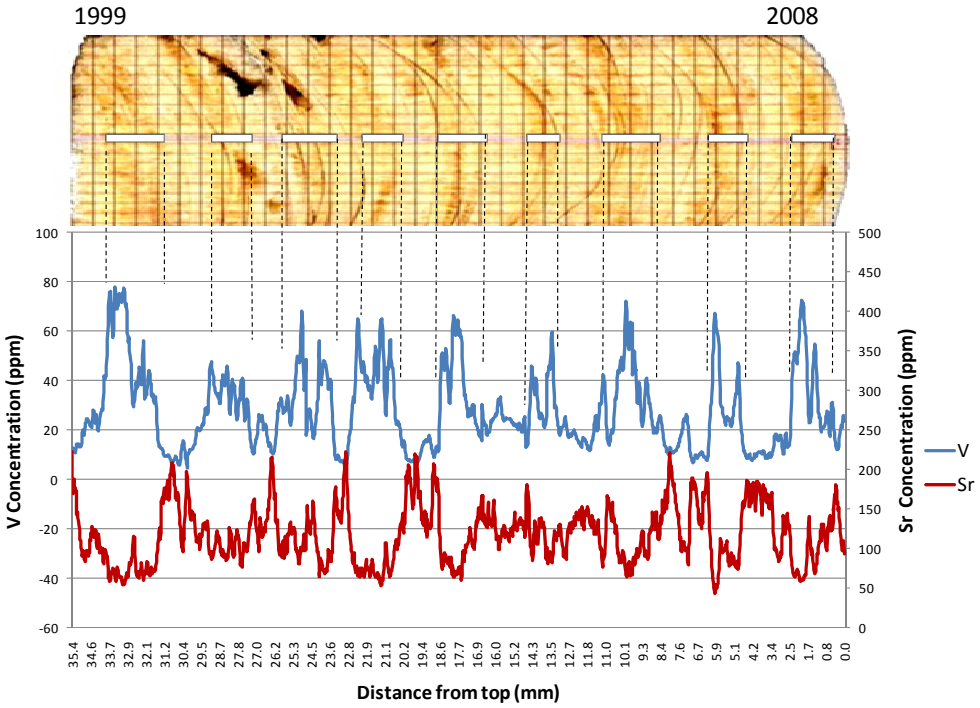

Figure 7.6 Variations in Sr and V concentration in stalagmite PC-08-1 (top) determined by LA-ICP-MS scaled to elemental concentrations in laminae dissolutions. Higher and lower concentrations of V and Sr, are shown to respectively coincide with dark laminae (marked with white rectangles and black dashed lines) in the sample. Because laminae colour was not a reliable measure of the boundary between dark and pale calcite Sr and V concentrations were used to delineate summer (pale) and winter (dark) layers.

Because the boundary between pale and dark layers is not a sharp feature and because there is considerable lateral variation in laminae colour, visual delineation of pale and dark laminae was not considered to be the most reliable approach. Instead, trace element

variations were used to delineate winter growth from summer growth. This was possible because the trace metals V and Co showed distinct antipathetic variance with Sr and Ba. Of these elements, V and Sr showed the clearest association with growth fabric: V being enriched in dark laminae and Sr being enriched in pale laminae (Fig. 7.6). Thus, the boundary between pale and dark laminae was designated as the median V/Sr value in adjacent laminae.

7.5 RESULTS

7.5.1 Partitioning of NOM-metal complexes between solution and speleothem

Contiguous pale and dark laminae in the PC-08-1 sample were drilled and the powders dissolved by dropwise addition of Ultrapure HCl and diluted using deionised water. The dissolution samples were then analysed for TOC, fluorescence, and trace elements. Organic carbon concentrations in PC-08-1 fell within the normal range for cave samples 0-1% by mass (A. Blyth, *pers. comm.*), varying between 0.2 and 1.6 mg g^{-1} of calcite (Fig. 7.7). Organic carbon was most concentrated in pale laminae formed in the years 2005-2008, possibly indicative of a growth rate effect on OC incorporation, or higher NOM concentrations in dripwater, as found in PE1 dripwater in Summer 2008 (Chapter 6).

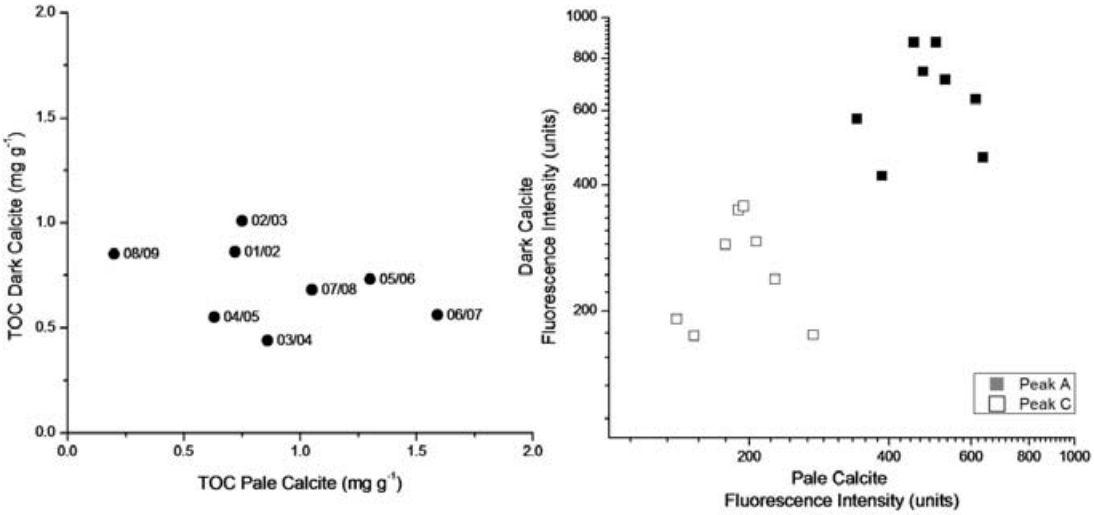

Figure 7.7 Total organic carbon concentrations and fluorescence intensities in contiguous subsamples from pale and dark lamina couplets in the PC-08-1 stalagmite.

Stalagmite fluorescence has been examined by the non-perturbing methods of fluorescence microscopy (Baker *et al*., 1993) and scanning fluorescence spectroscopy (Baker *et al*., 1999a), but stalagmite dissolutions have not been previously characterised using fluorescence Emission Excitation Matrices (EEMs). The results of the fluorescence analyses demonstrate that the fluorescent characteristics of NOM released from stalagmite laminae closely resemble the dripwater NOM signal (Fig. 3.1) with no apparent compositional differences evident between laminae (Fig. 7.8).

Fluorescence analysis of laminae dissolutions cannot be quantitatively compared to analyses in dripwaters because of several factors, including their high acidity and high Ca^{2+} and OC concentrations. However, the TOC and fluorescence data (Fig. 7.7) indicate that fluorescence was marginally higher in dark laminae, consistent with stalagmite PC-97-1 (Baker *et al*., 1999c). With respect to several trace elements (e.g. Cu, Ni, Al, Fe, Cr, Pb),

the compositions of dark and pale laminae dissolutions were found to be similar. Although darker layers contained marginally greater concentrations of Cu, Ni, Al and Pb, there was no clear systematic association with fabric type. Contrastingly, darker laminae were characterised by clear enrichments in Co, V and Br, and marked depletion in Sr, and to a lesser extent, Ba (Appendix VII).

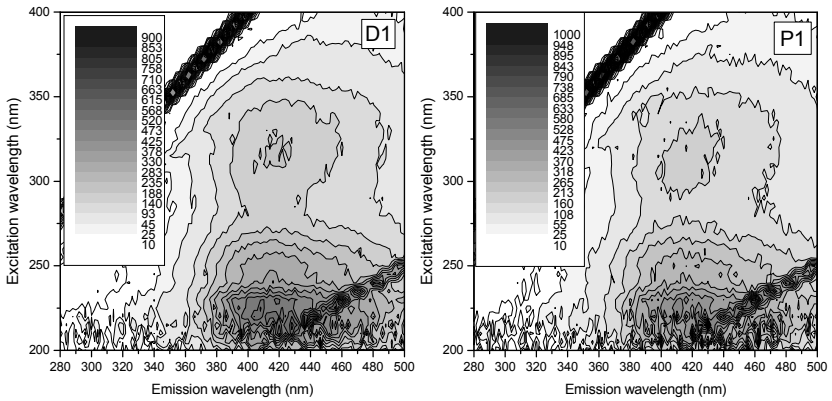

Figure 7.8 Fluorescence EEMs from laminae D1 winter 2007/2008 and P1 spring/summer 2008 and from the PC-08-1 stalagmite. Aliquots were diluted 10x from original dissolution sample.

Partitioning of OC and trace metals between PE1 dripwater and PC-08-1 stalagmite was examined for a suite of metals which have been shown to form aqueous complexes with NOM in PE1 dripwater (Cu, Ni, V, and Co; Chapter 5) and the alkaline earth metals Ba and Sr. Partitioning of trace elements and NOM was assessed by comparing the ratio of trace metals (Tr) to organic carbon (OC) in the stalagmite with that in dripwater samples collected between June 2008 and August 2009 (Fig. 7.9).

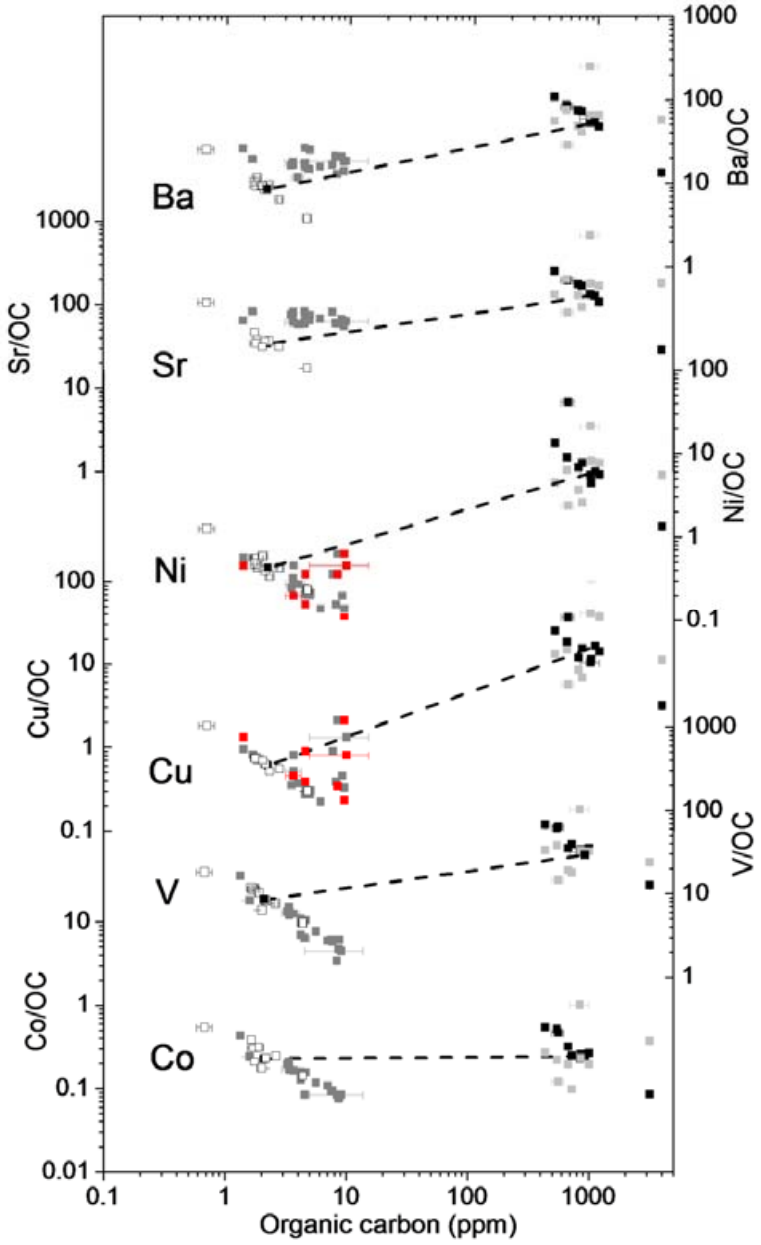

Figure 7.9 Ratios of trace metals (Sr, Ba, Ni, Cu, V and Co) to organic carbon in PE1 dripwater and the PC-08-1 stalagmite. Lines connect points of mean ratio calculated from the average organic carbon to trace metal contents of filtered PE1 dripwater samples (100 nm) and PC-08-1 stalagmite dissolutions (■ = Raw PE1 dripwater, ■ = Raw PE1 dripwater (High Flux), □ = PE1 dripwater <100 nm; ■ = PC-08-1 pale laminae, ■ = PC-08-1 dark laminae).

Cobolt was found to be the least DGT-labile element in PE1 dripwater samples (Chapter 5), and like V, was principally transported by NOM in the nominally dissolved (ca. ≤1 nm) size fraction (Chapter 6). In Fig. 7.9, the Tr/OC ratio vs. OC concentration in PE1 dripwater and PC-08-1 calcite are given. In Table 7.1 the empirical distribution coefficients (K_d) for a range of cations are shown in comparison to experimental values for cation partitioning into calcite from purely inorganic solutions. Distribution coefficients were calculated (Eqn. 2.5) from the average concentrations in PE1 dripwater and PC-08-1, and also from mean concentrations in dripwater between October-March (autumn/winter) and April-September (spring/summer) and pale and dark calcite, respectively.

Ratios of Co to OC in the dripwater and speleothem were close to unity, providing strong evidence for Type B ternary complex formation by NOM-Co in PC-08-1 (Fig. 7.9 and 7.10). The mean ratio of V to OC in PC-08-1 was around three times the mean dripwater ratio (Fig. 7.9), indicating either Type A complex formation by the more labile metal, or additional incorporation of non-complexed V species (e.g. HVO_4^{2-}, $V_2O_7^{4-}$; Wanty and Goldhaber, 1992), as may occur at defect sites in response to an imbalance in surface charge (Fairchild and Treble, 2009), e.g. arising from surface-adsorbed NOM.

Ratios of Ni:OC and Cu:OC were substantially higher (ca. 10x) in PC-08-1 than in PE1 dripwater (Fig. 7.9). This is indicative of Type A surface complexation by NOM-Cu and NOM-Ni and is consistent with their common speciation and similar lability (Chapter 5). Preferential Type A complexation is also consistent with the high affinity of Cu for binding at the calcite surface (Elzinga *et al*., 2006). Higher K_d values for Cu and Ni (Table 7.1) may

be related to their more complex speciation compared to Co and V, i.e. lower stability of coarse/particulate NOM surface complexes, relative to those between fulvic-like NOM and calcite. Ratios of Ni/OC and Cu/OC corresponding to high-flux events in PE1 dripwaters are also plotted in Fig. 7.9 (red symbols). The high-flux ratios occupied a similar range to ratios from low-flux periods, indicating that although Cu/Ni increased at high-flux, the ratios of Cu and Ni to OC did not substantially change. This is consistent with the hypothesis that pH is the dominant control on the total concentration of NOM-complexed metals in hyperalkaline dripwaters (Fairchild and Hartland, 2010).

Both Sr and Ba are mainly present as free ions or in ion pairs, e.g. $SrOH_2$ (Chapter 5). Over the timescales involved in speleothem deposition (i.e. minutes to hours) the available proportion of Sr and Ba is much greater than the labile proportion of transition metals (Cu, Ni, Co, V) held in NOM-Tr complexes (Chapter 5). The values of Sr/OC and Ba/OC in PE1 dripwater and PC-08-1 are also given in Fig. 7.9.

Trace metals with valence two are normally considered to substitute for Ca^{2+} lattice sites (Huang & Fairchild, 2001). Most Sr^{2+} and Ba^{2+} partitioning probably occurred via this mechanism, with Type B surface complexation by NOM-Sr and NOM-Ba probably being of negligible importance. This is supported by very high distribution (K_d) coefficients for Sr and Ba between PE1 dripwater and PC-08-1(0.3 and 0.5, respectively) compared to K_{Sr} of between 0.01 and 0.15 for calcite precipitation under karst analogue conditions (Huang and Fairchild, 2001), and higher again than the K_d values derived from other experimental studies (Table 7.1; values given at $\log_{10}$). The extension rate of PC-08-1 (ca. 4 mm yr^{-1})

was around two orders of magnitude greater than is typically encountered for normal speleothem deposition; normal deposition rates are of the order of tens to hundreds of μm yr^{-1} (Baker *et al*., 1998; McDermott *et al*., 1999). Partition coefficients for trace elements converge on 1 at very high growth rates (Lorens, 1981), and K_{Sr} is known to be particularly sensitive to fluctuations in growth rate (Huang & Fairchild, 2001). High values of K_{Ba} and K_{Sr} calculated here are consistent with strong enhancement of Sr and Ba partitioning at high extension rates in PC-08-1 and this accounts for much of the intra-annual variability in Sr and Ba (Table 7.1). These data demonstrate that sufficiently high proportions of Sr and Ba in PE1 dripwater were available as free ions (or in freely exchangeable inorganic complexes) to allow growth rate to be the dominant control on their partitioning behaviour.

In contrast to Sr and Ba, empirical distribution coefficients for transition metals in PC-08-1 (Table 7.1) were uniformly lower than values derived from purely inorganic studies (data compiled by Böttcher & Dietzel, 2010). Values of K_d for the NOM-complexed transition metals (Cu, Ni and Co; Chapter 5) were much lower than experimental values, indicating that kinetic restrictions on dissociation from aqueous complexes with NOM limited the availability of free metal ions for substitution into Ca^{2+} lattice sites. The average partition coefficient for Co was calculated at 0.06 (log K_d -1.00) indicating that on average ca. 6% of NOM-Co adsorbed at the PC-08-1 growth surface and that partitioning of NOM-Co complexes between solution and speleothem occurred consistently throughout the annual cycle (Table 7.1). In summary, the calculated K_d for summer and winter deposition indicate that incorporation of V was slightly enhanced in winter growth, while proportions of Cr and

Zn may have been reduced. These data also indicate that incorporation of Ni and Cu was more efficient in winter growth, $K_d \approx 1$ (Table 7.1), and that Co provides a measure of humic-like NOM adsorption in PC-08-1.

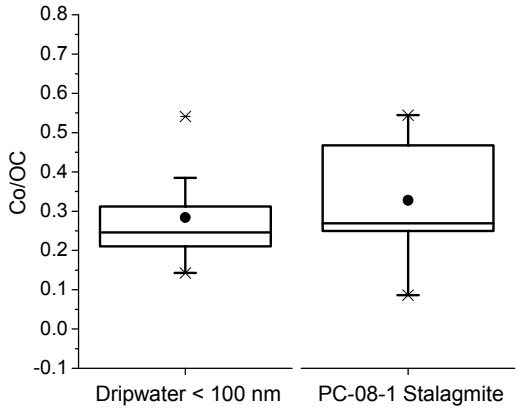

Figure 7.10 Box plot showing the ratios of cobolt (Co) to organic carbon (OC) in 100 nm filtered PE1 dripwater samples and in the PC-08-1 stalagmite. Ratios occupied a similar range in both, dripwater and speleothem, the median and mean values being slightly higher in the stalagmite consistent with minor dissociation of Co complexes during incorporation.

7.5.2 High-flux and low-flux trace element signals in PC-08-1

The association between trace elements in the PC-08-1 stalagmite was investigated using principal components analysis (Fig. 7.11). In Fig. 7.11a, PC1 explains 36% of the variability and separates the low-flux metals (Co and V) and Br, and the alkaline earth metals (Sr and Ba); PC2 explains 20% of the data and separates the high-flux metals (Cu, Zn, Ni) as well as Cr, from the low-flux metals (Co and V) and also separates Al and Pb from both low- and high-flux end-members (Fig. 7.11a). This analysis shows that trace elements in PC-08-1 may be sub-divided into three behavioural classes based on the results

of dripwater monitoring studies: low-flux (Co, V), high-flux (Cu, Zn) and the alkaline earth metals (Sr and Ba); with the low-flux and growth rate dominated (Sr and Ba) components showing strong anti-correlation (Fig. 7.11a).

Cation	Experimentally -derived log K_d	PE1/ PC-08-1 log K_d	Summer/Pale laminae log K_d	Winter/Dark laminae log K_d
Sr	-1.68	-0.49	-0.45	-0.55
Ba	-2.00	-0.31	-0.30	-0.33
Al		-1.72	-1.71	-1.71
V		-0.58	-0.64	-0.51
Cr		-2.00	-1.89	-1.96
Fe	0.57	-0.38	-0.76	-0.12
Co	0.92	-1.22	-1.22	-1.15
Ni	-0.92	-0.19	-0.44	0.00
Cu	1.40	-0.11	-0.21	-0.07
Zn	1.70	-1.10	-0.98	-1.10

Table 7.1 Experimentally-derived trace element calcite partition coefficients (K_d) compiled by Böttcher & Dietzel (2010) and empirical partition coefficients for trace metal incorporation from PE1 dripwater into the PC-08-1 stalagmite. Value for Ni taken from Lakshtanov & Stipp (2007). With the exception of Sr and Ba calculated log K_d for PE1 – PC-08-1 were much smaller than K_d data from purely inorganic experiments.

Principle components analysis was also employed to explore the relationships between metal pairs in PC-08-1 for those metals which show shifts in their ratios between low- and high-flux modes. The ratios of trace metals with the clearest association to the high-flux and low-flux end-members (Fig. 7.11a) established from dripwater monitoring (Chapter 6) were chosen. In Fig. 7.11b, principal component 1 explains 58% of the variability and separates high-flux vs. low-flux (HF/LF) and low-flux vs. high-flux (LF/HF) metal ratios.

Both end-members load equally on PC2 which explains 22% of the data. Thus, variations in the HF/LF metal pairs were well correlated, corroborating the findings from dripwater monitoring.

Data presented in Fig. 7.12 indicate that NOM speciation and competitive binding impact on the partitioning of NOM-metal complexes into calcite. Competitive interactions determine the ratio of metal bound to aqueous NOM in dripwaters (Chapter 6), and this extends to the speleothem growth surface where the most surface-reactive metals (e.g. Cu) partition more strongly than less-reactive metals (e.g. Ni). In Fig. 7.12, cross plots of Cu vs. Ni (Fig 7.12a) and Cu vs. Co (Fig. 7.12b) are shown as exemplars of the typical distribution of high-flux and low-flux metal pairs.

The Cu and Ni data (Fig. 7.12a) from PC-08-1 indicate that humic-like NOM-Cu and NOM-Ni complexes were captured closer to their ratio in dripwater than high-flux complexes. Thus, Type B complex formation by Cu and Ni may occur more readily for aqueous complexes between metals and humic/fulvic compounds, but that Type A complex formation may occur preferentially for particulate SOM-metal aqueous complexes, possibly because SOM forms less-stable surface complexes with calcite than fulvics. However, growth rate effects on the high-flux end-member cannot be ruled out.

Cross-plots of Pb vs. Co and Al vs. Co (Fig. 7.12d-e) indicate both low-flux and high-flux trends- not detected in monitoring studies because of the low Pb concentration (<0.5 μg L^{-}

[1]) and presumably because of the more complex speciation of Al, i.e. present as inorganic complexes (e.g. $Al(OH)_4^-$), insoluble particles and in complexes with NOM (Chapter 5). The Co and V data demonstrate preferential incorporation of V over Co (Fig. 7.12f), consistent with the greater lability of NOM-V (Chapter 5) and probable incorporation of non-complexed V species at times of high NOM-Co co-adsorption (the correlation between V and Co in the stalagmite is stronger than in PE1 water; Fig. 7.9c).

Some of the variation in Br, Sr and Ba can also be linked to greater adsorption of NOM in PC-O8-1. Higher trace element incorporation at defects is a feature of faster crystal growth at high supersaturation (Frisia *et al*., 2000). Bromium incorporation was not higher in summer (pale) growth, possibly indicative that defects in PC-08-1 were relatively more abundant when NOM adsorption was highest. Bromium is weakly correlated with Co in the stalagmite and similarly to V (Fig. 7.9f-g), Br vs. Co show secondary trends possibly consistent with high- and low-flux transport. Although high-flux transport was not considered to be a major vector for V (Chapter 6), the PC-08-1 data reveal features which may be of systematic importance.

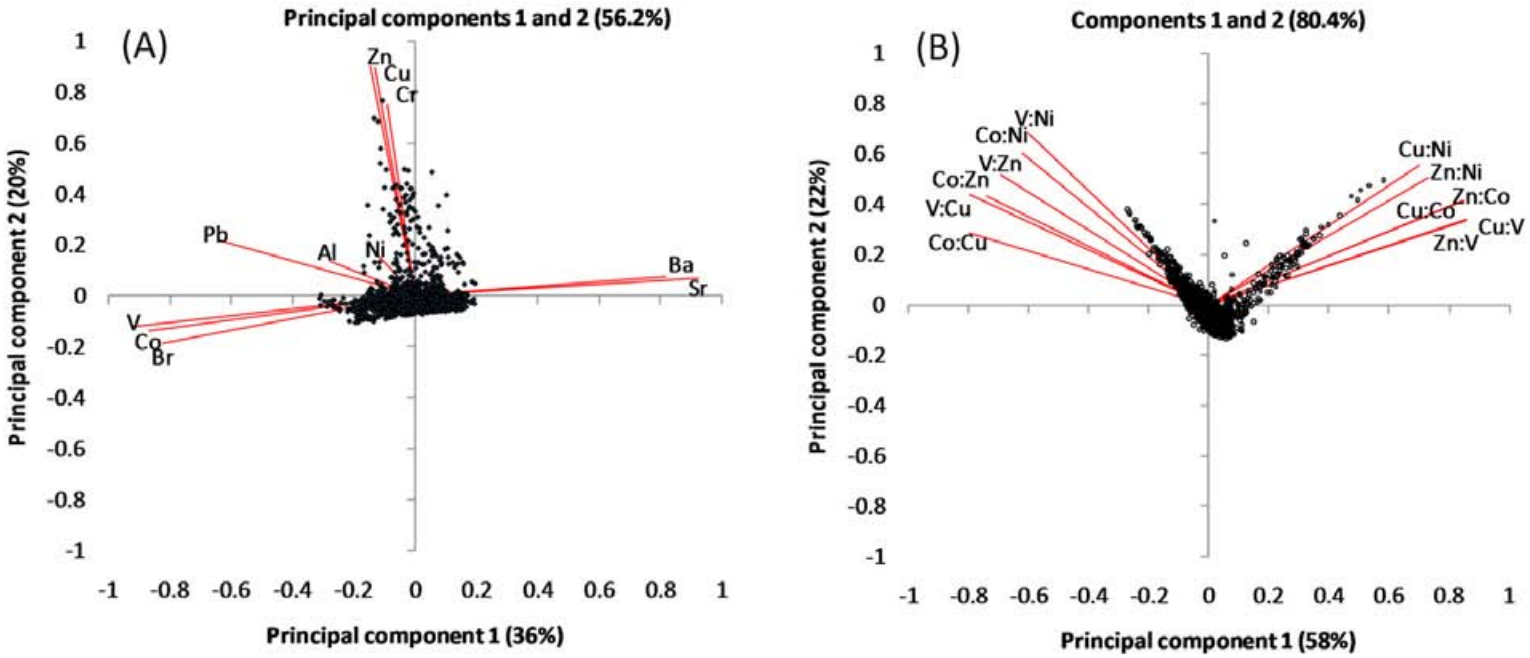

Figure 7.11 (a) Principal components analysis of mean trace metal LA-ICP-MS data acquired from two parallel traverses of the PC-08-1 stalagmite (b) inferred high-flux (right) and low-flux metal pairs (left).

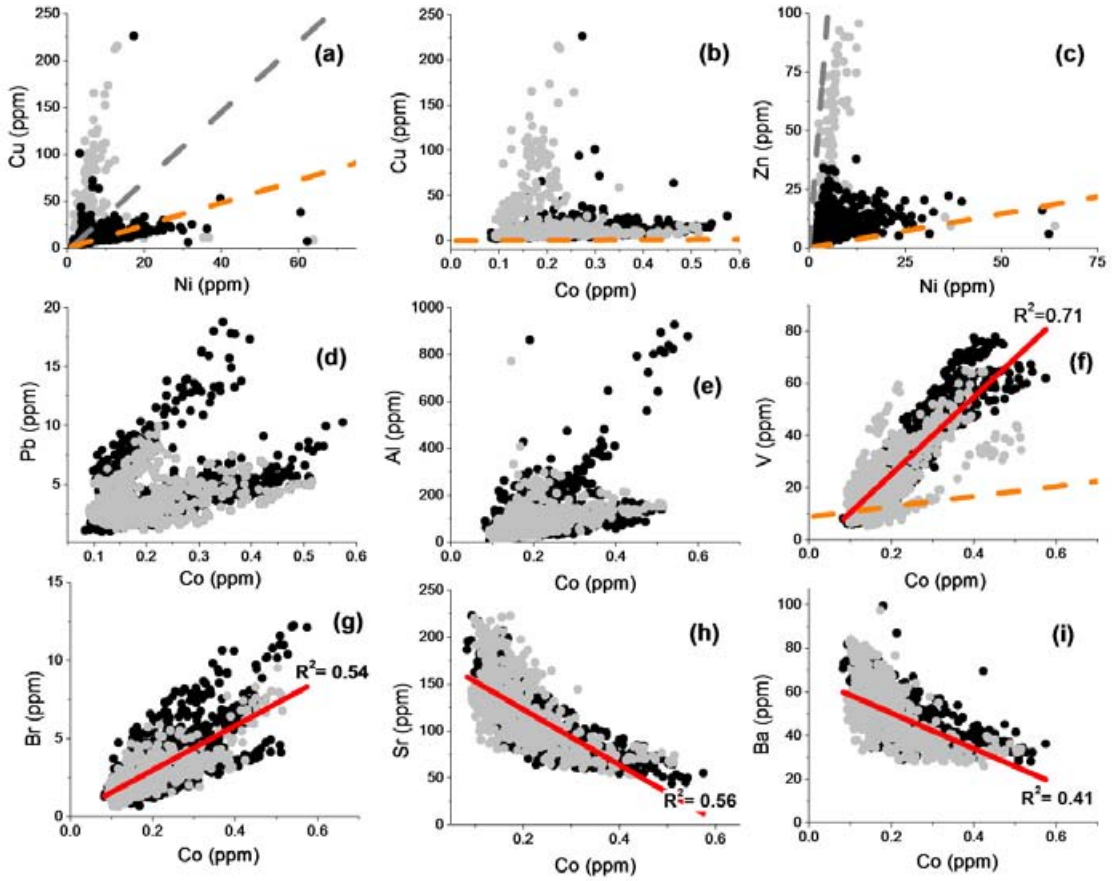

Figure 7.12 Cross plots of (a) Cu vs. Ni, (b) Cu vs. Co and (c) Zn vs. Ni, in the PC-08-1 stalagmite. Metals which directly compete for binding sites in NOM produce characteristic 'L' shaped distributions corresponding to high- and low-flux modes of NOM-metal transport. Cross plots (d) Pb vs. Co, and (e) Al vs. Co, are consistent with both high- and low-flux transport signatures; (f) increased V:Co in PC-08-1 consistent with preferential Type A complex formation by NOM-V complexes. Plots (g-i) show linear regression (solid red) trend-lines and coefficients of determination for Br vs. Co, Sr vs. Co and Ba vs. Co. ● = pale laminae, ● = dark laminae. Dashed lines show trace metal ratio trends in dripwater corresponding to high- (grey dashed line) and low-flux (orange dashed line) NOM-metal transport.

Strontium and barium were the only metals to be anti-correlated with Co, consistent with lower growth rates at peak NOM adsorption (Inskeep & Bloom, 1986). However, other factors including inter-specific competition (Borsato *et al.*, 2007) and

crystallographic effects (Fairchild *et al*., 2010) may also be of importance for Sr and Ba incorporation.

7.5.3 High- and low-flux time series in PC-08-1

In Chapter 6, variations in trace metals associated with divergent modes of NOM transport in PE1 dripwater were shown to behave in hydrologically distinct manners. Those trace metals (Co and V >> Cu and Ni) associated with the fine and nominally dissolved fractions (materials with a dimension <100 nm) showed an attenuated response to effective infiltration, increasing and declining in concentration over several months. This was contrasted with metals associated with particulate SOM (Cu, Zn, Ni, Ti, Mn, Fe) which rapidly migrated to the PE1 drip point in short order (days to weeks) following peak infiltration events. High-flux SOM-metal transport was found to be linked to increases in Cu:Ni and as shown in Section 7.5.2, the trace metal data clearly subdivide into low-flux and high-flux subsets (Fig. 7.11 and Fig. 7.12). Thus, in the following section, trace metal profiles in PC-08-1 are examined according to their mode of transport in dripwater.

High-flux metals in PC-08-1

Data from soil leachates (Chapter 6) indicated that Fe and Mn showed the greatest association with coarse soil fraction and were mobilised only during high-flux events. Because of interference between CaO and Fe at mass 56, Fe was not measured in the PC-08-1 sample by LA-ICP-MS, but Fe concentrations in PC-08-1 powders measured

by solution ICP-MS are given in Figure 7.13. The PC-08-1 trace metal data clearly sub-divide into high-flux (Cu, Zn) and low-flux (Co, V) components and these metal pairs were used to derive an index of high-flux/low-flux transport (HF/LF) which is considered to provide a measure of NOM aromaticity. The metal ratios Cu:Ni, Cu:Co, Zn:Ni and Zn:Co were averaged and then normalized to derive the HF/LF index presented in Fig. 7.13.

Trace metal concentrations are also given for Cu and Mn (Fig. 7.13). The stochastic signal of the transition metals in the PC-08-1 stalagmite is consistent with the rapid, particle-based transmission of these metals observed in PE1 dripwater during monitoring between 2008 and 2009 (Chapter 6). The most prominent feature in the trace metal data is a large peak (composed of several successive peaks) in Cu around the winter of 2001. This peak in Cu coincided with a much higher HF/LF index, consistent with high NOM aromaticity (Fig. 7.13). The peaks in high-flux metals were followed by subsequent peaks in Mn and Fe in the winter of 2002. Thus, the data indicate substantial mobilisation and transmission of particulate SOM over the period 2001-2002, at a time of known surface disruption above the cave (A. Walker, Cave Manager, *pers. comm*.). Indeed, at this time, fluorescence intensity in PE1 dripwater was being monitored as part of continuing study of Poole's Cavern dripwaters and speleothems, after Baker *et al*. (1999c). Monitoring of fluorescence attributes in PE1 dripwater continued until December 2002 when an apparent breakdown in the annual fluorescence cyclicity occurred (low in summer, high in winter) (Hartland *et al*., 2010a).

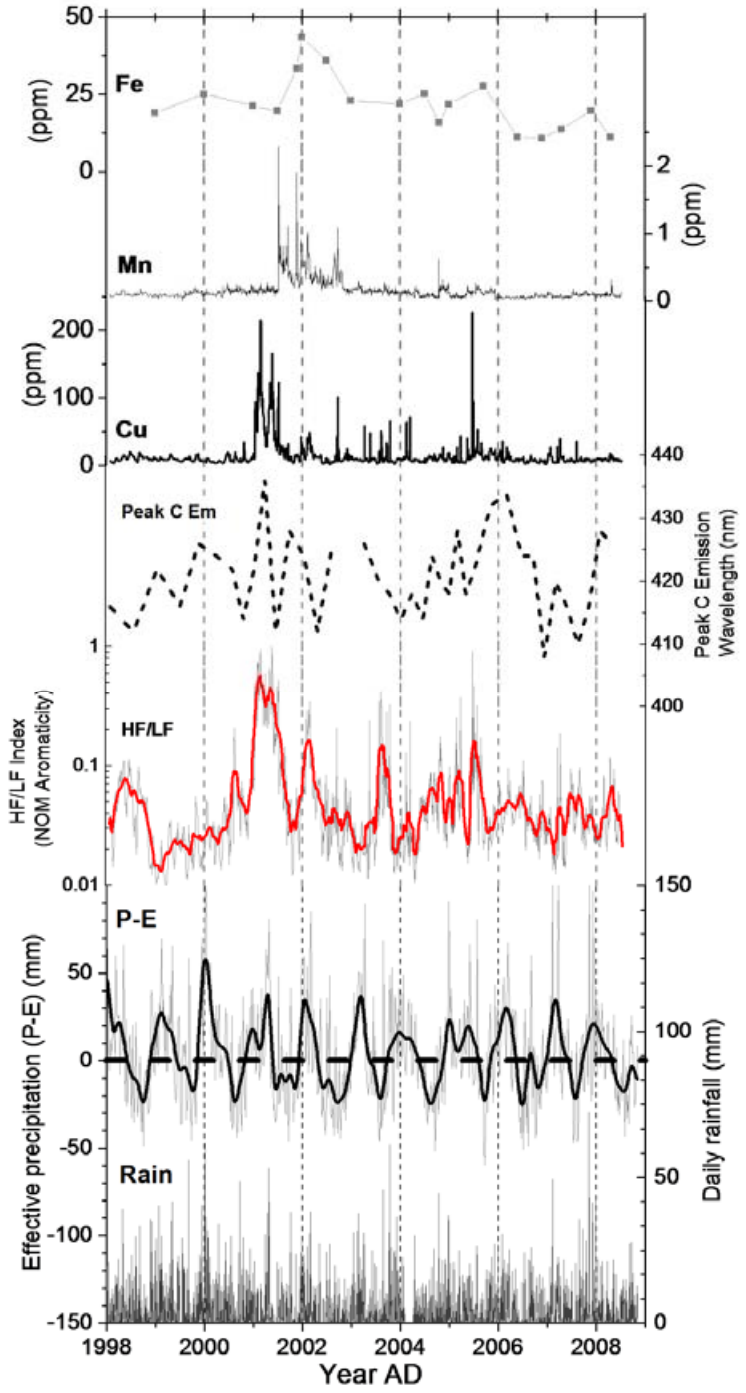

Figure 7.13 Trace element time series (Fe, Mn, Cu) and NOM parameters (peak C emission wavelength, HF/LF aromaticity index) in the PC-08-1 stalagmite plotted against effective precipitation (P-E; black line 5 pt FFT smooth) and daily rainfall over the period of formation (1998 – 2008). Smoothed HF/LF line is 20 point Savitzky-Golay filter. Disruption of surface environment by ditch digging may be related to disruption of dripwater winter fluorescence signal in 2002 (Hartland *et al*., 2010a). HF/LF index indicates enhanced competitive binding by Cu and Zn for more aromatic NOM at high values.

Low-flux metals in PC-08-1

Low-flux metal transport in PE1 dripwater corresponds to the very slow migration of Co and V bound to fluorescent NOM with diameters below 100 nm and dominated by fulvic-like compounds with dimensions of ca. ≤1 nm (Chapters 5 and 6). In Fig. 7.14, Co and V time series are shown in relation to rainfall variations over the growth period of PC-08-1.

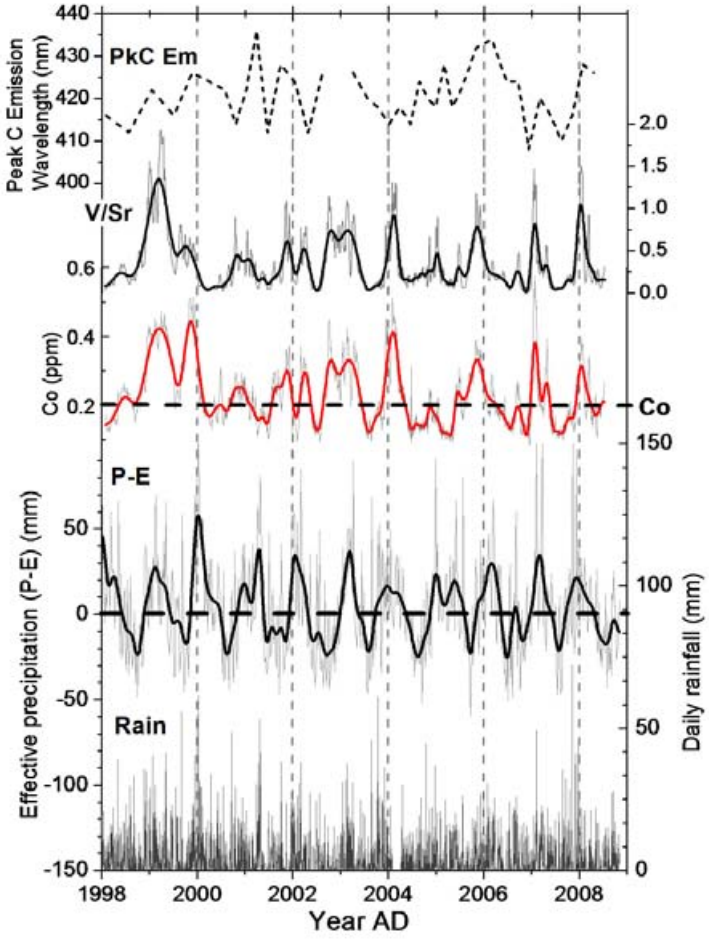

Figure 7.14 Time series of Co and V/Sr in the PC-08-1 stalagmite plotted against effective precipitation (P-E) and daily rainfall over the period of formation (1998 – 2008). Smoothed Co and V/Sr lines are 15 point fast Fourier transform (FFT) filter of LA-ICP-MS data. Dashed line intersecting Co data is the average Co concentration in PC-08-1. P-E data smoothed using a 5 pt FFT filter.

In PC-08-1, both V and Co showed a strong annual cyclicity with a near sinusoidal pattern, reflecting low-flux NOM transmission and the tendency for effective rainfall to be spread out across the winter months (Fig. 7.14). It is noteworthy that the peak shapes of both V and Co also reveal an internal structure, with certain peaks being characterised by a double or triple band structure (Fig. 7.14). The near-sinusoidal shape of the oscillations in Co and V and their multiple band structure bears very strong similarity to the structure of fluorescence banding measured in the PC-97-1 stalagmite by Baker *et al*. (1999c). The internal structure of these peaks may reflect brief interruptions in fulvic-like NOM transport, and a similar structure to Co and V profiles in PE1 dripwater time-series was also observed (Chapter 6).

Over the period, winter 1997 to winter 2002, fluorescence in the PE1 dripwater was monitored at regular intervals and the results of this monitoring work were given in Hartland *et al*., (2010a) (monitoring conducted by A. Baker). Fluorescence monitoring over this period demonstrated the annual occurrence of winter fluorescence maxima, consistent with the slow migration of fine and nominally dissolved NOM in PE1 dripwater following autumn/winter rainfalls (Chapter 6). In the winter of 2002 this signal disappeared and no peak in fluorescent NOM was measured (Hartland *et al*., 2010a). However, the inferred disruption in the transmission of fine and nominally dissolved (fluorescent) NOM is not reflected in the Co and V signals in the PC-08-1 stalagmite (Fig. 7.11). The annual peak in Co and V, although small and of comparatively short duration, was captured by the stalagmite. Therefore it is probable that the observed breakdown in the annual fluorescence signal in unfiltered PE1

dripwater samples may have been related to quenching by the coarse fraction (Chapter 4).

7.7 DISCUSSION

7.7.1 Partitioning of NOM-metal complexes into speleothem calcite

This study has provided the first evidence for NOM-metal complex formation in speleothems. It has been shown that the extent of partitioning between aqueous complexes in solution and adsorbed complexes at the speleothem surface can be explained by the stability of NOM-metal aqueous complex (i.e. its tendency to dissociate) and the binding affinity for metal ions for the calcite surface (e.g. Cu has higher affinity than Ni causing greater Cu partitioning). It is likely that partitioning is also impacted by NOM speciation, with particulate SOM (corresponding to high-flux transport) possibly forming less stable surface complexes with calcite than fulvic-like compounds (Lee *et al*., 2005).

In PE1 dripwater, Co is the least labile metal and is predominantly bound by humic- or fulvic-like NOM with diameters ca. 1 nm (Chapters 5 and 6). An analysis of the NOM-Co ratio in solution and in PC-08-1 showed that NOM:Co was essentially constant between dripwater (< ca. 100 nm) and speleothem. Hence, the data provide strong evidence supporting the co-adsorption and co-precipitation of NOM-Co complexes in PC-08-1 and therefore demonstrate that aspects of the inorganic geochemistry of speleothems may be quantitatively linked to their organic compositions.

Higher trace element incorporation at defects was anticipated to be a feature of the PC-08-1 stalagmite since more defect sites occur at faster crystal growth at high supersaturation (Frisia *et al*., 2000). The extension rates of Poole's Cavern's hyperalkaline speleothems (1-10 mm yr^{-1}) is around two orders of magnitude greater than is typical of speleothems (10-100 μm yr^{-1}) (Hartland *et al*., 2010a). However, defects arising from growth rate variations are not the cause of co-variation between Co, V, Br, and Al, since growth rates were faster in the pale [summer] layers, coinciding with low Co, V, Br and Al. In contrast, Ba and Sr concentrations were uniformly higher in summer growth, consistent with higher partition coefficients at faster growth rates (Huang and Fairchild, 2001). However, the distinct antipathy between Sr and Ba to low flux elements (Co, V, Br and Al) in PC-08-1 has also been observed between alkaline earth metals (Sr and Mg) and colloid-associated metals (Cu, Pb, Y, Br) in stalagmites precipitated at growth rates two orders of magnitude slower (Borsato *et al*., 2007). A substantial increase in defect sites is associated with the shift from columnar to micro-crystalline growth fabric which coincides with increased metal adsorption and slower growth rates (Borsato *et al*., 2007). Thus, decreases in alkaline earth metal incorporation may be associated with increased competition for lattice sites (e.g. from Cu, Ni, Zn) with simultaneous adsorption of V, Al and Br at defects. Strontium is known to have complex controls in calcite (Huang and Fairchild, 2001; Fairchild *et al*., 2010) and more work is needed to elucidate the mechanisms involved. However, higher adsorption of NOM-metal complexes is certainly linked to the characteristic cyclicity in the trace metal profiles observed in PC-08-1 and other samples (Borsato *et al*., 2007).

It is reasonable to speculate that the physical size of NOM (e.g. particulates, colloidal aggregates, fine colloids) will also influence its adsorption and physical occlusion in calcite. But, to date, no experimental studies have examined the processes affecting the incorporation of particulate and coarse colloidal NOM in calcite. Other factors such as the degree of hydrophilicity/hydrophobicity of NOM are also likely to play a role and this issue deserves scrutiny in its own right (Blyth *et al*., 2008).

Characteristic increases in the ratios of trace metals that show an increased affinity for highly aromatic SOM (e.g. Cu and Zn) relative to those that bind less strongly (e.g. Ni and Co) have been observed in dripwaters during periods of high particulate SOM flux following peak infiltration events (Chapter 6). Indeed, the data from PC-08-1 demonstrates that increases in trace metal ratios are captured in speleothems, resulting in metal ratios (e.g. Cu:Ni and Zn:Ni) representative of high-flux transport. Since increases in metal ratios reflect changes in competitive interactions arising from compositional shifts from humic- or fulvic-like NOM to highly aromatic SOM, changes in the ratio of these metals in PC-08-1 encode information on such shifts. However, as shown, metal partitioning from aqueous complexes with particulate SOM is not uniform, reflecting a competitive hierarchy of metal adsorption from complexes in solution (i.e. Cu >> Ni), and this partitioning may be exacerbated by the relative instability of SOM surface complexes. Certainly the indicative data suggest that fulvic-like NOM-metal complexes are incorporated at closer to their ratio in solution than are SOM-metal complexes.

7.7.2 Trace metal ratios and NOM composition

As discussed, characteristic shifts in trace metal ratios (e.g. Cu:Ni and Zn:Ni) in PC-08-1 reflect changes in the competitive binding of metals in aqueous complexes with organic ligands in dripwaters, which represent shifts in metal speciation from humic-like NOM to highly aromatic SOM. Increases in metal ratios are also indicative of rapid particulate transport (Chapter 6); however it is uncertain whether particulates are incorporated in calcite. Metal ratios in PC-08-1 indicate that SOM-Cu partitions more strongly than SOM-Ni and SOM-Zn, which appeared to be incorporated at close to their ratios in PE1 dripwater for both high- and low-flux trends. Assuming that the greater partitioning of Cu over Zn and Ni reflects the greater specificity of Cu for binding with calcite (Zachara *et al.*, 1991; Godelitsas *et al.*, 2003, Chada *et al.*, 2005; Elzinga *et al*., 2006), these results suggest that particulate SOM is incorporated during high-flux events. This needs to be tested by specific studies of the organic fraction of speleothems to elucidate the relationship between trace metal ratios and NOM composition. However, these results point to a means of targeting compound specific investigations to enable optimal extraction of organic components of interest (Blyth *et al*., 2008).

7.7.3 NOM-metal complexes and hydrology

Low-flux NOM-metal transport in PC-08-1 bore strong similarity to the distribution of effective rainfall over the annual cycle. Several studies have demonstrated the utility of organic matter as a tracer of cave hydrology (e.g. Baker *et al*., 1997a; Cruz *et al*., 2005; Ban *et al*., 2008) and the data presented here indicate that for the most strongly

complexed metals (e.g. Co), speleothems capture a record of NOM-metal complexes that is correlated with humic-like NOM transport at the time of formation. Therefore, where strong correlations are found between NOM transmission and precipitation variations, such as in regions with large seasonal shifts in effective rainfall (e.g. monsoonal regions; Ban *et al*., 2008), it is probable that NOM-metal complexes record these changes in speleothems. Indeed, Jo *et al*. (2010) have provided strong evidence for particle or colloid-facilitated transport of Pb in a modern stalactite from Seopdong cave on the Korean Peninsula. The excess (or unsupported) ^{210}Pb in the stalactite was strongly correlated (R^2= 0.9) with variations rainfall amount over the growth period (Jo *et al*., 2010). This indicates therefore, that where infiltration is sufficiently strong, particle-facilitated transport in speleothems may provide at least a qualitative record of effective precipitation in palaeoclimates.

7.8 SUMMARY

It is becoming clear that NOM in cave dripwaters extends a pervasive influence over the abundance of surface-reactive metals and that this is linked to effective precipitation patterns, mediated by processes in soils (colloid and particle release), epikarst, and aquifer (flow routing) (Chapter 6). Ultimately, however, what drives our interest in these processes is their potential for informing our understanding of the palaeoenvironmental signal encoded in the trace element composition of speleothems. The data presented here demonstrate that NOM-metal complexes are captured by speleothems and that the degree of partitioning between solution and speleothem is dictated by the stability of aqueous complex and the stability of the adsorbed complex at

the calcite surface. Thus, the trace metal composition of speleothems may be linked to their organic contents, potentially providing a record of particle-facilitated transport, NOM character and concentration.

8. COLLOID-MEDIATED TRACE METAL VARIATIONS IN STALAGMITES

8.1 INTRODUCTION

This chapter presents evidence for the widespread occurrence of colloid-mediated trace metal variations in stalagmites, which may encode important information on the prevailing environmental conditions during speleothem formation. The changing abundance of colloid-metal complexes in speleothems is likely to be most strongly influenced by soil processes (i.e. colloid and DOM production and release (Sen & Khilar, 2006)), which ultimately may be related to changes in climatic parameters (e.g. ambient temperature, infiltrating precipitation), except where human activity disrupts this balance. The resulting colloid-metal signal is likely to be delayed between soil and speleothem (Genty *et al*., 1998) and be subject to non-linearities, e.g. decoupling of the soil-aquifer system due to soil moisture deficit (Baker *et al*., 1997a) and the interplay between mobilisation by hydrodynamic and chemical factors (Rousseau *et al*., 2004; El-Farhan *et al*., 2000). Further complexities may be imposed by flow-routing (Tooth & Fairchild, 2003) and the hydrodynamic behaviour of different metal carrier phases (McCarthy & McKay, 2004). Nevertheless, the indicative data suggest that colloid-mediated trace metal variations in speleothems have the potential to at least record qualitative information on the occurrence of wet and dry periods (Zhou *et al*., 2008; Jo *et al*., 2010).

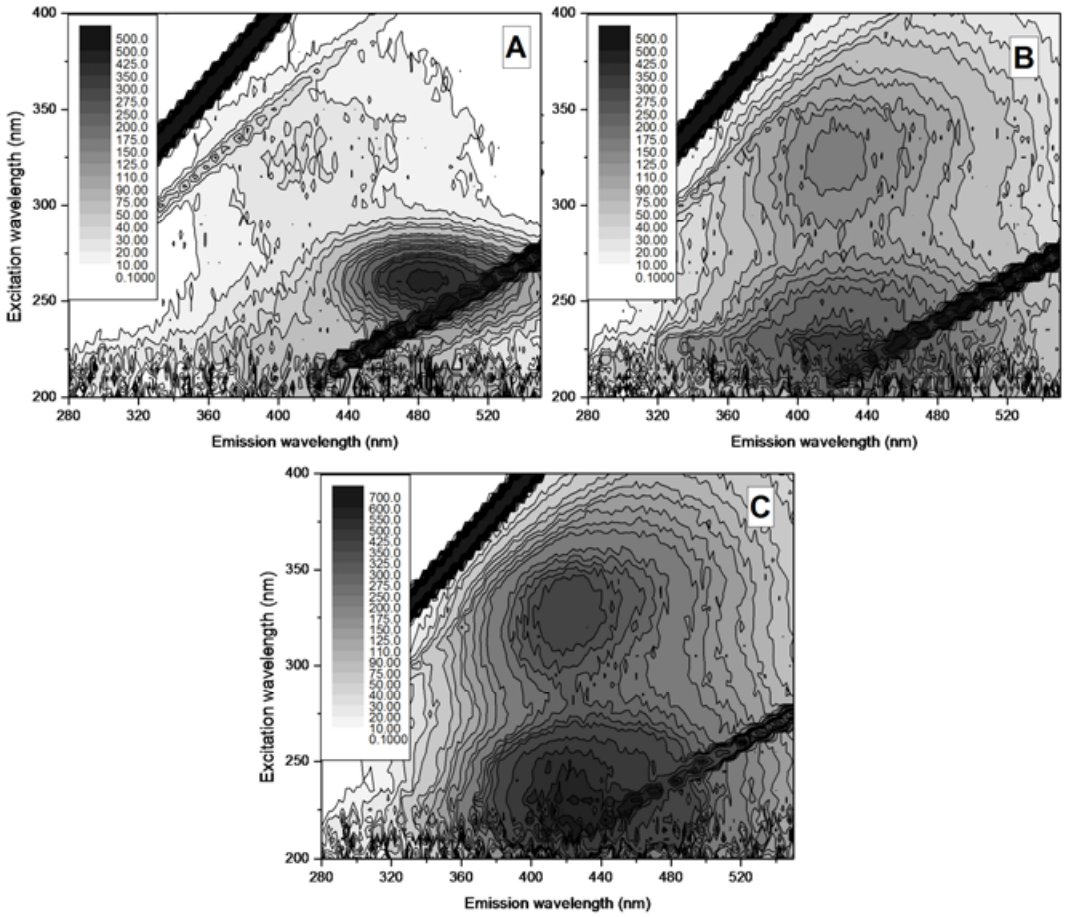

Figure 8.1 Representative fluorescence EEMs showing NOM fluorescence in powdered stalagmite dissolution samples from stalagmites (A) OB81 (Obir Cave, Austrian Alps), (B) ER77 (Grotta di Ernesto, Italian Alps) and (C) LB3 (Lower Balls Green Mine, English Midlands). The OB81 sample was taken from a homogenised fragment of the OB81 stalagmite. The ER77 sub-sample corresponds approximately to Little Ice Age (LIA) growth and the LB3 sub-sample corresponds to the early twentieth century. Fluorescence in OB81 shows two distinct signatures, the first consistent with aquatic NOM fluorescence in ER77 and LB3, and a second signature more typical of a highly aromatic, peat-like NOM source at longer emission wavelength (red-shifted) relative to aquatic humic and fulvic acids (Senesi *et al*., 1991a). TOC concentrations were highest in LB3 and ER77, 0.4-0.6% and 0.3-0.6%, respectively, and lowest in OB81 0.1-0.2% (Appendix VII).

Soil development determines colloid properties as well as the availability of metal ions (Jenny, 1941). Away from equatorial zones, where mineral colloids (e.g. oxides of Fe and Mn) may be of greater importance (Ashman & Puri, 2002), NOM is probably the

dominant colloid class for metal binding and transport (Chapter 5 and 6), with co-transported oxide and aluminosilicate phases being of lesser importance, i.e. because of their low concentrations, the presence of NOM surface coatings and competition from organic ligands (Buerge-Weirich *et al.,* 2002).

The composition of NOM (Fig. 8.1) and the availability of trace ions are likely to be highly variable between environmental systems, but because NOM-metal complexation is fundamentally competitive in nature (Marang *et al*., 2009), this process may become manifest in the trace element composition of speleothems (Chapter 7), i.e. as low-flux and high-flux trends.

In the following chapter, trace metal variations are examined in stalagmites from three contrasting sites in the temperate mid-latitudes, two of which (Brown's Folly Mine (BFM) and Grotta di Ernesto (ERN)) have experienced substantial changes in their surface vegetative cover as a result of human action, while the third (Uamh an Tartair (TAR)) remains undisturbed. Building on the findings in Chapter 7 relating to hyperalkaline stalagmite PC-08-1 from Poole's Cavern, the hypotheses are tested that (1) competitive trace metal binding with NOM in cave waters produces characteristic 'L' or 'V' shaped distributions in high-flux (HF) vs. low-flux (LF) metal pairs in speleothems, and (2) that the HF:LF signal encodes information on soil-aquifer processes with links to climate.

8.2 MATERIAL AND METHODS

Trace element profiles and calculated metal indices are presented here from three stalagmites which have already been studied in detail and have established chronologies: Boss (BFM; Baldini *et al*., 2005), ER77 (ERN; Frisia *et al*., 2003) and SU-96-7 (TAR; Baker *et al*., 1999a; Proctor *et al*., 2000; 2002) (Fig. 8.2).

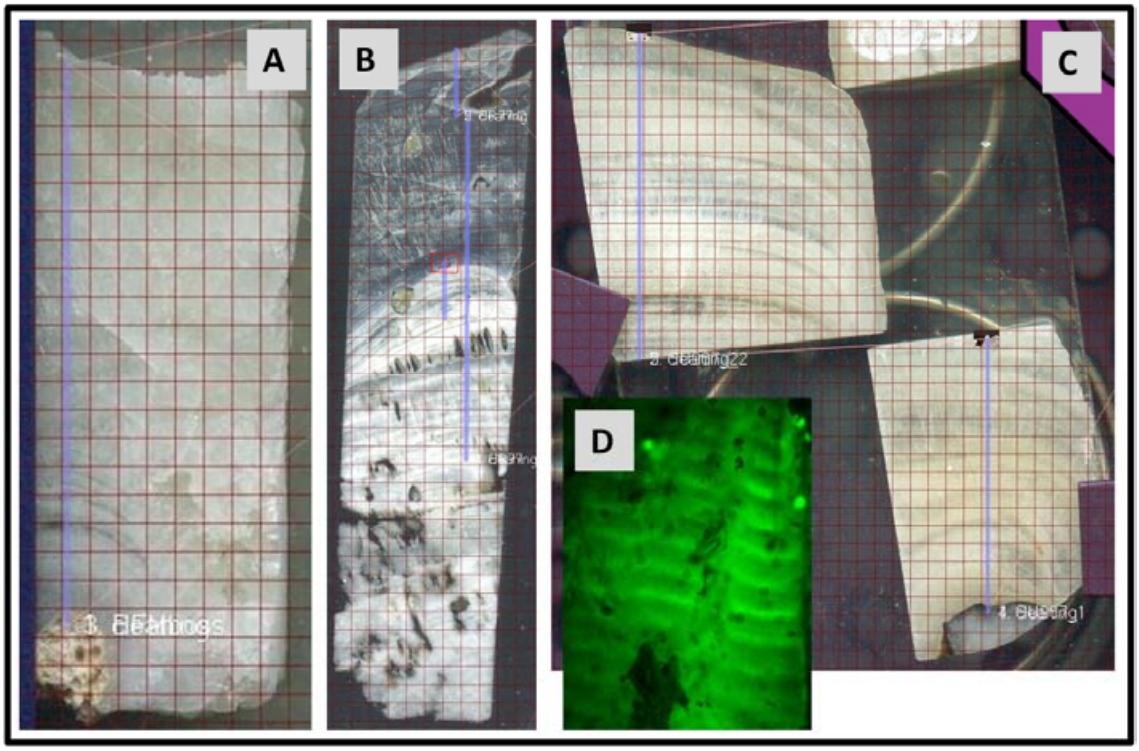

Figure 8.2 Images of sectioned stalagmite samples (A) BFM-Boss (B) ER77 and (C) SU-96-7, mounted for LA-ICP-MS analysis. (D) Fluorescence micrograph of organic-bearing laminae in stalagmite SU-96-7 (Source: I. J. Fairchild). Blue lines show tracks of LA-ICP-MS analyses. Images are overlain by a 1 mm grid.

8.2.1 Site descriptions

Mining at BFM (Bathford Hill, Wiltshire, England) was in the Bath Oolite member of the Jurassic Great Oolite series limestone, between 5 and 15 m below-surface. Mining

commenced in 1836 and ended in 1886, although mining continued at other mines in Bathford Hill until ca. 1904, when the area was converted to a nature reserve (Baldini *et al*., 2005). The surface environment above BFM was gradually re-vegetated between 1904 and the present (Baldini *et al*., 2005). BFM is climatically similar to LBGM (being ca. 20 km south of Minchinhampton) having a temperate maritime climate with a mean annual precipitation of 842 mm and mean annual temperature of 10.0 °C. Rainfall occurs throughout the year, with slightly more in the winter (Baldini *et al*., 2005). Contrastingly, both ERN and TAR are characterised by a distinct seasonality in infiltrating precipitation. At ERN (Valsugana valley, Trentino, NE Italian Alps) precipitation peaks in the spring and autumn, although infiltration is enhanced in the autumn because of lower rates of evapotranspiration and reduced canopy interception (see Chapter 3 and 6 for more details on ERN).

Uamh an Tartair (Traligill Basin, Sutherland, NW Scotland) is developed in Cambro-Ordovician dolomites and is overlain by thin peat blanket bog (0.1 – 0.6 m thick), located in a maritime climate with annual precipitation >1900 mm, 250-270 rain days and 4-6 snow days per year- based on the 1971-2000 averages (Baker *et al*., 2011). The Assynt area shows a relationship between precipitation and the winter North Atlantic Oscillation (NAO) index, and temperature and ocean circulation via the North Atlantic Drift Current (Colman, 1997; Hurrell, 1995). Both raised and blanket peats record information on rainfall variations through cycles of humification (Holl *et al*., 2009), and this may be reflected in the organic composition of speleothems (Baker *et al*., 1998). Drip point discharge feeding SU-96-7 is very low (median= 0.05–0.06 μL s^{-1}) and dripwater $\delta^{18}O$ shows little variability (-7.07 ± 0.36 ‰) demonstrating the dominance of

storage flow for most of the year (Baker *et al*., 2011); but the drip is also fed by a short-duration event water component supplying peat-derived OM and associated trace elements (Fairchild *et al*., 2001). Thus, the small (ca. 5-10 yr) lag between soil organic matter (SOM) production and transport seen in other systems (Genty *et al*., 1998), may not apply at TAR.

8.2.2 Instrumental techniques

Methodologies used in sample preparation and analysis have been described in detail in Chapter 3. LA-ICP-MS analyses were performed in the laboratory of Wolfgang Müller at Royal Holloway University of London. Trace element time series for stalagmite samples Boss, ER77 and SU-96-7 were constructed from single LA-ICP-MS profiles. Samples were pre-ablated in two identical traverses in the direction of growth and perpendicular to growth laminae at a speed of 6 mm min^{-1} using a rectangular 280 μm (height= 13 μm, width= 310 μm) sized slit and pulsing the laser at 50 Hz. Trace element profiles were then obtained by traversing along the pre-ablated track at a scan speed of 0.6 mm min^{-1} using an identical spot size and pulsing the laser at 15 Hz. The masses of ^{23}Na, ^{25}Mg, ^{27}Al, ^{31}P, ^{43}Ca, ^{47}Ti, ^{51}V, ^{53}Cr, ^{55}Mn, ^{57}Fe, ^{59}Co, ^{60}Ni, ^{65}Cu, ^{66}Zn, ^{79}Br, ^{88}Sr, ^{89}Y, ^{138}Ba, ^{139}La, ^{140}Ce, ^{208}Pb and ^{238}U were measured with an integration time of 0.7 s. This method produces approximately 139 analyses per mm, enabling trace element concentrations in the samples to be determined at a spatial resolution between 2 and ca. 20 measurements per year, depending on speleothem growth rate.

Background counts (gas background, measured with the laser off) were subtracted from the raw data. All data were then ratioed to the calcium signal and standardised to the MACS3 (USGS) carbonate standard.

Total organic carbon concentration and fluorescence analyses were also performed on a selection of powdered stalagmite samples (ER77, LB3 and OB-81) to provide information on the variability of OC concentrations and composition in stalagmites formed in temperate climate zones (Fig. 8.1).

8.2.3 A proposed framework for identifying and interpreting high-flux and low-flux trace metal variations in stalagmites

High-flux (HF), low-flux (LF) trace metal signatures in Boss, ER77 and SU-96-7 were identified by comparison of transition metal ratios in LA-ICP-MS data. As shown in Chapter 7, metal pairs which actively compete for binding sites in aquatic NOM (e.g. Cu vs. Ni, Cu vs. Co) produce characteristic 'L' or 'V' shaped distributions in stalagmites. Although the heterogeneity of aquatic NOM makes modelling of NOM-metal binding very challenging (Unsworth *et al*., 2006; Groenenberg *et al*., 2010), the hierarchy of metal ion reactivity for binding sites in humic-like NOM is fairly well understood (Milne *et al*., 2003). Thus, despite the heterogeneous composition of NOM between cave systems (Fig. 8.1) and differences in the relative availability of metal ions in soils between different sites, the consistency with which metals compete for binding sites in humic-like NOM (i.e. low-flux end-member; Chapter 6), provides a theoretical basis for the identification of high-flux trends in speleothems (Chapter 7). The high-flux

component of metal transport is less-well characterised and probably corresponds to more highly aromatic SOM, which may be compositionally much more variable than the fine colloidal, "humic-like" component (Chapter 6). Thus, the estimated ratio for binding to humic acids (derived from n_1 binding parameter ratios (Milne *et al*., 2003; Chapter 6 and 7)) was used as the principal criterion for identifying the LF end-member.

The interpretive framework developed here for identifying HF and LF trends, is based entirely on these theoretical arguments, and has not been substantiated by studies of either dripwaters or soils at BFM and TAR because the data are not available. Examples of inferred HF:LF signatures in metals from the three studied samples are given in Figure 8.3. Offsets between the 'humic' trend lines (Fig. 8.3) and the 'low-flux' trace metal end-members in these stalagmites are inevitable, i.e. given the heterogeneity of NOM (i.e., not all metal is bound to the humic component) in environmental systems and differential partitioning of metals between aqueous NOM-metal complexes and the speleothem growth surface (Chapter 7).

HF:LF metal pairs in the three stalagmites were delineated on the theoretical basis outlined above. However, n_1 values (Milne *et al*., 2003) are not available for all the metals measured in the stalagmites (e.g. Y, La) and in those instances the identification of HF:LF end-members was based on their co-variation with other HF:LF pairs identified using the aforementioned criteria. To reduce noise in the derived signal, the HF:LF pairs which showed the greatest consistency, i.e. least scatter between HF and LF end-members were used in the derivation of HF:LF indices. The indices were constructed by taking ratio of the HF:LF metal pair, and where more than one ratio was

used the mean value was taken and then the index was normalised to the maximum value. The metal pairs used to derive HF:LF indices in each sample are as follows:

- **BFM-Boss**: Pb:Cu.
- **ER77**: Cu:Pb, Cu:Y, Pb:Y.
- **SU-96-7**: Ni:Co, Cu:Co.

The utility of this approach is based on the fact that metals partition between the dissolved phase and complexation sites in NOM based on their affinity for binding at available functional groups (Milne *et al*., 2003) and thus certain groups of elements are in direct competition for binding sites in HS, e.g. Al vs. Pb (Kerndorff and Schnitzer, 1980; Alberts and Filip, 1998; Pinheiro *et al.,* 2000) and Cu vs. Eu (Marang *et al*., 2009), whilst others are not: e.g. Ca vs. Pb (Tipping *et al.*, 1988; Pinheiro *et al.*, 1999). The efficacy of competition depends mainly on the binding site distribution in NOM (Marang *et al*., 2009), metal concentration and pH (essentially constant at pH 8 ± 0.5 in most cave waters) (Tipping, 2001).

Assuming the consistent availability of trace metal ions in the soils at each site, changes in the pattern of trace metal complexation with NOM are suggested to arise from compositional variations in the NOM mobilised into the groundwater (Chapter 6). For example, the assumption is made here that in Ernesto soils and dripwaters, Cu competes with Pb and Y for binding sites, while Pb and Y also compete, but less effectively than Cu. The data from BFM-Boss indicate competition between Cu and Pb, but conversely, Pb appears to have shown a greater affinity for binding with the high-flux NOM end-

member at this site. If these inferences are correct, then differences in the HF:LF status of the same metal pairs between sites are probably a function of the variability in NOM composition (Fig. 8.1), but may also be related to metal availability for binding at each site. These interpretations are tested in the following section against published data from each site.

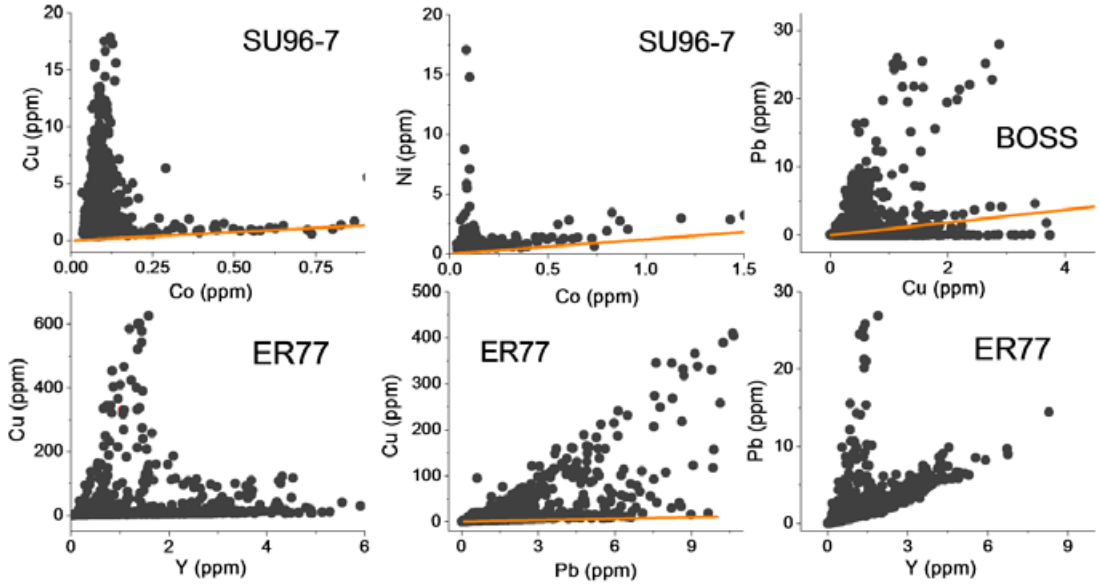

Figure 8.3 Examples of inferred high-flux and low-flux trace metal transport encoded in stalagmites from three contrasting sites: SU-96-7 (Uamh an Tartair), Boss (Brown's Folly Mine) and ER77 (Grotta di Ernesto). Humic trend lines are estimated based on the equivalent ratios of based on the NICA-Donnan competitive binding parameters (n_1) given in Milne *et al*. (2003).

8.3 RESULTS AND DISCUSSION

8.3.1 High-flux, low-flux metal indices in stalagmites

In the following section the relationship between HF:LF indices (inferred NOM aromaticity) and surface processes is explored. At two sites (BFM and ERN), significant degrees of change in their surface vegetative cover occurred over the twentieth century. The third site (TAR) is somewhat unusual because of the influence of the process of peat humification on NOM composition (Baker *et al*., 1999a; Holl *et al*., 2009).

8.3.1.1 Browns Folly Mine, Boss

The BFM-Boss stalagmite grew over the period ca. 1916 to 1995 (Baldini *et al*., 2005). Stalagmite deposition in BFM began in the years following the end of mining activities in Bathford Hill and the establishment of a nature reserve in ca. 1904. Variations in lamina thickness and $\delta^{13}C$ in BFM-Boss and two other coeval stalagmites have been studied in detail, and collectively they provide strong evidence for the influence of surface biomass changes on both deposition rates and isotope ratios (Baldini *et al*., 2005). Essentially, the results of Baldini *et al*. (2005) indicate that the recovery of the surface ecosystem overlying BFM during the twentieth century was predominantly responsible for declining $\delta^{13}C$, driven by higher [isotopically-light] biogenic CO_2 production and therefore higher dripwater pCO_2 and faster $CaCO_3$ deposition. In Fig. 8.4, the HF:LF index derived from Pb to Cu ratios in BFM-Boss is shown in relation to

the lamina thickness record and rainfall variations at Yeovil (ca. 55 km SSW). These data indicate that NOM aromaticity declined markedly over the twentieth century, consistent with an increasing retention of highly aromatic SOM in the developing soil system over this time period. The spiky HF:LF signal is consistent with rapid transmission of coarse SOM in Poole's Cavern drip PE1 (HF end-member; Chapter 6), which may be the signature of the HF mode of NOM-metal transport. Declining HF transmission may also be linked to a general decreasing trend in annual precipitation over the final 30 years of growth; however, any feedback between climate and NOM-metal transmission was insignificant compared to the slow reestablishment of surface vegetation and soils (Baldini *et al*., 2005).

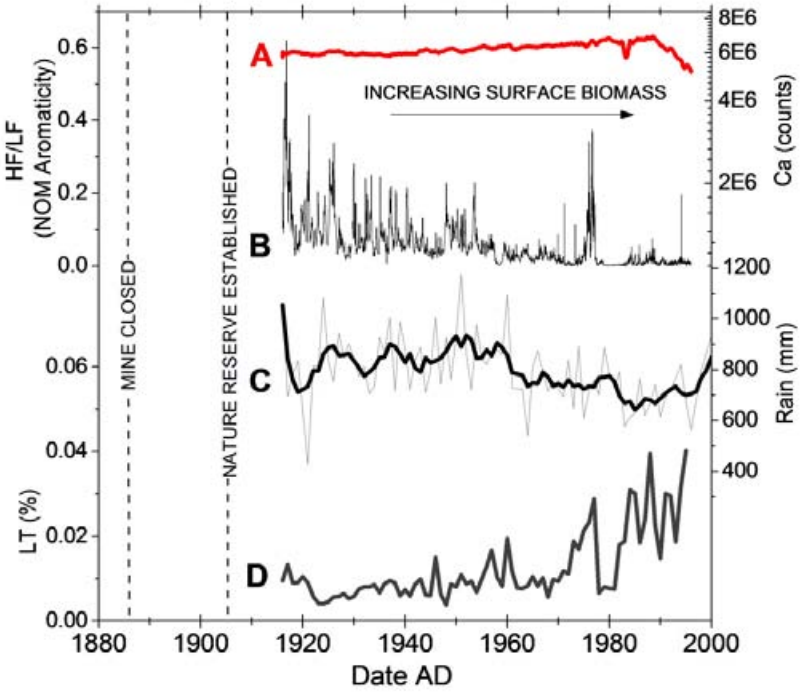

Figure 8.4 (A) Ca counts in LA-ICP-MS transect of BFM-Boss (B) secular reduction in NOM aromaticity in the stalagmite inferred from variations in Pb:Cu (high-flux/low-flux) ratios measured by LA-ICP-MS (RSD Ca 7.8%) (C) annual precipitation at Yeovil (thick black line 5 year running mean), (D) lamina thickness (% deposition) in Brown's Folly Mine stalagmite Boss. The reduction in NOM aromaticity in was most probably related to the increasing retention of coarse SOM by the overlying ecosystem during its reestablishment over the twentieth century.

8.3.1.2 Grotta di Ernesto, ER77

Similarly to BFM, a large degree of anthropogenic change affected the vegetated surface environment above Grotta di Ernesto (ERN) in the twentieth century. Large-scale deforestation of the overlying hillsides occurred during World War One (WW1) (Apolloni, 1996) and this has been argued to be reflected in the composition of stalagmites in the underlying cave (Borsato *et al*., 2007), leading to distinctly dark, inclusion-rich laminae identified in contemporaneous stalagmite [ER78] deposition. This period of particularly inclusion-rich deposition in ER78 should not be confused with the annual trace element signal in ERN stalagmites corresponding to peak infiltration events in the autumn and winter (Chapter 6; Borsato *et al*., 2007), although deforestation may have had a synergistic [complicating] effect on this process.

Trace metal concentrations in ER77 were determined by scaling of LA-ICP-MS data to the external standard and by solution ICP-MS analysis of dissolved ER77 powders (Table 8.1). Concentrations of Cu, Y and Pb (elements used in construction of the ER77 HF:LF index) were of a similar order to the concentrations of these metals in stalagmite ER78 (Borsato *et al*., 2007) determined by ion microprobe analyses (Table 8.1), with the exception that Cu and Pb were more concentrated in ER77.

In Borsato *et al*. (2007) trace element profiles in ER78 were determined by micrometer-scale XRF analyses between 5 and 8.6 mm from the top of the stalagmite. This analysis revealed annual [autumnal] peaks in Y, Zn, Cu, Pb, P and Br, with Br and Y being most specifically enriched in dark inclusion-rich laminae at the start of the twentieth century

(associated with tree-felling). The μ-XRF analyses of Cu, Y and Pb were (after scaling to ion probe measurements; Table 8.1) used to examine whether HF:LF signals could be identified in ER78 growth corresponding to 5 – 6.9 mm below-top. This section of ER78 corresponds to a twenty year period of faster growth which started in 1902 ± 2 yrs and ended in 1929 ± 2 yrs, the marked visible annual laminae in ER78 were identified as spanning the late 1910s (Borsato *et al*., 2007). However, the distribution of Cu, Y and Pb in ER78 were not consistent with the HF and LF end-members identified in stalagmite ER77. Cross-plots of Cu vs. Y and Pb (Fig. 8.5B-C) showed only a weak relation between metals and with much more scatter than in LA-ICP-MS analyses of ER77 (Fig. 8.3), although Pb vs. Y in ER78 did show trends characteristic of HF and LF end-members, but with lots of scatter (Fig. 8.5A).

Distance from top (mm)	ER77 LA-ICP-MS Concentration (ppm)			ER78 Ion Micro-probe Concentration (ppm)		
	Cu	Y	Pb	Cu	Y	Pb
0 - 1	2.52	0.29	0.23	8.71	0.28	0.61
1 - 2.5	1.09	0.07	0.07	2.26	0.16	0.35
2.5 - 4	1.30	0.09	0.08	1.88	0.16	0.13
4 - 5.5	6.99	0.35	0.48	1.81	0.20	0.18
5.5 - 7	3.74	0.14	0.26	1.96	0.24	0.16
7 – 9	9.22	0.21	0.45	4.15	0.37	0.49
9 - 13	69.7	0.58	2.83	4.73	0.19	0.43
Mean concentration in top 1 cm	13.5	0.25	0.63	3.64	0.23	0.34
Concentration by ICP-MS	8.72	< LOD	2.00			

Table 8.1 Comparison of trace element (Cu, Y and Pb) concentrations in the top thirteen centimetres of coeval stalagmites (ER77 and ER78) from Grotta di Ernesto. Concentration data in ER78 derived from Ion Micro-probe analyses by I.J. Fairchild was used in standardisation of μ-XRF trace element profiles (Borsato *et al*., 2007) used in the calculation of an ER78 HF:LF index (Fig. 8.4).

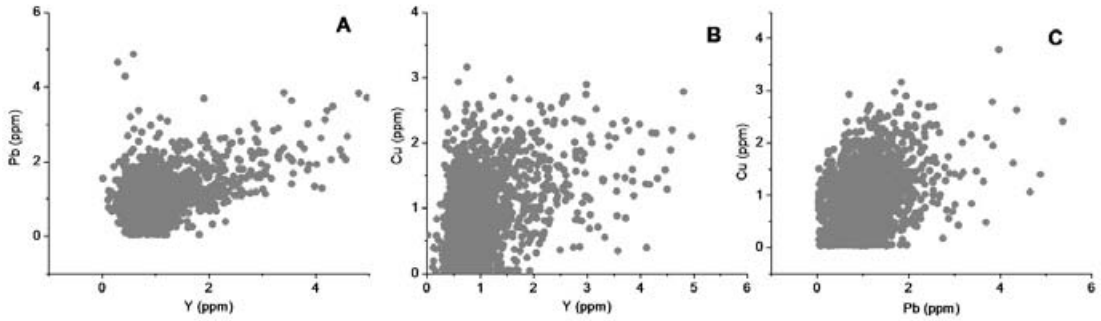

Figure 8.5 Cross plots of trace metals in stalagmite ER78 from Grotta di Ernesto (A) Pb vs. Y, (B) Cu vs. Y and (C) Cu vs. Pb. Trace element concentrations in ER78 were determined by scaling μ-XRF line scans to Ion micro-probe data (Borsato *et al*., 2007).

In Figure 8.6, the HF:LF index from ER77 (Fig. 8.6B) is plotted next to Pb:Y calculated from ER78 μ-XRF data (Fig. 8.6C) roughly corresponding to the period 1902 to 1929 ± 2 yrs. Calcium counts in ER77 (Fig. 8.6A) show a prominent downward spike in the second decade of the twentieth century, indicating an increase in sample porosity. Overall, the ER77 HF:LF index and Pb:Y in ER78 reveal similar trends, possibly consistent with a gradual increase in NOM aromaticity during the 1920s (Fig. 8.6B-C). Meteorological data (Fig. 8.6D-E) from Trento for the period 1902 to 1929 indicate that the increase in HF:LF indices after ca. 1915 was not related to regional climate.

As found with sample PC-08-1 (Chapter 7), the laser ablation data from stalagmite ER77 revealed both HF and LF metal pairs in ER77 (Fig. 8.3). In Figure 8.7, the HF:LF index (A; 20-pt running mean) is shown with the reconstructed precipitation (B; 7-yr running mean), LA-ICP-MS Ca counts (C) and concentrations of trace metals La, Y, Cu and Pb (D-G). Clear co-variation is seen in Y, La, Cu and Pb in ER77 (Fig. 8.7D-G), with lower concentrations of all metals being recorded in late LIA growth (ca. 1600 - 1780).

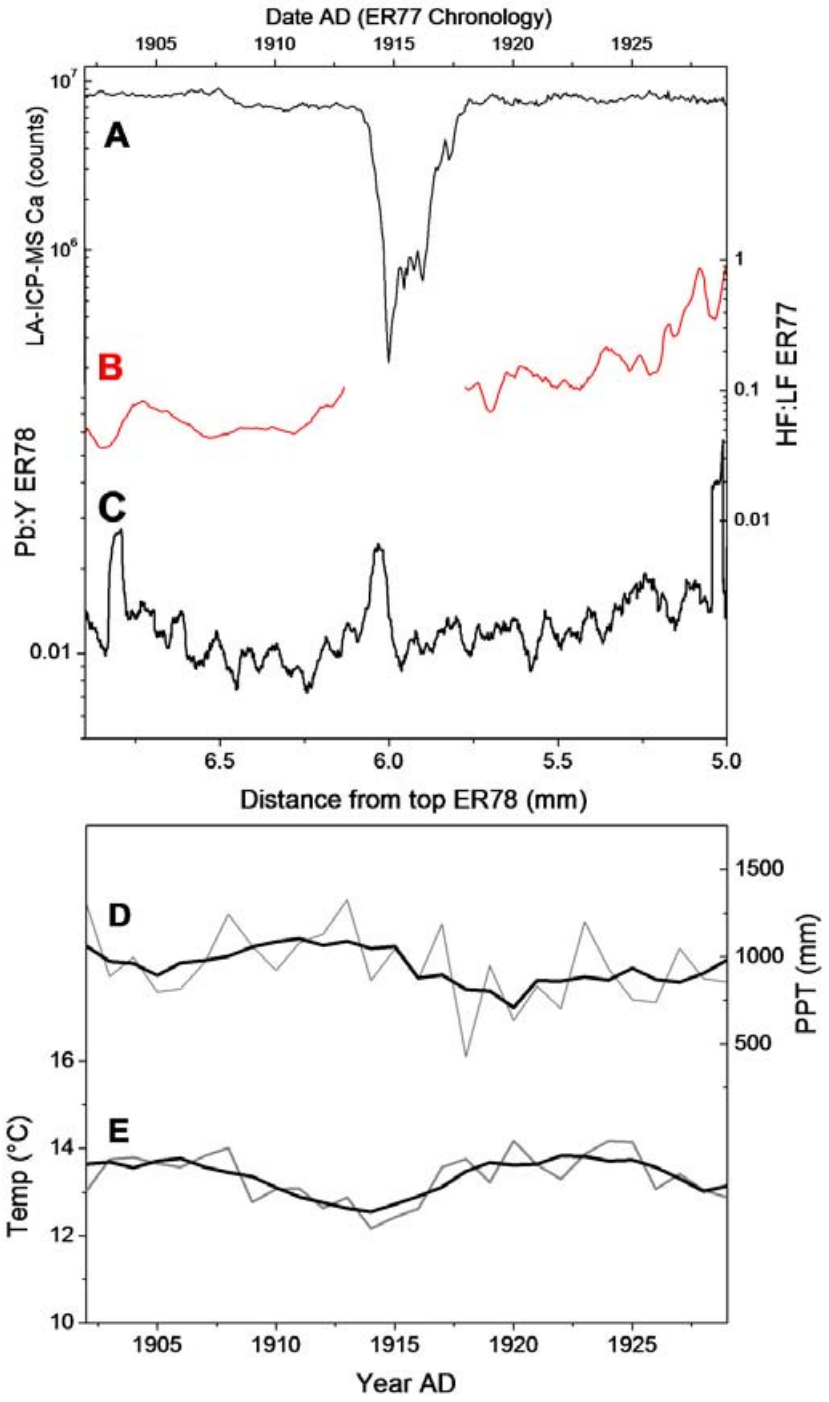

Figure 8.6 Comparison between high-flux, low-flux metals in coeval stalagmites ER77 and ER78 from Grotta di Ernesto (A) Ca counts measured in ER77 by LA-ICP-MS corresponding to the period 1902 to 1929, (B) the HF:LF index in ER77 (5 pt running average) for the same period; (C) Pb:Y in ER78 (10 pt running average) derived from μ-XRF line scans following scaling to concentrations measured by Ion Micro-probe analyses (Borsato *et al*., 2007); (D) mean annual rainfall (PPT) and (E) temperature for Trento between 1902 and 1929.

Assuming that this group of metals are commonly complexed and transported by NOM, the data indicate that NOM-metal transport declined during the LIA, a period of generally higher meteoric precipitation (Casty *et al*., 2005). Crucially, however, the ER77 HF:LF index indicates that during this period, the aromaticity of NOM captured by the stalagmite increased (Fig. 8.7A), suggesting enhanced HF transport of trace metals in the wetter periods with an overall reduction in NOM-facilitated transport.

NOM aromaticity (HF:LF index) in ER77 (Fig. 8.7A) shows an order-of-magnitude increase at the start of the twentieth century, consistent with substantial disturbance of the overlying soils and subsequent mobilisation of highly aromatic SOM. Trace metals (La, Y, Cu and Pb) and the HF:LF index show increased mean point-to-point variability in twentieth century growth, similar to that seen in BFM-Boss. Similarities are also seen in the long-term effects of surface disturbance at ERN, with an elevated HF:LF index occurring throughout the remainder of the twentieth century (Fig. 8.7A), although this may be partially attributed to generally wetter conditions compared to the LIA (Fig. 8.7B).

In Figure 8.8, the ER77 HF:LF index corresponding to the period 1500-1680 is plotted against the reconstructed precipitation at 45°75'N/11°25'E (Casty *et al*., 2005). These data show a reasonable visual fit between the smoothed HF:LF index and the reconstructed precipitation. This preliminary result is consistent with greater mobilisation of highly aromatic SOM during periods of higher precipitation.

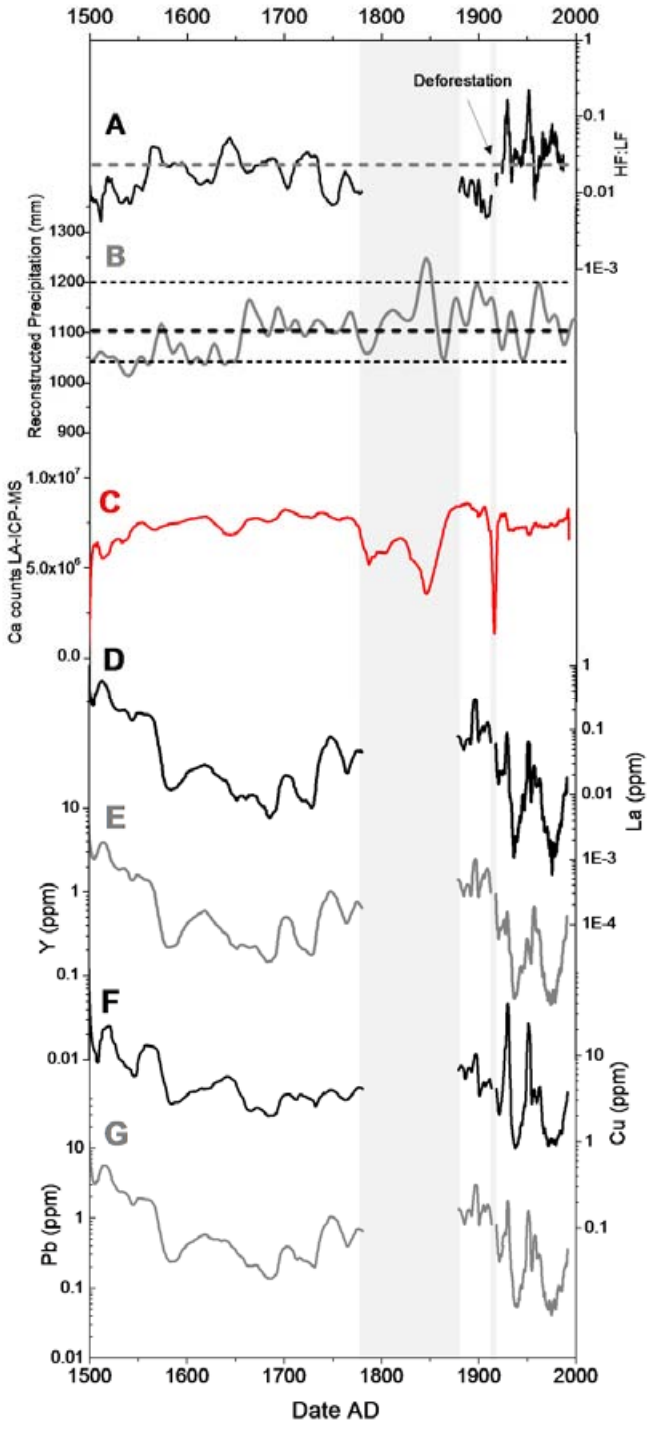

Figure 8.7 (A) Twenty point running mean of the ER77 HF:LF index with periods of low LA-ICP-MS Ca counts excluded (vertical grey lines) (B) Seven year FFT smooth of reconstructed precipitation from (Casty *et al*., 2005) (C) LA-ICP-MS Ca counts and (D) La, (E) Y, (F) Cu and (G) Pb concentrations in the ER77 stalagmite calculated from the LA-ICP-MS profile scaled to the MACS-3 carbonate standard.

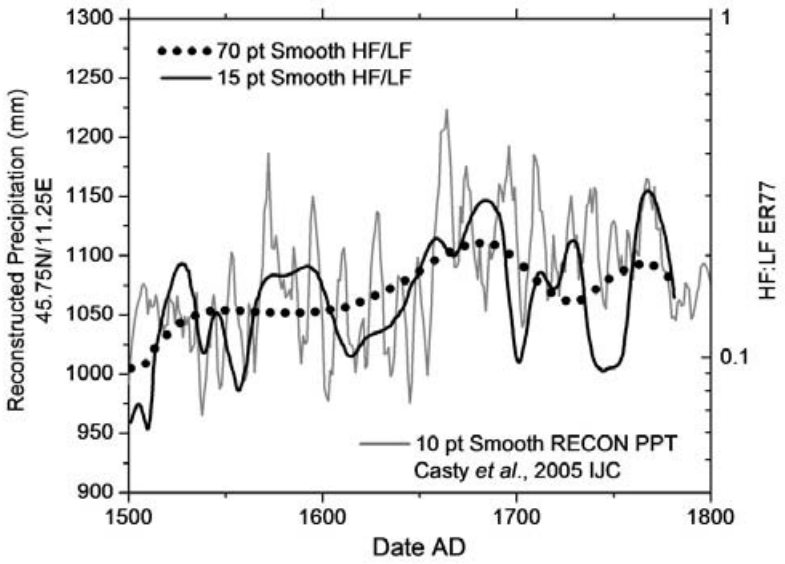

Figure 8.8 Ten year running mean of reconstructed precipitation (grey line) from (Casty *et al*., 2005) for 45°75'N/11°25'E plotted against the smoothed HF:LF aromaticity index (7-year FFT black line, 32-year FFT black dotted line) from ER77 over the period 1500 to 1780.

8.3.1.3 Uamh an Tartair, SU-96-7

LA-ICP-MS analysis of SU-96-7 produced two contiguous profiles of trace element variations spanning the entire sample (Fig. 8.2c). Calcium counts in SU-96-7 were highly stable, showing flat profiles in each transect (Ca RSD ± 5.3%). In Figure 8.9, the HF:LF index in SU-96-7 (Fig. 8.9C) is plotted against the fluorescence index (Fig. 8.9A) and lamina thickness record (Fig. 8.9B) and the annual proportions of Mg and Sr (% of total) (Fig. 8.9D-E). Variations in the HF:LF index were largely in-phase with both the normalised lamina thickness (Fig. 8.9b) and variations in NOM aromaticity derived from the ratio of fluorescence emission at 470 and 430 nm (Proctor *et al*., 2000).

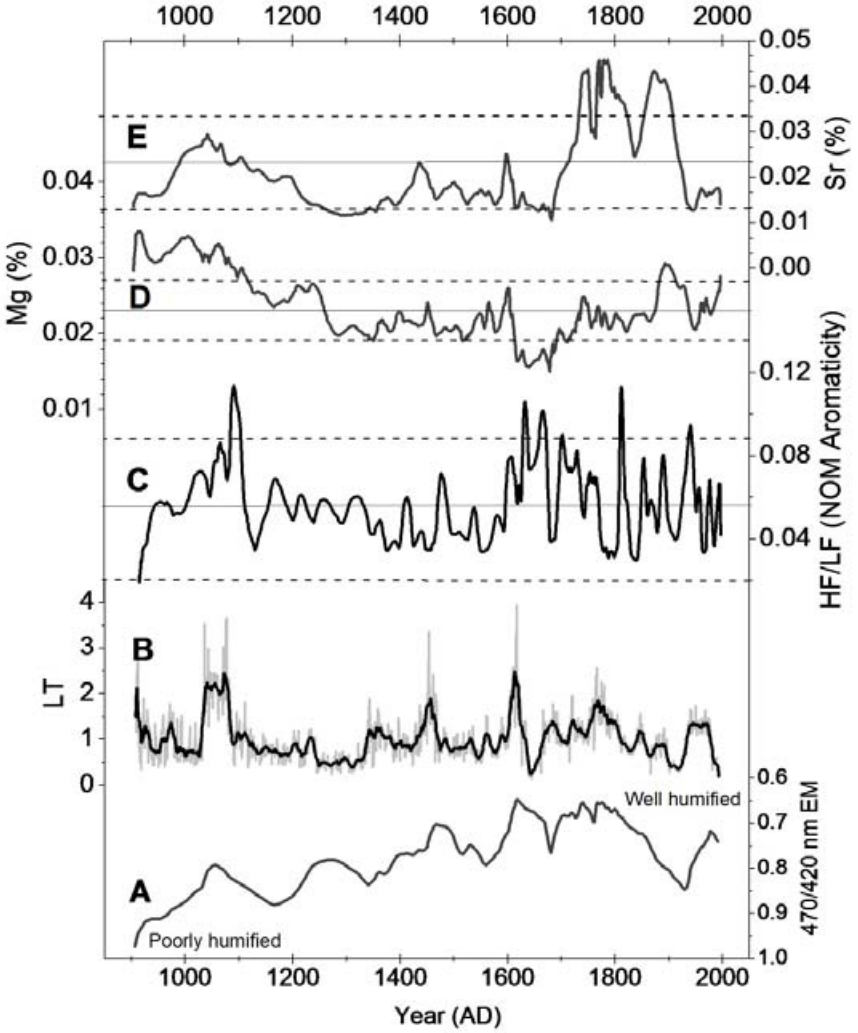

Figure 8.9 Time series of climate-sensitive variables from SU-96-7 (A) ratio of peak fluorescence intensity at emission wavelengths of 470/420 nm (B) normalised lamina thickness record (black line 10 yr running average) (A and B; Proctor *et al*., 2000) (C) 20 yr running average of HF:LF index of NOM aromaticity and (D and E) variations in Mg and Sr (% of total) determined by LA-ICP-MS analysis.

Variations in NOM aromaticity are linked to growth rate variations in SU-96-7 because of the dominant influence of wet and dry periods on peat humification (Baker *et al*., 1999a; Proctor *et al*., 2000). Humification increases during warmer/drier periods because of enhanced microbial breakdown of organic matter; whereas during wetter/colder periods, humification slows and the DOM generated is less aromatic and

more fulvic-like in character (Baker *et al*., 1999a). The humification or de-humification of peat bogs results in substantial shifts in NOM aromaticity over short timeframes, i.e. seasonal variations are detectable (Holl *et al*., 2009).

Stalagmite deposition increases in drier periods because soil pCO_2 is higher and thus bedrock dissolution increases, producing more highly supersaturated dripwaters (Proctor *et al*., 2000). Thus, peat humification and stalagmite growth rate are directly linked at this site. The inferred NOM aromaticity (HF:LF) signal in SU-96-7 (Fig. 8.9C) reproduces the main peaks in the lamina thickness (LT) record (Fig. 8.9B) but shows a much greater degree of variability than LT. Variations in the HF:LF index and Sr and Mg were also largely in phase, especially during the first 500 years of growth. Modern dripwater already has the Mg:Ca of dolomite (Fairchild & Hartland, 2010), so enhanced dolomite dissolution (Fairchild *et al*., 2000) can be discounted, and therefore elevated Mg and Sr may be linked to increases in prior calcite precipitation along the flow-path, possibly diagnostic of aquifer drying (Fairchild *et al*., 2000). Thus, increases in HF:LF, fluorescence ratio, LT, Sr and Mg are all linked to drier climatic conditions, but with variable degrees of sensitivity, and rates of change in response to climate forcing.

8.3.2 Stalagmite proxy interpretations

8.3.2.1 BFM-Boss and ER77

Stalagmite proxy evidence from ERN and BFM indicate that the timescales of recovery of soils and vegetation following large scale surface disturbance (e.g. between glacial-

interglacial cycles) are of the order of decades to centuries (Baldini *et al*., 2005). Recovery of a steady state condition between soils and cave dripwaters is a pre-requisite for a climatically-meaningful signal to emerge; and thus HF:LF metal ratios in stalagmites may not only encode information on climate, but also provide an indication of the speed of recovery of surface environments following major disturbance events, complementing isotopic approaches (Baldini *et al*., 2005). In stalagmite ER77, the direction and magnitude of fluctuations in the HF:LF index for the period 1500 – 1780 was consistent with reconstructed rainfall for the central European Alps (Casty *et al*., 2005). This indicates that with the exception of caves overlain by peats (i.e. TAR), greater NOM aromaticity in stalagmites may reflect increases in HF transport associated with peaks in effective precipitation- as observed in dripwater monitoring (Chapter 6). The HF signal appears to correspond to rapid, transient pulses of more aromatic coarse or particulate SOM (Chapter 6) and this is consistent with the spiky signal seen in stalagmites BFM-Boss (Fig. 8.4) and PC-08-1 (Chapter 7).

8.3.2.2 SU-96-7

The relationship between the HF:LF index in SU-96-7 and climate was investigated using data from the instrumental period (1850-1993) compiled and used in the climate reconstructions of Proctor *et al*. (2000), who derived a transfer function between annual temperature/precipitation (T/P) and lamina thickness. Similar features in HF:LF variations in SU-96-8 and decadal climate fluctuations were identified, but no significant correlations were found with annual T/P, amount, estimated effective rainfall or annual water excess. However, a visually impressive correlation was found between

spring T/P and the HF:LF index (Fig. 8.10). The best fit to the data was achieved by using calculated spring T/P (Feb-Apr) from 1900 to 1980 and the HF:LF index corresponding to the period of growth between 1890 and 1970 (Fig. 8.10).

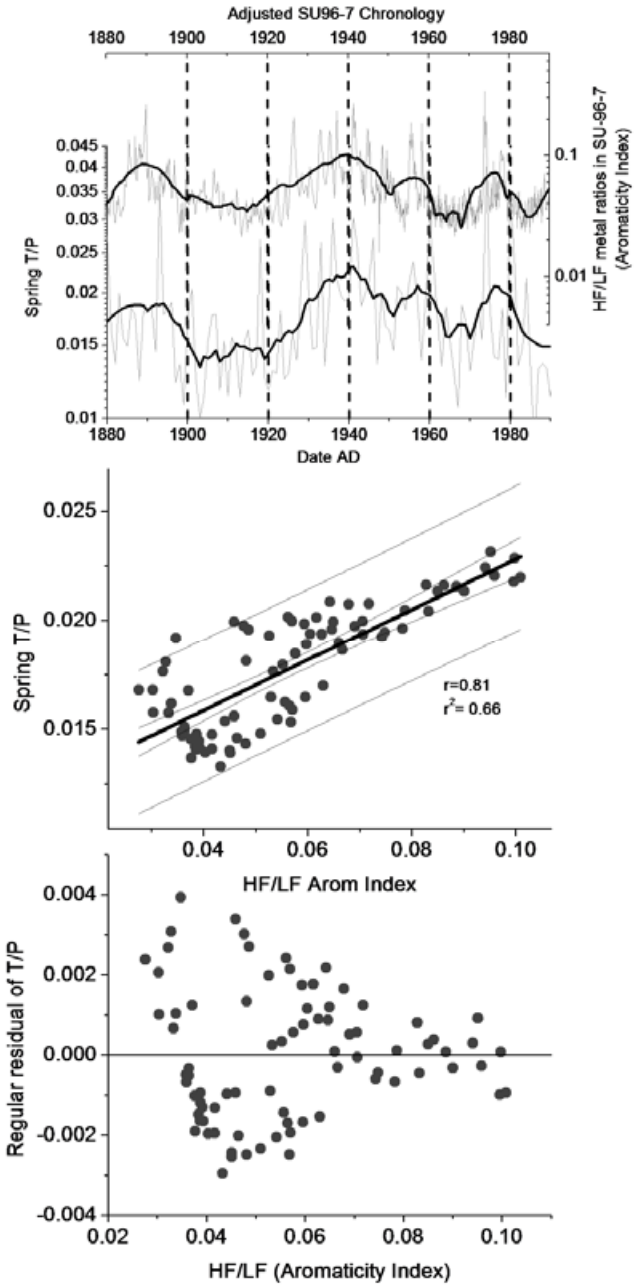

Figure 8.10 Correlation between HF:LF index in SU96-7 and spring T/P (average temperature divided by summed rainfall) following adjustment of the SU-96-7 chronology. Data used in correlation correspond to laminae deposited between 1890 and 1970 (based on the chronology from Proctor *et al*. (2000)) and climate data from 1900 to 1980.

Although caution must be exercised, there are reasonable grounds for adjusting the stalagmite chronology; Proctor *et al*. (2000) reported that "examination of the top of the counted section indicates that around 50-100 μm was lost from the edge of the cut section during polishing. With a bandwidth of 15-20 μm near the top, this implies that 2-8 bands were lost suggesting a date of AD 1988-1994 for the topmost counted band". Furthermore, there is an uncertainty in the SU-96-7 chronology of + or – ca. 20 yrs, given the occurrence of lamina couplets which may correspond to one or two years of growth. An adjustment of minus ten years would suggest a date of AD 1983 for the top-most counted band of the stalagmite. This date fits with the findings of recent lamina counting in the same slab of SU-96-7 which identified that the top 12 years of deposition were missing, suggesting a date of AD 1984 for the top of the sample (I.J. Fairchild, *pers. comm.*).

Hypothetically the relationship between NOM aromaticity and spring climate may be related to the interaction between snow-melt and aquifer recharge in the spring and the change in solution chemistry accompanying the dilution of peat water. This is because the release of fine colloids from soil solids into solution is most strongly controlled by solution chemistry, specifically by changes in surface charge arising from increases in pH and/or reductions in ionic strength (Rosseau *et al*., 2004; Sen and Khilar, 2006). Studies of water table fluctuations on DOM mobilisation from peats suggest that higher groundwater DOM concentrations are linked to reductions in redox potential (i.e. increases in pH) and increases in water table height (Kalbitz *et al*., 2002). Therefore, the relationship between spring T/P and HF:LF index may be linked to higher groundwater in spring associated with snow melt and subsequent aquifer recharge.

This relationship was examined further by comparing the summed two-monthly T/P between February and June 1880 to 1990 (Fig. 8.11). It was expected that the relationship might break down between months if the signal were not genuine. Overall, the agreement between HF:LF and T/P trends persisted between February and May, although the relationship became slightly weaker- the regression between HF:LF and T/P Feb-May had a coefficient of determination of 0.54. Therefore, it is plausible that this correlation is true. Based on the strength of correlation and a hypothetical mechanism for its occurrence, the equation of the regression equation was used to derive a transfer function between the HF:LF index and spring rainfall and this was used to estimate spring rainfall at Assynt over the last millennium using the estimated mean annual temperature of 7.02 ± 0.43 °C minus the difference (0.93) between the mean annual temperature and spring temperature over the instrumental period (Fig. 8.12).

It is difficult to test the validity of the derived spring rainfall record given in Figure 8.12a, because of the paucity of seasonal climate data from either proxies or historical records in the first half of the last millennium (Jones *et al*., 2009). The HF:LF signal in SU-96-7 implies that spring weather was substantially drier between ca. 950 and 1300 AD. This is inconsistent with the rainfall reconstruction of Proctor *et al*. (2000) which indicates a prevailing wetter climate over this period, although both records do indicate a marked shift to low NAO conditions between 1000 and 1100 AD (Fig. 8.12).

The disparity between the two records may reflect important differences between annual (Fig, 8.12B) and seasonal climate changes (Fig. 8.12A), however the extent to which

winter and spring precipitation differs as a function of NAO variability is not clear. There is currently a lack of information on the role of NAO on seasonal precipitation in the North Atlantic climate zone and this issue has received scant consideration in climate reconstructions to date because of the absence of long-term, seasonal resolution records of palaeoprecipitation. Therefore, the palaeoclimatic significance of the record presented in Figure 8.12A cannot be determined and is beyond the scope of this study.

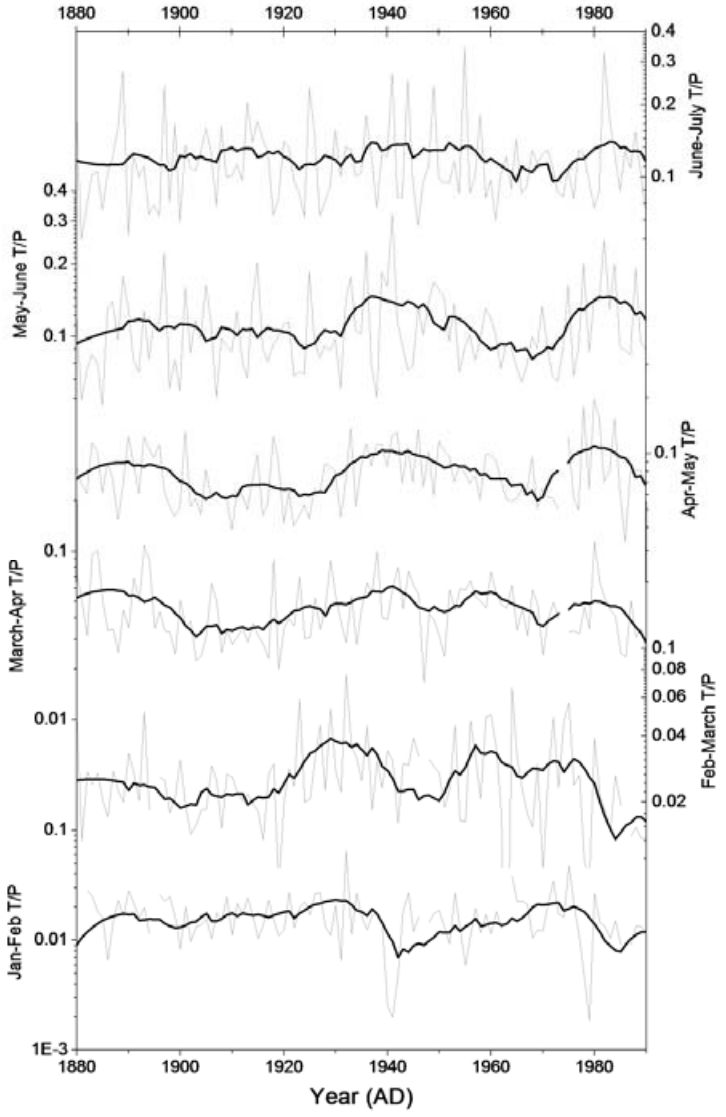

Figure 8.11 Stacked time series of summed two-month T/P data for the period 1880-1990 (thick black line is 20 pt Savitzky-Golay smooth). One outlier corresponding to April T/P in 1974 (2.68) was excluded from these data.

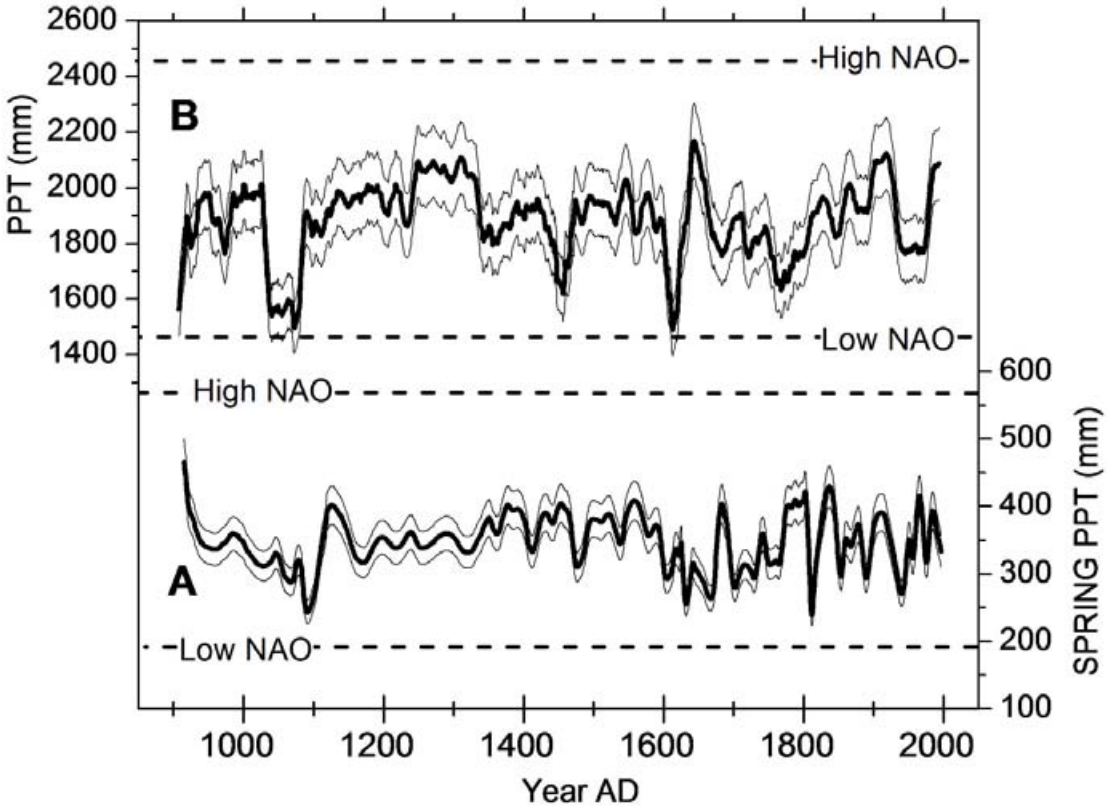

Figure 8.12 (A) Reconstructed Assynt mean spring precipitation record from SU-96-7 and (B) the reconstructed mean annual precipitation record of Proctor *et al*. (2000). Following Proctor *et al*. (2000) the mean and ± standard deviation values for annual temperature of 7.02 minus 0.93 (mean annual T – mean spring T between 1879 and 2004) ± 0.43 °C for 20 year smoothed data (Proctor *et al*. used decadal data) were used to construct the record by using the adjusted mean annual temperature to produce a mean spring precipitation curve (thick line), and the ± 2 sigma limits of temperature to derive upper and lower limits for the possible range of precipitation. Horizontal dotted lines show the two sigma range of annual (B) and spring rainfall recorded in the period of instrumental observations (1879 – 2004).

8.4 SUMMARY

This investigation of the relationship between inferred high-flux and low-flux metal variations in stalagmites and their relationship to environmental changes has demonstrated that HF:LF end-members may be discerned from trace element distributions in speleothems, and that shifts in HF:LF indices may be comprehended in terms of environmental or climatic processes. The interpretive framework developed here for applying HF:LF metal indices in palaeoenvironmental studies is supported by the good agreement between HF:LF indices and the extensive proxy data available. However, the application of colloid-mediated trace element variations in stalagmites to palaeoclimate reconstructions must be built on a solid understanding of the underlying mechanisms including the interaction between the mobilisation of NOM-metal species, infiltration, hydrology and partitioning in speleothem carbonate. Much more work is required to determine whether the HF:LF index recorded in the SU-96-7 stalagmite is a genuine record of spring rainfall and to understand the mechanism underlying the observed correlation.

A consistent Ca signal is a pre-requisite for the proper application of LA-ICP-MS for determining trace element (Tr) concentrations in stalagmites, since Tr concentrations are scaled to Ca as the internal reference element. Replication of LA-ICP-MS Tr profiles in stalagmites is needed in order to confidently interpret Tr signals in terms of palaeoclimate, and ideally the construction of composite records from multiple, coeval samples is required (Jones *et al*., 2009).

9. CONCLUSION

For the first time, the properties of natural aquatic colloids in dripwaters have been explored (Chapter 4 and 5) and the dominant role of colloidal NOM in metal binding and transport in cave waters has been substantiated (Chapter 5 and 6). Colloids and particulates reach caves, despite transport through a karst zone with potential for adsorption, and in both normal (pH 8) and hyperalkaline (pH 9-13) dripwaters, NOM in a range of sizes is involved in trace metal binding and transport (Chapter 5). The background concentration of most transition metals in dripwaters (e.g. Cu, Ni, Co) is linked to the finest size-fraction (Chapter 6) of NOM and this fraction is dominated by humic- and fulvic-like compounds with diameters close to 1 nm (Chapter 4 and 5). Complexation of metals by this fraction appears to occur more strongly than complexes formed at larger sizes (Chapter 5).

Ternary [mineral-ligand-metal] surface-complex formation by humic-like NOM-metal complexes may occur commonly for strongly bound metals, potentially resulting in minimal partitioning of NOM:Tr between solution and crystal (Chapter 7). For example, in the high-pH system studied here, preferential binding of Co to humic-like NOM in dripwater (Chapter 5) resulted in minimal partitioning of NOM-Co complexes into a conjugate stalagmite (Chapter 7), indicating that the efficiency of NOM incorporation from solution was around 5-10%.

Monitoring of dripwaters in contrasting cave systems has demonstrated the occurrence of metal transport by coarse SOM under hydrologically favourable conditions (Chapter 6). Termed 'high-flux', this mode of transport contrasts with the background humic-like or 'low-flux' mode, resulting in shifts in trace metal ratios (e.g. Cu:Ni) which are characteristic of changes in the competitive binding of metals for suitable sites in NOM. This process becomes manifest in speleothems, resulting in high- and low-flux trace metal end-members (Chapter 7 and 8). A method is proposed for the application of high-flux and low-flux metals in speleothems to derive information on the variable transport of relatively more or less aromatic NOM in dripwaters. NOM aromaticity in dripwaters is linked to processes in soils which are ultimately mediated by climate (Chapter 8). In most cases, highly aromatic SOM may be mobilised to a greater extent under wetter conditions, but in the case of caves overlain by blanket peats (e.g. Uamh an Tartair), this is reversed because of the interaction between humification and climate, i.e. humification advances under drier conditions (Chapter 8). Thus, the interpretation of high-flux and low-flux metal ratios in speleothems must be informed by an understanding of the processes occurring in surface environments.

At sites where anthropogenic surface disturbance has occurred, the steady state condition between particle mobilisation and transport is disrupted, leading to long-term, non-linear changes, which take decades to centuries to reach the former equilibrium (Chapter 8). This process becomes manifest as order-of-magnitude increases in HF:LF indices, and may provide useful information (combined with other proxy evidence, e.g.

$\delta^{13}C$) on the recovery of surface ecosystems following large scales environmental changes (Baldini *et al*., 2005) such as glacial episodes (Chapter 8).

The results presented here demonstrate that NOM-facilitated transport of trace metals in cave waters is a widespread phenomenon (Chapter 6). Previous reports of trace metal enrichments in dark, pigmented, or fluorescent growth laminae in speleothems (e.g. Richter *et al*., 2004) and generally higher concentrations in wetter climatic episodes (e.g. Zhou *et al*., 2008; Jo *et al*., 2010), are almost certainly linked to this process. It appears that colloids may accelerate the migration of metals even into deep caves (e.g. Obir cave, Austrian Alps) where intra-annual variations in drip point discharge are negligible (Fairchild *et al*., 2010), and yet a distinct seasonality in colloid-mediated trace metals is detectable, even being resolvable on an event-by-event basis within enriched zones (Fairchild *et al*., 2010).

Thus, NOM-metal transport and surface complex formation in speleothems is potentially a new palaeoenvironmental proxy which complements existing approaches and may be of particular value in palaeohydrological studies and in targeting compound-specific investigations such as biomarker studies.

REFERENCES

Alberts, J. J. and Filip, Z. (1998) Metal binding in estuarine humic and fulvic acids: FTIR analysis of humic acid-metal complexes. *Environmental Technology* **19**, 923-931.

Alcacio, T. E., Hesterberg, D., Chou, J. W., Martin, J. D., Beauchemin, S., and Sayers, D. E. (2001) Molecular scale characteristics of Cu(II) bonding in goethite-humate complexes. *Geochimica et Cosmochimica Acta* **65**, 1355-1366.

Allard, T., Menguy, N., Salomon, J., Calligaro, T., Weber, T., Calas, G., and Benedetti, M. F. (2004) Revealing forms of iron in river-borne material from major tropical rivers of the Amazon Basin (Brazil). *Geochimica et Cosmochimica Acta* **68**, 3079-3094.

Andersson, K., Dahlqvist, R., Turner, D., Stolpe, B., Larsson, T., Ingri, J., and Andersson, P. (2006) Colloidal rare earth elements in a boreal river: Changing sources and distributions during the spring flood. *Geochimica et Cosmochimica Acta* **70**, 3261-3274.

Apolloni, L. (1996) Aspetti dell'impatto antropico nella parte alta dell'Altopiano dei Sette Comini. Studi Trentini di Scienze Naturali. *Acta Geologica* **70**(1993), 153–164.

Ashman, M. R. and Puri, G. (2002) *Essential Soil Science: a clear and concise introduction to soil science*. Blackwell, Malden, USA.

Assemi, S., Hartley, P. G., Scales, P. J., and Beckett, R. (2004) Investigation of adsorbed humic substances using atomic force microscopy. *Colloids and Surfaces a-Physicochemical and Engineering Aspects* **248**, 17-23.

Atteia, O. (1998) Evolution of size distributions of natural particles during aggregation: modelling versus field results. *Colloids and Surfaces A: Physicochemical and Engineering Aspects* **139**, 171-188.

Atteia, O. and Kozel, R. (1997) Particle size distributions in waters from a karstic aquifer: from particles to colloids. *Journal of Hydrology* **201**, 102-119.

Atteia, O., Perret, D., Adatte, T., Kozel, R., and Rossi, P. (1998) Characterization of natural colloids from a river and spring in a karstic basin. *Environmental Geology* **34**, 257-269.

Avena, M. J. and De Pauli, C. P. (1998) Proton adsorption and electrokinetics of an Argentinean montmorillonite. *Journal of Colloid and Interface Science* **202**, 195-204.

Avena, M. J., Mariscal, M. M., and De Pauli, C. P. (2003) Proton binding at clay surfaces in water. *Applied Clay Science Clay Minerals and the Environment* **24**, 3-9.

Baalousha, M. (2009) Aggregation and disaggregation of iron oxide nanoparticles: Influence of particle concentration, pH and natural organic matter. *Science of the Total Environment* **407**, 2093-2101.

Baalousha, M., Kammer, F. V. D., Motelica-Heino, M., Baborowski, M., Hofmeister, C., and Le Coustumer, P. (2006) Size-based speciation of natural colloidal particles by flow field flow fractionation, inductively coupled plasma-mass spectroscopy, and transmission electron microscopy/X-ray energy dispersive spectroscopy: Colloids-trace element interaction. *Environmental Science & Technology* **40**, 2156-2162.

Baalousha, M. and Lead, J. R. (2007) Characterization of natural aquatic colloids (< 5 nm) by flow-field flow fractionation and atomic force microscopy. *Environmental Science & Technology* **41**, 1111-1117.

Baalousha, M., Manciulea, A., Cumberland, S., Kendall, K., and Lead, J. R. (2008) Aggregation and surface properties of iron oxide nanoparticles: Influence of pH and natural organic matter. *Environmental Toxicology and Chemistry* **27**, 1875-1882.

Baalousha, M., Le Coustumer, P., Jones, I., and Lead, J. R. (2010) Characterisation of structural and surface speciation of representative commercially available cerium oxide nanoparticles. *Environmental Chemistry* **7**, 377-385.

Baeyens, B. and Bradbury, M. H. (1997) A mechanistic description of Ni and Zn sorption on Na-montmorillonite .1. Titration and sorption measurements. *Journal of Contaminant Hydrology* **27**, 199-222.

Baker, A. (2001) Fluorescence Excitation-Emission Matrix Characterization of Some Sewage-Impacted Rivers. *Environmental Science & Technology* **35**, 948-953.

Baker, A. (2005) Thermal fluorescence quenching properties of dissolved organic matter. *Water Research* **39**, 4405-4412.

Baker, A., Smart, P. L., Edwards, R. L., and Richards, D. A. (1993) Annual Growth Banding in a Cave Stalagmite. *Nature* **364**, 518-520.

Baker, A., Barnes, W. L., and Smart, P. L. (1997a) Variations in the discharge and organic matter content of stalagmite drip waters in Lower Cave, Bristol. *Hydrological Processes* **11**, 1541-1555.

Baker, A., Ito, E., Smart, P. L., and McEwan, R. F. (1997b) Elevated and variable values of C-13 in speleothems in a British cave system. *Chemical Geology* **136**, 263-270.

Baker, A., Jones, G., and Genty, D. (1998) *Poole's Cavern Stalagmites*. British Cave Research Association Symposium. University of Keele, 7th March 1998.

Baker, A., Caseldine, C. J., Gilmour, M. A., Charman, D., Proctor, C. J., Hawkesworth, C. J., Phillips, N. (1999a) Stalagmite luminescence and peat humification records of palaeomoisture for the last 2500 years. *Earth and Planetary Science Letters* **165**, 157-162.

Baker, A., Mockler, N. J., and Barnes, W. L. (1999b) Fluorescence intensity variations of speleothem-forming groundwaters: Implications for paleoclimate reconstruction. *Water Resources Research* **35**, 407-413.

Baker, A., Proctor, C. J., and Barnes, W. L. (1999c) Variations in stalagmite luminescence laminae structure at Poole's Cavern, England, AD 1910-1996: calibration of a palaeoprecipitation proxy. *Holocene* **9**, 683-688.

Baker, A. and Genty, D. (1999) Fluorescence wavelength and intensity variations of cave waters. *Journal of Hydrology* **217**, 19-34.

Baker, A., Genty, D., and Fairchild, I. J. (2000) Hydrological characterisation of stalagmite dripwaters at Grotte de Villars, Dordogne, by the analysis of inorganic species and luminescent organic matter. *Hydrology and Earth System Sciences* **4**, 439-449.

Baker, A., Proctor, C. J., and Barnes, W. L. (2002) Stalagmite lamina doublets: A 1000 year proxy record of severe winters in northwest Scotland? *International Journal of Climatology* **22**, 1339-1345.

Baker, A., Tipping, E., Thacker, S. A., and Gondar, D. (2008) Relating dissolved organic matter fluorescence and functional properties. *Chemosphere* **73**, 1765-1772.

Baker, A., Wilson, R., Fairchild, I. J., Franke, J., Spötl, C., Mattey, D., Trouet, V., and Fuller, L. (2011) High resolution $\delta^{18}O$ and $\delta^{13}C$ records from an annually laminated Scottish stalagmite and relationship with last millennium climate. *Global and Planetary Change.* In Press, Corrected Proof.

Baldini, J. U. L., McDermott, F., Baker, A., Baldini, L. M., Mattey, D. P., and Railsback, L. B. (2005) Biomass effects on stalagmite growth and isotope ratios: A 20th century analogue from Wiltshire, England. *Earth and Planetary Science Letters* **240**, 486-494.

Ban, F. M., Pan, G. X., Zhu, J., Cai, B. G., and Tan, M. (2008) Temporal and spatial variations in the discharge and dissolved organic carbon of drip waters in Beijing Shihua Cave, China. *Hydrological Processes* **22**, 3749-3758.

Bargar, J. R., Brown, G. E., and Parks, G. A. (1997) Surface complexation of Pb(II) at oxide-water interfaces: I. XAFS and bond-valence determination of

mononuclear and polynuclear Pb(II) sorption products on aluminum oxides. *Geochimica et Cosmochimica Acta* **61**, 2617-2637.

Bashford, C. L. and Harris, D.A. (1987) *Spectrophotometry and Spectrofluorimetry*. The Practical approach series. IRL Press, Oxford, Washingon, D.C.

Beckett, R. (1987) The application of field-flow fractionation techniques to the characterization of complex environmental samples. *Environmental Technology Letters* **8**, 339-354.

Beckett, R., Jue, Z., and Giddings, J. C. (1987) Determination of molecular weight distributions of fulvic and humic acids using flow field-flow fractionation. *Environmental Science & Technology* **21**, 289-295.

Beckett, R. and Schimpf, M. (2000) Characterisation of humic substances. In *Field flow fractionation handbook* (eds. M. Schimpf, K. Caldwell and C. J. Giddings). Wiley-Interscience, Inc., New York. pp. 497-534.

Bekhit, H. M., El-Kordy, M. A., and Hassan, A. E. (2009) Contaminant transport in groundwater in the presence of colloids and bacteria: Model development and verification. *Journal of Contaminant Hydrology* **108**, 152-167.

Benedetti, M. F., Milne, C. J., Kinniburgh, D. G., Vanriemsdijk, W. H., and Koopal, L. K. (1995) Metal-ion binding to humic substances - application of the nonideal competitive adsorption model. *Environmental Science & Technology* **29**, 446-457.

Benedetti, M. F., Ranville, J. F., Allard, T., Bednar, A. J., and Menguy, N. (2003) The iron status in colloidal matter from the Rio Negro, Brasil. *Colloids and Surfaces a-Physicochemical and Engineering Aspects* **217**, 1-9.

Blyth, A. J., Baker, A., Collins, M. J., Penkman, K. E. H., Gilmour, M. A., Moss, J. S., Genty, D., and Drysdale, R. N. (2008) Molecular organic matter in speleothems and its potential as an environmental proxy. *Quaternary Science Reviews* **27**, 905-921.

Borsato, A. (1997) Dripwater monitoring at Grotta di Ernesto (NE Italy): a contribution to the understanding of karst hydrology and the kinetics of carbonate dissolution. *Proceedings of the 6th Conference on Limestone Hydrology and Fissured Media*, vol. 2: La Chaux de Fonds, International Union of Speleology: Switzerland; 57–60.

Borsato, A., Frisia, S., Fairchild, I. J., Somogyi, A., and Susini, J. (2007) Trace element distribution in annual stalagmite laminae mapped by micrometer-resolution X-ray fluorescence: Implications for incorporation of environmentally significant species. *Geochimica et Cosmochimica Acta* **71**, 1494-1512.

Böttcher, M. E. and Dietzel, M. (2010) Metal-ion partitioning during low-temperature precipitation and dissolution of anhydrous carbonates and sulfates. *EMU notes in mineralogy* **10**: 139-187.

Bourg, I. C., Sposito, G., and Bourg, A. C. M. (2007) Modeling the acid-base surface chemistry of montmorillonite. *Journal of Colloid and Interface Science* **312**, 297-310.

Boyanov, M. I., Kelly, S. D., Kemner, K. M., Bunker, B. A., Fein, J. B., and Fowle, D. A. (2003) Adsorption of cadmium to Bacillus subtilis bacterial cell walls: a pH-dependent X-ray absorption fine structure spectroscopy study. *Geochimica et Cosmochimica Acta* **67**, 3299-3311.

Bradl, H. B. (2004) Adsorption of heavy metal ions on soils and soils constituents. *Journal of Colloid and Interface Science* **277**, 1-18.

Brady, N. C. and Weil, R. R. (2002) *The nature and properties of soils*. Prentice Hall, New Jersey.

Buerge-Weirich, D., Hari, R., Xue, H. B., Behra, P., and Sigg, L. (2002) Adsorption of Cu, Cd, and Ni on goethite in the presence of natural groundwater ligands. *Environmental Science & Technology* **36**, 328-336.

Buffle, J. and Leppard, G. G. (1995) Characterization of Aquatic Colloids and Macromolecules .1. Structure and Behavior of Colloidal Material. *Environmental Science & Technology* **29**, 2169-2175.

Buffle, J., Wilkinson, K. J., Stoll, S., Filella, M., and Zhang, J. W. (1998) A generalized description of aquatic colloidal interactions: The three-colloidal component approach. *Environmental Science & Technology* **32**, 2887-2899.

Busenberg, E. and Plummer, L. N. (1985) Kinetic and thermodynamic factors controlling the distrubution of SO4(2-) and Na+ in calcites and selected aragonites. *Geochimica et Cosmochimica Acta* **49**, 713-725.

Carstea, E. M., Baker, A., Pavelescu, G., and Boomer, I. (2009) Continuous fluorescence assessment of organic matter variability on the Bournbrook River, Birmingham, UK. *Hydrological Processes* **23**, 1937-1946.

Casty, C., Wanner, H., Luterbacher, J., Esper, J., and Bohm, R. (2005) Temperature and precipitation variability in the European Alps since 1500. *International Journal of Climatology* **25**, 1855-1880.

Cerda, C. M. (1987) Mobilization of Kaolinite Fines in Porous-Media. *Colloids and Surfaces* **27**, 219-241.

Chada, V.G.R., Hausner, D.B., Strongin, D.R., Rouff, A.A. & Reeder, R.J. (2005) Divalent Cd and Pb uptake on calcite {10bar14} cleavage faces: An XPS and AFM study. *Journal of Colloid and Interface Science*, **288**, 350-360.

Chen, C. C. and Hayes, K. F. (1999) X-ray absorption spectroscopy investigation of aqueous Co(II) and Sr(II) sorption at clay-water interfaces. *Geochimica et Cosmochimica Acta* **63**, 3205-3215.

Chen, G., Flury, M., Harsh, J. B., and Lichtner, P. C. (2005) Colloid-facilitated transport of cesium in variably saturated Hanford sediments. *Environmental Science & Technology* **39**, 3435-3442.

Cheng, T. and Saiers, J. E. (2010) Colloid-Facilitated Transport of Cesium in Vadose-Zone Sediments: The Importance of Flow Transients. *Environmental Science & Technology* **44**, 7443-7449.

Clark, I.D., Fontes, J.-C. and Fritz, P. (1992) Stable isotope disequilibria in travertine from high pH waters: laboratory investigations and field observations from Oman. *Geochimica et Cosmochimica Acta,* **56**, 2041-2050.

Collins, C. R., Ragnarsdottir, K. V., and Sherman, D. M. (1999a) Effect of inorganic and organic ligands on the mechanism of cadmium sorption to goethite. *Geochimica et Cosmochimica Acta* **63**, 2989-3002.

Collins, C. R., Sherman, D. M., and Ragnarsdottir, K. V. (1999b) Surface complexation of Hg^{2+} on goethite: Mechanism from EXAFS spectroscopy and density functional calculations. *Journal of Colloid and Interface Science* **219**, 345-350.

Colman, A. (1997) Prediction of summer central England temperature from preceding North Atlantic winter sea surface temperature. *International Journal of Climatology* **17**, 1285–1300.

Companys, E., Puy, J., and Galceran, J. (2007) Humic acid complexation to Zn and Cd determined with the new electroanalytical technique AGNES. *Environmental Chemistry* **4**, 347-354.

Cruz, F. W., Karmann, I., Magdaleno, G. B., Coichev, N., and Viana, O. (2005) Influence of hydrological and climatic parameters on spatial-temporal variability of fluorescence intensity and DOC of karst percolation waters in the Santana Cave System, Southeastern Brazil. *Journal of Hydrology* **302**, 1-12.

Dai, M., Martin, J. M., and Cauwet, G. (1995) The significant role of colloids in the transport and transformation of organic-carbon and associated trace-metals (Cd, Cu and Ni) in the Rhone Delta (France). *Marine Chemistry* **51**, 159-175.

Daughney, C. J., Siciliano, S. D., Rencz, A. N., Lean, D., and Fortin, D. (2002) Hg(II) adsorption by bacteria: A surface complexation model and its application to

shallow acidic lakes and wetlands in Kejimkujik National Park, Nova Scotia, Canada. *Environmental Science & Technology* **36**, 1546-1553.

Davis, G., Ghabbour, E.A., Cherkasskiy, A. (2001) Tight metal binding by solid phase peat and soil humic acids. In: *Humic Substances and Chemical Contaminants*. Proceedings of a workshop and symposium cosponsored by the International Humic Substances Society, the Soil Science Society of America, and the American Society of Agronomy, Anaheim, USA, 26-27 October 1997 2001 pp. 371-395.

Davison, W. and Zhang, H. (1994) In-situ speciation measurements of trace components in natural-waters using thin-film gels *Nature* **367**, 546-548.

Diegoli, S., Manciulea, A. L., Begum, S., Jones, I. P., Lead, J. R., and Preece, J. A. (2008) Interaction between manufactured gold nanoparticles and naturally occurring organic macromolecules. *Science of the Total Environment* **402**, 51-61.

Doucet, F. J., Lead, J.R., and Santschi, P.H. (2007) Colloid-Trace Element Interactions in Aquatic Systems. In: Wilkinson, K. and Lead, J. (Ed.), *Environmental Colloids and Particles: Behaviour, Separation and Characterisation.* Wiley Inter-Science, Hoboken, 702 pp.

Duc, M., Gaboriaud, F., and Thomas, F. (2005) Sensitivity of the acid-base properties of clays to the methods of preparation and measurement - 2. Evidence from continuous potentiometric titrations. *Journal of Colloid and Interface Science* **289**, 148-156.

Einsiedl, F., Hertkorn, N., Wolf, M., Frommberger, M., Schmitt-Kopplin, P., and Koch, B. P. (2007) Rapid biotic molecular transformation of fulvic acids in a karst aquifer. *Geochimica et Cosmochimica Acta* **71**, 5474-5482.

El-Farhan, Y. H., Denovio, N. M., Herman, J. S., and Hornberger, G. M. (2000) Mobilization and transport of soil particles during infiltration experiments in an agricultural field, Shenandoah Valley, Virginia. *Environmental Science & Technology* **34**, 3555-3559.

Elliott, S., Lead, J. R., and Baker, A. (2006) Thermal quenching of fluorescence of freshwater, planktonic bacteria. *Analytica Chimica Acta* **564**, 219-225.

Elzinga, E. J. and Reeder, R. J. (2002) X-ray absorption spectroscopy study of Cu2+ and Zn2+ adsorption complexes at the calcite surface: Implications for site-specific metal incorporation preferences during calcite crystal growth. *Geochimica et Cosmochimica Acta* **66**, 3943-3954.

Engel, A. S., Stern, L. A., and Bennett, P. C. (2004) Microbial contributions to cave formation: New insights into sulfuric acid speleogenesis. *Geology* **32**, 369-372.

Fairchild, I. J. and Treble, P. C. (2009) Trace elements in speleothems as recorders of environmental change. *Quaternary Science Reviews* **28**, 449-468.

Fairchild, I. J. and Hartland, A. (2010) Trace element variations in stalagmites: controls by climate and by karst system processes. *EMU notes in mineralogy* **10**: 259-287.

Fairchild, I. J., Borsato, A., Tooth, A. F., Frisia, S., Hawkesworth, C. J., Huang, Y. M., McDermott, F., and Spiro, B. (2000) Controls on trace element (Sr-Mg) compositions of carbonate cave waters: implications for speleothem climatic records. *Chemical Geology* **166**, 255-269.

Fairchild, I. J., Baker, A., Borsato, A., Frisia, S., Hinton, R. W., McDermott, F., and Tooth, A. F. (2001) Annual to sub-annual resolution of multiple trace-element trends in speleothems. *Journal of the Geological Society* **158**, 831-841.

Fairchild, I. J., Smith, C. L., Baker, A., Fuller, L., Spotl, C., Mattey, D., McDermott, F. (2006a) Modification and preservation of environmental signals in speleothems. *Earth-Science Reviews* **75**, 105-153.

Fairchild, I. J., Tuckwell, G. W., Baker, A., and Tooth, A. F. (2006b) Modelling of dripwater hydrology and hydrogeochemistry in a weakly karstified aquifer (Bath, UK): Implications for climate change studies. *Journal of Hydrology* **321**, 213-231.

Fairchild, I. J., Frisia, S., Borsato, A. and Tooth, A.F. (2007) Speleothems. In: Nash, D. J. and McLaren, S.J. (Ed.), *Geochemical Sediments and Landscapes.* Blackwells, Oxford, 488 pp.

Fairchild, I. J., Loader, N. J., Wynn, P. M., Frisia, S., Thomas, P. A., Lageard, J. G. A., De Momi, A., Hartland, A., Borsato, A., La Porta, N., and Susini, J. (2009) Sulfur Fixation in Wood Mapped by Synchrotron X-ray Studies: Implications for Environmental Archives. *Environmental Science & Technology* **43**, 1310-1315.

Fairchild, I. J., Spotl, C., Frisia, S., Borsato, A., Susini, J., Wynn, P. M., Cauzid, J., and EIMF (2010) Petrology and geochemistry of annually laminated stalagmites from an Alpine cave (Obir, Austria): seasonal cave physiology. Geological Society, London, Special Publications **336**, 295-321.

Farnleitner, A. H., Wilhartitz, I., Ryzinska, G., Kirschner, A. K. T., Stadler, H., Burtscher, M. M., Hornek, R., Szewzyk, U., Herndl, G., and Mach, R. L. (2005) Bacterial dynamics in spring water of alpine karst aquifers indicates the presence of stable autochthonous microbial endokarst communities. *Environmental Microbiology* **7**, 1248-1259.

Fein, J. B. (2002) The effects of ternary surface complexes on the adsorption of metal cations and organic acids onto mineral surfaces. In: Hellmann,R. and Wood, S.

A. (Ed.), *Water-rock interactions, ore deposits, and environmental geochemistry. A tribute to David A. Crerar.* The Geochemical Society, St. Louis.

Filella, M. (2008) NOM site binding heterogeneity in natural waters: Discrete approaches. *Journal of Molecular Liquids* **143**, 42-51.

Ford, D. C. and Williams, P. (2007) Karst Hydrogeology and Geomorphology. John Wiley & Sons, Oxford.

Ford, T. D. and Gunn, J. (1992) *Caves and Karst of the Peak District*. BCRA Cave Studies, Vol.3.

Frisia, S., Borsato, A., Fairchild, I. J., and McDermott, F. (2000) Calcite fabrics, growth mechanisms, and environments of formation in speleothems from the Italian Alps and southwestern Ireland. *Journal of Sedimentary Research* **70**, 1183-1196.

Frisia, S., Borsato, A., Preto, N., and McDermott, F. (2003) Late Holocene annual growth in three Alpine stalagmites records the influence of solar activity and the North Atlantic Oscillation on winter climate. *Earth and Planetary Science Letters* **216**, 411-424.

Frisia, S., Borsato, A., Fairchild, I. J., and Susini, J. (2005) Variations in atmospheric sulphate recorded in stalagmites by synchrotron micro-XU and XANES analyses. *Earth and Planetary Science Letters* **235**, 729-740.

Frisia, S., Fairchild, I. J., Fohlmeister, J., Miorandi, R., Spotl, C., and Borsato, A. (2011) Carbon mass-balance modelling and carbon isotope exchange processes in dynamic caves. *Geochimica et Cosmochimica Acta* **75**, 380-400.

Gabrovsek, F., Menne, B., and Dreybrodt, W. (2000) A model of early evolution of karst conduits affected by subterranean CO_2 sources. *Environmental Geology* **39**, 531-543.

Gaillard, J. F. (2007) Probing Environmental Colloids and Particles with X-rays. In: Wilkinson, K. and Lead, J. (Ed.), *Environmental Colloids and Particles: Behaviour, Separation and Characterisation.* Wiley Inter-Science, Hoboken,702 pp.

Garmo, O. A., Lehto, N. J., Zhang, H., Davison, W., Royset, O., and Steinnes, E. (2006) Dynamic aspects of DGT as demonstrated by experiments with lanthanide complexes of a multidentate ligand. *Environmental Science & Technology* **40**, 4754-4760.

Genty, D., Vokal, B., Obelic, B., and Massault, M. (1998) Bomb C-14 time history recorded in two modern stalagmites - importance for soil organic matter dynamics and bomb C-14 distribution over continents. *Earth and Planetary Science Letters* **160**, 795-809.

Genty, D., Baker, A., Massault, M., Proctor, C., Gilmour, M., Pons-Branchu, E., and Hamelin, B. (2001) Dead carbon in stalagmites: Carbonate bedrock paleodissolution vs. ageing of soil organic matter. Implications for C-13 variations in speleothems. *Geochimica et Cosmochimica Acta* **65**, 3443-3457.

Gerrard, J. (2000) *Fundamentals of soils*. Routledge, London. 212 pp.

Gibson, C. T., Turner, I. J., Roberts, C. J., and Lead, J. R. (2007) Quantifying the dimensions of nanoscale organic surface layers in natural waters. *Environmental Science & Technology* **41**, 1339-1344.

Gill, D. W. and Beck, J. S. (1991) *Caves of the Peak District*. Lancaster: Dalesman. 272 pp.

Gimpel, J., Zhang, H., Davison, W., and Edwards, A. C. (2003) In situ trace metal speciation in lake surface waters using DGT, dialysis, and filtration. *Environmental Science & Technology* **37**, 138-146.

Glaus, M. A., Hummel, W., and Van Loon, L. R. (2000) Trace metal-humate interactions. I. Experimental determination of conditional stability constants. *Applied Geochemistry* **15**, 953-973.

Godelitsas, A., Astilleros, J.M., Hallam, K., Harissopoulos, S. & Putnis, A. (2003) Interaction of calcium carbonates with lead in aqueous solutions. *Environmental Science and Technology*, **37**, 3351-3360.

Goppert, N. and Goldscheider, N. (2008) Solute and colloid transport in karst conduits under low- and high-flow conditions. *Ground Water* **46**, 61-68.

Grant, R., Laubel, A., Kronvang, B., Andersen, H. E., Svendsen, L. M., and Fuglsang, A. (1996) Loss of dissolved and particulate phosphorus from arable catchments by subsurface drainage. *Water Research* **30**, 2633-2642.

Groenenberg, J. E., Koopmans, G. F., and Comans, R. N. J. (2010) Uncertainty Analysis of the Nonideal Competitive Adsorption-Donnan Model: Effects of Dissolved Organic Matter Variability on Predicted Metal Speciation in Soil Solution. *Environmental Science & Technology* **44**, 1340-1346.

Hartland, A., Fairchild, I.J., Lead, J.R., Dominguez-Villar, D., Baker, A., Gunn, J., Baalousha, M., and Ju-Nam, Y. (2010a) The dripwaters and speleothems of Poole's Cavern: a review of recent and ongoing research. *Cave and Karst Science* **36**, 37-46.

Heathwaite, L., Haygarth, P., Matthews, R., Preedy, N., and Butler, P. (2005) Evaluating colloidal phosphorus delivery to surface waters from diffuse agricultural sources. *Journal of Environmental Quality* **34**, 287-298.

Heinrich, C. A., Pettke, T., Halter, W. E., Aigner-Torres, M., Audétat, A., Günther, D., Hattendorf, B., Bleiner, D., Guillong, M., and Horn, I. (2003) Quantitative multi-element analysis of minerals, fluid and melt inclusions by laser-ablation inductively-coupled-plasma mass-spectrometry. *Geochimica et Cosmochimica Acta* **67**, 3473-3497.

Hering, J. G. (1995) Interaction of organic-matter with mineral surfaces - effects on geochemical processes at the mineral-water interface. *Aquatic Chemistry* **244**, 95-110.

Hiemstra, T., Antelo, J., van Rotterdam, A. M. D., and van Riemsdijk, W. H. (2010) Nanoparticles in natural systems II: The natural oxide fraction at interaction with natural organic matter and phosphate. *Geochimica et Cosmochimica Acta* **74**, 59-69.

Hoffmann, M. R. (1981) Thermodynamic, kinetic, and extrathermodynamic considerations in the development of equilibrium models for aquatic systems. *Environmental Science & Technology* **15**, 345-353.

Holl, B. S., Fiedler, S., Jungkunst, H. F., Kalbitz, K., Freibauer, A., Drosler, M., and Stahr, K. (2009) Characteristics of dissolved organic matter following 20 years of peatland restoration. *Science of the Total Environment* **408**, 78-83.

Howard, A. G. (1998) *Aquatic Environmental Chemistry*. Oxford University Press, Oxford. 96 pp.

Hu, C. Y., Huang, J. H., Fang, N. Q., Xie, S. C., Henderson, G. M., and Cai, Y. J. (2005) Adsorbed silica in stalagmite carbonate and its relationship to past rainfall. *Geochimica et Cosmochimica Acta* **69**, 2285-2292.

Huang, H. M., Fairchild, I. J., Borsato, A., Frisia, S., Cassidy, N. J., McDermott, F., and Hawkesworth, C. J. (2001) Seasonal variations in Sr, Mg and P in modern speleothems (Grotta di Ernesto, Italy). *Chemical Geology* **175**, 429-448.

Hudson, N., Baker, A., and Reynolds, D. (2007) Fluorescence analysis of dissolved organic matter in natural, waste and polluted waters - A review. *River Research and Applications* **23**, 631-649.

Hummel, W., Glaus, M. A., and Van Loon, L. R. (2000) Trace metal-humate interactions. II. The "conservative roof" model and its application. *Applied Geochemistry* **15**, 975-1001.

Hurrell, J.W. (1995) Decadal trends in the North Atlantic Oscillation: regional temperatures and precipitation. *Science* **269**, 676–679.

Inskeep, W. P. and Bloom, P. R. (1986) Kinetics of calcite precipitation in the presence of water-soluble organic-ligands. *Soil Science Society of America Journal* **50**, 1167-1172.

Jacobsen, O. H., Moldrup, P., Larsen, C., Konnerup, L., and Petersen, L. W. (1997) Particle transport in macropores of undisturbed soil columns. *Journal of Hydrology* **196**, 185-203.

Jenny, H. (1941) *Factors of soil formation: a system of quantitative pedology*. Dover Publications, New York. 191 pp.

Jo, K. N., Woo, K. S., Hong, G. H., Kim, S. H., and Suk, B. C. (2010) Rainfall and hydrological controls on speleothem geochemistry during climatic events (droughts and typhoons): An example from Seopdong Cave, Republic of Korea. *Earth and Planetary Science Letters* **295**, 441-450.

Jones, P. D., Briffa, K. R., Osborn, T. J., Lough, J. M., van Ommen, T. D., Vinther, B. M., Luterbacher, J., Wahl, E. R., Zwiers, F. W., Mann, M. E., Schmidt, G. A., Ammann, C. M., Buckley, B. M., Cobb, K. M., Esper, J., Goosse, H., Graham, N., Jansen, E., Kiefer, T., Kull, C., Kattel, M., Mosley-Thompson, E., Overpeck, J. T., Riedwyl, N., Schulz, M., Tudhope, A. W., Villalba, R., Wanner, H., Wolff, E., and Xoplaki, E. (2009) High-resolution palaeoclimatology of the last millennium: a review of current status and future prospects. *The Holocene* **19**, 3-49.

Kalbitz, K., Rupp, H., and Meissner, R. (2002) N,P- and DOC-dynamics in soil and groundwater after restoration of intensively cultivated fens. *Wetlands in Central Europe*, 99-116.

Kaplan, D. I., Bertsch, P. M., Adriano, D. C., and Miller, W. P. (1993) Soil-borne mobile colloids as influenced by water flow and organic carbon. *Environmental Science & Technology* **27**, 1193-1200.

Kaplan, D. I., Sumner, M. E., Bertsch, P. M., and Adriano, D. C. (1996) Chemical conditions conducive to the release of mobile colloids from ultisol profiles. *Soil Science Society of America Journal* **60**, 269-274.

Kaufhold, S. and Dohrmann, R. (2008) Detachment of colloidal particles from bentonites in water. *Applied Clay Science* **39**, 50-59.

Kelleher, B. P. and Simpson, A. J. (2006) Humic Substances in Soils: Are They Really Chemically Distinct? *Environmental Science & Technology* **40**, 4605-4611.

Kerndorff, H. and Schnitzer, M. (1980) Sorption of metals on humic-acid. *Geochimica et Cosmochimica Acta* **44**, 1701-1708.

Kersting, A. B., Efurd, D. W., Finnegan, D. L., Rokop, D. J., Smith, D. K., Thompson, J. L. (1999) Migration of plutonium in ground water at the Nevada Test Site. *Nature* **397**, 56-59.

Khilar, K. C. and Fogler, H. S. (1984) The Existence of a Critical Salt Concentration for Particle Release. *Journal of Colloid and Interface Science* **101**, 214-224.

Kia, S. F., Fogler, H. S., and Reed, M. G. (1987) Effect of pH on Colloidally Induced Fines Migration. *Journal of Colloid and Interface Science* **118**, 158-168.

Kim, Y., James Kirkpatrick, R., and Cygan, R. T. (1996) 133Cs NMR study of cesium on the surfaces of kaolinite and illite. *Geochimica et Cosmochimica Acta* **60**, 4059-4074.

Kinniburgh, D. G., van Riemsdijk, W. H., Koopal, L. K., Borkovec, M., Benedetti, M. F., Avena, M. J. (1999) Ion binding to natural organic matter: competition, heterogeneity, stoichiometry and thermodynamic consistency. *Colloids and Surfaces a-Physicochemical and Engineering Aspects* **151**, 147-166.

Laegdsmand, M., Villholth, K. G., Ullum, M., and Jensen, K. H. (1999) Processes of colloid mobilization and transport in macroporous soil monoliths. *Geoderma* **93**, 33-59.

Lakshtanov, L. Z. and Stipp, S. L. S. (2007) Experimental study of nickel(II) interaction with calcite: Adsorption and coprecipitation. *Geochimica et Cosmochimica Acta* **71**, 3686-3697.

Lamelas, C., Avaltroni, F., Benedetti, M., Wilkinson, K. J., and Slaveykova, V. I. (2005a) Quantifying Pb and Cd complexation by alginates and the role of metal binding on macromolecular aggregation. *Biomacromolecules* **6**, 2756-2764.

Lamelas, C., Wilkinson, K. J., and Slaveykova, V. I. (2005b) Influence of the composition of natural organic matter on Pb bioavailability to microalgae. *Environmental Science & Technology* **39**, 6109-6116.

Lead, J. R., Davison, W., Hamilton-Taylor, J., and Buffle, J. (1997) Characterising Colloidal Material in Natural Waters. *Analytical Geochemistry* **3**, 213-232.

Lead, J. R., Hamilton-Taylor, J., Davison, W., and Harper, M. (1999) Trace metal sorption by natural particles and coarse colloids. *Geochimica et Cosmochimica Acta* **63**, 1661-1670.

Lead, J. R., Wilkinson, K. J., Balnois, E., Cutak, B. J., Larive, C. K., Assemi, S., and Beckett, R. (2000) Diffusion coefficients and polydispersities of the Suwannee River fulvic acid: Comparison of fluorescence correlation spectroscopy, pulsed-field gradient nuclear magnetic resonance, and flow field-flow fractionation. *Environmental Science & Technology* **34**, 3508-3513.

Lead, J. R., Starchev, K., and Wilkinson, K. J. (2003) Diffusion coefficients of humic substances in agarose gel and in water. *Environmental Science & Technology* **37**, 482-487.

Lead, J. R., Muirhead, D., and Gibson, C. T. (2005) Characterization of freshwater natural aquatic colloids by atomic force microscopy (AFM). *Environmental Science & Technology* **39**, 6930-6936.

Lead, J. R., De Momi, A., Goula, G., and Baker, A. (2006) Fractionation of freshwater colloids and particles by SPLITT: Analysis by electron microscopy and 3D excitation-emission matrix fluorescence. *Analytical Chemistry* **78**, 3609-3615.

Lead, J. R. and Wilkinson, K. J. (2006) Aquatic colloids and nanoparticles: Current knowledge and future trends. *Environmental Chemistry* **3**, 159-171.

Lee, Y. J., Elzinga, E. J., and Reeder, R. J. (2005) Cu(II) adsorption at the calcite-water interface in the presence of natural organic matter: Kinetic studies and molecular-scale characterization. *Geochimica et Cosmochimica Acta* **69**, 49-61.

Le Chevalier, S. (1977) The historical development of limeburning and waste deposition on Grin Low, Derbyshire. (Derbyshire Archaeological Society, Derby).

Lehmann, J., Solomon, D., Kinyangi, J., Dathe, L., Wirick, S., and Jacobsen, C. (2008) Spatial complexity of soil organic matter forms at nanometre scales. *Nature Geoscience* **1**, 238-242.

Leppard, G. G., Burnison, B. K., and Buffle, J. (1990) Transmission electron-microscopy of the natural organic-matter of surface waters. *Analytica Chimica Acta* **232**, 107-121.

Liu, R. and Lead, J. R. (2006) Partial validation of cross flow ultrafiltration by atomic force microscopy. *Analytical Chemistry* **78**, 8105-8112.

Liu, R., Lead, J. R., and Baker, A. (2007) Fluorescence characterization of cross flow ultrafiltration derived freshwater colloidal and dissolved organic matter. *Chemosphere* **68**, 1304-1311.

Longerich, H. P., Jackson, S. E., and Gunther, D. (1996) Laser ablation inductively coupled plasma mass spectrometric transient signal data acquisition and analyte concentration calculation. *Journal of Analytical Atomic Spectrometry* **11**, 899-904.

Lorens, R. B. (1981) Sr, Cd, Mn and Co distribution coefficients in calcite as a function of calcite precipitation rate. *Geochimica et Cosmochimica Acta* **45**, 553-561.

Luster, J., Lloyd, T., Sposito, G., and Fry, I. V. (1996) Multi-wavelength molecular fluorescence spectrometry for quantitative characterization of copper(II) and aluminum(III) complexation by dissolved organic matter. *Environmental Science & Technology* **30**, 1565-1574.

Lyvén, B., Hassellöv, M., Turner, D. R., Haraldsson, C., and Andersson, K. (2003) Competition between iron- and carbon-based colloidal carriers for trace metals in a freshwater assessed using flow field-flow fractionation coupled to ICPMS. *Geochimica et Cosmochimica Acta* **67**, 3791-3802.

Macleod, G., Fallick, A. E., and Hall, A. J. (1991) The mechanism of carbonate growth on concrete structures, as elucidated by carbon and oxygen isotope analyses. *Chemical Geology* **86**, 335-343.

Majzik, A. and Tombácz, E. (2007) Interaction between humic acid and montmorillonite in the presence of calcium ions I. Interfacial and aqueous phase equilibria: Adsorption and complexation. *Organic Geochemistry* **38**, 1319-1329.

Marang, L., Eidner, S., Kumke, M. U., Benedetti, M. F., and Reiller, P. E. (2009) Spectroscopic characterization of the competitive binding of Eu(III), Ca(II), and Cu(II) to a sedimentary originated humic acid. *Chemical Geology* **264**, 154-161.

Martin, H. W. and Kaplan, D. I. (1998) Temporal changes in cadmium, thallium, and vanadium mobility in soil and phytoavailability under field conditions. *Water Air and Soil Pollution* **101**, 399-410.

Mason, H. E., Frisia, S., Tang, Y., Reeder, R. J., and Phillips, B. L. (2007) Phosphorus speciation in calcite speleothems determined from solid-state NMR spectroscopy. *Earth and Planetary Science Letters* **254**, 313-322.

Massei, N., Lacroix, M., Wang, H. Q., Mahler, B. J., and Dupont, J. P. (2002) Transport of suspended solids from a karstic to an alluvial aquifer: the role of the karst/alluvium interface. *Journal of Hydrology* **260**, 88-101.

Massei, N., Wang, H. Q., Dupont, J. P., Rodet, J., and Laignel, B. (2003) Assessment of direct transfer and resuspension of particles during turbid floods at a karstic spring. *Journal of Hydrology* **275**, 109-121.

Mavrocordatos, D., Mondi-Couture, C., Atteia, O., Leppard, G. G., and Perret, D. (2000) Formation of a distinct class of Fe-Ca(-C-org)-rich particles in a complex peat-karst system. *Journal of Hydrology* **237**, 234-247.

Mayer, L. M. and Xing, B. S. (2001) Organic matter-surface area relationships in acid soils. *Soil Science Society of America Journal* **65**, 250-258.

McBride, M. B. (1994) *Environmental Chemistry of Soils*. Oxford University Press. 416 pp.

McCarthy, J. F., Sanford, W. E., and Stafford, P. L. (1998) Lanthanide field tracers demonstrate enhanced transport of transuranic radionuclides by natural organic matter. *Environmental Science & Technology* **32**, 3901-3906.

McCarthy, J. F. and Shevenell, L. (1998) Processes controlling colloid composition in a fractured and karstic aquifer in eastern Tennessee, USA. *Journal of Hydrology* **206**, 191-218.

McCarthy, J. F. and McKay, L. D. (2004) Colloid transport in the subsurface: Past, present, and future challenges. *Vadose Zone Journal* **3**, 326-337.

McDermott, F., Frisia, S., Huang, Y. M., Longinelli, A., Spiro, B., Heaton, T. H. E., Hawkesworth, C. J., Borsato, A., Keppens, E., Fairchild, I. J., van der Borg, K., Verheyden, S., and Selmo, E. (1999) Holocene climate variability in Europe: Evidence from delta O-18, textural and extension-rate variations in three speleothems. *Quaternary Science Reviews* **18**, 1021-1038.

McDonald, S., Bishop, A. G., Prenzler, P. D., and Robards, K. (2004) Analytical chemistry of freshwater humic substances. *Analytica Chimica Acta* **527**, 105-124.

McGechan, M. B. (2002) Transport of particulate and colloid-sorbed contaminants through soil, part 2: Trapping processes and soil pore geometry. *Biosystems Engineering* **83**, 387-395.

McKay, L. D., Gillham, R. W., and Cherry, J. A. (1993) Field Experiments in a Fractured Clay Till .2. Solute and Colloid Transport. *Water Resources Research* **29**, 3879-3890.

McKay, L. D., Sanford, W. E., and Strong, J. M. (2000) Field-scale migration of colloidal tracers in a fractured shale saprolite. *Ground Water* **38**, 139-147.

McMillan, E. A., Fairchild, I. J., Frisia, S., Borsato, A., and McDermott, F. (2005) Annual trace element cycles in calcite-aragonite speleothems: evidence of drought in the western Mediterranean 1200-1100 yr BP. *Journal of Quaternary Science* **20**, 423-433.

Meyer, H. J. (1984) The influence of impurities on the growth-rate of calcite. *Journal of Crystal Growth* **66**, 639-646.

Miano, T. M., Sposito, G., Martin, J.P. (1998) Fluorescence spectroscopy of humic substances. *Soil Science America Journal* **52**, 1016–1019.

Milne, C. J., Kinniburgh, D. G., Van Riemsdijk, W. H., and Tipping, E. (2003) Generic NICA-Donnan model parameters for metal-ion binding by humic substances. *Environmental Science & Technology* **37**, 958-971.

Miorandi, R., Borsato, A., Frisia, S., Fairchild, I. J., and Richter, D. K. (2010) Epikarst hydrology and implications for stalagmite capture of climate changes at Grotta di Ernesto (NE Italy): results from long-term monitoring. *Hydrological Processes* **24**, 3101-3114.

Mobed, J. J., Hemmingsen, S. L., Autry, J. L., and McGown, L. B. (1996) Fluorescence characterization of IHSS humic substances: Total luminescence spectra with absorbance correction. *Environmental Science & Technology* **30**, 3061-3065.

Moberly, J. G., Borch, T., Sani, R. K., Spycher, N. F., Sengor, S. S., Ginn, T. R., and Peyton, B. M. (2009) Heavy Metal-Mineral Associations in Coeur d'Alene River Sediments: A Synchrotron-Based Analysis. *Water Air and Soil Pollution* **201**, 195-208.

Morse, J. W. and Bender, M. L. (1990) Partition-coefficients in calcite – examination of factors influencing the validity of experimental results and their application to natural systems. *Chemical Geology* **82**, 265-277.

Müller, W., Shelley, M., Miller, P., and Broude, S. (2009) Initial performance metrics of a new custom-designed ArF excimer LA-ICPMS system coupled to a two-volume laser-ablation cell. *Journal of Analytical Atomic Spectrometry* **24**, 209-214.

Murphy, E. M., Zachara, J. M., Smith, S. C., and Phillips, J. L. (1990) The sorption of humic acids to mineral surfaces and their role in contaminant binding. 5th International Meeting of the International Humic Substances Society: *Advances in Humic Substances Research*, Nagoya, Japan.

Nachtegaal, M. and Sparks, D. L. (2003) Nickel Sequestration in a Kaolinite-Humic Acid Complex. *Environmental Science & Technology* **37**, 529-534.

NSRI (2008) Soils Site Report, National Grid Reference ST8790099194; Area 1km x 1km. National Soil Resources Institute, Cranfield University. Accessed via https://www.landis.org.uk/sitereporter/.

O'Day, P. A., Brown, G. E., and Parks, G. A. (1994) X-Ray Absorption Spectroscopy of Cobalt(II) Multinuclear Surface Complexes and Surface Precipitates on Kaolinite. *Journal of Colloid and Interface Science* **165**, 269-289.

Oste, L. A., Temminghoff, E. J. M., Lexmond, T. M., and Van Riemsdijk, W. H. (2002) Measuring and Modeling zinc and cadmium binding by humic acid. *Analytical Chemistry* **74**, 856-862.

Pabich, W. J., Valiela, I., and Hemond, H. F. (2001) Relationship between DOC concentration and vadose zone thickness and depth below water table in groundwater of Cape Cod, USA. *Biogeochemistry* **55**, 247-268.

Parkman, R. H., Charnock, J. M., Livens, F. R., and Vaughan, D. J. (1998) A study of the interaction of strontium ions in aqueous solution with the surfaces of calcite and kaolinite. *Geochimica et Cosmochimica Acta* **62**, 1481-1492.

Patel-Sorrentino, N., Mounier, S., and Benaim, J. Y. (2002) Excitation-emission fluorescence matrix to study pH influence on organic matter fluorescence in the Amazon basin rivers. *Water Research* **36**, 2571-2581.

Peacock, C. L. (2009) Physiochemical controls on the crystal-chemistry of Ni in birnessite: Genetic implications for ferromanganese precipitates. *Geochimica et Cosmochimica Acta* **73**, 3568-3578.

Peavy, H. S., Rowe, D. R. and Tchobanoglous, G. (1985) *Environmental Engineering*. McGraw-Hill, New York. 640 pp.

Pedrot, M., Dia, A., Davranche, M., Bouhnik-Le Coz, M., Henin, O., Gruau, G. (2008) Insights into colloid-mediated trace element release at the soil/water interface. *Journal of Colloid and Interface Science* **325**, 187-197.

Pinheiro, J. P., Mota, A. M., and van Leeuwen, H. P. (1999) On lability of chemically heterogeneous systems - Complexes between trace metals and humic matter. *Colloids and Surfaces a-Physicochemical and Engineering Aspects* **151**, 181-187.

Pinheiro, J. P., Mota, A. M., and Benedetti, M. F. (2000) Effect of aluminum competition on lead and cadmium binding to humic acids at variable ionic strength. *Environmental Science & Technology* **34**, 5137-5143.

Pitty, A. F. (1966) An approach to the study of kart water. University of Hull *Occasional Papers in Geography* **5**.

Plaschke, M., Rothe, J., Denecke, M. A., and Fanghanel, T. (2004) Soft X-ray spectromicroscopy of humic acid europium(III) complexation by comparison to model substances. *Journal of Electron Spectroscopy and Related Phenomena* **135**, 53-62.

Proctor, C. J., Baker, A., Barnes, W. L., and Gilmour, R. A. (2000) A thousand year speleothem proxy record of North Atlantic climate from Scotland. *Climate Dynamics* **16**, 815-820.

Proctor, C. J., Baker, A., and Barnes, W. L. (2002) A three thousand year record of North Atlantic climate. *Climate Dynamics* **19**, 449-454.

Ramos-Tejada, M. M., de Vicente, J., Ontiveros, A., and Duran, J. D. G. (2001) Effect of humic acid adsorption on the rheological properties of sodium montmorillonite suspensions. *Journal of Rheology* **45**, 1159-1172.

Randall, S. R., Sherman, D. M., and Ragnarsdottir, K. V. (1998) An extended X-ray absorption fine structure spectroscopy investigation of cadmium sorption on cryptomelane (KMn8O16). *Chemical Geology* **151**, 95-106.

Richter, D. K., Gotte, T., Niggemann, S., and Wurth, G. (2004) REE3+ and Mn2+ activated cathodoluminescence in lateglacial and Holocene stalagmites of central Europe: evidence for climatic processes? *Holocene* **14**, 759-767.

Ritchie, J. D. and Perdue, E. M. (2003) Proton-binding study of standard and reference fulvic acids, humic acids, and natural organic matter. *Geochimica et Cosmochimica Acta* **67**, 85-96.

Roberts, M. S., Smart, P. L., and Baker, A. (1998) Annual trace element variations in a Holocene speleothem. *Earth and Planetary Science Letters* **154**, 237-246.

Rose, J., Vilge, A., Olivie-Lauquet, G., Masion, A., Frechou, C., and Bottero, J.-Y. (1998) Iron speciation in natural organic matter colloids. *Colloids and Surfaces A: Physicochemical and Engineering Aspects* **136**, 11-19.

Rossum, J. R. (1975) Checking accuracy of water analyses through use of conductivity. *Journal American Water Works Association* **67**, 204-205.

Rousseau, M., Di Pietro, L., Angulo-Jaramillo, R., Tessier, D., and Cabibel, B. (2004) Preferential transport of soil colloidal particles: Physicochemical effects on particle mobilization. *Vadose Zone Journal* **3**, 247-261.

Rouzaud, J. N. and Oberlin, A., 1989. Structure, microtexture, and optical properties of anthracene and saccharose-based carbons. *Carbon* **27**, 517-529.

Rozan, T. F., Luther, G. W., Ridge, D., and Robinson, S. (2003) Determination of Pb complexation in oxic and sulfidic waters using pseudovoltammetry. *Environmental Science & Technology* **37**, 3845-3852.

Ryan, J. N. and Gschwend, P. M. (1994) Effects of Ionic-Strength and Flow-Rate on Colloid Release - Relating Kinetics to Intersurface Potential-Energy. *Journal of Colloid and Interface Science* **164**, 21-34.

Ryan, J. N. and Elimelech, M. (1996) Colloid mobilization and transport in groundwater. *Colloids and Surfaces a-Physicochemical and Engineering Aspects* **107**, 1-56.

Sadiq, M. (1988) Thermodynamic solubility relationships of inorganic vanadium in the marine environment. *Marine Chemistry* **23**, 87-96.

Scheidegger, A. M., Lamble, G. M., and Sparks, D. L. (1997) Spectroscopic Evidence for the Formation of Mixed-Cation Hydroxide Phases upon Metal Sorption on Clays and Aluminum Oxides. *Journal of Colloid and Interface Science* **186**, 118-128.

Schelde, K., Moldrup, P., Jacobsen, O. H., de Jonge, H., de Jonge, L. W., Komatsu, T. (2002) Diffusion-Limited Mobilization and Transport of Natural Colloids in Macroporous Soil. *Vadose Zone Journal* **1**, 125-136.

Schlegel, M. L., Charlet, L., and Manceau, A. (1999) Sorption of Metal Ions on Clay Minerals: II. Mechanism of Co Sorption on Hectorite at High and Low Ionic

Strength and Impact on the Sorbent Stability. *Journal of Colloid and Interface Science* **220**, 392-405.

Schlegel, M. L., Manceau, A., Charlet, L., and Hazemann, J.-l. (2001) Adsorption Mechanisms of Zn on Hectorite as a Function of Time, pH, and Ionic Strength. *American Journal of Science* **301**, 798-830.

Seaman, J. C., Bertsch, P. M., and Miller, W. P. (1995) Chemical Controls on Colloid Generation and Transport in a Sandy Aquifer. *Environmental Science & Technology* **29**, 1808-1815.

Seaman, J. C., Bertsch, P. M., and Schwallie, L. (1999) In situ Cr(VI) reduction within coarse-textured, oxide-coated soil and aquifer systems using Fe(II) solutions. *Environmental Science & Technology* **33**, 938-944.

Sen, T. K. and Khilar, K. C. (2006) Review on subsurface colloids and colloid-associated contaminant transport in saturated porous media. *Advances in Colloid and Interface Science* **119**, 71-96.

Senesi, N., Miano, T. M., and Provenzano, M. R. (1991a) Fluorescence Spectroscopy as a Means of Distinguishing Fulvic and Humic Acids from Dissolved and Sedimentary Aquatic Sources and Terrestrial Sources. *Humic Substances in the Aquatic and Terrestrial Environment* **33**, 63-73.

Senesi, N., Miano, T. M., Provenzano, M. R., and Brunetti, G. (1991b) Characterization, Differentiation, and Classification of Humic Substances by Fluorescence Spectroscopy. *Soil Science* **152**, 259-271.

Seredyńska-Sobecka, B., Baker, A., and Lead, J. R. (2007) Characterisation of colloidal and particulate organic carbon in freshwaters by thermal fluorescence quenching. *Water Research* **41**, 3069-3076.

Shaw, E. M. (1994) *Hydrology in Practice*. Routledge, Abingdom. 392 pp.

Shevenell, L. and McCarthy, J. F. (2002) Effects of precipitation events on colloids in a karst aquifer. *Journal of Hydrology* **255**, 50-68.

Shopov, Y. Y., Ford, D. C., and Schwarcz, H. P. (1994) Luminescent Microbanding in Speleothems - High-Resolution Chronology and Paleoclimate. *Geology* **22**, 407-410.

Simon, K. S., Pipan, T., and Culver, D. C. (2007) A conceptual model of the flow and distribution of organic carbon in caves. *Journal of Cave and Karst Studies* **69**, 279-284.

Sjöstedt, C., Wällstedt, T., Gustafsson, J. P., and Borg, H. (2009) Speciation of aluminium, arsenic and molybdenum in excessively limed lakes. *Science of the Total Environment* **407**, 5119-5127.

Sonke, J. E. and Salters, V. J. M. (2004) Determination of neodymium-fulvic acid binding constants by capillary electrophoresis inductively coupled plasma mass spectrometry (CE-ICP-MS). *Journal of Analytical Atomic Spectrometry* **19**, 235-240.

Sonke, J. E. and Salters, V. J. M. (2006) Lanthanide-humic substances complexation. I. Experimental evidence for a lanthanide contraction effect. *Geochimica et Cosmochimica Acta* **70**, 1495-1506.

Sparks, D. L. (1995) *Environmental soil chemistry*. Academic Press, San Diego. 352 pp.

Spencer, R. G. M., Bolton, L., and Baker, A. (2007) Freeze/thaw and pH effects on freshwater dissolved organic matter fluorescence and absorbance properties from a number of UK locations. *Water Research* **41**, 2941-2950.

Stamberg, K., Benes, P., Mizera, J., Dolansky, J., Vopalka, D., and Chalupska, K. (2003) Modeling of metal-humate complexation based on the mean molecular weight and charge of humic substances: Application to Eu(III) humate complexes using ion exchange. *Journal of Radioanalytical and Nuclear Chemistry* **258**, 329-345.

Stern, J. C., Sonke, J. E., and Salters, V. J. M. (2007) A capillary electrophoresis-ICP-MS study of rare earth element complexation by humic acids. *Chemical Geology* **246**, 170-180.

Stevenson, F. J. (1994) *Humus Chemistry: Genesis, Composition, Reactions*. John Wiley & Sons, New York. 512 pp.

Stockdale, A., Davison, W., and Zhang, H. (2008) High-resolution two-dimensional quantitative analysis of phosphorus, vanadium and arsenic, and qualitative analysis of sulfide, in a freshwater sediment. *Environmental Chemistry* **5**, 143-149.

Stolpe, B., Hassellöv, M., Andersson, K., and Turner, D. R. (2005) High resolution ICPMS as an on-line detector for flow field-flow fractionation; multi-element determination of colloidal size distributions in a natural water sample. *Analytica Chimica Acta* **535**, 109-121.

Strawn, D. G., Scheidegger, A. M., and Sparks, D. L. (1998) Kinetics and Mechanisms of Pb(II) Sorption and Desorption at the Aluminum Oxide-Water Interface. *Environmental Science & Technology* **32**, 2596-2601.

Strawn, D. G. and Sparks, D. L. (1999) The Use of XAFS to Distinguish between Inner- and Outer-Sphere Lead Adsorption Complexes on Montmorillonite. *Journal of Colloid and Interface Science* **216**, 257-269.

Strawn, D. G. and Sparks, D. L. (2000) Effects of Soil Organic Matter on the Kinetics and Mechanisms of Pb(II) Sorption and Desorption in Soil. *Soil Science Society of America Journal* **64**, 144-156.

Stumm, W. and Morgan, J. J. (1996) *Aquatic Chemistry*. Wiley-Interscience, John Wiley & Sons, Inc. 1040 pp.

Sumbler, M. G., Barron, A. J. M. and Morigi, A. N. (2000) *Geology of the Cirencester district*. Memoir of the British Geological Survey. British Geological Survey, Wallingford. 111 pp.

Taillefert, M., Lienemann, C.-P., Gaillard, J.-F., and Perret, D. (2000) Speciation, reactivity, and cycling of Fe and Pb in a meromictic lake. *Geochimica et Cosmochimica Acta* **64**, 169-183.

Tam, S. C. and Sposito, G. (1993) Fluorescence specroscopy of aqueous pine litter extracts - effects of humification and aluminium complexation. *Journal of Soil Science* **44**, 513-524.

Tan, M., Baker, A., Genty, D., Smith, C., Esper, J., Cai, B. G. (2006) Applications of stalagmite laminae to paleoclimate reconstructions: Comparison with dendrochronology/climatology. *Quaternary Science Reviews* **25**, 2103-2117.

Tang, J. W. and Johannesson, K. H. (2003) Speciation of rare earth elements in natural terrestrial waters: Assessing the role of dissolved organic matter from the modeling approach. *Geochimica et Cosmochimica Acta* **67**, 2321-2339.

Thurman, E. M. (1985) *Organic Geochemistry of Natural Waters*. Martinus Nijhoff/Dr. W. Junk Publishers.

Tiede, K., Neumann, T., and Stueben, D. (2007) Suitability of Mn-oxyhydroxides from karst caves as filter material for drinking water treatment in Gunung Sewu, Indonesia. *Journal of Soils and Sediments* **7**, 53-58.

Tipping, E. (1998) Humic ion-binding model VI: An improved description of the interactions of protons and metal ions with humic substances. *Aquatic Geochemistry* **4**, 3-48.

Tipping, E. (2001) *Cation binding by humic substances*. University Press, Cambridge. 448 pp.

Tipping, E. and Higgins, D. C. (1982) The effect of adsorbed humic substances on the colloid stability of hematite particles. *Colloids and Surfaces* **5**, 85-92.

Tipping, E. and Hurley, M. A. (1992) A unifying model of cation binding to humic substances. *Geochimica et Cosmochimica Acta* **56**, 3627-3641.

Tipping, E., Lofts, S., and Lawlor, A. J. (1998) Modelling the chemical speciation of trace metals in the surface waters of the Humber system. *Science of the Total Environment* **210**, 63-77.

Tombacz, E., Szekeres, M., Baranyi, L., and Micheli, E. (1998) Surface modification of clay minerals by organic polyions. *Colloids and Surfaces a-Physicochemical and Engineering Aspects* **141**, 379-384.

Tooth, A. F. and Fairchild, I. J. (2003) Soil and karst aquifer hydrological controls on the geochemical evolution of speleothem-forming drip waters, Crag Cave, southwest Ireland. *Journal of Hydrology* **273**, 51-68.

Tyler, G. (2004) Vertical distribution of major, minor, and rare elements in a Haplic Podzol. *Geoderma* **119**, 277-290.

Unsworth, E. R., Warnken, K. W., Zhang, H., Davison, W., Black, F., Buffle, J., Cao, J., Cleven, R., Galceran, J., Gunkel, P., Kalis, E., Kistler, D., Van Leeuwen, H. P., Martin, M., Noel, S., Nur, Y., Odzak, N., Puy, J., Van Riemsdijk, W., Sigg, L., Temminghoff, E., Tercier-Waeber, M. L., Toepperwien, S., Town, R. M., Weng, L. P., and Xue, H. B. (2006) Model predictions of metal speciation in freshwaters compared to measurements by in situ techniques. *Environmental Science & Technology* **40**, 1942-1949.

Van Der Veeken, P. L. R., Pinheiro, J. P., and Van Leeuwen, H. P. (2008) Metal Speciation by DGT/DET in Colloidal Complex Systems. *Environmental Science & Technology* **42**, 8835-8840.

Verdugo, P., Orellana, M. V., Chin, W. C., Petersen, T. W., van den Eng, G., Benner, R. and Hedges, J. I. (2008) Marine biopolymer self-assembly: implications for carbon cycling in the ocean. *Faraday Discussions* **139**, 393-398.

Waeles, M., Tanguy, V., Lespes, G., and Riso, R. D. (2008) Behaviour of colloidal trace metals (Cu, Pb and Cd) in estuarine waters: An approach using frontal ultrafiltration (UF) and stripping chronopotentiometric methods (SCP). *Estuarine Coastal and Shelf Science* **80**, 538-544.

Wan, J. M. and Wilson, J. L. (1994a) Colloid transport in unsaturated porous-media. *Water Resources Research* **30**, 857-864.

Wan, J. M. and Tokunaga, T. K. (1997) Film straining of colloids in unsaturated porous media: Conceptual model and experimental testing. *Environmental Science & Technology* **31**, 2413-2420.

Wang, D. and Wilhelmy, S. A. S. (2009) Vanadium speciation and cycling in coastal waters. *Marine Chemistry* **117**, 52-58.

Wang, Y. J., Cheng, H., Edwards, R. L., He, Y. Q., Kong, X. G., An, Z. S., Wu, J. Y., Kelly, M. J., Dykoski, C. A., and Li, X. D. (2005) The Holocene Asian

monsoon: Links to solar changes and North Atlantic climate. *Science* **308**, 854-857.

Wanty, R. B. and Goldhaber, M. B. (1992) Thermodynamics and kinetics of reactions involving vanadium in natural systems - accumulation of vanadium in sedimentary rocks. *Geochimica et Cosmochimica Acta* **56**, 1471-1483.

Warnken, K. W., Davison, W., Zhang, H., Galceran, J., and Puy, J. (2007) In situ measurements of metal complex exchange kinetics in freshwater. *Environmental Science & Technology* **41**, 3179-3185.

Warnken, K. W., Lawlor, A. J., Lofts, S., Tipping, E., Davison, W., and Zhang, H. (2009) In Situ Speciation Measurements of Trace Metals in Headwater Streams. *Environmental Science & Technology* **43**, 7230-7236.

Wehrli, B. and Stumm, W. (1989) Vanadyl in natural waters- adsorption and hydrolysis promote oxygenation *Geochimica et Cosmochimica Acta* **53**, 69-77.

White, H. K., Xu, L., Lima, A. L. C., Eglinton, T. I., and Reddy, C. M. (2005) Abundance, composition, and vertical transport of PAHs in marsh sediments. *Environmental Science & Technology* **39**, 8273-8280.

Whitehead, N. E., Ditchburn, R. G., Williams, P. W., and McCabe, W. J. (1999) Pa-231 and Th-230 contamination at zero age: a possible limitation on U/Th series dating of speleothem material. *Chemical Geology* **156**, 359-366.

Wilkinson, K. J., Negre, J. C., and Buffle, J. (1997) Coagulation of colloidal material in surface waters: The role of natural organic matter. *Journal of Contaminant Hydrology* **26**, 229-243.

Wilkinson, K. J., Balnois, E., Leppard, G. G., and Buffle, J. (1999) Characteristic features of the major components of freshwater colloidal organic matter revealed by transmission electron and atomic force microscopy. *Colloids and Surfaces a-Physicochemical and Engineering Aspects* **155**, 287-310.

Williams, D. B. and Carter, C. B. (1996) *Transmission electron microscopy: A textbook for materials science.* Plenum Press, New York. 832 pp.

Wynn, P. M., Fairchild, I. J., Baker, A., Frisia, S., Borsato, A., Miorandi, M., Spotl, C. (2007) High resolution ion microprobe analysis of sulphur isotopes in speleothem carbonate. *Geochimica et Cosmochimica Acta* **71**, A1130-A1130.

Wynn, P. M., Fairchild, I. J., Baker, A., Baldini, J. U. L., and McDermott, F. (2008) Isotopic archives of sulphate in speleothems. *Geochimica et Cosmochimica Acta* **72**, 2465-2477.

Xia, K., Bleam, W., and Helmke, P. A. (1997a) Studies of the nature of binding sites of first row transition elements bound to aquatic and soil humic substances using

X-ray absorption spectroscopy. *Geochimica et Cosmochimica Acta* **61**, 2223-2235.

Xia, K., Bleam, W., and Helmke, P. A. (1997b). Studies of the nature of Cu2+ and Pb2+ binding sites in soil humic substances using X-ray absorption spectroscopy. *Geochimica et Cosmochimica Acta* **61**, 2211-2221.

Zachara, J.M., Cowan, C.E. & Resch, C.T. (1991) Sorption of divalent metals on calcite. *Geochimica et Cosmochimica Acta*, **55**, 1549-1562.

Zhang, H. and Davison, W. (1995) Performance-characteristics of diffusion gradients in thin-films for the in-situ measurement of trace metals in aqueous solution *Analytical Chemistry* **67**, 3391-3400.

Zhang, H. and Davison, W. (1999) Diffusional characteristics of hydrogels used in DGT and DET techniques. *Analytica Chimica Acta* **398**, 329-340.

Zhang, P.-C., Brady, P. V., Arthur, S. E., Zhou, W.-Q., Sawyer, D., and Hesterberg, D. A. (2001) Adsorption of barium(II) on montmorillonite: an EXAFS study. *Colloids and Surfaces A: Physicochemical and Engineering Aspects* **190**, 239-249.

Zhang, H. (2003) *DGT –for measurements in waters, soils and sediments*. DGT Research LTD, Lancaster, UK. Available at: http://www.dgtresearch.com/dgtresearch/dgtresearch.pdf. Last accessed: January 2011.

Zhang, H. (2004) In-situ speciation of Ni and Zn in freshwaters: Comparison hetween DGT measurements and speciation models. *Environmental Science & Technology* **38**, 1421-1427.

Zhou, H., Wang, Q., Zhao, J., Zheng, L., Guan, H., Feng, Y., and Greig, A. (2008) Rare earth elements and yttrium in a stalagmite from Central China and potential paleoclimatic implications. *Palaeogeography, Palaeoclimatology, Palaeoecology* **270**, 128-138.

Appendix I Blanks data

Filter	Concentration µg L^{-1}	Al	Ti	V	Cr	Mn	Fe	Co	Ni	Cu	Zn	Br	Sr	Y	Cd	Ba	Pb
1 µm	Average	4.1	< 0.2	0.2	< 0.2	< 0.1	0.8	< 0.1	< 0.2	< 0.2	19	< 0.5	0.3	< 0.1	< 0.1	13	< 0.5
	SD	8.2	-	0.0	-	-	2.0	-	-	-	10	-	0.1	-	-	3.2	-
	LOD	25	-	0.1	-	-	6.0	-	-	-	30	-	0.4	-	-	9.7	-
100 nm	Average	17	< 0.2	0.1	< 0.2	< 0.1	4.4	< 0.1	< 0.2	< 0.2	< 0.2	< 0.5	0.1	< 0.1	< 0.1	< 0.1	< 0.5
	SD	3.7	-	0.0	-	-	7.5	-	-	-	8.4	-	0.1	-	-	4.8	-
	LOD	11	-	0.1	-	-	23	-	-	-	25	-	0.4	-	-	14	-
1 kDa	Average	4.5	< 0.2	0.1	< 0.2	< 0.1	< 0.5	< 0.1	< 0.2	< 0.2	< 0.2	< 0.5	< 0.1	< 0.1	< 0.1	< 0.1	< 0.5
	SD	13	-	0.3	-	-	3.1	-	-	-	3.0	-	0.1	-	-	3.1	-
	LOD	38	-	0.9	-	-	9.2	-	-	-	9.1	-	0.2	-	-	9.3	-

Table S1 Summary trace element blanks data from analysis of procedural filter blanks (n=5). SD= standard deviation; LOD = limit of detection (3x SD of blank); ND = not determined. Procedural blanks followed same filtration procedure as used for field samples using a starting volume of 500 mL DIW.

Resin		Al	Ti	V	Cr	Mn	Fe	Co	Ni	Cu	Zn	Br	Sr	Y	Cd	Ba	Pb
FeO_x	Average mass eluted (ng)	9.7	<1	<0.5	9.7	1.3	ND	<0.5	<1	4.1	8.3	5.3	<0.5	<0.5	<0.5	<0.5	<1
	SD (ng)	1.8	-	-	4.2	0.2	-	-	-	0.4	3.3	0.6	-	-	-	-	-
	LOD (ng)	5.4	-	-	12.6	0.6	-	-	-	1.1	10	1.7	-	-	-	-	-
Chelex	Average mass eluted (ng)	<2.5	1.4	<0.5	4.0	1.2	20.6	<0.5	<1	1.8	14.8	3.3	5.6	<0.5	<0.5	2.6	<1
	SD (ng)	-	0.2	-	2.7	0.4	1.0	-	-	0.9	0.4	0.0	1.1	-	-	0.5	-
	LOD (ng)	-	0.6	-	8.2	1.1	3.0	-	-	2.6	1.2	0.0	3.2	-	-	1.4	-

Table S2 Summary trace element blanks data from triplicate analysis of DGT Chelex and FeO_x resins. SD= standard deviation; LOD = limit of detection (3x SD of blank); ND = not determined.

Pore size (μm)	Material	Manufacturer	OC (mg L^{-1})	1 σ
0.001	Regenerated cellulose	Millpore	1.32	0.11
0.001	Regenerated cellulose	Millpore	1.40	0.08
0.001	Regenerated cellulose	Millpore	0.38	0.07
0.1	Cellulose nitrate	Whatman	0.85	0.18
0.1	Cellulose nitrate	Whatman	0.75	0.07
0.1	Cellulose nitrate	Whatman	0.31	0.05
0.2	Nylon (Syringe)	PALL	0.80	0.05
0.2	Nylon (Syringe)	PALL	0.70	0.07
0.2	Nylon (Syringe)	PALL	0.97	0.10
0.2	Nylon (Syringe)	Whatman	0.71	0.04
0.2	Nylon (Syringe)	Whatman	0.37	0.03
0.2	Nylon (Syringe)	Whatman	0.37	0.07
0.45	Glass micro-fibre	Whatman	1.28	0.08
0.45	Glass micro-fibre	Whatman	4.09	0.11
0.45	Glass micro-fibre	Whatman	1.40	0.07
0.45	Nylon (Syringe)	PALL	0.74	0.10
0.45	Nylon (Syringe)	PALL	0.42	0.08
0.45	Nylon (Syringe)	PALL	0.96	0.03
0.45	Cellulose acetate	VWR	0.65	0.05
0.45	Cellulose acetate	VWR	0.18	0.10
0.45	Cellulose acetate	VWR	0.36	0.07
1	Glass micro-fibre	Whatman	0.48	0.07
1	Glass micro-fibre	Whatman	0.43	0.03
1	Glass micro-fibre	Whatman	0.31	0.05

Table S3 Organic carbon blanks (concentration in 10 mL DIW) for a range of filter types following filter cleaning with dilute acid (10% HNO_3) and DIW in a ratio of one to three.

Pore size (μm)	Material	Manufacturer	OC (mg L^{-1})	1 σ	3 σ (LOD)
1	Glass micro-fibre	Whatman	0.73	0.08	0.25
0.1	Cellulose nitrate	Whatman	1.26	0.28	0.83
0.001	Regenerated cellulose	Millpore	1.04	0.59	1.76

Table S4 Results of procedural filter blanks for total organic carbon correction of filtered dripwaters (LOD= limit of detection).

Appendix II Trace element and organic carbon data repository (dripwaters and soil leachates)

		Concentration in size class (mg L^{-1})	Element concentration in size class (μg L^{-1})											
Site	Size class	TOC	Si	Na	Mg	Al	Ti	V	Cr	Ni	Co	Cu	Br	Sr
LB2 Lower Balls Green Mine (n=3)	Particulate	**1.1** ± 0.1	0.0 ± 0.1	**0.1** ± 0.2	**0.1** ± 0.1	0.0 ± 1.5	0.0 ± 0.1	0.0 ± 0.0	nd	nd	0.0 ± 0.0	**0.1** ± 0.1	**1.3** ± 1.7	**3.9** ± 4.8
	Coarse colloidal	**0.9** ± 0.1	**0.9** ± 1.6	**2.4** ± 4.1	**0.9** ± 1.6	0.0 ± 9.4	**0.1** ± 0.2	0.0 ± 0.0	nd	nd	**0.1** ± 0.2	0.0 ± 0.2	**14** ± 24	**46** ± 85
	Fine colloidal	**0.6** ± 0.1	0.0 ± 1.6	0.0 ± 4.1	0.0 ± 1.6	0.0 ± 13	0.0 ± 0.2	0.0 ± 0.0	nd	nd	0.0 ± 0.2	0.0 ± 0.2	0.0 ± 24	0.0 ± 85
	ND	**1.0** ± 0.1	**2.8** ± 0.1	**7.1** ± 0.3	**2.7** ± 0.1	**36** ± 8.6	**0.5** ± 0.1	**0.2** ± 0.0	nd	nd	**0.3** ± 0.0	**0.5** ± 0.0	**44** ± 1.8	**145** ± 5.0
BC2 Poole's Cavern (n=3)	Particulate	**0.2** ± 0.3	0.0 ± 0.1	0.0 ± 0.1	0.0 ± 0.0	0.0 ± 0.5	0.0 ± 0.0	0.0 ± 0.0	0.0 ± 0.0	nd	0.0 ± 0.0	0.0 ± 0.0	0.0 ± 0.9	0.0 ± 1.1
	Coarse colloidal	**0.2** ± 0.3	**0.1** ± 0.1	**0.2** ± 0.1	0.0 ± 0.0	0.0 ± 1.0	0.0 ± 0.1	0.0 ± 0.0	0.0 ± 0.0	nd	0.0 ± 0.0	0.0 ± 0.0	**0.1** ± 1.7	**4.1** ± 1.7
	Fine colloidal/	**1.1** ± 0.2	**0.1** ± 1.3	**0.2** ± 0.2	0.0 ± 0.0	**0.1** ± 1.0	**0.1** ± 0.1	**0.1** ± 0.0	0.0 ± 0.0	nd	0.0 ± 0.0	**0.1** ± 0.0	**2.3** ± 2.2	**2.6** ± 2.2
	ND		**2.6** ± 0.1	**3.4** ± 0.1	**0.9** ± 0.0	**5.7** ± 0.4	**0.7** ± 0.0	**0.4** ± 0.0	**0.2** ± 0.0	nd	**0.2** ± 0.0	**0.2** ± 0.0	**44** ± 1.7	**55** ± 1.7
St-2 Grotta d'Ernesto (n=1)	Particulate	**1.5** ± 0.4	0.0 ± 0.1	0.0 ± 0.0	0.0 ± 0.1	0.0 ± 1.2	0.0 ± 0.0	0.0 ± 0.1	0.0 ± 0.0	0.0 ± 0.1	0.0 ± 0.0	0.0 ± 0.0	0.0 ± 0.1	0.0 ± 0.3
	Coarse colloidal	**0.8** ± 0.2	**0.1** ± 0.0	**0.1** ± 0.0	**0.2** ± 0.1	**1.8** ± 1.6	0.0 ± 0.0	0.0 ± 0.0	0.0 ± 0.0	0.0 ± 0.0	0.0 ± 0.0	0.0 ± 0.0	**0.5** ± 0.2	**0.5** ± 0.3
	Fine colloidal	**0.2** ± 0.8	0.0 ± 0.0	0.0 ± 0.0	**0.1** ± 0.1	**2.7** ± 1.6	0.0 ± 0.1	0.0 ± 0.0	0.0 ± 0.0	**0.1** ± 0.0	0.0 ± 0.0	**0.1** ± 0.0	**0.1** ± 0.2	**0.3** ± 0.4
	ND	**1.6** ± 0.8	**2.2** ± 0.6	**0.4** ± 0.0	**4.1** ± 0.0	**6.1** ± 1.2	0.6 ± 0.0	**0.1** ± 0.0	**0.1** ± 0.0	**0.1** ± 0.0	**0.1** ± 0.0	**0.2** ± 0.0	**4.5** ± 0.2	**18** ± 0.2
St-ER77 Grotta d'Ernesto (n=1)	Particulate/	**0.8 ± 0.1**	0.0 ± 0.1	0.0 ± 0.0	0.0 ± 0.1	0.0 ± 0.5	0.0 ± 0.0	0.0 ± 0.0	0.0 ± 0.0	0.0 ± 0.0	0.0 ± 0.0	0.0 ± 0.0	**0.3** ± 0.2	0.0 ± 0.3
	Coarse colloidal		0.0 ± 0.0	0.0 ± 0.0	0.0 ± 0.1	**4.5** ± 0.5	0.0 ± 0.0	0.0 ± 0.0	0.0 ± 0.0	0.0 ± 0.0	0.0 ± 0.0	0.0 ± 0.0	**0.3** ± 0.1	**1.1** ± 0.4
	Fine colloidal	**0.7** ± 0.2	0.0 ± 0.0	0.0 ± 0.0	0.0 ± 0.1	0.0 ± 0.4	0.0 ± 0.0	0.0 ± 0.0	0.0 ± 0.0	0.0 ± 0.0	0.0 ± 0.0	0.0 ± 0.0	**0.8** ± 0.4	0.0 ± 0.4
	ND	**2.4** ± 0.2	**2.0** ± 0.0	**0.4** ± 0.0	**4.1** ± 0.0	**7.3** ± 0.3	**0.6** ± 0.0	**0.1** ± 0.0	**0.1** ± 0.0	**0.1** ± 0.0	**0.1** ± 0.0	**0.2** ± 0.0	**6.3** ± 0.0	**17** ± 0.3

Table S5 Averaged partitioning of organic carbon and trace metals in triplicate analyses of sequentially filtered dripwater samples from Lower Balls Green Mine, Poole's Cavern, and Grotta di Ernesto. Nd = not determinable. Triplicate analyses were not performed on fractionated samples from Poole's Cavern drips RC1 and RC2. Concentrations of Al in filter blanks were too variable to enable blank correction. Instead, outliers in Al data from the triplicate analyses were excluded (values >1 standard deviation from the mean value were excluded). ND = nominally dissolved.

		------Concentration (mg L^{-1})------	----------Concentration (μg L^{-1})----------															
Date	Filter permeate	TOC	Si	Na	Mg	Al	Ti	V	Cr	Mn	Fe	Ni	Co	Cu	Zn	Br	Sr	Ba
29/07/2008	Raw	-	2.54	3.30	0.82	2.41	0.49	0.38	0.25	< 0.1	0.71	< 0.1	0.27	0.22	0.34	35.2	48.7	34.8
	1 μm	-	2.55	3.26	0.82		0.50	0.36	0.23	< 0.1		< 0.1	0.26	0.23		34.4	48.8	
	100 nm	-	2.48	3.10	0.78		0.50	0.35	0.23	< 0.1		< 0.1	0.23	0.23		34.7	48.1	
	1 nm	-	2.47	3.08	0.77		0.49	0.36	0.22	< 0.1		< 0.1	0.23	0.23		34.3	47.8	
27/08/2008	Raw	0.80	2.91	4.04	4.04	9.34	0.88	0.47	0.28	0.14	1.46	< 0.1	0.31	0.23	0.26	48.6	61.2	39.8
	1 μm	< 0.3	2.90	3.71	4.09		0.88	0.45	0.28	< 0.1		< 0.1	0.31	0.23		43.6	62.4	
	100 nm	< 0.9	2.71	3.19	0.88		0.87	0.41	0.24	< 0.1		< 0.1	0.23	0.24		39.9	56.5	
	1 nm	< 1.7	2.67	3.14	0.87		0.86	0.40	0.21	< 0.1		< 0.1	0.22	0.16		37.8	54.3	
22/09/2008	Raw	2.49	2.89	3.40	0.94	12.8	0.53	0.41	0.26	0.13	1.52	0.10	0.21	0.26	0.28	50.1	72.3	46.0
	1 μm	1.28	2.86	3.32	0.92		0.47	0.33	0.26	0.10		0.10	0.19	0.26		45.6	65.8	
	100 nm	0.86	2.87	3.26	0.92		0.45	0.34	0.25	0.10		0.12	0.20	0.24		47.3	69.7	
	1 nm	< 1.7	2.56	2.95	0.81		0.42	0.31	0.24	0.10		0.11	0.18	0.17		40.2	63.2	
20/10/2008	Raw	2.37	3.00	3.33	0.97	4.51	0.75	0.36	0.85	0.10	0.71	0.12	0.30	0.26	0.20	48.0	66.3	44.1
	1 μm	1.58	3.01	3.61	0.97		0.80	0.40	0.26	0.12		< 0.1	0.31	0.28		48.5	69.1	
	100 nm	< 0.9	2.82	3.14	0.91		0.77	0.36	0.22	< 0.10		< 0.1	0.31	0.25		47.5	64.7	
	1 nm	< 1.7	2.90	3.18	0.92		0.73	0.36	0.25	< 0.10		< 0.1	0.29	0.25		47.1	64.4	
23/11/2008	Raw	1.94	2.78	3.90	1.02	8.17	0.52	0.34	0.24	< 0.1	0.56	0.16	0.20	0.30	0.41	52.4	64.8	41.0
	1 μm	-	3.06	3.92	0.99		0.56	0.32	0.27	< 0.1		< 0.1	0.19	0.27		52.9	63.4	
	100 nm	1.97	2.69	3.45	0.96		0.46	0.32	0.22	< 0.1		< 0.1	0.20	0.32		50.1	65.3	
	1 nm	< 1.7	2.71	2.98	0.82		0.46	0.26	0.24	< 0.1		< 0.1	0.18	0.29		43.7	59.6	
19/12/2008	Raw	0.94	3.09	3.89	0.99	2.88	0.56	0.39	0.23	< 0.1	1.19	0.11	0.19	0.30	0.34	48.1	60.9	39.5
	1 μm	0.73	2.70	3.70	0.96		0.48	0.33	0.23	< 0.1		0.11	0.19	0.28		48.7	63.3	
	100 nm	< 0.9	2.81	3.38	0.90		0.54	0.40	0.24	< 0.1		< 0.1	0.19	0.30		46.9	61.2	
	1 nm	< 1.7	2.72	3.43	0.92		0.54	0.38	0.22	< 0.1		< 0.1	0.19	0.29		46.5	62.2	

Table S6 Trace element and organic carbon concentrations in sequentially filtered dripwater samples from Poole's Cavern drip point BC1 August to December 2008. Concentrations of Cd, Y (<0.1 μg L^{-1}) and Pb (<0.5 μg L^{-1}) were below ICP-MS detection limits in all samples. Filter blanks for Ba, Al and Zn were too variable to allow blank-correction of concentrations in singly analysed samples.

		------Concentration (mg L^{-1})------				----------Concentration (μg L^{-1})----------												
Date	Filter permeate	TOC	Si	Na	Mg	Al	Ti	V	Cr	Mn	Fe	Ni	Co	Cu	Zn	Br	Sr	Ba
20/01/2009	Raw	2.10	2.64	3.19	0.78	6.41	0.37	0.30	0.24	< 0.1	< 0.5	< 0.1	0.14	0.18	0.16	41.3	53.7	34.9
	1 μm	1.62	2.62	3.23	0.78		0.37	0.31	0.26	< 0.1		< 0.1	0.14	0.19		43.2	55.6	
	100 nm	1.13	2.62	3.10	0.77		0.37	0.30	0.26	< 0.1		< 0.1	0.14	0.19		40.6	52.5	
	1 nm	< 1.7	2.17	2.66	0.66		0.31	0.27	0.24	< 0.1		< 0.1	0.12	0.18		35.1	44.9	
20/02/2009	Raw	0.53	2.39	3.20	0.75	7.23	0.33	0.31	0.27	< 0.1	1.41	< 0.1	0.10	0.34	0.31	43.3	53.1	33.4
	1 μm	< 0.3	2.41	3.18	0.76		0.33	0.32	0.26	< 0.1		< 0.1	0.10	0.32		45.7	55.6	
	100 nm	< 0.9	2.34	3.11	0.77		0.29	0.20	0.23	< 0.1		< 0.1	0.10	0.19		42.3	53.9	
	1 nm	< 1.7	2.33	3.00	0.74		0.30	0.21	0.21	< 0.1		< 0.1	0.10	0.19		42.7	50.8	
24/03/2009	Raw	2.61	2.26	2.97	0.72	10.4	0.28	0.23	0.23	< 0.1	0.79	< 0.1	0.09	0.22	< 0.1	37.6	51.9	33.2
	1 μm	1.70	2.22	3.10	0.72		0.32	0.24	0.25	< 0.1		< 0.1	0.10	0.20		38.8	54.5	
	100 nm	1.08	2.21	2.87	0.71		0.29	0.24	0.23	< 0.1		< 0.1	0.10	0.19		39.3	52.4	
	1 nm	< 1.7	2.11	2.72	0.67		0.31	0.24	0.23	< 0.1		< 0.1	0.10	0.16		36.6	49.4	
20/04/2009	Raw	1.67	2.65	3.51	0.72	12.3	0.49	0.34	0.24	< 0.1	2.15	< 0.1	0.18	< 0.1	< 0.1	39.4	54.0	35.4
	1 μm	0.72	2.40	3.34	0.72		0.43	0.33	0.25	< 0.1		< 0.1	0.17	< 0.1		39.1	52.2	
	100 nm	< 0.9	2.39	3.07	0.71		0.39	0.33	0.24	< 0.1		< 0.1	0.17	< 0.1		41.5	50.8	
	1 nm	< 1.7	2.41	3.18	0.66		0.39	0.33	0.24	< 0.1		< 0.1	0.18	< 0.1		39.7	53.7	
30/06/2009	Raw	4.23	2.33	3.26	0.78	21.4	0.58	0.66	0.34	< 0.1	1.81	< 0.1	0.18	0.35	< 0.1	33.3	50.5	32.7
	1 μm	4.15	2.33	3.35	0.74		0.57	0.38	0.36	< 0.1		< 0.1	0.17	0.30		35.3	52.1	
	100 nm	2.38	2.32	3.31	0.70		0.56	0.34	0.25	< 0.1		< 0.1	0.18	0.26		35.7	53.9	
	1 nm	1.85	2.30	2.99	0.73		0.50	0.30	0.27	< 0.1		< 0.1	0.16	-		31.1	49.4	
20/07/2009	Raw	1.34	2.97	3.72	0.70	11.5	0.59	0.39	0.28	0.10	1.60	< 0.1	0.22	0.27	< 0.1	35.3	61.3	40.9
	1 μm	-	3.04	3.84	0.72		0.60	0.42	0.27	0.10		< 0.1	0.21	0.24		36.4	63.8	
	100 nm	-	2.86	3.43	0.75		0.57	0.41	0.25	< 0.1		< 0.1	0.20	0.25		35.2	60.4	
	1 nm	-	2.87	3.40	0.67		0.54	0.40	0.23	< 0.1		< 0.1	0.20	0.23		33.7	60.6	
15/08/2009	Raw	-	2.82	3.68	0.91	26.9	0.59	0.46	0.23	< 0.1	1.29	< 0.1	0.21	< 0.1	< 0.1	39.7	64.3	44.2
	1 μm	-	2.67	3.49	0.92		0.58	0.36	0.23	< 0.1		< 0.1	0.20	< 0.1		37.9	59.7	
	100 nm	-	2.65	3.46	0.87		0.57	0.33	0.23	< 0.1		< 0.1	0.22	< 0.1		40.3	65.2	
	1 nm	-	2.59	3.26	0.86		0.53	0.30	0.22	< 0.1		< 0.1	0.20	< 0.1		35.5	58.3	

Table S7 Trace element and organic carbon concentrations in sequentially filtered dripwater samples from Poole's Cavern drip point BC1 January to August 2009. Concentrations of Cd, Y (<0.1 μg L^{-1}) and Pb (<0.5 μg L^{-1}) were below ICP-MS detection limits in all samples. Filter blanks for Ba, Al, Fe and Zn were too variable to allow blank-correction of concentrations in filtered samples.

		------Concentration (mg L^{-1})------	----------Concentration (µg L^{-1})----------															
Date	Filter permeate	TOC	Si	Na	Mg	Al	Ti	V	Cr	Mn	Fe	Ni	Co	Cu	Zn	Br	Sr	Ba
29/07/2008	Raw	-	2.37	3.58	0.85	2.05	0.46	0.37	0.25	< 0.1	0.78	< 0.1	0.27	0.26	0.55	39.3	48.3	36.5
	1 µm	-	2.39	3.61	0.86		0.46	0.36	0.25	< 0.1		< 0.1	0.27	0.22		39.6	49.1	
	100 nm	-	2.51	3.57	0.88		0.50	0.36	0.22	< 0.1		< 0.1	0.23	0.25		39.7	50.0	
	1 nm	-	2.47	3.43	0.85		0.47	0.34	0.25	< 0.1		< 0.1	0.23	0.26		40.4	49.1	
27/08/2008	Raw	3.04	2.91	3.52	0.96	7.58	0.70	0.47	0.27	< 0.1	< 0.5	< 0.1	0.33	0.21	0.29	44.6	60.6	39.8
	1 µm	2.39	2.90	3.71	1.00		0.72	0.45	0.29	< 0.1		< 0.1	0.32	0.19		40.9	62.5	
	100 nm	1.71	2.74	3.62	0.96		1.04	0.45	0.29	< 0.1		< 0.1	0.28	0.19		44.1	57.7	
	1 nm	< 1.7	2.63	3.39	0.90		0.87	0.38	0.25	< 0.1		< 0.1	0.23	0.17		46.9	53.3	
22/09/2008	Raw	2.22	2.68	3.52	0.92	8.01	0.54	0.39	0.26	0.12	1.18	0.12	0.18	0.24	0.66		64.2	41.6
	1 µm	0.94	2.77	3.62	0.94		0.48	0.35	0.26	< 0.1		0.12	0.18	0.23			64.0	
	100 nm	0.99	2.75	3.49	0.93		0.44	0.34	0.27	< 0.1		0.11	0.18	0.22		47.4	64.2	
	1 nm	< 1.7	2.68	3.39	0.90		0.43	0.33	0.27	< 0.1		0.11	0.17	0.22		44.1	60.2	
20/10/2008	Raw	2.22	2.96	3.84	1.03	5.10	0.84	0.36	0.30	0.19	1.62	0.11	0.29	0.24	0.71	52.1	65.1	44.9
	1 µm	2.55	2.94	3.85	1.02		0.77	0.36	0.24	0.10		0.11	0.28	0.25		52.6	64.5	
	100 nm	1.39	2.77	3.43	0.96		0.74	0.35	0.25	0.10		0.10	0.29	0.24		53.2	63.4	
	1 nm	< 1.7	2.70	3.22	0.92		0.71	0.34	0.23	0.11		0.10	0.27	0.19		49.3	61.1	
23/11/2008	Raw	1.48	2.78	3.90	1.02	8.17	0.56	0.34	0.24	< 0.1	0.56	< 0.1	0.20	0.30	0.41	52.4	64.8	41.0
	1 µm	-	3.06	3.91	0.99		0.56	0.32	0.27	< 0.1		< 0.1	0.19	0.27		52.9	63.4	
	100 nm	0.93	2.86	3.89	1.07		0.57	0.32	0.23	< 0.1		< 0.1	0.20	0.29		62.6	66.5	
	1 nm	< 1.7	3.02	4.09	1.11		0.53	0.33	0.23	< 0.1		< 0.1	0.21	0.25		57.8	68.6	
19/12/2008	Raw	1.29	3.09	3.89	0.99	2.88	0.56	0.31	0.23	0.12	1.18	< 0.1	0.19	0.30	0.44	48.0	60.9	39.5
	1 µm	1.27	2.70	3.70	0.96		0.48	0.33	0.23	< 0.1		< 0.1	0.19	0.28		48.7	63.3	
	100 nm	< 0.9	2.58	3.32	0.88		0.41	0.31	0.23	< 0.1		< 0.1	0.18	0.27		47.5	59.6	
	1 nm	< 1.7	2.71	3.55	0.96		0.40	0.32	0.22	< 0.1		< 0.1	0.20	0.23		50.0	63.6	

Table S8 Trace element and organic carbon concentrations in sequentially filtered dripwater samples from Poole's Cavern drip point BC2 August to December 2008. Concentrations of Cd, Y (<0.1 µg L^{-1}) and Pb (<0.5 µg L^{-1}) were below ICP-MS detection limits in all samples. Filter blanks for Ba, Al and Zn were too variable to allow blank-correction of concentrations in singly analysed samples.

		------Concentration (mg L^{-1})------				----------Concentration (µg L^{-1})----------												
Date	Filter permeate	TOC	Si	Na	Mg	Al	Ti	V	Cr	Mn	Fe	Ni	Co	Cu	Zn	Br	Sr	Ba
20/01/2009	Raw	1.83	2.51	3.43	0.84	6.41	0.38	0.30	0.24	< 0.1	< 0.5	< 0.1	0.14	0.19	0.21	48.6	59.3	38.1
	1 µm	-	2.62	3.50	0.84		0.39	0.31	0.26	< 0.1		< 0.1	0.14	0.18		48.4	58.6	
	100 nm	1.07	2.50	3.39	0.83		0.39	0.31	0.23	< 0.1		< 0.1	0.14	0.17		46.3	55.6	
	1 nm	< 1.7	2.51	3.38	0.83		0.39	0.29	0.24	< 0.1		< 0.1	0.14	0.13		46.6	56.9	
20/02/2009	Raw	0.43	2.41	3.46	0.85	6.61	0.30	0.24	0.23	< 0.1	< 0.5	< 0.1	0.11	0.33	0.23	47.1	58.7	35.7
	1 µm	-< 0.3	2.38	3.44	0.83		0.33	0.25	0.22	< 0.1		< 0.1	0.11	0.29		48.9	59.2	
	100 nm	< 0.9	2.39	3.38	0.83		0.26	0.19	0.24	< 0.1		< 0.1	0.11	0.23		48.3	58.2	
	1 nm	< 1.7	2.34	3.29	0.81		0.25	0.19	0.21	< 0.1		< 0.1	0.10	0.18		47.3	57.1	
24/03/2009	Raw	2.21	2.22	3.28	0.78	9.58	0.27	0.29	0.23	< 0.1	3.87	< 0.1	0.10	0.20	0.15	44.1	56.6	34.8
	1 µm	2.01	2.23	3.50	0.78		0.32	0.28	0.27	< 0.1		< 0.1	0.10	0.23		45.3	61.1	
	100 nm	0.86	2.18	3.18	0.76		0.36	0.26	0.24	< 0.1		< 0.1	0.11	0.22		43.0	57.1	
	1 nm	< 1.7	2.11	3.06	0.73		0.33	0.24	0.22	< 0.1		< 0.1	0.10	0.18		42.5	54.3	
20/04/2009	Raw	1.22	2.51	3.64	0.81	12.1	0.49	0.34	0.27	0.33	7.88	< 0.1	0.21	< 0.1	< 0.1	43.7	57.9	38.4
	1 µm	0.97	2.46	3.49	0.77		0.39	0.36	0.26	< 0.1		< 0.1	0.18	< 0.1		44.4	54.5	
	100 nm	0.94	2.47	3.40	0.76		0.39	0.34	0.25	< 0.1		< 0.1	0.19	< 0.1		48.9	54.0	
	1 nm	< 1.7	2.46	3.41	0.77		0.38	0.34	0.23	< 0.1		< 0.1	0.18	< 0.1		44.4	53.4	
30/06/2009	Raw	-	2.49	3.58	0.78	24.8	0.73	0.38	0.25	0.52	7.82	< 0.1	0.21	0.34	0.41	40.8	54.5	36.8
20/07/2009	Raw	0.61	2.87	4.02	0.94	45.5	0.87	1.04	0.36	0.55	10.2	< 0.1	0.22	0.67	0.20	39.4	61.7	41.4
	1 µm	0.38	2.96	4.18	0.98		0.70	0.61	0.28	0.41		< 0.1	0.22	-		42.1	61.1	
	100 nm	< 0.9	2.74	3.86	0.92		0.57	0.44	0.29	0.21		< 0.1	0.20	0.48		37.6	60.7	
	1 nm	< 1.7	2.72	3.82	0.91		0.58	0.42	0.27	0.21		< 0.1	0.20	0.33		37.3	60.6	
15/08/2009	Raw	-	2.73	3.85	0.91	24.3	0.53	0.44	0.23	< 0.1	4.51	< 0.1	0.21	< 0.1	0.27	42.8	62.6	44.15
	1 µm	-	2.71	3.75	0.88		0.53	0.39	0.22	< 0.1		< 0.1	0.21	< 0.1		42.2	61.4	
	100 nm	-	2.48	3.48	0.81		0.47	0.34	0.24	< 0.1		< 0.1	0.18	< 0.1		37.0	56.6	
	1 nm	-	2.69	3.45	0.89		0.54	0.34	0.22	< 0.1		< 0.1	0.20	< 0.1		41.3	61.8	

Table S9 Trace element and organic carbon concentrations in sequentially filtered dripwater samples from Poole's Cavern drip point BC2 January to August 2009. Concentrations of Cd, Y (<0.1 µg L^{-1}) and Pb (<0.5 µg L^{-1}) were below ICP-MS detection limits in all samples. Filter blanks for Ba, Al, Fe and Zn were too variable to allow blank-correction of concentrations in filtered samples.

		------Concentration (mg L^{-1})------	----------Concentration (μg L^{-1})----------															
Date	Filter permeate	TOC	Si	Na	Mg	Al	Ti	V	Cr	Mn	Fe	Ni	Co	Cu	Zn	Br	Sr	Ba
29/07/2008	Raw	5.95	3.46	3.70	< 0.05	1209	0.76	20.0	10.1	< 0.1	< 0.5	0.78	0.66	1.44	0.41	35.2	55.2	14.0
	1 μm	-	3.89	4.05	< 0.05		0.73	21.1	9.45	< 0.1		0.75	0.65	1.42		34.7	57.3	
	100 nm	-	3.60	3.84	< 0.05		0.69	19.8	9.35	< 0.1		0.76	0.57	1.37		33.6	47.0	
	1 nm	-	3.35	3.73	< 0.05		0.70	18.7	8.10	< 0.1		0.57	0.46	1.06		32.4	45.0	
27/08/2008	Raw	4.82	3.83	4.00	< 0.05	1267	0.88	24.9	10.5	0.10	8.68	0.96	0.74	2.08	0.39	34.6	60.0	12.8
	1 μm	2.15	3.82	3.98	< 0.05		0.88	24.2	10.5	< 0.1		0.94	0.73	1.40		33.8	59.1	
	100 nm	< 0.9	3.21	3.92	< 0.05		0.72	22.4	10.1	< 0.1		0.94	0.70	1.44		33.4	57.9	
	1 nm	< 1.7	3.06	3.82	< 0.05		0.70	21.2	9.89	< 0.1		0.95	0.65	1.45		31.6	56.4	
22/09/2008	Raw	4.25	3.36	3.39	< 0.05	1285	0.55	21.3	9.21	0.17	0.50	1.04	0.58	1.39	0.57	34.8	71.9	15.6
	1 μm	2.13	3.46	3.56	< 0.05		0.60	20.8	9.24	0.10		1.03	0.59	1.36		34.6	70.0	
	100 nm	1.73	3.41	3.50	< 0.05		0.53	19.3	9.13	< 0.1		0.96	0.53	1.30		32.8	66.3	
	1 nm	< 1.7	3.46	3.58	< 0.05		0.53	19.7	9.10	< 0.1		0.73	0.45	0.99		33.5	67.6	
20/10/2008	Raw	4.72	3.76	3.74	< 0.05	1251	1.35	23.0	9.43	< 0.1	< 0.5	1.01	0.73	1.45	0.25	33.1	69.7	16.9
	1 μm	4.20	3.55	3.91	< 0.05		1.00	21.7	9.26	< 0.1		1.02	0.70	1.41		33.3	67.3	
	100 nm	4.12	3.28	3.56	< 0.05		0.89	19.8	9.14	< 0.1		1.04	0.63	1.33		33.0	59.7	
	1 nm	4.24	3.01	3.42	< 0.05		0.85	19.5	8.54	< 0.1		0.67	0.49	0.96		32.1	60.3	
23/11/2008	Raw	3.40	3.31	3.58	< 0.05	1249	0.83	23.4	9.69	0.11	6.19	1.20	0.73	1.55	0.39	37.4	83.3	17.4
	1 μm	-	3.20	3.60	< 0.05		0.83	23.2	9.73	< 0.1		1.22	0.72	1.52		34.7	82.7	
	100 nm	2.64	3.01	3.44	< 0.05		0.57	20.3	10.1	< 0.1		1.14	0.65	1.46		33.4	76.6	
	1 nm	2.30	2.91	3.25	< 0.05		0.57	18.9	8.85	< 0.1		0.71	0.50	1.08		32.2	72.5	
19/12/2008	Raw	3.73	3.34	3.47	< 0.05	943	0.51	21.4	10.1	< 0.1	< 0.5	1.15	0.61	1.38	0.10	36.9	82.9	19.4
	1 μm	2.31	-	4.05	< 0.05		0.50	-	8.10	< 0.1		1.13	0.60	1.36		34.6	80.9	
	100 nm	1.92	3.33	3.67	< 0.05		0.46	19.7	10.4	< 0.1		1.14	0.61	1.34		33.4	79.9	
	1 nm	< 1.7	3.22	3.56	< 0.05		0.44	18.0	9.20	< 0.1		0.43	0.39	0.71		32.6	75.4	

Table S10 Trace element and organic carbon concentrations in sequentially filtered dripwater samples from Poole's Cavern drip point PE1 July to December 2008. Concentrations of Cd, Y (<0.1 μg L^{-1}), Mg (<0.05 mg L^{-1}) and Pb (<0.5 μg L^{-1}) were below ICP-MS detection limits in all samples. Filter blanks for Ba, Al and Zn were too variable to allow blank-correction of concentrations in singly analysed samples.

		------Concentration (mg L^{-1})------				----------Concentration (µg L^{-1})----------												
Date	Filter permeate	TOC	Si	Na	Mg	Al	Ti	V	Cr	Mn	Fe	Ni	Co	Cu	Zn	Br	Sr	Ba
20/01/2009	Raw	2.53	3.21	3.39	< 0.05	964	0.51	18.9	10.2	< 0.1	< 0.5	0.87	0.54	1.17	0.11	35.3	75.2	16.4
	1 µm	2.57	3.14	3.47	< 0.05		0.44	18.2	9.91	< 0.1		0.79	0.52	1.15		34.0	76.1	
	100 nm	2.19	3.12	3.41	< 0.05		0.43	18.0	9.59	< 0.1		0.75	0.51	1.13		32.6	72.9	
	1 nm	2.09	3.03	3.37	< 0.05		0.43	15.7	8.33	< 0.1		0.30	0.32	0.60		30.2	66.8	
20/02/2009	Raw	1.61	3.36	3.43	< 0.05	954	0.56	13.4	10.0	< 0.1	< 0.5	0.91	0.39	1.33	0.10	37.5	81.6	16.7
	1 µm	0.97	3.30	3.42	< 0.05		0.35	12.8	10.4	< 0.1		0.96	0.37	1.26		32.9	79.2	
	100 nm	< 0.9	3.14	3.27	< 0.05		0.35	12.4	9.45	< 0.1		0.86	0.37	1.25		32.8	77.7	
	1 nm	< 1.7	3.08	3.34	< 0.05		0.34	11.6	9.43	< 0.1		0.43	0.24	0.80		33.2	76.6	
24/03/2009	Raw	3.30	3.10	3.21	< 0.05	945	0.39	13.5	10.3	< 0.1	< 0.5	0.93	0.40	1.25	0.10	34.4	81.6	16.5
	1 µm	2.38	3.08	3.23	< 0.05		0.40	14.1	8.75	< 0.1		0.78	0.40	1.34		36.4	88.6	
	100 nm	2.03	2.82	3.16	< 0.05		0.40	12.9	9.50	< 0.1		0.81	0.36	1.28		34.6	82.7	
	1 nm	< 1.7	2.62	3.12	< 0.05		0.34	10.8	7.96	< 0.1		0.27	0.19	0.55		33.2	78.0	
20/04/2009	Raw	2.54	3.43	3.66	< 0.05	1310	0.77	20.0	10.4	0.25	3.11	0.82	0.65	1.17	< 0.1	35.3	74.6	17.2
	1 µm	2.16	3.56	3.76	< 0.05		0.75	20.1	10.0	< 0.1		0.84	0.66	1.19		34.1	75.2	
	100 nm	1.66	3.55	3.86	< 0.05		0.73	19.8	10.3	< 0.1		0.79	0.64	1.22		33.6	73.4	
	1 nm	< 1.7	3.52	3.83	< 0.05		0.68	19.3	9.78	< 0.1		0.66	0.60	0.97		34.6	73.1	
30/06/2009	Raw	3.42	3.34	3.74	< 0.05	1254	0.78	20.3	11.3	< 0.1	2.71	0.95	0.58	1.78	0.49	32.5	65.4	14.7
	1 µm	2.67	3.43	3.82	< 0.05		0.73	20.9	11.1	< 0.1		0.92	0.58	1.41		31.9	65.1	
	100 nm	1.76	3.32	3.82	< 0.05		0.67	20.4	9.34	< 0.1		0.76	0.52	1.26		30.6	60.2	
	1 nm	< 1.7	3.38	3.78	< 0.05		0.64	17.6	8.02	< 0.1		0.32	0.29	0.58		31.4	56.6	
20/07/2009	Raw	1.35	3.52	3.86	< 0.05	1295	0.90	22.1	9.81	< 0.1	< 0.5	0.77	0.58	1.38	< 0.1	31.3	58.8	11.7
	1 µm	1.00	3.41	3.90	< 0.05		0.94	21.3	9.92	< 0.1		0.78	0.55	1.40		31.4	57.1	
	100 nm	< 0.9	3.53	4.13	< 0.05		0.86	22.2	9.90	< 0.1		0.76	0.54	1.40		32.2	54.8	
	1 nm	< 1.7	3.42	3.96	< 0.05		0.88	21.0	9.18	< 0.1		0.49	0.34	0.97		30.6	53.4	
15/08/2009	Raw	-	3.34	3.71	< 0.05	1105	0.63	23.1	10.5	< 0.1	14.7	1.00	0.58	1.22	0.31	32.8	60.3	12.7
	1 µm	-	3.07	3.85	< 0.05		0.63	23.4	9.73	< 0.1		0.94	0.59	1.24		32.4	61.4	
	100 nm	-	2.94	3.80	< 0.05		0.58	23.0	9.87	< 0.1		0.99	0.60	1.18		32.0	61.6	
	1 nm	-	2.75	3.56	< 0.05		0.53	20.9	8.90	< 0.1		0.60	0.39	0.77		30.6	57.2	

Table S11 Trace element and organic carbon concentrations in sequentially filtered dripwater samples from Poole's Cavern drip point PE1 January to August 2009. Concentrations of Cd, Y (<0.1 µg L^{-1}), Mg (<0.05 mg L^{-1}) and Pb (<0.5 µg L^{-1}) were below ICP-MS detection limits in all samples. Filter blanks for Ba, Al, Fe and Zn were too variable to allow blank-correction of concentrations in filtered samples.

		------Concentration (mg L^{-1})------			----------Concentration (μg L^{-1})----------														
Date	Filter permeate	TOC	Si	Na	Mg	Al	Ti	V	Cr	Mn	Fe	Ni	Co	Cu	Zn	Br	Sr	Ba	Pb
22/09/2008	Raw	5.94	0.45	4.01	< 0.05	133	0.13	1.52	9.00	0.10	2.67	4.63	0.64	4.59	0.75	47.1	59.1	31.1	< 0.5
	1 μm	2.98	0.49	3.92			0.18	1.43	8.61	0.13		4.49	0.71	4.82		50.4	78.3		
	100 nm	-	0.53	3.75			0.14	1.64	8.20	0.10		4.51	0.65	4.73		45.5	72.6		
	1 nm	2.54	0.54	3.89			0.12	1.47	8.51	< 0.1		2.82	0.50	2.70		45.1	72.0		
20/10/2008	Raw	4.89	0.43	4.01	< 0.05	173	0.10	0.80	8.64	0.10	< 0.5	4.55	0.79	4.56	0.23	47.9	106	58.5	< 0.5
	1 μm	4.39	0.59	4.25			0.15	0.73	8.69	0.20		4.27	0.75	4.47		46.9	103		
	100 nm	3.28	0.47	3.90			0.10	0.60	8.54	0.10		4.65	0.71	4.44		46.2	100		
	1 nm	2.65	0.45	3.71			0.11	0.57	7.40	< 0.1		1.69	0.42	1.58		41.7	89.5		
23/11/2008	Raw	4.75	0.34	3.94	< 0.05	103	< 0.1	0.58	9.97	< 0.1	0.66	4.81	0.75	4.06	0.23	47.2	107	53.8	< 0.5
	1 μm	1.28	0.42	4.19				0.49	7.64			3.78	0.67	3.67		40.7	93.7		
	100 nm	< 0.9	0.44	3.99				0.39	6.94			3.54	0.59	3.62		35.9	83.3		
	1 nm	< 1.7	0.41	3.94				0.41	7.72			2.95	0.45	2.23		40.0	90.7		
19/12/2008	Raw	3.22	0.53	4.31	< 0.05	117	< 0.1	1.47	9.52	< 0.1	< 0.5	4.69	1.05	4.21	0.44	48.4	158	102	2.11
	1 μm	2.97	0.59	4.35				1.47	10.2			5.05	1.09	3.94		45.9	146		< 0.5
	100 nm	2.22	0.56	4.20				0.97	9.54			4.64	1.03	3.86		41.7	142		< 0.5
	1 nm	1.87	0.55	4.15				0.89	9.09			1.78	0.76	1.43		40.2	134		< 0.5

Table S12 Trace element and organic carbon concentrations in sequentially filtered dripwater samples from Poole's Cavern drip point RC1 September to December 2008. Concentrations of Cd, Y (<0.1 μg L^{-1}) and Mg (<0.05 mg L^{-1}) were below ICP-MS detection limits in all samples. Filter blanks for Ba, Al and Zn were too variable to allow blank-correction of concentrations in singly analysed samples.

		------Concentration (mg L^{-1})------				----------Concentration (µg L^{-1})----------													
Date	Filter permeate	TOC	Si	Na	Mg	Al	Ti	V	Cr	Mn	Fe	Ni	Co	Cu	Zn	Br	Sr	Ba	Pb
20/01/2009	Raw	4.39	0.44	4.05	< 0.05	111	0.21	1.08	8.90	0.38	9.65	4.12	0.95	4.34	1.74	44.3	155	101	2.20
	1 µm	3.27	0.55	4.50	< 0.05		0.23	1.10	9.63	0.17		4.35	1.01	4.02		45.7	154		< 0.5
	100 nm	2.38	0.52	4.34	< 0.05		0.11	0.78	9.86	< 0.1		4.44	1.01	3.68		41.8	146		< 0.5
	1 nm	2.47	0.53	4.22	< 0.05		0.10	0.78	9.64	< 0.1		3.62	0.98	3.86		43.9	150		< 0.5
20/02/2009	Raw	2.61	0.40	3.90	< 0.05	106	< 0.1	1.52	9.17	< 0.1	< 0.5	4.53	0.94	4.18	0.41	50.2	164	96.5	< 0.5
	1 µm	2.11	0.51	3.94	< 0.05			1.27	8.58			4.17	0.86	3.91		47.7	152		
	100 nm	1.22	0.45	3.89	< 0.05			0.41	8.52			4.09	0.79	3.69		43.2	143		
	1 nm	< 1.7	0.46	3.86	< 0.05			0.46	7.67			1.69	0.52	1.77		42.8	133		
24/03/2009	Raw	4.38	0.32	3.72	< 0.05	116	0.47	0.80	10.0	< 0.1	3.69	4.94	0.67	4.09	0.18	46.9	119	61.0	< 0.5
	1 µm	4.38	0.40	3.71	< 0.05		0.11	0.57	9.38			4.71	0.61	3.89		45.6	114		
	100 nm	2.85	0.38	3.70	< 0.05		0.42	0.57	8.96			4.65	0.58	3.83		44.0	105		
	1 nm	2.54	0.39	3.58	< 0.05		0.12	0.49	9.12			2.59	0.45	2.19		44.0	103		
20/04/2009	Raw	3.41	0.56	4.16	< 0.05	104	0.19	1.47	8.76	< 0.1	< 0.5	4.36	1.22	4.52	0.25	48.7	152	102	1.44
	1 µm	3.25	0.57	3.99	< 0.05		< 0.1	1.20	9.23			4.75	1.09	4.18		45.2	143		< 0.5
	100 nm	2.96	0.55	4.05	< 0.05		< 0.1	0.86	9.33			4.54	1.12	4.26		47.4	150		< 0.5
	1 nm	2.08	0.54	3.96	< 0.05		< 0.1	0.93	9.06			3.89	1.06	3.34		46.8	147		< 0.5
30/06/2009	Raw	6.04	0.51	4.19	< 0.05	90.3	0.19	1.68	9.42	< 0.1	2.71	4.88	0.78	4.68	< 0.1	48.4	82.9	48.2	< 0.5
20/07/2009	Raw	3.34	0.78	4.51	< 0.05	165	0.34	2.48	9.33	3.12	0.89	5.10	0.86	6.01	0.69	47.9	76.5	50.0	< 0.5
15/08/2009	Raw	-	0.56	4.31	< 0.05	129	< 0.1	2.05	9.63	< 0.1	1.41	4.98	0.76	4.55	< 0.1	48.5	78.8	45.6	< 0.5

Table S13 Trace element and organic carbon concentrations in sequentially filtered dripwater samples from Poole's Cavern drip point RC1 January to April 2009, and unfiltered (raw) dripwaters from June to August 2009. Concentrations of Cd, Y (<0.1 µg L^{-1}) and Mg (<0.05 mg L^{-1}) were below ICP-MS detection limits in all samples. Filter blanks for Ba, Al, Fe and Zn were too variable to allow blank-correction of concentrations in filtered samples.

		------Concentration (mg L^{-1})------				----------Concentration (μg L^{-1})----------													
Date	Filter permeate	TOC	Si	Na	Mg	Al	Ti	V	Cr	Mn	Fe	Ni	Co	Cu	Zn	Br	Sr	Ba	Pb
22/09/2008	Raw	4.29	0.51	3.70	< 0.05	152	0.13	1.06	8.05	0.10	1.17	4.54	0.95	4.60	1.03	48.1	145	90.2	< 0.5
	1 μm	4.23	0.55	3.77	< 0.05		0.13	0.97	8.44	< 0.1		4.57	0.97	4.69		47.9	146		
	100 nm	-	0.53	3.82	< 0.05		0.12	0.70	8.50	< 0.1		4.54	0.96	4.57		47.9	145		
	1 nm	3.24	0.56	3.80	< 0.05		0.13	0.59	8.47	< 0.1		3.04	0.76	2.78		45.4	134		
20/10/2008	Raw	3.99	0.62	4.00	< 0.05	138	0.12	1.44	8.36	0.10	< 0.5	4.27	1.05	4.19	0.36	46.7	153	95.7	< 0.5
	1 μm	3.72	0.81	4.25	< 0.05		0.12	1.41	8.24	< 0.1		4.19	1.07	4.26		46.1	153		
	100 nm	3.75	0.56	3.87	< 0.05		0.12	0.45	7.85	< 0.1		4.14	0.99	4.25		45.8	152		
	1 nm	2.35	0.56	3.69	< 0.05		0.11	0.38	7.24	< 0.1		1.79	0.69	1.64		40.8	133		
23/11/2008	Raw	5.54	0.43	4.37	< 0.05	99.3	< 0.1	0.92	8.71	< 0.1	< 0.5	4.29	1.11	4.05	0.37	44.7	160	96.0	1.50
	1 μm	-	0.53	4.54	< 0.05			0.97	8.35	< 0.1		4.16	1.10	4.11		44.9	159		< 0.5
	100 nm	2.67	0.48	4.57	< 0.05			0.85	7.78	< 0.1		3.91	1.10	4.09		46.4	161		< 0.5
	1 nm	2.21	0.46	4.30	< 0.05			0.53	7.89	< 0.1		2.53	0.88	2.61		42.9	150		< 0.5
19/12/2008	Raw	3.00	0.66	4.51	< 0.05	105	0.10	1.18	9.07	< 0.1	< 0.5	4.20	1.09	3.48	0.29	44.5	152	98.2	1.69
	1 μm	2.84	0.69	4.41	< 0.05		< 0.1	1.01	8.99	< 0.1		4.08	1.05	3.40		41.9	147		< 0.5
	100 nm	1.11	0.64	3.50	< 0.05		< 0.1	1.02	10.5	< 0.1		1.08	0.60	1.37		29.2	73.3		< 0.5
	1 nm	< 1.7	0.65	3.38	< 0.05		< 0.1	1.04	9.44	< 0.1		0.68	0.41	0.91		29.5	75.1		< 0.5

Table S14 Trace element and organic carbon concentrations in sequentially filtered dripwater samples from Poole's Cavern drip point RC2 September to December 2008. Concentrations of Cd, Y (<0.1 μg L^{-1}) and Mg (<0.05 mg L^{-1}) were below ICP-MS detection limits in all samples. Filter blanks for Ba, Al and Zn were too variable to allow blank-correction of concentrations in singly analysed samples.

		------Concentration (mg L^{-1})------				----------Concentration (µg L^{-1})----------													
Date	Filter permeate	TOC	Si	Na	Mg	Al	Ti	V	Cr	Mn	Fe	Ni	Co	Cu	Zn	Br	Sr	Ba	Pb
20/01/2009	Raw	3.91	0.55	4.36	< 0.05	108	< 0.1	0.75	9.63	< 0.1	< 0.5	4.35	0.96	3.85	0.21	44.3	151	92.8	1.21
	1 µm	2.95	0.63	4.45				0.77	9.56			4.24	0.96	3.67		43.6	146		< 0.5
	100 nm	2.79	0.55	4.31				0.47	9.48			4.13	0.91	3.63		44.5	149		< 0.5
	1 nm	2.58	0.54	4.25				0.48	9.37			2.33	0.78	1.98		40.9	142		< 0.5
20/02/2009	Raw	2.89	0.56	4.09	< 0.05	250	0.12	1.22	9.04	< 0.1	< 0.5	4.49	0.63	4.74	0.10	49.5	88.6	49.2	< 0.5
	1 µm	2.38	0.61	4.13			0.10	1.20	9.30			4.58	0.62	4.58		47.9	85.6		
	100 nm	1.79	0.57	4.03			0.10	1.08	9.64			4.86	0.58	4.56		46.3	79.7		
	1 nm	< 1.7	0.58	4.00			0.10	1.15	8.65			1.59	0.35	1.93		47.1	82.9		
24/03/2009	Raw	3.25	0.60	4.25	< 0.05	124	0.22	0.71	8.73	0.11	1.65	4.44	0.85	4.24	0.15	46.8	140	82.0	< 0.5
	1 µm	3.26	0.67	4.57			0.18	0.80	7.68	< 0.1		3.86	0.85	4.29		47.8	143		
	100 nm	2.47	0.62	4.61			0.14	0.42	9.17	< 0.1		4.33	0.76	4.25		49.1	146		
	1 nm	2.25	0.65	4.69			0.17	0.45	8.71	< 0.1		2.52	0.70	2.53		49.1	146		
20/04/2009	Raw	3.39	0.61	3.95	< 0.05	186	< 0.1	1.33	9.88	< 0.1	< 0.5	4.95	0.69	5.12	< 0.1	46.9	71.6	40.7	0.97
	1 µm	3.19	0.72	4.03				1.31	9.46			4.81	0.68	5.10		46.6	69.5		< 0.5
	100 nm	2.25	0.68	3.94				1.30	9.25			4.72	0.65	4.93		44.8	64.4		< 0.5
	1 nm	< 1.7	0.75	4.18				1.34	8.92			2.42	0.48	2.88		45.3	65.9		< 0.5
30/06/2009	Raw	-	1.92	4.51	< 0.05	129	0.42	22.3	8.64	0.11	1.69	4.00	1.02	4.90	0.35	48.7	82.2	43.0	< 0.5
15/08/2009	Raw	-	0.58	4.29	< 0.05	121	< 0.1	1.26	9.43	< 0.1	0.82	4.74	0.65	4.56	< 0.1	48.3	45.4	21.9	< 0.5
	1 µm	-	0.67	4.32				1.27	9.14			4.59	0.64	4.52		48.2	44.4		
	100 nm	-	0.63	4.27				1.23	9.29			4.78	0.62	4.63		47.7	43.6		
	1 nm	-	0.77	4.22				1.24	8.40			2.33	0.37	2.48		47.8	43.8		

Table S15 Trace element and organic carbon concentrations in sequentially filtered dripwater samples from Poole's Cavern drip point RC2 January to April 2009, and unfiltered (raw) dripwaters from June to August 2009. Concentrations of Cd, Y (<0.1 µg L^{-1}) and Mg (<0.05 mg L^{-1}) were below ICP-MS detection limits in all samples. Filter blanks for Ba, Al, Fe and Zn were too variable to allow blank-correction of concentrations in filtered samples.

		------Concentration (mg L^{-1})------				----------Concentration (μg L^{-1})----------												
Date	Filter permeate	TOC	Si	Na	Mg	Al	Ti	V	Cr	Mn	Fe	Ni	Co	Cu	Zn	Br	Sr	Ba
9/09/2008	Raw	3.06	2.89	7.81	2.75	15.6	0.84	0.26	< 0.1	0.19	3.43	0.35	0.34	0.68	0.51	41.7	139	7.57
	1 μm	3.07	3.15	7.88	2.77		0.61	0.23		0.14		0.35	0.35	0.63		42.0	146	
	100 nm	2.80	2.93	7.43	2.61		0.59	0.23		0.10		0.32	0.34	0.53		39.4	135	
	1 nm	2.81	3.05	7.31	2.57		0.60	0.20		0.10		0.28	0.31	0.50		38.8	138	
13/10/2008	Raw	3.55	2.56	6.42	2.55	7.89	0.36	0.10	< 0.1	< 0.1	3.77	0.29	0.13	0.37	0.19	41.6	160	7.11
	1 μm	3.39	2.48	6.14	2.37		0.32	0.10				0.25	0.12	0.37		39.5	152	
	100 nm	1.81	2.51	6.11	2.46		0.33	0.11				0.23	0.12	0.37		42.0	157	
	1 nm	1.74	2.07	5.04	2.01		0.30	0.10				0.15	0.10	0.22		31.6	129	
18/11/2008	Raw	7.46	2.47	8.75	2.45	7.24	0.34	0.13	< 0.1	0.34	24.0	1.04	0.13	0.38	1.24	43.0	158	7.51
	1 μm	2.43	2.57	8.98	2.49		0.32	0.12		< 0.1		0.23	0.12	0.33		43.0	161	
	100 nm	1.07	2.58	8.68	2.48		0.33	0.12		< 0.1		0.21	0.12	0.32		41.3	158	
	1 nm	< 1.7	2.52	8.25	2.34		0.32	0.12		< 0.1		0.22	0.11	0.27		37.5	149	

Table S16 Trace element and organic carbon concentrations in sequentially filtered dripwater samples from Lower Balls Green Mine drip point LB1 September to November 2008. Concentrations of Mg (<0.05 mg L^{-1}), Cd, Y, Cr (<0.1 μg L^{-1}) and Pb (<0.5 μg L^{-1}) were below ICP-MS detection limits in all samples. Filter blanks for Ba, Al, Fe and Zn were too variable to allow blank-correction of concentrations in filtered samples.

		------Concentration (mg L^{-1})------				----------Concentration (µg L^{-1})----------												
Date	Filter permeate	TOC	Si	Na	Mg	Al	Ti	V	Cr	Mn	Fe	Ni	Co	Cu	Zn	Br	Sr	Ba
9/09/2008	Raw	2.96	2.80	6.16	2.74	11.4	0.59	0.12	< 0.1	< 0.1	0.55	0.40	0.34	0.47	0.47	45.7	150	6.25
	1 µm	2.43	2.95	6.10	2.81		0.57	0.13				0.40	0.33	0.37		44.4	142	
	100 nm	1.31	2.86	6.35	2.72		0.57	0.12				0.36	0.30	0.31		43.5	148	
	1 nm	< 1.7	2.74	5.83	2.62		0.50	0.13				0.31	0.21	0.32		43.6	144	
13/10/2008	Raw	3.41	2.29	6.17	2.35	6.07	0.33	0.10	< 0.1	< 0.1	< 0.5	0.24	0.12	0.31	0.20	42.1	157	5.73
	1 µm	2.75	2.53	6.68	2.51		0.33	0.12				0.24	0.13	0.32		44.8	166	
	100 nm	2.53	2.42	6.39	2.43		0.34	0.10				0.25	0.12	0.34		42.9	161	
	1 nm	< 1.7	2.45	6.40	2.44		0.33	0.10				0.24	0.11	0.26		42.8	162	
18/11/2008	Raw	2.71	2.39	7.14	2.40	5.72	0.32	0.10	< 0.1	< 0.1	< 0.5	0.30	0.12	0.33	1.13	39.2	163	5.84
	1 µm	2.21	2.49	7.37	2.38		0.32	0.10				0.29	0.12	0.31		39.1	160	
	100 nm	0.89	2.54	7.11	2.46		0.33	0.12				0.27	0.12	0.30		41.6	166	
	1 nm	< 1.7	2.37	6.84	2.26		0.31	0.10				0.26	0.11	0.24		36.5	154	

Table S17 Trace element and organic carbon concentrations in sequentially filtered dripwater samples from Lower Balls Green Mine drip point LB2 September to November 2008. Concentrations of Mg (<0.05 mg L^{-1}), Cd, Y, Cr, Mn (<0.1 µg L^{-1}) and Pb (<0.5 µg L^{-1}) were below ICP-MS detection limits in all samples. Filter blanks for Ba, Al, Fe and Zn were too variable to allow blank-correction of concentrations in filtered samples.

		------Concentration (mg L^{-1})------				----------Concentration (μg L^{-1})----------												
Date	Filter permeate	TOC	Si	Na	Mg	Al	Ti	V	Cr	Mn	Fe	Ni	Co	Cu	Zn	Br	Sr	Ba
9/09/2008	Raw	2.50	3.03	7.29	2.85	12.2	0.60	0.10	< 0.1	< 0.1	< 0.5	0.78	0.32	0.28	0.33	42.4	150	6.09
	1 μm	1.89	3.01	7.23	2.81		0.57	0.10				0.76	0.31	0.31		42.8	147	
	100 nm	1.03	3.24	7.14	2.82		0.58	0.10				0.76	0.30	0.30		42.5	151	
	1 nm	< 1.7	3.08	7.29	2.81		0.59	0.10				0.57	0.32	0.31		43.3	149	
13/10/2008	Raw	5.26	2.47	6.31	2.47	5.24	0.40	< 0.1	< 0.1	< 0.1	< 0.5	0.19	0.11	0.20	0.13	41.0	164	5.77
	1 μm	3.07	2.64	6.60	2.59		0.37					0.21	0.12	0.20		43.7	172	
	100 nm	1.92	2.37	5.96	2.35		0.35					0.19	0.10	0.19		39.6	157	
	1 nm	1.87	2.49	6.21	2.44		0.34					0.17	0.12	0.21		42.9	164	
18/11/2008	Raw	2.75	2.52	6.07	2.38	7.36	0.31	< 0.1	< 0.1	< 0.1	< 0.5	0.19	0.12	0.21	0.26	41.5	162	5.67
	1 μm	2.33	2.50	5.86	2.29		0.32					0.21	0.11	0.21		39.6	156	
	100 nm	< 0.9	2.40	5.69	2.29		0.30					0.17	0.12	0.21		37.7	153	
	1 nm	< 1.7	2.59	6.11	2.40		0.28					0.18	0.11	0.20		36.7	165	

Table S18 Trace element and organic carbon concentrations in sequentially filtered dripwater samples from Lower Balls Green Mine drip point LB3 September to November 2008. Concentrations of Mg (<0.05 mg L^{-1}), Cd, Y, Cr, Mn (<0.1 μg L^{-1}), Pb and Fe (<0.5 μg L^{-1}) were below ICP-MS detection limits in all samples. Filter blanks for Ba, Al, Fe and Zn were too variable to allow blank-correction of concentrations in filtered samples.

			------Concentration (mg L^{-1})-----				----------Concentration (μg L^{-1})----------											
Date	Drip	Filter permeate	TOC	Si	Na	Mg	Al	Ti	V	Cr	Mn	Fe	Ni	Co	Cu	Zn	Br	Sr	Ba
8/11/2008	St-1	Raw	3.79	2.49	0.47	4.60	8.06	0.70	0.14	0.12	0.10	0.69	0.10	0.15	0.25	0.38	6.10	19.0	2.00
		1 μm	2.55	2.44	0.46	4.49		0.66	0.12	0.11	< 0.1		0.10	0.15	0.23		5.77	18.7	
		100 nm	2.06	2.41	0.40	4.42		0.66	0.12	0.12	< 0.1		0.11	0.15	0.26		5.70	18.7	
		1 nm	< 1.7	2.35	0.39	4.30		0.64	0.10	0.10	< 0.1		0.10	0.14	0.18		4.79	18.5	
8/11/2008	St-2	Raw	2.95	2.34	0.45	4.37	10.5	0.69	0.15	0.12	0.10	0.65	0.10	0.14	0.23	0.19	5.14	18.6	2.01
		1 μm	3.01	2.35	0.45	4.33		0.66	0.14	0.12	< 0.1		0.10	0.14	0.22		5.11	18.7	
		100 nm	1.77	2.24	0.38	4.16		0.64	0.10	0.10	< 0.1		0.12	0.14	0.21		4.60	18.2	
		1 nm	< 1.7	2.22	0.37	4.09		0.63	0.10	0.10	< 0.1		0.10	0.14	0.16		4.54	17.9	
8/11/2008	St-ER77	Raw	3.84	1.98	0.47	4.13	9.40	0.62	0.13	0.13	< 0.1	< 0.5	0.10	0.14	0.31	0.17	7.70	17.6	1.71
		1 μm	-	2.01	0.46	4.13		0.64	0.15	0.13			0.10	0.13	0.27		7.39	18.1	
		100 nm	3.06	1.97	0.44	4.08		0.64	0.10	0.12			0.10	0.14	0.24		7.09	16.9	
		1 nm	-	1.98	0.44	4.06		0.62	0.11	0.12			0.10	0.13	0.21		6.30	17.0	
8/11/2008	St-ER78	Raw	2.93	2.29	0.44	5.76	6.47	0.67	0.14	0.12	< 0.1	< 0.5	0.10	0.13	0.20	0.19	5.44	18.8	1.95
		1 μm	3.01	2.26	0.40	5.57		0.65	0.14	0.11			0.10	0.13	0.19		5.36	18.5	
		100 nm	2.52	2.14	0.38	5.39		0.68	0.12	0.11			0.10	0.12	0.17		4.88	17.8	
		1 nm	2.05	2.14	0.38	5.34		0.64	0.12	0.11			0.10	0.12	0.14		4.82	17.7	

Table S17 Average trace element and organic carbon concentrations in sequentially filtered dripwater samples from Grotta di Ernesto drip points St-1, St-2, St-ER77 and St-ER78 taken in November 2008. Concentrations of Cd, Y, (<0.1 μg L^{-1}) and Pb (<0.5 μg L^{-1}) were below ICP-MS detection limits in all samples. Filter blanks for Ba, Al, Fe and Zn were too variable to allow blank-correction of concentrations in filtered samples.

		Fluorescence intensity (units)			----Concentration (mg L^{-1})---	----------Concentration (μg L^{-1})----------																
Date	Drip	Peak A	Peak C	Peak T	TOC	Si	Na	Mg	Al	Ti	V	Cr	Mn	Fe	Ni	Co	Cu	Zn	Br	Sr	Y	Ba
4/11/2008	St-1	43.4	24.4	20.9	8.22	2.19	0.51	3.23	20.4	1.08	0.10	< 0.1	2.06	3.87	0.72	0.17	1.98	136	9.22	19.1	0.10	4.82
6/11/2008		32.7	17.3	10.2	3.31	2.40	0.50	3.66	19.9	1.33	0.10	0.10	0.95	1.98	0.58	0.15	0.92	81.9	6.77	18.8	< 0.1	5.10
7/11/2008		36.1	17.4	34.5	7.53	2.41	0.67	3.95	27.4	1.49	0.10	0.10	1.31	5.83	1.21	0.16	3.65	235	7.77	19.7	< 0.1	5.51
8/11/2008		25.8	18.9	11.0	3.79	2.49	0.47	4.60	8.06	0.70	0.14	0.12	0.10	0.69	0.10	0.15	0.25	0.38	6.10	19.0	< 0.1	2.00
6/11/2008	St-2	36.8	22.3	21.4	4.07	2.41	0.53	3.73	6.38	1.15	0.10	< 0.1	1.14	10.8	0.80	0.16	1.12	180	7.13	18.6	< 0.1	5.75
7/11/2008		40.2	23.3	65.4	5.19	2.46	0.77	4.14	6.66	1.24	0.11	0.10	2.25	1.71	2.06	0.18	5.44	143	5.56	18.1	< 0.1	5.86
8/11/2008		28.7	20.0	12.5	2.95	2.34	0.45	4.37	10.5	0.69	0.15	0.12	0.10	0.65	0.10	0.14	0.23	0.19	5.14	18.6	< 0.1	2.01

Table S19 Average trace element and organic carbon concentrations in raw dripwater samples from Grotta di Ernesto drip points St-1 and St-2 taken 4th – 8th November 2008. Concentrations of Cd, Y, (<0.1 μg L^{-1}) and Pb (<0.5 μg L^{-1}) were below ICP-MS detection limits in all samples.

	Fluorescence intensity (units)		Concentration (mg L^{-1})			----------Concentration (μg L^{-1})----------												
Date	Peak A	Peak C	TOC	Si	Na	Al	Ti	V	Cr	Mn	Fe	Ni	Co	Cu	Zn	Br	Sr	Ba
26/06/2008	174.1	96.2	2.60	-	-	-	-	-	-	-	-	-	-	-	-	-	-	-
8/07/2008	224.1	135.4	7.02	-	-	-	-	-	-	-	-	-	-	-	-	-	-	-
15/07/2008	136.7	83.8	7.09	-	-	-	-	-	-	-	-	-	-	-	-	-	-	-
18/07/2008	168.9	96.4	5.65	-	-	-	-	-	-	-	-	-	-	-	-	-	-	-
6/08/2008	178.1	97.1	14.7	10.10	3.70	1208	0.63	20.0	10.1	< 0.1	< 0.5	0.78	0.66	1.26	0.41	35.2	55.2	14.0
22/08/2008	186.2	104.6	8.70	--	-	-	-	-	-	-	-	-	-	-	-	-	-	-
26/08/2008	296.0	148.6	8.75	3.80	4.00	1255	3.34	18.9	3.71	0.86	6.80	1.21	0.70	2.88	96.8	24.7	58.8	18.0
1/09/2008	215.5	127.2	7.75	9.21	3.91	1266	0.88	24.9	10.5	< 0.1	< 0.5	0.94	0.74	2.08	0.39	34.6	60.0	12.8
17/09/2008	202.1	115.3	-	3.35	4.42	984	2.38	20.5	6.83	3.31	29.8	4.87	0.90	16.6	40.5	28.7	64.5	26.0
22/09/2008	229.2	145.9	4.25	3.16	4.19	36	0.76	13.6	6.67	0.17	< 0.5	1.53	0.68	1.46	6.83	27.7	62.1	17.8
27/09/2008	179.4	106.8	9.12	3.36	4.00	1285	0.55	21.3	9.21	0.10	< 0.5	1.04	0.58	1.39	0.57	34.8	71.9	15.6
5/10/2008	139.1	91.5	8.41	9.21	4.18	1453	4.61	18.8	3.96	3.00	16.5	4.15	0.77	12.1	78.0	23.4	59.6	26.4
13/10/2008	173.0	107.4	4.65	3.51	4.08	681	1.54	13.2	4.00	0.68	3.04	1.67	0.71	3.86	107	31.8	63.5	18.3
24/10/2008	134.9	213.5	4.72	-	-	-	-	-	-	-	-	-	-	-	-	-	-	-
29/10/2008	144.5	227.9	7.54	3.45	3.60	1384	0.95	22.6	9.45	< 0.1	< 0.5	1.00	0.73	1.42	0.26	33.4	68.4	15.8
5/11/2008	145.2	216.9	7.08	9.45	3.74	1454	1.35	21.2	8.62	0.15	3.98	1.18	0.71	2.92	23.2	30.3	66.7	20.8
21/11/2009	227.2	142.5	-	3.70	4.03	1187	3.01	19.4	6.24	0.91	9.33	2.57	0.77	6.35	44.7	30.3	74.3	25.2
25/11/2008	213.9	141.8	3.40	3.63	3.87	1398	4.58	18.8	3.93	0.49	5.50	1.56	0.68	2.74	78.7	28.8	60.1	21.0
18/12/2008	211.0	148.2	3.73	9.69	3.58	1249	0.83	23.4	9.69	0.11	6.19	1.10	0.72	1.55	0.39	37.4	83.3	17.4
23/01/2009	257.2	162.1	4.24	10.1	3.47	943	0.51	21.4	10.1	< 0.1	< 0.5	1.01	0.61	1.38	0.10	36.9	82.9	19.4
26/01/2009	230.9	147.7	2.53	10.2	3.39	964	0.51	19.0	10.2	< 0.1	< 0.5	0.87	0.53	1.17	0.11	35.3	75.2	16.4
23/02/2009	248.9	155.8	1.61	10.0	3.43	954	0.56	13.4	10.0	< 0.1	< 0.5	0.91	0.39	1.33	0.10	37.5	81.6	16.7
20/03/2009	-	-	4.58	10.3	3.21	945	0.34	13.5	10.3	< 0.1	< 0.5	0.93	0.39	1.25	0.10	34.4	81.6	16.5
23/03/2009	248.6	146.4	3.30	-	-	-	-	-	-	-	-	-	-	-	-	-	-	-
20/04/2009	182.8	108.0	2.54	3.43	3.66	1310	0.77	19.8	10.4	< 0.1	< 0.5	0.82	0.65	1.17	< 0.1	35.3	74.6	17.2
1/06/2009	190.1	123.6	1.64	3.69	4.02	1017	0.57	21.3	9.72	< 0.1	< 0.5	0.80	0.54	1.06	< 0.1	32.9	69.3	13.6
30/06/2009	183.4	119.2	1.64	3.34	3.74	1254	0.78	20.4	11.3	< 0.1	< 0.5	0.95	0.58	1.78	0.49	32.5	65.4	14.7
20/07/2009	211.0	124.6	3.42	3.52	3.86	1295	0.70	22.2	9.81	< 0.1	< 0.5	0.77	0.58	1.28	< 0.1	31.3	58.8	11.7
15/08/2009	251.4	124.7	1.35	3.34	3.71	1105	0.63	23.0	10.5	< 0.1	< 0.5	1.00	0.58	1.22	0.31	32.8	60.3	12.7

Table S20 Trace element and organic carbon concentrations in raw dripwater samples from Poole's Cavern drip point PE1 sampled between 26/06/2008 and 15/08/2008. Concentrations of Cd, Y, (<0.1 μg L^{-1}) and Pb (<0.5 μg L^{-1}) were below ICP-MS detection limits in all samples.

Appendix III Poole's Cavern major ion data repository

Month	BC1 Ca (mg L^{-1})	1 σ	BC2 Ca (mg L^{-1})	1 σ	PE1 Ca (mg L^{-1})	1 σ	RC1 Ca (mg L^{-1})	1 σ	RC2 Ca (mg L^{-1})	1 σ
Aug	92.7	15.9	-	-	-	-	-	-	-	-
Sept	101	3.9	103	9.2	62.2	7.0	40.0	0.2	235	10.8
Oct	107	14.9	111	5.0	-	-	130	15.3	279	8.8
Nov	99.4	80.7	96.1	7.8	94.6	54.3	123	15.4	283	31.1
Dec	98.3	20.2	92.1	17.3	102	11.4	294	51.8	304	19.9
Jan	85.8	10.4	91.1	16.5	75.4	7.5	286	6.9	247	22.6
Feb	86.0	13.1	89.0	12.5	90.0	2.5	280	72.0	63.2	9.7
Mar	85.4	5.1	81.7	15.1	90.8	9.2	123	11.7	189	9.1
Apr	85.0	5.8	88.0	11.0	86.1	12.2	290	18.3	41.7	21.8
May	86.8	8.1	87.0	11.7	72.0	38.4	63.5	14.2	-	-
June	-	-	-	-	55.4	9.3	93.3	17.3	-	-
July	98.5	9.5	97.6	33.2	38.2	5.1	-	-	-	-
Aug	101	20.7	97.9	14.7	54.6	6.3	77.5	29.3	41.7	21.8

Table S21 Total calcium concentrations in unfiltered Poole's Cavern dripwater samples from August 2008 to August 2009. Values are the average of triplicate analyses by F-AAS.

	PE1		RC1		RC2	
Date	K (mg L^{-1})	1 σ	K (mg L^{-1})	1 σ	K (mg L^{-1})	1 σ
Sep-08	3.85	0.00	6.33	0.06	4.65	0.08
Oct-08	5.59	0.01	7.32	0.06	9.91	0.09
Nov-08	6.77	0.13	6.50	0.02	8.54	0.07
Dec-08	7.11	0.01	7.59	0.02	4.72	0.01
Jan-09	4.30	0.01	3.83	0.00	7.93	0.06
Feb-09	4.84	0.06	4.83	0.06	1.28	0.07
Mar-09	4.63	0.01	6.18	0.10	4.48	0.05
Apr-09	9.90	-	-	-	-	-
May-09	-	-	-	-	-	-
Jun-09	10.43	-	-	-	-	-
Jul-09	10.16	-	-	-	-	-

Table S22 Total potassium concentrations in unfiltered Poole's Cavern dripwater samples from September 2008 to July 2009. Values are the average of triplicate analyses by F-AAS. Potassium concentrations in BC1 and BC2 drips were not determinable. Discharge at drip points RC1 and RC2 from April to July 2009 was not sufficient to complete the full range of analyses.

Drip	Date	Cl (mg L^{-1})	1 σ	NO_3 (mg L^{-1})	1 σ	SO_4 (mg L^{-1})	1 σ
BC1	Jul-08	9.86	1.71	8.43	0.16	9.06	0.65
BC1	Aug-08	9.82	2.33	7.25	0.77	7.93	0.92
BC1	Sep-08	9.27	0.17	8.64	1.20	8.56	0.20
BC1	Oct-08	3.78	-	11.69	-	13.41	-
BC1	Jan-09	5.41	-	12.00	0.85	6.78	0.09
BC1	Feb-09	6.30	-	10.56	-	6.25	-
BC1	Mar-09	0.03	0.04	0.78	0.41	0.04	0.01
BC1	Apr-09	6.48	0.29	9.30	0.64	6.14	0.27
BC1	May-09	3.88	4.00	5.89	5.18	3.64	3.87
BC1	Jun-09	13.58	0.96	7.75	0.21	6.33	0.50
BC1	Jul-09	5.86	1.67	15.83	10.93	5.94	2.09
BC1	Aug-09	6.97	0.07	7.87	0.12	6.13	0.03
BC2	Jul-08	9.40	0.72	7.48	0.52	8.03	0.01
BC2	Aug-08	9.37	0.92	5.56	0.13	6.96	1.26
BC2	Sep-08	8.42	0.07	4.63	0.00	7.34	0.08
BC2	Oct-08	2.92	1.26	3.86	0.35	2.51	0.19
BC2	Jan-09	6.72	0.13	12.09	0.96	7.71	0.09
BC2	Feb-09	7.18	0.02	11.36	0.54	7.02	0.09
BC2	Mar-09	7.59	0.27	19.66	5.89	8.49	0.98
BC2	Apr-09	2.27	0.02	7.35	0.06	2.70	0.05
BC2	May-09	8.09	0.49	17.68	0.11	7.80	1.09
BC2	Jun-09	6.71	1.88	9.20	2.83	6.28	1.84
BC2	Jul-09	8.70	1.77	11.40	3.97	7.27	1.50
BC2	Aug-09	0.00	0.00	0.32	0.09	0.06	0.04
PE1	Jul-08	7.05	0.05	3.94	0.33	55.62	0.83
PE1	Aug-08	6.68	0.42	4.55	0.61	47.21	2.91
PE1	Sep-08	8.04	0.04	8.36	2.91	52.04	1.22
PE1	Oct-08	3.18	0.18	3.89	0.74	9.57	10.58
PE1	Jan-09	6.65	0.32	7.56	0.70	41.34	2.55
PE1	Feb-09	7.53	0.01	6.47	0.08	43.16	0.07
PE1	Mar-09	6.61	0.39	5.84	0.93	37.69	4.98
PE1	Apr-09	4.62	4.12	7.33	2.57	27.28	26.06
PE1	May-09	6.73	1.11	5.18	1.66	39.65	5.13
PE1	Jun-09	0.46	0.45	1.66	0.91	2.60	2.49
PE1	Jul-09	5.90	2.35	3.52	1.27	34.67	12.69
RC1	Aug-08	8.36	1.79	6.13	1.00	17.72	0.42
RC1	Sep-08	8.50	0.07	4.70	0.03	25.18	0.17
RC1	Oct-08	3.35	1.56	13.48	0.40	3.91	1.91
RC1	Jan-09	8.96	1.63	8.75	1.74	30.43	5.99
RC1	Feb-09	0.10	0.02	4.38	0.29	0.79	0.07
RC1	Mar-09	8.37	0.12	13.91	0.42	27.15	0.60
RC1	Apr-09	8.17	0.70	10.53	8.68	23.08	1.86
RC1	May-09	8.46	0.06	10.96	7.77	20.27	1.27
RC1	Jun-09	10.33	2.74	17.55	17.17	18.84	0.77
RC1	Aug-08	8.73	0.06	10.12	3.08	19.05	0.85
RC2	Sep-08	8.61	0.01	5.95	0.00	27.15	0.08
RC2	Oct-08	0.40	0.37	2.82	1.28	1.48	1.16
RC2	Jan-09	7.55	0.11	8.68	3.45	27.86	0.40
RC2	Feb-09	5.19	7.24	10.40	12.78	9.91	13.40
RC2	Mar-09	8.59	0.22	20.37	19.39	28.48	0.72
RC2	Apr-09	8.36	0.01	8.38	2.09	19.36	0.05
RC2	May-09	8.69	0.16	11.35	1.52	19.02	0.33
RC2	Jun-09	9.93	1.90	9.56	4.23	22.79	4.90

Table S23 Total anion concentrations in unfiltered Poole's Cavern dripwater samples from July 2008 to July 2009. Values are the average of triplicate analyses by IC.

Appendix IV Stable isotope data repository: Poole's Cavern dripwaters

		δD (‰ VSMOW)		$\delta^{18}O$(‰ VSMOW)	
Drip point	**Date**	**Mean**	**1 σ**	**Mean**	**1 σ**
PE1	22/09/2008	-47.61	0.21	-7.37	0.13
PE1	21/10/2008	-48.10	0.37	-7.47	0.08
PE1	29/10/2008	-48.29	0.08	-7.24	0.09
PE1	5/11/2008	-47.78	0.43	-7.36	0.12
PE1	14/11/2008	-47.52	0.48	-7.10	0.02
PE1	21/11/2008	-46.14	0.50	-7.01	0.00
PE1	27/11/2008	-48.84	0.36	-7.38	0.04
PE1	19/12/2008	-48.81	0.32	-7.55	0.04
PE1	26/01/2009	-48.61	0.26	-7.68	0.04
PE1	23/02/2009	-49.03	0.08	-7.48	0.26
PE1	24/03/2009	-48.94	1.29	-7.51	0.12
PE1	20/04/2009	-49.00	0.02	-7.57	0.11
PE1	1/07/2009	-49.32	0.14	-7.59	0.07
PE1	20/07/2009	-48.86	0.17	-6.75	0.11
BC1	27/11/2008	-47.04	0.19	-7.18	0.17
BC1	19/12/2008	-48.82	0.28	-7.53	0.00
BC1	26/01/2009	-52.04	0.22	-8.02	0.11
BC1	23/02/2009	-51.75	0.23	-7.88	0.17
BC1	24/03/2009	-52.27	0.19	-7.91	0.15
BC1	20/04/2009	-52.37	1.13	-8.04	0.21
BC1	25/05/2009	-52.70	0.57	-8.26	0.04
BC1	1/07/2009	-52.14	0.20	-7.98	0.03
BC1	20/07/2009	-52.72	0.31	-7.98	0.10
BC2	27/11/2008	-46.50	0.40	-7.27	0.03
BC2	19/12/2008	-48.88	0.10	-7.53	0.01
BC2	23/02/2009	-50.46	0.20	-7.85	0.01
BC2	24/03/2009	-50.25	0.13	-7.79	0.19
BC2	20/04/2009	-50.56	0.03	-7.72	0.04
BC2	25/05/2009	-51.85	0.22	-8.07	0.04
BC2	1/07/2009	-51.70	0.74	-8.12	0.09
BC2	20/07/2009	-52.45	0.52	-8.19	0.02
RC1	21/10/2008	-49.94	0.26	-7.69	0.11
RC1	27/11/2008	-47.96	0.13	-7.52	0.08
RC1	19/12/2008	-49.12	0.74	-7.49	0.04
RC1	23/02/2009	-48.10	0.29	-7.55	0.01
RC1	24/03/2009	-49.58	0.11	-7.83	0.09
RC1	20/04/2009	-49.93	1.11	-7.57	0.02
RC1	25/05/2009	-49.94	0.19	-7.64	0.12
RC1	20/07/2009	-49.93	0.27	-7.61	0.10
RC2	21/10/2008	-46.74	0.09	-7.05	0.09
RC2	27/11/2008	-49.46	0.40	-7.52	0.02
RC2	19/12/2008	-47.74	0.10	-7.33	0.11
RC2	26/01/2009	-49.26	0.42	-7.45	0.03
RC2	23/02/2009	-47.95	0.11	-7.47	0.08
RC2	24/03/2009	-49.29	0.14	-7.62	0.01
RC2	20/04/2009	-48.89	0.34	-7.70	0.12
RC2	25/05/2009	-49.02	0.04	-7.56	0.02

Table S24 Summary water isotope data from Poole's Cavern dripwater samples

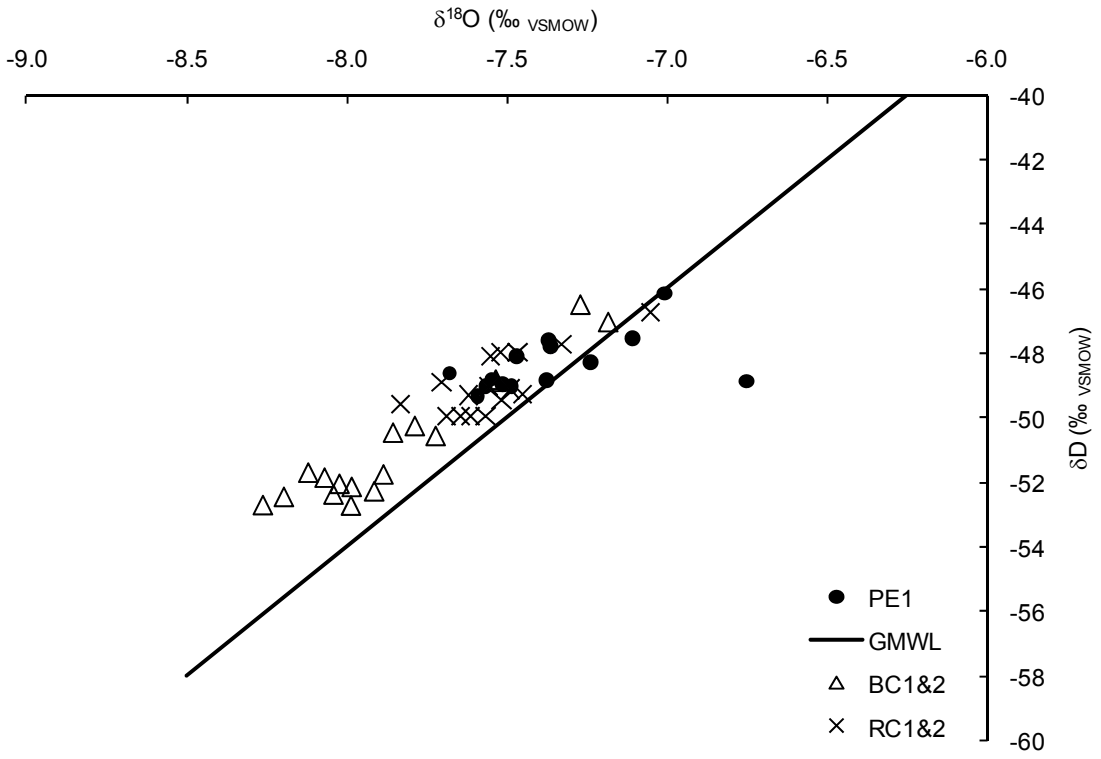

Figure S1 Cross plot of δD and $\delta^{18}O$ data from Poole's Cavern dripwaters. Solid line is the global mean water line (GMWL).

Appendix V Fluorescence data repository: Poole's Cavern sequentially filtered dripwater samples

Date	Fraction	Peak C Intensity	Emission wavelength (nm)	Peak A Intensity	Emission wavelength (nm)
21/09/2008	Raw	179	411	275	410
23/10/2008	Raw	328	401	416	413
25/11/2008	Raw	306	396	367	396
18/12/2008	Raw	350	395	457	397
26/01/2009	Raw	347	402	401	404
23/02/2009	Raw	333	394	433	394
21/03/2009	Raw	333	398	509	402
20/04/2009	Raw	377	394	477	412
30/05/2009	Raw	301	402	395	420
30/06/2009	Raw	186	408	259	414
20/07/2009	Raw	216	404	359	402
15/08/2009	Raw	367	406	207	398
21/09/2008	< 1 μm	306	396	440	407
23/10/2008	< 1 μm	333	398	407	418
25/11/2008	< 1 μm	254	402	452	410
18/12/2008	< 1 μm	341	395	402	410
26/01/2009	< 1 μm	339	392	410	406
23/02/2009	< 1 μm	306	402	364	412
21/03/2009	< 1 μm	333	398	509	402
20/04/2009	< 1 μm	373	388	473	406
30/05/2009	< 1 μm	237	394	365	408
21/09/2008	≤ 100 nm	301	400	446	408
23/10/2008	≤ 100 nm	320	394	425	394
25/11/2008	≤ 100 nm	94	414	132	411
18/12/2008	≤ 100 nm	353	395	430	418
26/01/2009	≤ 100 nm	347	406	430	402
23/02/2009	≤ 100 nm	320	402	467	414
21/03/2009	≤ 100 nm	333	398	509	402
20/04/2009	≤ 100 nm	383	394	470	406
30/05/2009	≤ 100 nm	191	404	361	412
21/09/2008	≤ 1 nm	314	401	437	415
23/10/2008	≤ 1 nm	329	401	504	411
25/11/2008	≤ 1 nm	81	424	125	417
18/12/2008	≤ 1 nm	365	404	462	402
26/01/2009	≤ 1 nm	313	402	380	420
23/02/2009	≤ 1 nm	302	400	492	402
21/03/2009	≤ 1 nm	333	398	509	402
20/04/2009	≤ 1 nm	366	398	525	406
30/05/2009	≤ 1 nm	154	408	257	416

Table S25 Raman-corrected peak fluorescence intensities and emission wavelengths from sequentially-filtered dripwater samples from Poole's Cavern drip point RC1.

Date	Fraction	Peak C Intensity	Emission wavelength (nm)	Peak A Intensity	Emission wavelength (nm)
21/09/2008	Raw	337	393	470	404
23/10/2008	Raw	347	389	423	395
25/11/2008	Raw	314	398	365	410
18/12/2008	Raw	325	400	395	400
26/01/2009	Raw	327	388	384	406
23/02/2009	Raw	322	392	418	406
21/03/2009	Raw	333	398	509	402
20/04/2009	Raw	323	390	404	412
30/05/2009	Raw	337	394	428	408
30/06/2009	Raw	198	398	351	406
15/08/2009	Raw	205	404	362	400
21/09/2008	< 1 μm	336	399	529	398
23/10/2008	< 1 μm	334	408	453	395
25/11/2008	< 1 μm	314	397	532	411
18/12/2008	< 1 μm	313	395	376	405
26/01/2009	< 1 μm	321	398	374	416
23/02/2009	< 1 μm	143	414	222	420
21/03/2009	< 1 μm	333	398	509	402
20/04/2009	< 1 μm	333	396	415	414
30/05/2009	< 1 μm	324	392	489	400
15/08/2009	< 1 μm	188	406	328	418
21/09/2008	≤ 100 nm	329	399	534	405
23/10/2008	≤ 100 nm	350	393	488	402
25/11/2008	≤ 100 nm	293	397	383	406
18/12/2008	≤ 100 nm	159	407	253	416
26/01/2009	≤ 100 nm	317	394	389	408
23/02/2009	≤ 100 nm	330	402	473	400
21/03/2009	≤ 100 nm	333	398	509	402
20/04/2009	≤ 100 nm	343	396	518	404
30/05/2009	≤ 100 nm	314	298	456	398
15/08/2009	≤ 100 nm	193	406	363	410
21/09/2008	≤ 1 nm	369	397	460	401
23/10/2008	≤ 1 nm	341	392	545	401
25/11/2008	≤ 1 nm	290	398	342	407
18/12/2008	≤ 1 nm	88	409	273	421
26/01/2009	≤ 1 nm	313	402	380	420
23/02/2009	≤ 1 nm	332	398	508	402
21/03/2009	≤ 1 nm	333	398	509	402
20/04/2009	≤ 1 nm	331	392	506	414
30/05/2009	≤ 1 nm	311	396	456	404
15/08/2009	≤ 1 nm	187	410	391	410

Table S26 Raman-corrected peak fluorescence intensities and emission wavelengths from sequentially-filtered dripwater samples from Poole's Cavern drip point RC1.

Date	Fraction	Peak C Intensity	Emission wavelength (nm)	Peak A Intensity	Emission wavelength (nm)
26/08/2008	Raw	16	418	34	412
21/09/2008	Raw	17	416	26	420
23/10/2008	Raw	21	428	34	423
25/11/2008	Raw	18	412	30	438
18/12/2008	Raw	17	418	29	418
26/01/2009	Raw	30	422	39	416
23/02/2009	Raw	24	390	39	430
21/03/2009	Raw	48	418	59	420
20/04/2009	Raw	20	412	30	446
30/05/2009	Raw	14	422	24	432
1/07/2009	Raw	19	418	27	430
20/07/2009	Raw	20	402	33	426
29/07/2008	< 1 μm	18	416	37	429
26/08/2008	< 1 μm	25	428	42	418
23/10/2008	< 1 μm	21	429	35	423
21/03/2009	< 1 μm	48	418	71	416
30/05/2009	< 1 μm	17	412	28	420
1/07/2009	< 1 μm	17	416	28	436
20/07/2009	< 1 μm	20	428	37	438
29/07/2008	≤ 100 nm	18	424	31	430
21/03/2009	≤ 100 nm	46	418	76	416
30/05/2009	≤ 100 nm	21	410	33	424
1/07/2009	≤ 100 nm	17	404	35	414
20/07/2009	≤ 100 nm	20	424	33	416
29/07/2008	≤ 1 nm	17	416	28	418
21/03/2009	≤ 1 nm	43	418	75	408
30/05/2009	≤ 1 nm	16	416	30	410
1/07/2009	≤ 1 nm	14	414	37	418
20/07/2009	≤ 1 nm	20	430	41	430

Table S27 Raman-corrected peak fluorescence intensities and emission wavelengths from sequentially-filtered dripwater samples from Poole's Cavern drip point BC1.

Date	Fraction	Peak C Intensity	Emission wavelength (nm)	Peak A Intensity	Emission wavelength (nm)
26/08/2008	Raw	17	418	32	408
21/09/2008	Raw	14	424	26	416
23/10/2008	Raw	17	416	30	424
25/11/2008	Raw	18	424	31	416
18/12/2008	Raw	20	416	31	442
26/01/2009	Raw	28	418	40	414
23/02/2009	Raw	25	416	45	418
21/03/2009	Raw	45	420	59	418
20/04/2009	Raw	18	408	33	406
30/05/2009	Raw	16	424	30	416
30/06/2009	Raw	16	430	28	432
20/07/2009	Raw	17	424	37	422
29/07/2008	< 1 μm	16	412	27	418
26/08/2008	< 1 μm	22	430	39	418
23/10/2008	< 1 μm	21	404	36	412
30/05/2009	< 1 μm	16	412	30	416
20/07/2009	< 1 μm	18	420	37	412
29/07/2008	≤ 100 nm	18	410	30	416
26/08/2008	≤ 100 nm	18	424	38	414
30/05/2009	≤ 100 nm	16	434	32	410
20/07/2009	≤ 100 nm	18	424	35	446
29/07/2008	≤ 1 nm	19	436	27	418
26/08/2008	≤ 1 nm	18	410	40	396
30/05/2009	≤ 1 nm	15	422	33	428
20/07/2009	≤ 1 nm	18	424	38	420

Table S28 Raman-corrected peak fluorescence intensities and emission wavelengths from sequentially-filtered dripwater samples from Poole's Cavern drip point BC2.

Date	Fraction	Peak C Intensity	Emission wavelength (nm)	Peak A Intensity	Emission wavelength (nm)
26/08/2008	Raw	145	414	290	417
21/09/2008	Raw	144	395	227	417
23/10/2008	Raw	138	400	218	419
25/11/2008	Raw	141	406	213	409
18/12/2008	Raw	148	315	210	412
26/01/2009	Raw	162	406	257	419
23/02/2009	Raw	146	348	228	412
21/03/2009	Raw	156	412	249	422
20/04/2009	Raw	161	404	274	412
30/05/2009	Raw	101	416	172	408
30/06/2009	Raw	119	414	183	416
20/07/2009	Raw	125	410	211	422
15/08/2009	Raw	125	406	251	404
29/07/2008	< 1 μm	92	410	162	427
26/08/2008	< 1 μm	151	415	341	417
21/09/2008	< 1 μm	148	400	282	404
23/10/2008	< 1 μm	141	408	245	423
25/11/2008	< 1 μm	161	402	343	416
18/12/2008	< 1 μm	315	392	401	409
26/01/2009	< 1 μm	153	405	250	423
23/02/2009	< 1 μm	152	404	260	406
21/03/2009	< 1 μm	158	402	278	398
20/04/2009	< 1 μm	161	397	264	422
30/05/2009	< 1 μm	131	400	260	416
30/06/2009	< 1 μm	128	408	228	410
20/07/2009	< 1 μm	108	418	189	428
15/08/2009	< 1 μm	111	404	227	412
29/07/2008	≤ 100 nm	88	403	152	410
26/08/2008	≤ 100 nm	114	424	318	422
21/09/2008	≤ 100 nm	137	403	273	410
23/10/2008	≤ 100 nm	148	412	241	421
25/11/2008	≤ 100 nm	119	405	186	423
18/12/2008	≤ 100 nm	174	402	266	412
26/01/2009	≤ 100 nm	152	409	241	418
23/02/2009	≤ 100 nm	158	410	240	416
21/03/2009	≤ 100 nm	149	404	267	404
20/04/2009	≤ 100 nm	167	398	257	407
30/05/2009	≤ 100 nm	126	404	241	414
30/06/2009	≤ 100 nm	132	406	256	410
20/07/2009	≤ 100 nm	91	400	197	406
15/08/2009	≤ 100 nm	119	412	228	418
29/07/2008	≤ 1 nm	89	408	168	412
26/08/2008	≤ 1 nm	136	421	289	423
21/09/2008	≤ 1 nm	111	401	212	415
23/10/2008	≤ 1 nm	113	416	190	415
25/11/2008	≤ 1 nm	68	417	112	421
18/12/2008	≤ 1 nm	156	318	261	418
26/01/2009	≤ 1 nm	133	411	212	425
23/02/2009	≤ 1 nm	149	398	236	420
21/03/2009	≤ 1 nm	159	406	293	408
20/04/2009	≤ 1 nm	153	402	294	419
30/05/2009	≤ 1 nm	127	412	255	411
30/06/2009	≤ 1 nm	113	400	228	424
20/07/2009	≤ 1 nm	99	412	193	416
15/08/2009	≤ 1 nm	112	414	225	424

Table S29 Raman-corrected peak fluorescence intensities and emission wavelengths from sequentially-filtered dripwater samples from Poole's Cavern drip point PE1.

Appendix VI Colloid characterisation data

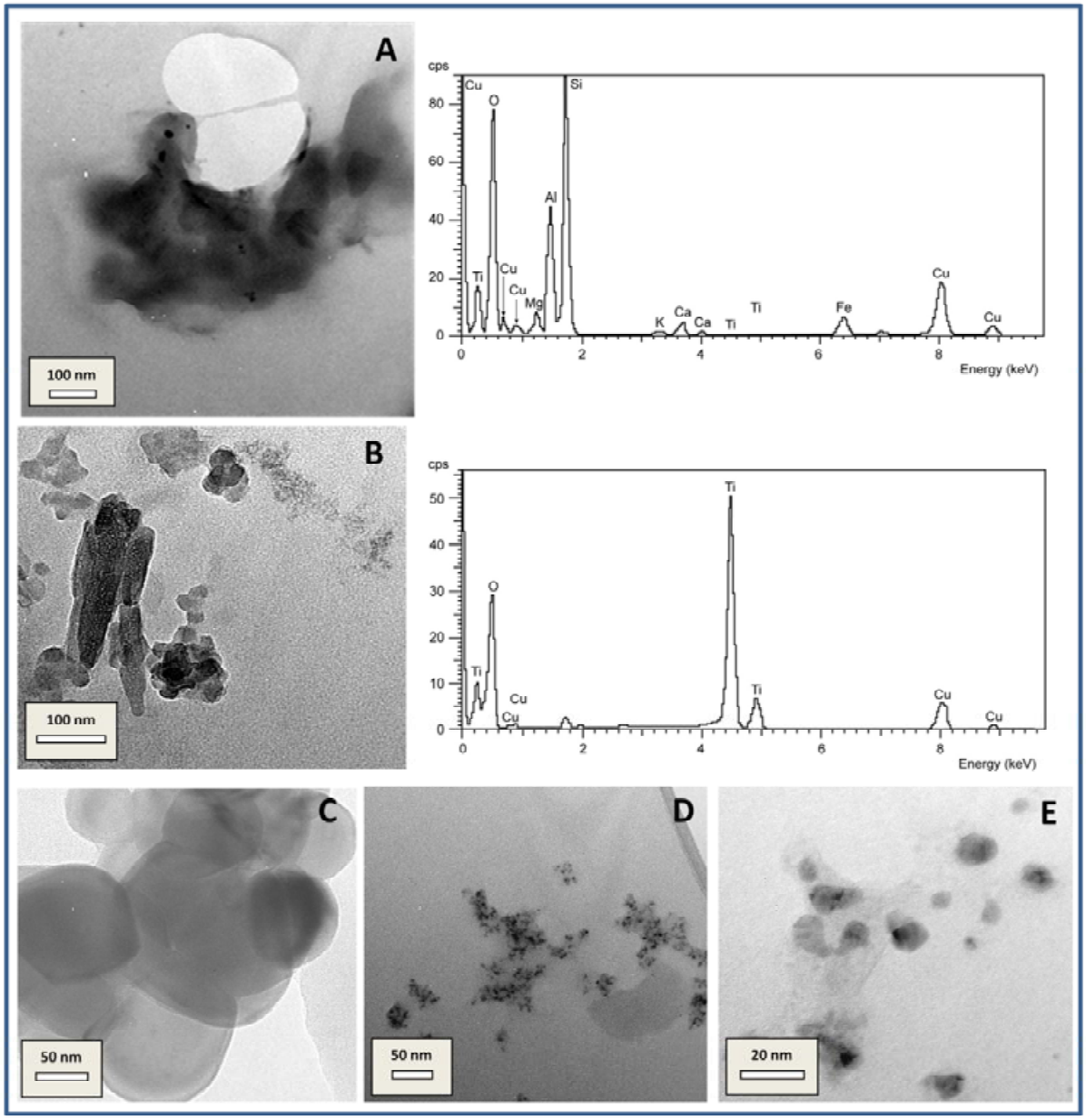

Figure S2 Representative TEM images and X-EDS spectra for colloidal entities in Grotta d'Ernesto dripwaters sampled in November 2008. Images and spectra from St-1 samples (a) coarse colloidal aggregate of NOM, aluminosilicates and FeOx, (b) rod-shaped Ti bearing coarse colloidal aggregate. Image (c), an aggregate of large globular colloids in St-1 dripwater. Images from St-ER77 drip (d) fine colloidal aggregates and (e) small globular colloids resembling humic and fulvic macromolecules. Cu peaks in X-EDS spectra originate from supporting grid (TEM analyses by M. Baalousha).

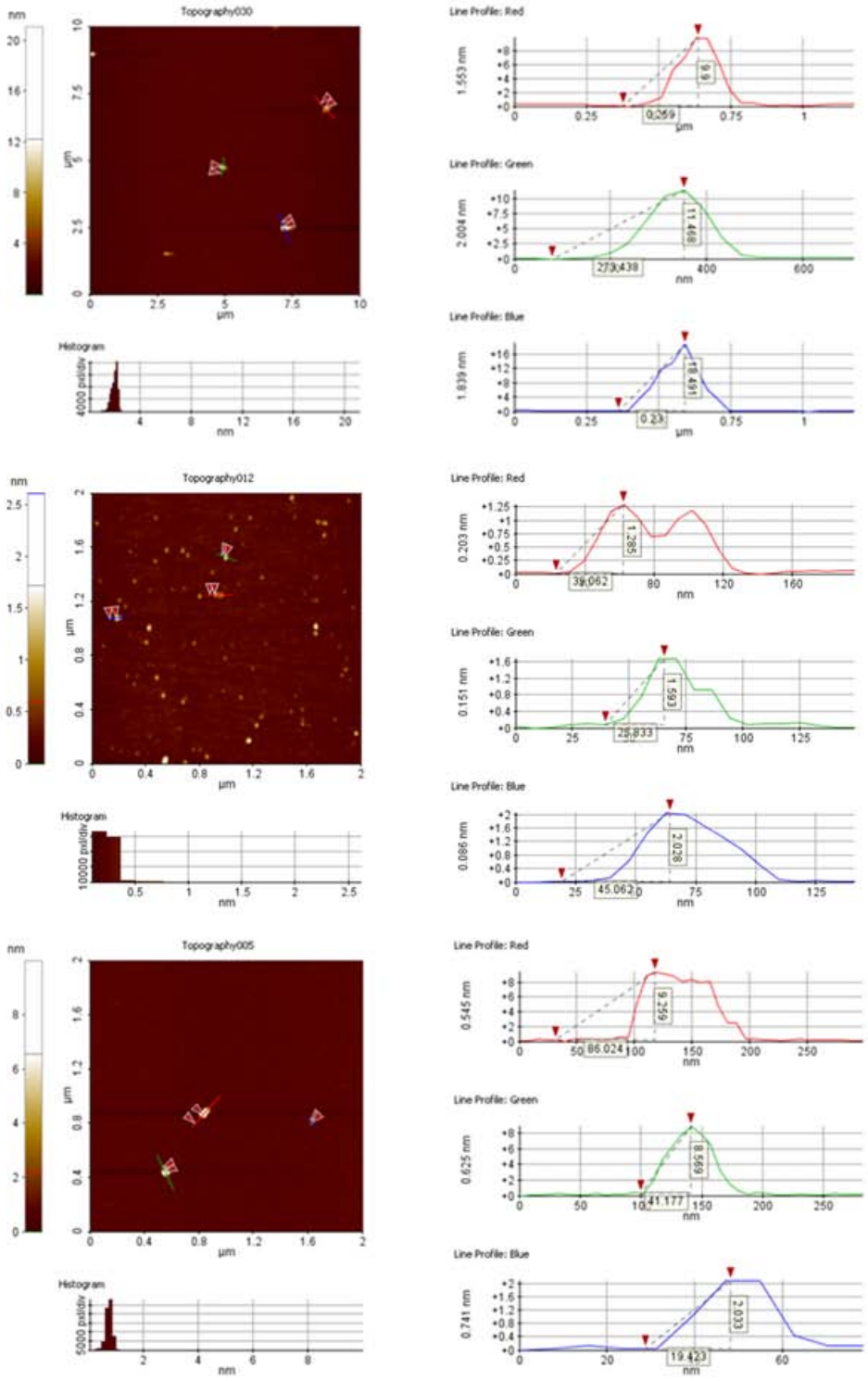

Figure S3 Atomic force microscopy images with particle height measurements from analyses of (top) PE1, (middle) LB3 and (bottom) ER77 dripwater samples. These analyses confirm the ubiquitous presence of nanoparticles in cave dripwaters (AFM analyses by Y. Ju-Nam).

Appendix VII Stalagmite dissolution analyses

	Concentration (ppm calcite)																	
Sample	TOC	Mg	Al	Ti	V	Cr	Mn	Fe	Co	Ni	Cu	Zn	Br	Sr	Y	Cd	Ba	Pb
OBIR A	130	1103	54.3	-	-	-	1.02	330.1	-	4.38	13.1	-	8.74	24.8	-	3.09	174.2	707.7
OBIR B	170	1079	31.0	-	-	-	-	7.91	-	3.31	8.17	-	-	22.8	-	2.83	162.8	735.2
OBIR C	140	1106	27.6	-	-	-	-	8.47	-	3.31	8.00	-	4.51	24.4	-	2.74	165.9	800.7
ER77 A	320	808	35.0	-	-	-	-	30.2	0.19	38.6	8.72	32.3	4.18	9.93	-	0.02	2.47	2.00
ER77 B	370	783	27.7	-	-	-	-	19.3	0.18	59.3	8.62	7.56	4.45	10.3	-	0.09	2.31	0.95
ER77 C	520	694	37.7	-	-	-	-	22.1	0.01	4.47	11.5	15.2	4.97	9.22	1.37	1.29	2.67	2.28
ER77 D1	495	672	27.6	-	-	-	-	16.9	0.12	4.22	9.71	14.7	-	10.2	-	0.89	11.74	1.73
ER77 D2	515	667	31.1	-	-	-	-	19.1	0.07	5.16	9.66	11.3	-	10.2	-	0.74	2.97	1.33
ER77 C2	610	768	30.1	-	-	-	-	19.8	0.08	7.29	17.0	19.7	4.22	9.96	1.54	1.47	2.91	2.28
PC-08-1 P1	200	-	203.5	0.89	20.7	0.38	-	11.1	0.20	4.28	8.17	4.64	3.42	134.5	-	-	53.4	2.46
PC-08-1 D1	850	-	186.3	0.08	26.9	0.29	-	19.9	0.19	4.70	8.85	36.8	4.50	114.5	-	-	50.3	8.92
PC-08-1 P2	1050	-	62.8	0.15	20.1	0.37	-	13.7	0.21	3.87	8.97	5.23	1.82	137.1	-	-	53.5	2.51
PC-08-1 D2	680	-	263.0	0.07	24.0	0.34	-	10.9	0.22	4.68	8.11	4.69	4.20	119.7	-	-	50.6	2.66
PC-08-1 P3	1590	-	92.5	0.69	23.3	0.12	-	11.2	0.19	3.80	9.05	6.00	2.49	128.1	-	-	49.1	3.06
PC-08-1 D3	560	-	62.9	0.23	35.6	0.41	-	27.7	0.26	23.2	20.6	12.0	3.14	109.5	-	-	45.9	3.40
PC-08-1 P4	1300	-	65.8	-0.06	23.3	0.17	-	21.9	0.13	3.37	8.94	4.89	2.21	121.8	-	-	50.0	3.40
PC-08-1 D4	730	-	139.1	0.44	28.5	0.19	-	16.0	0.18	5.65	11.3	7.13	4.91	123.8	-	-	53.2	3.61
PC-08-1 P5	630	-	59.7	0.03	23.9	0.38	-	25.3	0.14	4.01	9.33	5.31	1.90	127.0	-	-	50.8	3.06
PC-08-1 D5	550	-	97.6	0.03	33.9	0.85	-	21.9	0.29	4.96	10.2	5.46	2.37	111.6	-	-	47.5	3.67
PC-08-1 P6	860	-	92.1	1.89	28.6	0.43	-	23.1	0.23	3.88	11.4	6.98	2.50	114.0	-	-	45.9	3.72
PC-08-1 D6	440	-	71.6	0.10	29.7	0.57	1.32	36.0	0.24	5.92	11.1	9.72	3.44	111.6	-	-	47.8	3.51
PC-08-1 P7	750	-	96.7	0.40	24.1	0.96	2.70	43.6	0.15	5.82	27.7	16.5	3.63	126.7	-	-	56.0	4.57
PC-08-1 D7	1010	-	126.9	0.25	35.4	0.72	1.92	33.5	0.27	5.65	14.3	9.65	3.33	108.1	-	-	48.0	4.49
PC-08-1 P8	720	-	189.2	0.03	23.6	1.34	-	19.7	0.17	5.85	78.1	51.5	2.08	128.7	-	-	51.6	6.37
PC-08-1 D8	860	-	79.9	0.46	29.1	0.27	-	21.3	0.23	3.84	9.75	16.3	3.75	113.4	-	-	46.2	2.98
PC-08-1 P9	740	-	77.4	-0.08	17.6	0.83	-	25.2	0.27	4.08	8.24	5.17	0.17	133.4	-	-	52.3	2.48
PC-08-1 P9	3210	-	68.5	0.41	40.6	0.27	-	19.1	0.28	4.31	10.2	5.60	4.54	93.4	-	-	42.7	3.52
LB3 A	485	-	29.5	-	-	-	-	27.0	0	24.1	22.3	22.7	4.35	76.8	-	-	5.54	1.23
LB3 B	455	-	30.6	-	-	-	1.64	48.2	0	61.2	8.69	5.59	5.16	72.7	-	-	4.47	0.96
LB3 C	445	-	66.5	-	-	-	1.26	55.1	0	5.03	8.21	5.56	3.95	73.3	-	-	4.92	0.80
LB3 D	630	-	37.3	-	-	-	-	44.0	0	9.40	12.7	9.74	4.76	74.1	-	-	4.92	0.87

Table S30 Results of total organic carbon (TOC) and ICP-MS analyses of dissolved calcite powders from the samples OB81, ER77, PC-08-1 and LB3. Elements which were not determinable are marked with a dash. Analyses of OB81 were sub-samples from the same homogenised fragment. Samples A, B, C and D from ER77 were drilled from the top of the sample and working toward the base at around 2 mm resolution. Samples A, B, C and D from the LB3 stalagmite are contiguous sub-samples working from the base of the sample toward the top at approximately 2 mm resolution.

Appendix VIII Suplementary hydrological information

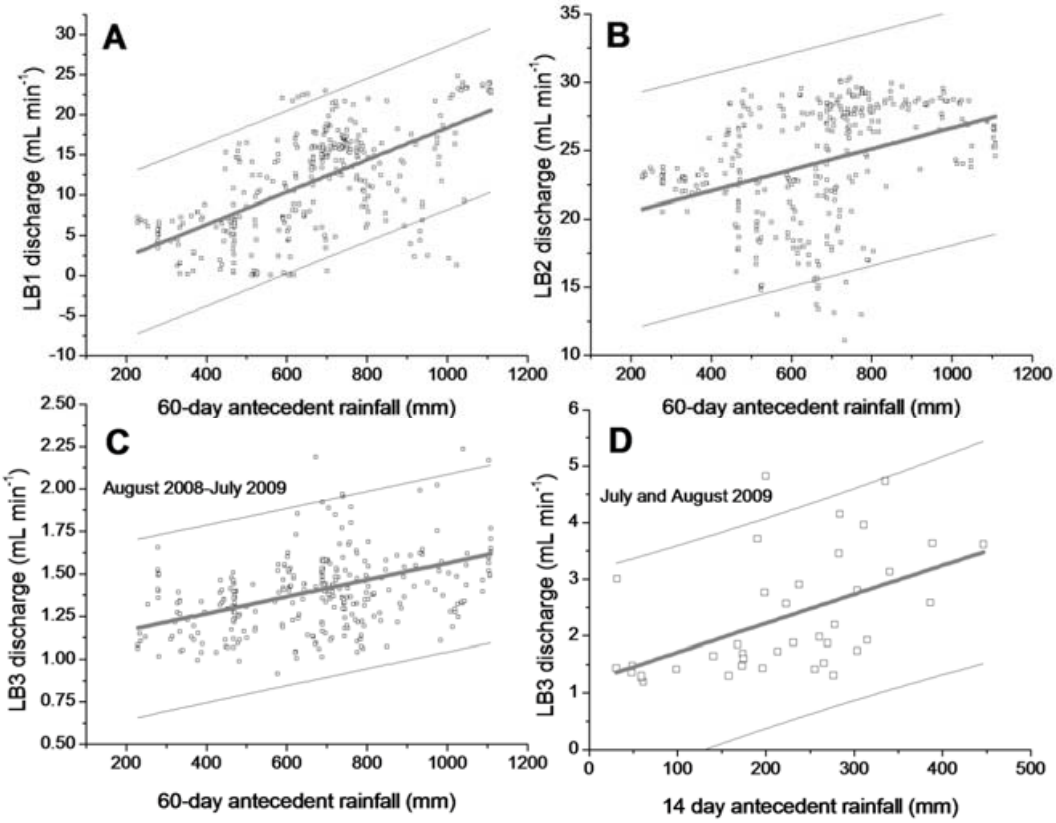

Figure S4 Cross-plots of discharge vs antecedent rainfall for Lower Balls Green Mine drip points LB1 (a) and LB2 (b) corresponding to the period June 2008 to August 2009, (c) LB3 for the period of August 2008-July 2009 and (d) LB3 over the period July-August 2009. Grey lines are linear regression trendlines and black lines are 95% prediction bands. Antecedent rainfall calculated from the daily mean rainfall for Gloucestershire. Discharge estimated based on average drop volume of 0.15 mL.

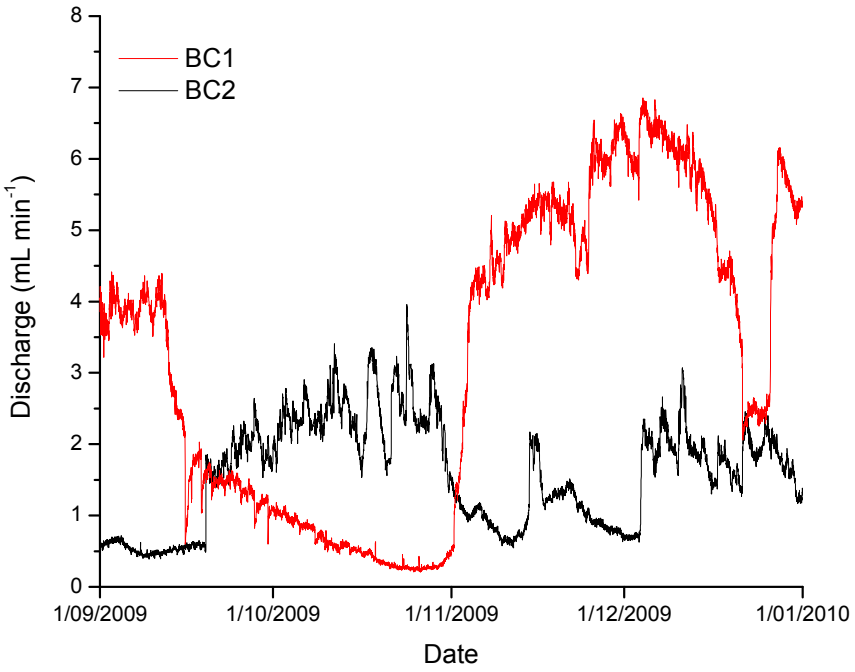

Figure S5 Overflow-underflow type relationship between discharge of BC1 and BC2 drips at Poole's Cavern between 1/9/2009 and 31/12/2009. Discharge estimated based on average drop volume of 0.15 ml.

Appendix IX Supplementary information on DGT experiments and speciation modelling

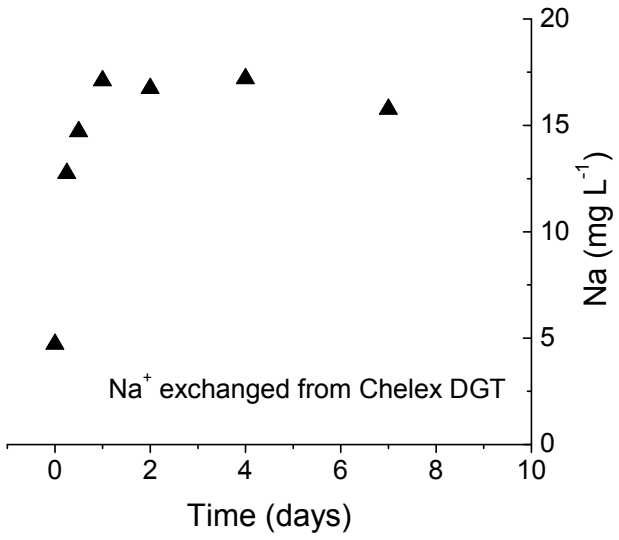

Figure S6 Sodium concentration in solution in the DGT depletion experiment with PE1 dripwater from June 2009. Sodium ions are released from the Chelex ion exchange resin in response to binding by metal ions from solution. The plateau in Na concentration coincided with the cessation of Sr and Ba depletion in solution. This is argued to reflect the blocking of DGT binding sites by Ca which would directly compete with the other alkaline earth metals.

Ion	r_{ion}	z/r_{ion}	n_1	PE1 (mg L^{-1})	$pCO_2 = 10^{-5}$ M-HA (%) pH 11	$pCO_2 = 10^{-5}$ inorg (%) pH 11	$pCO_2 = 10^{-5}$ Precip (%) pH 11	$pCO_2 = 10^{-4}$ M-HA (%) pH 11	$pCO_2 = 10^{-4}$ inorg (%) pH 11	$pCO_2 = 10^{-4}$ Precip (%) pH 11
Al^{3+}	0.5	6	0.42	1200	0.06	100	0	0.03	100	0
Cr^{3+}	0.69	4.3	-	11.3	1.10	98.9	0	0.96	99.0	0
V^{3+}	0.74	4.1	-	20.3	0.00	98.9	0	0.00	98.9	0
Cu^{2+}	0.69	2.9	0.53	1.78	99.1	0.86	0	99.9	0.11	0
Ni^{2+}	0.72	2.8	0.65	0.95	29.0	70.9	0	20.3	79.7	0
Zn^{2+}	0.74	2.7	0.67	0.49	99.9	0.09	0	100	0.06	0
Co^{2+}	0.74	2.7	0.71	0.58	14.1	85.9	0	7.71	92.3	0
Fe^{2+}	0.76	2.6	0.3	2.71	100	0.01	0	100	0.01	0
Ca^{2+}	0.99	2	0.85	74493	0.68	99.3	0	0.69	99.3	0
Sr^{2+}	1.13	1.8	0.85	65.4	7.61	92.4	0	6.38	93.6	0
Ba^{2+}	1.35	1.5	0.9	14.7	9.8	90.2	0	8.3	91.7	0

Table S31 The ionic radii (r_{ion}), ionic potentials (z/r) and the NICA-Donnan binding parameters (n_1) of cationic elements studied and predicted metal speciation in PE1 dripwater in the presence of humic acid (2.7 mg L^{-1}) using visual MINTEQ at pCO_2 values of 1 x 10^{-5} and 1 x 10^{-4}. Values of z/r and n_1 are included as indicative measures of the relative binding affinity of metal ions for binding with humic-like NOM (n_1 values are from Milne *et al*., 2003). M-HA= percentage of metal in complexes with humic acid; Inorg= percentage inorganic fraction of metal; Precip= percentage of metal precipitated as inorganic solids.